WARWICK
THE UNIVERSITY OF WARWICK

A Thesis Submitted for the Degree of PhD at the University of Warwick

Permanent WRAP URL:

http://wrap.warwick.ac.uk/149590

Copyright and reuse:
This thesis is made available online and is protected by original copyright.
Please scroll down to view the document itself.
Please refer to the repository record for this item for information to help you to cite it.
Our policy information is available from the repository home page.

For more information, please contact the WRAP Team at: wrap@warwick.ac.uk

warwick.ac.uk/lib-publications

Interaction of Self-Assembling Cyclic Peptide-Polymer Nanotubes with Biological Models

Sean Heinere Ellacott

A thesis submitted in partial fulfilment of the requirements for the degree of

Doctor of Philosophy in Chemistry

Department of Chemistry

University of Warwick

May 2020

If there's a book that you want to read, but it hasn't been written yet, then you must write it – Toni Morrison

Ville au bout de la route et route prolongeant la ville : ne choisis donc pas l'une ou l'autre, mais l'une et l'autre bien alternées.
Montagne encerclant ton regard le rabat et le contient que la plaine ronde libère. Aime à sauter roches et marches ; mais caresse les dalles où le pied pose bien à plat.
Repose-toi du son dans le silence, et, du silence, daigne revenir au son. Seul si tu peux, si tu sais être seul, déverse-toi parfois jusqu'à la foule.
Garde bien d'élire un asile. Ne crois pas à la vertu d'une vertu durable : romps-la de quelque forte épice qui brûle et morde et donne un goût même à la fadeur.
Ainsi, sans arrêt ni faux pas, sans licol et sans étable, sans mérites ni peines, tu parviendras, non point, ami, au marais des joies immortelles,

Mais aux remous pleins d'ivresses du grand fleuve Diversité.

- Victor Segalen, *Conseils au bon voyageur* in Stèles.

Ipse se nihil scire id unum sciat - Socrates

TABLE OF CONTENTS

Content

LIST OF FIGURES

LIST OF TABLES

LIST OF SCHEMES

ABBREVIATIONS

AA	Acrylic acid
AIC	Akaike Information Criteria
ANOVA	Analysis of Variance
AR	Aspect ratio
ATR-FTIR	Attenuated Total Reflection Fourier Transform Infrared spectroscopy
AUC	Area Under the Curve
BA	*n*-Butyl acrylate
Boc	tert-Butoxycarbonyle
CB-7	Cucurbit[7]uril
CDSA	Crystallisation Driven Self-Assembly
CEMA	2-chloroethylmethacrylate
CL	Cardiolipin or Diphosphatidyl glycerol
CLSM	Confocal Laser Scanning Microscopy
CP	Cyclic Peptide
CPPC	Cyclic Peptide-Polymer Conjugate
CPNT	Cyclic Peptide-Polymer Nanotube
CROP	Cationic Ring Opening Polymerisation
CSC	Core-shell cylinder model
ctRNA	Counter-transcribed RNA
CuAAc	Copper catalysed Azide-alkyne cycloaddition
Cy3	Cyanine 3
Cy5.5	Cyanine 5.5
DCM	Dichloromethane
DDS	Drug delivery system
DIPEA	N,N-Diisopropylethylamine
DMA	N,N-Dimethylacrylamide
DMF	N,N-Dimethylformamide
DMPC	1,2-Dimyristoyl-sn-glycero-3-phosphocholine
DMPG	1,2-Dimyristoyl-sn-glycero-3-phosphoglycerol
DMSO	Dimethylsufoxide
DMTMM.BF4	4-(4,6-dimethoxy-1,3,5-triazin-2-yl)-4-methyl-morpholinium tetrafluoroborate
DNA	Deoxyribonucleic acid
DOX	Doxorubicin
DPAEMA	2-(Diisopropylamino)ethyl methacrylate
EggPC	Egg Phosphatidylcholine
EPR	Enhanced Permeation and Retention
ER	Endoplasmic Reticulum
ESI-microTOF	Electrospray Ionization - micro Time of Flight
EtOx	2-ethyl-2-oxazoline
Fmoc	Fluorenylmethoxycarbonyl
FRET	Förster Resonance Energy Transfer
GEAM	Guanindine ethylacrylamide
HCTU	O-(1H-6-Chlorobenzotriazole-1-yl)-1,1,3,3-tetramethyluronium hexafluorophosphate

HEA	2-Hydroxyethyl acrylate
HEAm	2-Hydroxyethyl acrylamide
HEPES	4-(2-Hydroxyethyl)-1-piperazineethanesulfonic acid
HPLC	High Performance Liquid Chromatography
HPMA	N-(2-Hydroxypropyl)methacrylamide
IC50	Half maximal inhibitory concentration
IR	Infrared
JAcoP	Just Another Colocalisation Plugin
LUV	Large Unilamellar Vesicles
MCMC	Monte Carlo Markov Chain
MCTS	MultiCellular Tumour Spheroids
MIC	Minimum Inhibitory Concentration
MPS	Mononuclear Phagocytic System (also called RES: reticuloendothelial system)
MTT	3-(4,5-Dimethylthiazol-2-yl)-2,5-diphenyltetrazolium bromide
NAM	4-Acryloylmorpholine
NAS	N-Acryloxysuccinimide
NC analysis	Non-Compartmental Analysis
NES	Nuclear Envelope Statin
NHS	N-Hydroxysuccinimide
NIPAAm	N-Isopropylacrylamide
NMM	4-Methylmorpholine
NMR	Nuclear Magnetic Resonance
NR	Neutron reflectivity
PABTC	Propanoic Acid)yl Butyl Trithiocarbonate
PBS	Phosphate Buffer Saline
PCC	Pearson's Correlation Coefficient
PCL	poly(caprolactone)
PEG	poly(ethyleneglycol), also commonly known as poly(ethylenoxide) or PEO
PEG	poly(ethylene)
PEGMA	PEG methacrylate
PEI	poly(ethyleneimine)
PFS	poly(ferrocenyldimethylsilane)
PI	Propidium iodide
PISA	Polymerisation-Induced Self-Assembly
PK	Pharmacokinetic
PLLA	poly(L-lactide)
PMS	N-Methyl dibenzopyrazine methyl sulfate
POPC	1-Palmitoyl-2-oleoyl-sn-glycero-3-phosphocholine
POPG	1-Palmitoyl-2-oleoyl-sn-glycero-3-phosphoglycerol
PRINT	Particle Replication In Nonwetting Templates
PS	poly(styrene)
PUEMA	2-(3-(Pyridin-4-ylmethyl)ureido)ethyl)methacrylate
PVP	poly(2-vinylpyridine)
QCM-D	Quartz Crystal Microbalance with Dissipation Monitoring
RAFT	Reversible Addition Fragmentation chain transfer
RNA	Ribonucleic acid

SANS	Small Angle Neutron Scattering
SAXS	Small Angle X-Ray Scattering
SD	Standard Deviation
SDS	Sodium Dodecyl Sulfate
SE	Standard Error
SEC	Size exclusion Chromatography (also GPC: Gel Permeation Chromatography)
shRNA	Short hairpin RNA
SLD	Scattering Length Density
SLS	Static Light Scattering
SPPS	Solid Phase Peptide Synthesis
TAX	Paclitaxel
TEA	Triethylamine
TEM	Transmission Electron Microscopy
TFA	Trifluoroacetic acid
THF	Tetrahydrofuran
TIPS	Triisopropylsilane
TMV	Tobacco Mosaic Virus
UV	Ultraviolet
V601	Dimethyl 2,2'-azobis(2-methylpropionate)
VA-044	2,2'-azobis[2-(2-imidazolin-2-yl) propane] dihydrochloride
XTT	2,3-Bis-(2-Methoxy-4-Nitro-5-Sulfophenyl)-2H-Tetrazolium-5-Carboxanilide

ACKNOWLEDGEMENTS

Throughout my PhD, I have often wondered what it would feel like to write this section of my thesis. I must say, I never imagined it would be in the middle of a pandemic! Today, more than ever, the day has come to thank all the people who contributed to this work, but also to my personal life over the past three years and a half.

First, I would like to thank my supervisor Pr. Sébastien Perrier, who gave me this once in a lifetime opportunity to work on a multidisciplinary project that has brought me to so many places I've never been, both literally and figuratively. His guidance helped me become an independent researcher and realise the importance of critically assessing my and other people's work.

I would like to thank my examiners, Pr Matthew Gibson and Pr Hans Boerner for accepting to evaluate my work. I hope that you will find it interesting and somewhat useful to your own work.

I would then like to thank all the research fellows, past and present, who have helped me in the course of my PhD. I will start with Dr. Matthias Hartlieb who taught me the joys of poly(oxazoline) synthesis. I would also like to thank Dr. Raoul Peltier, who showed me the dark side of science and guided me through my discovery of biology. Thank you for teaching me how to cultivate cells, run a confocal microscope, do a toxicity assay and so many other things whilst remaining funny and zen. It was a real pleasure to work with you during my time at Warwick! I would equally like to thank Dr. Carlos Sanchez-Cano who showed me how to grow and work with spheroids, taking my 2D cell work to the next dimension! I cannot talk about working in Life Sciences without mentioning Ji Song, who pretty much changed our lives in the bio labs. Thank you so much for catering to my cells' needs and maintaining our labs! Likewise, I would like to thank Dr. Alexia Hapeshi for the discussions we had about my project and for her useful insights, we are very lucky to have you around! Coming back to Chemistry, I would like thank Dr. Edward Mansfield, who started at the same time as I did. It was nice to have you around for our office chats on data fitting (among other things), your down-to-earth advice, your proofreading skills and for all the beam times we have had together. In the cyclic peptide team, I'd equally like to thank Dr. Jie Yang for his advice and his uplifting mood, as well as his great T-shirts that kept me entertained. I am also very grateful to have worked with Dr. Qiao Song, thank you for your help and for your extensive knowledge on supramolecular systems! Last but not least, I'd like to thank Dr. Stephen Hall, without whom Chapter 4 probably would not have gone as far! Thanks for helping to arrange my 5th beam time (in Grenoble !), spending some time fitting my NR data and being so helpful and always prompt to respond to my – many - inquiries.

Looking back on my Monash experience, I'd like to thank Dr. Joaquin Sanchis-Matinez (*aka* Ximo) for hosting me at Monash and for his general enthusiasm. I'd also like to thank Dr. Estelle Suys for helping during the PK experiments, for proofreading Chapter 3 and for her kindness and positive attitude (I think I won't forget that croissant you left on my desk after two intense days of sampling and organ collection). Equally, thanks to Erny Sagita who I would honestly entrust with any surgery as she was incredibly swift and efficient. Thank you for showing me around the labs and for your constant agreeableness. Last, I'd like to thank all the people from Monash for their welcome: Cheng Sun (who I apologise to again for our little incident in the radioactive lab), Carlos Arellano, all members of the Porter group and people from D4. Special mention to my APS travel companions, Nam, John F., Meike, Alex and Matt for the beach excursions in the morning and the bar outings at night. Special thanks to now Dr. Emily Pilkington for showing me around Monash and also for the nice chats we had when she visited Warwick, living my true dream of a never-ending spring-summer. Oddly enough, I cannot help but drawing a parallel with the end of your PhD as I will also have to submit that thesis online. All the best to all of you in your future careers.

Next, I would like to thank the students who I had the pleasure to work with during my PhD. First, I'd like to thank Lizzie Eyre for her patience with me and for her perseverance during her project. Your contribution was greatly appreciated and I hope to see you again in the future.

Second, I would like to thank Gabrielle Han who I had the chance to work with for her Summer project in 2019. Thank you Gabby, for being a shining spark of joy in our lab and for sharing your enthusiasm and optimism with us. I am still deeply sorry for your loss, since you have left this world in February 2020. I wish I had spent more time in your company, as you never ceased to bring such a positive energy to our group. I will never forget the first time we managed to see thermoresponsive behaviour for the CPNT you made and how happy and excited you were that day. I am convinced that you would have become a great scientist. I am dedicating the third chapter of that thesis to you, as your work also helped me in that study.

My PhD journey would probably not have been the same if I hadn't shared that experience with other people. Starting with past members, I would first like to thank the "initial" cyclic peptide *aficionadas,* Dr. Tammie Barlow and Dr. Sophie Larnaudie. Even if I only shared an office with you for a year or so, your presence had a lasting impact on all of us. I would also like to thank Dr. Julia Rho who I pretty much spent my first three years with. Thanks for all the chats, delightful food, driving me back after our outings, giving me the opportunity to organise Sebinar 3.0 and for your help on all cyclic peptide matters.

Moving on to the second office, I'd like to thank my first life sciences companion, Dr. Caroline Bray, who I was lucky enough to meet again in Australia. I'd also like to thank Dr. Pratik Gurnani for the pleasant conversations we've had and for understanding my nerdy references. I am also grateful to Dr. Andrew Kerr for his help with setting up my trip to Australia. In the last (or first) office, I'd like to thank Dr. Joji Tanaka for being such a wild soul, you will be hard to forget (e.g. that faithful evening at Terrace Bar, your viva celebration, our trip to Scotland, to name a few). Thank you to Dr. Agnes Kuroki, who I have got to know more at Warwick despite being from the same university. Agnes, you taught me all about the rules of jet-setting and also about guanidinium moieties; thanks again for accepting to come to ISIS with us and for bringing Exploding Kittens. You were always fun to be around and to sing with!

Coming back to present members of the group, I'd first like to thank my CP co-workers. Thank you, Sophie Hill, for being around to discuss ideas with or just casually chatting about life. Thanks to Maria Kariuki for always keeping me entertained with the latest gossip and for her sympathy. I am glad I got to introduce you to the joys of Eurovision in Scotland. To Zihe/Cathy Zheng, good luck for your PhD ! All my wishes of solubility and self-assembly to you three, do not hesitate to contact me if you need to. I'd then like to thank my fellow French citizen, Fannie Burgevin. I will not forget our trip to Scotland and our narrow escape from the cows. Always a pleasure to chat with you! Bonne chance pour la suite! To Satu, I wish you all the best for the rest of your PhD. I am very lucky to have met you and really appreciated your company in our office. I cannot thank you enough for the pizzas and all your other small but significant acts of kindness. To Tom Floyd, thanks for taking over the Pox legacy and for all the fun times. I'd also like to thank Ramon Garcia-Maset for coming along to the ILL (I'm sorry for your phone) and on other adventures! Vito, I am truly happy to have met you, I will always remember your never-ending enthusiasm for science and how pleasant you are to be around. Finally, thanks to Sophie Laroque for the fun she brought us, I won't forget your leaving due and the games we played that night. Tomos Morgan, thank you for deep-diving into mass spec analysis of some of my compounds. Never have I seen anyone with that much energy in my life!

Last, I cannot thank my housemate/friend/colleague/confidante/etc., Robert Richardson enough. Besides all the proofreading I made you go through (your mildly sassy comments were always useful), I'd like to thank you for your friendship and company over the past few years. We have created countless memories together, from our trip to Dublin to those last few weeks of social distancing in the flat doing jigsaw puzzles or playing with our respective DS. You have managed to keep me entertained – and as you put it, intellectually stimulated - for all this time; surprisingly you still do! To you, I leave the responsibility to maintain an appropriate level of queerness in this group at all times, whatever it may entail.

To avoid lengthening that thesis too much, I will not go into too much details on how all the other people I haven't mentioned yet took part in my journey. Thus, I'd like to thank: Drs. Liam Martin, Alexander Cook, Junliang Zhang, Andrew Lunn, Guillaume Moriceau, Maryam Obaid and all the visiting, master and summer students I had the pleasure to meet.

Special thanks to Dr. Ann Dixon who gave me the idea of working with Trp fluorescence for the last experimental chapter of that thesis; your help was greatly appreciated. I'd also like to thank all the academics who supported me through my thesis, as well as the technical staff in charge of the many instruments I got to play with.

Aside from work, one has to maintain a healthy social life. Therefore, I'd like to thank all my Warwick friends (mostly the *Friends of Dorothy*, among other names) for all the adventures and moments we shared. Special thanks to my cohort friends, Scott (who I went to my first Prides with), Thomas and Ellis but also to all the others: Spencer J., Andrew G., Gabriel, Andrew A., Eduardo, John P., Grant, Gerald, Somak, etc. For the rest of this, I'll finish in French.

Je tiens à remercier tous mes amis, d'ici et d'ailleurs pour leur soutien constant. Grâce à vous, j'ai pu m'échapper et voyager, que ce soit en Italie, en Suède ou simplement à Paris. Merci à: Michèle, Johanna, Bastien, Camille, Pierre, Héloise, Sophie J., Clément et à tous ceux que je n'ai pas pu revoir depuis quelques années mais qui, je le sais, auront une pensée pour moi. J'espère tous vous revoir très bientôt! Enfin, je voudrais remercier ceux qui ont toujours cru en moi, par delà les océans, sur la petite île de Bora Bora. Alain et Linda, merci pour votre éternel soutien ! Merci à mes parents et à ma famille pour leurs encouragements et pour m'avoir laissé suivre mon propre chemin.

DECLARATION

Experimental work contained in this thesis is original research carried out by the author, unless stated otherwise, in the Department of Chemistry at the University of Warwick, and in the Department of Drug Delivery, Disposition and Dynamics at Monash Institute of Pharmaceutical Sciences, Monash University, between October 2016 and April 2020. No material contained here has been submitted for any other degree, or at any other institution.

Results from other authors are referenced in the text in the usual manner.

The work presented was carried out by the author with the following exceptions:

Chapter 2: Some repeats of the XTT cellular viability assay were carried out by Ji-Inn Song. The Transmission Electron Microscopy presented was acquired by Dr. Julia Y. Rho (University of Warwick).

Chapter 4: The script for the model used to fit the neutron reflectivity data was written by Dr. Stephen C.L. Hall, who also performed the ATR-FTIR spectroscopy experiments at ISIS-Neutron Muon Source. Antibacterial assays were performed by Dr Agnes Kuroki and Ramon Garcia-Maset (University of Warwick).

ABSTRACT

Cyclic peptide-polymer nanotubes (CPNT) are an emerging class of nanomaterials with a strong potential for biological applications. This thesis aims to investigate the interaction of different CPNT systems with different biological models. Firstly, the place of CPNT in the wider family of synthetic nanocylinders is put into perspective, with a focus on existing applications.

Secondly, the behaviour of a library of CPNT with differing polymer composition and proclivity for self-assembly was studied in cellular models (cell lines and tumour spheroids). This study focuses on the relationship between self-assembly and cellular uptake and its findings show that relatively short CPNT (~15 nm) are taken up the most effectively, with specific patterns in intracellular localisation in both type of models.

Thirdly, the cellular uptake and the *in vivo* properties of stabilised elongated CPNT (>100 nm) are compared to those of short dynamic CPNT (~10 nm), using cell lines and rat models. Despite exhibiting lower levels of cellular uptake than their dynamic counterparts, stabilised CPNT are shown to be promising drug delivery vehicles thanks to their longer circulation *in vivo* allied to an efficient excretion. In parallel, the addition of integrin-targeting moieties to dynamic CPNT is also looked into. Targeting CPNT promote uptake in cell lines overexpressing $\alpha_v\beta_3$ integrins. Clear limitations for any use for drug delivery purposes can be highlighted, as their blood clearance is accelerated compared to non-targeting CPNT. This was explained by a higher propensity for recognition by the immune system as demonstrated by the high levels detected in the liver and spleen.

Fourthly, the interaction of a library of charged polymers and CPNT with lipid bilayer models is investigated, using complementary techniques. Charged CPNT show higher levels of interaction than charged polymers and neutral CPNT on the lipid model employed. Further studies employing spectroscopy techniques and neutron reflectivity support a model of interaction for charged CPNT. The interaction is demonstrated to lead to the formation of pores in the bilayer, excluding any embedding of the CP in the hydrophobic tail regions. By anchoring to negatively charged head groups, the CPNT can insert in the bilayer and form a diffuse hydrated layer at the surface of the outer leaflet. Antibacterial activity is also briefly assessed in this work.

Overall, this thesis gathers key insights on the behaviour of various CPNT in lipid bilayer, cellular and animal models.

Chapter 1

Therapeutic Applications of Self-Assembling Cylindrical Polymer-based Nanoparticles: the Example of Cyclic Peptide-Polymer Nanotubes

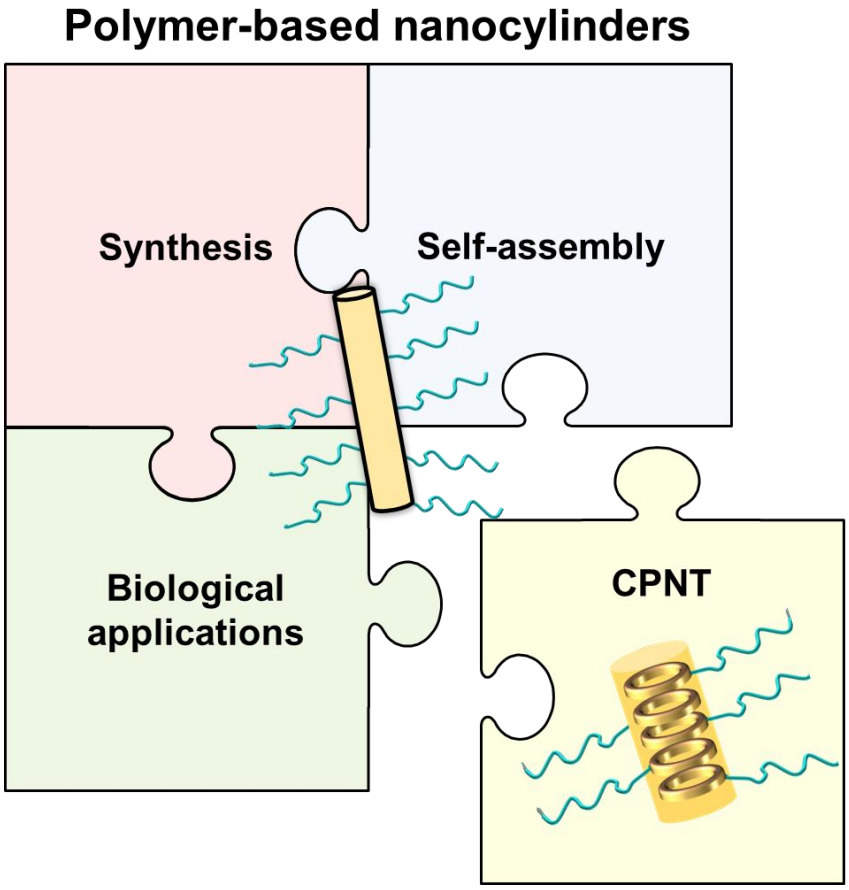

1.1 Introduction

Interest in nanotechnology (the design and production of atomic or molecular objects up to a few hundreds of nm) has been increasing over the past few years. Multiple applications have been found, spanning across a wide range of fields (healthcare, electronics, personal care, etc).[1] In particular, nanomedicine, which focuses on engineering nanoscale objects for applications in medicine, has revolutionised healthcare research. Nanomedicine is currently tackling some of the greatest modern challenges in medicine, summarised by a review from Pelaz *et al.*: efficient drug delivery, cancer diagnosis and therapy, *in vivo* imaging, antibiotic resistance and generating artificial organs.[2] An abundance of nanomaterials for therapeutic applications have been designed, featuring an impressive diversity in their nature and physical properties including: surface functionality, composition, size, charge and shape. Among such design parameters, shape has shown to play an important role, especially for the delivery of bioactive molecules.[3] Nanocylinders (also described as nanoworms, filomicelles, nanotubes when the core is hollow), in particular, have recently garnered considerable attention in the nanomedicine community as an interesting alternative to spherical nanoparticles due to their high aspect ratio architecture.[4, 5] A range of both inorganic (silica[6, 7] and gold[8] nanoparticles, quantum dots[9]) and organic (carbon nanotubes,[10] virus-based nanoparticles,[11, 12] polymeric nanoparticles[4]) nanoparticles have been used for biological applications. Self-assembled organic structures, formed by non-covalent interactions (hydrogen bonding, electrostatic interactions, π-π stacking, etc.) between primary molecular units are a non-negligible subset of these nanomaterials.

The potential for structural disassembly of such structures is key to the design of biodegradable and biocompatible nanocylinders that can be easily excreted from the body after use. This chapter will discuss the behaviour of self-assembled nanocyclinders in different biological models as well as their therapeutic applications. It will give a rapid overview of existing biological nano-cylindrical systems focusing on polymer-based nanocylinders and the example of self-assembling cyclic peptides and cyclic peptide-polymer nanotubes (CPNT).

1.2 Cylindrical nanostructures from the biological world

1.2.1 Tubular structures in cellular biology

Self-assembly is perhaps the most powerful tool utilized by nature to create an astoundingly diverse range of macromolecular objects. A good illustration of this phenomenon is the formation of cellular membranes and cellular organelles by the self-assembly of lipids and proteins. Cellular organelles come in a variety of shapes, depending on their membrane curvature determined by their unique lipid and protein compositions. The structure of the Endoplasmic Reticulum (ER), a eukaryotic cell organelle, is an interesting example of the intrinsic connection between shape and function in cellular biology. It is made of two distinct substructures, of varying sizes depending on the cell type: the rough ER, with sheet-like structures covered with ribosomes for protein synthesis, and the tubular-shaped smooth ER, involved in lipid synthesis.[13, 14]

An example of biological self-assembly into cylindrical nanostructures is the cytoskeleton, which is responsible for the cell's overall architectural integrity. The cytoskeleton is made of different types of tubular filaments, constituted from sub-protein units.[15] Microtubules are the largest type of filament (25 nm of diameter); they are synthesised through the self-assembly of the dimer made by α-tubulin and β-tubulin into long tubes.[16, 17] Actin filaments are smaller filaments (6 nm diameter), coming from the stacking of single actin monomer units; intermediate filaments (~10 nm diameter) are the third component of the cytoskeleton, they are quite diverse and composed of rod-like protein subunits of various dimensions.[18-20] The dynamic nature of these self-assemblies is key to the cell motility and structural adaptability (see **Scheme 1-1**).

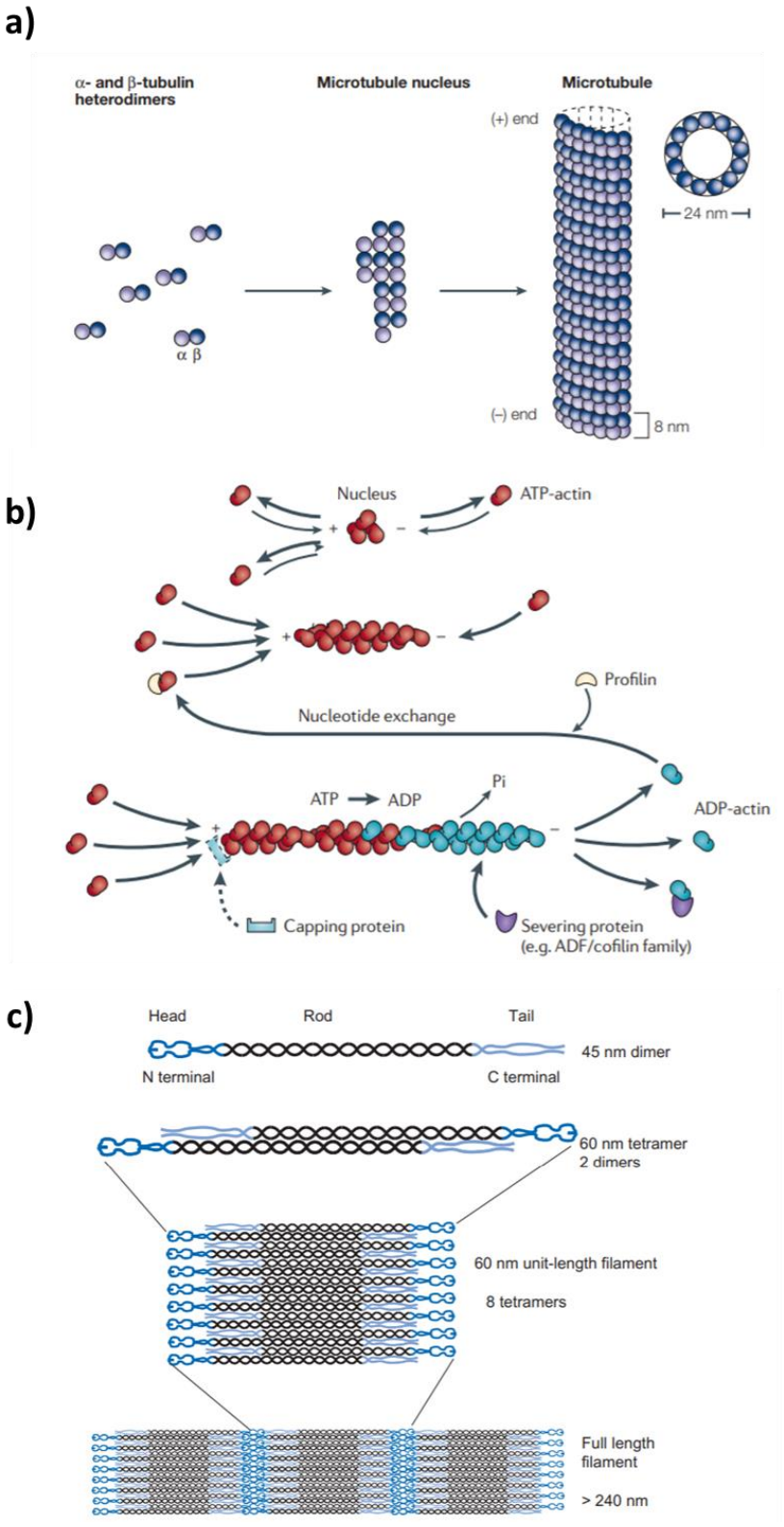

Scheme 1-1: Components and self-assembly of the cytoskeleton filaments. a) Microtubule formation, from the self-assembly of α-tubulin and β-tubulin dimers.[17] b) Actin filament self-assembly mechanism, from the actin monomer unit.[19] c) Intermediate filaments self-assembly, from a variety of elongated rod-like subunits.[20] Adapted from the reviews published by Nurnberg *et al.*, Jordan *et al.* and the book chapter from Feher.[17, 19, 20]

There are also a few examples of nanotube self-assembly in bacterial and cellular membrane systems. For instance, mammalian cell membranes can be compromised and perforated by bacterial toxins. Proteins such as α-hemolysin,[21] secreted by *S. Aureus*, or the cholera pentamer[22] can form nanopores by self-assembling in the lipophilic cellular membrane. This principle is also employed by certain antibiotics, such as Gramicidin A, a linear peptide that can coil into a nanotube and form a membrane ion channel in bacteria; toxicity is achieved by disrupting the cation exchange regulation within the bacteria.[23]

1.2.2 Nanocylinders inspired from virus biology

The realms of the viruses are another source of inspiration for those involved in the study of biocompatible nanocylinders. Viruses are microorganisms capable of replicating within a cellular host and come in many different morphologies, resulting from the complex self-assembly of proteins with genetic material (RNA, DNA). They are extremely efficient at delivering genetic material to a cell; the former generally resides within a protective capsid, itself covered with a complex pattern of lipids, receptor ligands and sugars.[24] Some viruses can adopt a cylindrical filament-like structure, such as the members of the *Filoviridae* family, which includes infectious agents such as the Ebola virus.[25, 26] There is little known in the literature about the sole influence of shape on the efficiency of the virus uptake in cells, as viruses of different shapes will also have very different surface functionalities and physical properties.

A few studies have however looked at varying the aspect ratio of nanotubes based on the cylindrical Tobacco Mosaic Virus (TMV). This virus usually infects plant leaves leading to their discoloration and degradation.[27] Its structure has been elucidated,[28] making it a suitable system for a wide range of medical applications (vaccine design,[12] tissue engineering scaffold,[29] etc.). In order to evaluate the impact of different aspect ratios on cellular uptake and bio-distribution, Steinmetz and coworkers synthesised TMV-based nanoparticles using different lengths of RNA templates that co-assembled with purified viral coat proteins from the virus capsid; the TMV particles were then functionalised with polyethyleneglycol (PEG) or an integrin targeting moiety (RGD peptide). They found that their shorter PEGylated TMV nanoparticles (aspect ratio of 3.5) had a better passive tumour accumulation than the PEGylated particles of aspect ratio of 7 and 16.5 (native TMV dimension); however, when they contained a targeting moiety, mid-size structures (AR of 7) were best at accumulating into tumours (see **Figure 1-1**).[30]

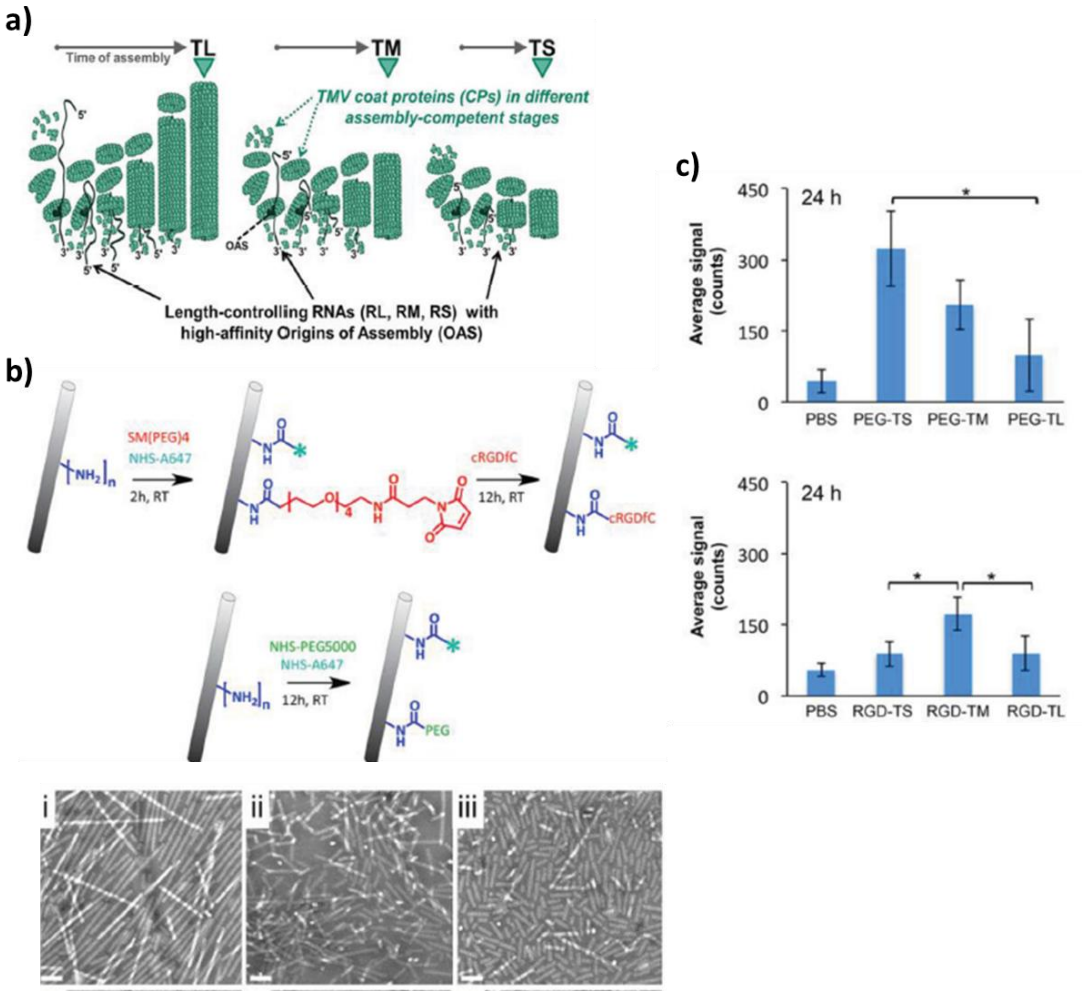

Figure 1-1: a) Bottom-up assembly for the Tobacco Mosaic Virus (TMV) nanoparticles described, using a RNA templates and coat proteins: TL (long NPs), TM (medium-sized NPs), and TS (small NPs). b) Top: Bioconjugation reaction scheme for polymer attachment/labelling on the nanoparticles. Bottom: TEM micrographs of the TMV particles of different lengths (long, medium-sized, small). c) Tumour accumulation after 24 h for non-targeted (top) and RGD-labelled (bottom) TMV nanoparticles.

Models have also been developed by this group to describe tumour accumulation in multicellular tumour spheroid (MCTS) models, showing a longer uptake and diffusion for high aspect ratio cylindrical TMV particles.[31] Interestingly, it is possible to engineer virus nanoparticles that are of a different shape than the virus in its native form, as proven by Mukherjee *et al.*, who formed a nanocylindrical structure from the spherical coat protein of the cowpea chlorotic mottle virus.[32] Similarly, Steinmetz and co-workers generated spherical TMV-based nanoparticles by heating TMV nanocylinders.[33]

The main factor limiting the use of virus-based nanoparticles is the potential presence of residual active viruses, which requires extensive purification; the cost and the scale at which these experiments are done can also be prohibitive, reinforcing the current need for readily accessible self-assembling organic nanocylinders.[34] Other synthetic alternatives therefore need to be considered.

1.3 Self-assembling polymer-based nanocylinders

Within the scope of the literature on organic nanocylinders, polymer-based nanoparticles are excellent candidates for biological applications. They exhibit remarkable properties such as: their scalability, the access to controlled architectures and molecular weights, the potential for functionalisation, their biodegradability and biocompatibility, etc.[35] Covalent cylindrical polymer brushes and combs have been investigated for different uses in the field of nanomedicine: drug and gene delivery, imaging, etc., as reviewed by Müllner.[36] Other major non-self-assembling polymer nanocylinders that have been explored include nanoparticles made by the film stretching[37] and the Particle Replication In Nonwetting Templates (PRINT) processes.[38] This part will solely focus on self-assembling systems and is aimed to present briefly a selection of the most prominent techniques employed in the field to synthesize self-assembling polymer nanocylinders; it will pay particular attention to their applications in biology.

1.3.1 Block copolymer self-assembly (microphase separation in solution)

1.3.1.1 Towards cylindrical micelles generated by block copolymer self-assembly

Advances in characterisation sciences, whether using direct imaging by electron microscopy or *via* the use of scattering and spectroscopy techniques, have helped to reach a better understanding of the self-assembly of polymers. Amphiphilic diblock copolymers can self-assemble into aqueous media into micellar structures.[39] It is possible to generate rod-like structures in solution, employing an appropriate ratio of hydrophobic/hydrophilic monomer in the system and adequate experimental conditions.[40] A few studies first reported the self-assembly of PEG-poly(butadiene) and PEG-poly(ethylene) (PE) diblocks into long worms, analogous to the cytoskeletal filaments mentioned *vide supra* (see 1.2.1).[41, 42] Molecular dynamics simulations were also used to evaluate the importance of the molecular weight and the amphiphilicity ratio in the self-assembly process.[43] A typical method to form such cylindrical micelles, when an appropriate ratio of PEG to the hydrophobic moiety was determined, consisted in first dissolving both blocks in a good solvent such as chloroform. The solvent was then evaporated, leaving a film in the vial into which water was added at high temperature, leading to the formation of filomicelles (see **Scheme 1-2**).[42, 44]

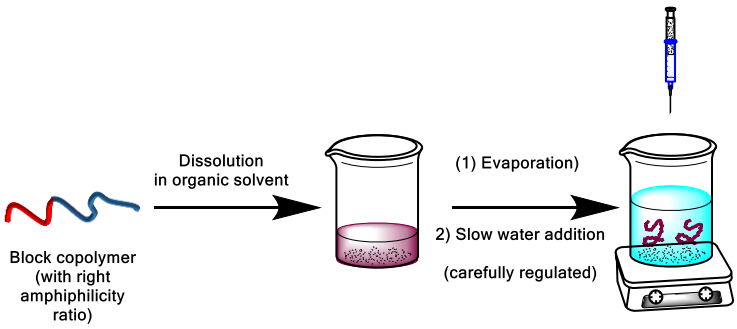

Scheme 1-2: Typical preparation of filomicelles by block copolymer self- assembly (evaporation performed when the first organic solvent is not miscible with water).

Discher and co-workers were pioneers in the use of filomicelles for biological applications, following the aforementioned preparation process. They developed biodegradable self-assembled filomicelles by replacing the hydrophobic polymer segment with degradable poly(ε-caprolactone) (PCL).[44]

1.3.1.2 Cylindrical micelles from block copolymer self-assembly for biological applications

In 2004, Discher and co-workers reported the use of targeted biotin-labelled filomicelles *in vitro*.[45] They then conducted an in-depth study of the *in vitro* and *in vivo* behaviour of filomicelles of different lengths in rodent models.[46] Fluorescently labelled bioinert (PE-based) or biodegradable (PCL-based) filomicelles with initial lengths ranging from 2 to 18 µm, were generated. The inert filomicelle showed a longer circulation than previously studied stealth vesicles; degradable filomicelles' circulation time increased with their length, from a 2 day half-life for 2 µm systems up to 5 days for systems with lengths of 8 and 18 µm. Following the length of the self-assemblies thanks to direct imaging in the blood plasma, the authors found that the filomicelles were shrinking into smaller nanocylinders after circulating for a few days. Such behaviour was attributed to cell and flow-induced fragmentation. Most of the nanocylinders accumulated in the liver and spleen, as well as the lungs; the authors noticed a higher kidney content for PCL-based filomicelles, due to their propensity to break into smaller fragments. The filomicelles were then loaded with anticancer drug Paclitaxel; a study on A549 human tumour-grafted mice determined that the longest filomicelles were leading to the highest reduction in tumour size.[46] These first observations were further confirmed by another study looking at the biodistribution in tumour-bearing mice and at cell interactions of Paclitaxel-loaded filomicelles.[47]

Briefly, the cylindrical morphology helped increasing the maximum tolerable Paclitaxel dose to 16 mg/kg, 2 and 18 times higher than the one for spheres (generated by sonication of the diblock copolymer) and for the free drug respectively, leading to a higher level of tumour apoptosis (see **Figure 1-2**).[47]

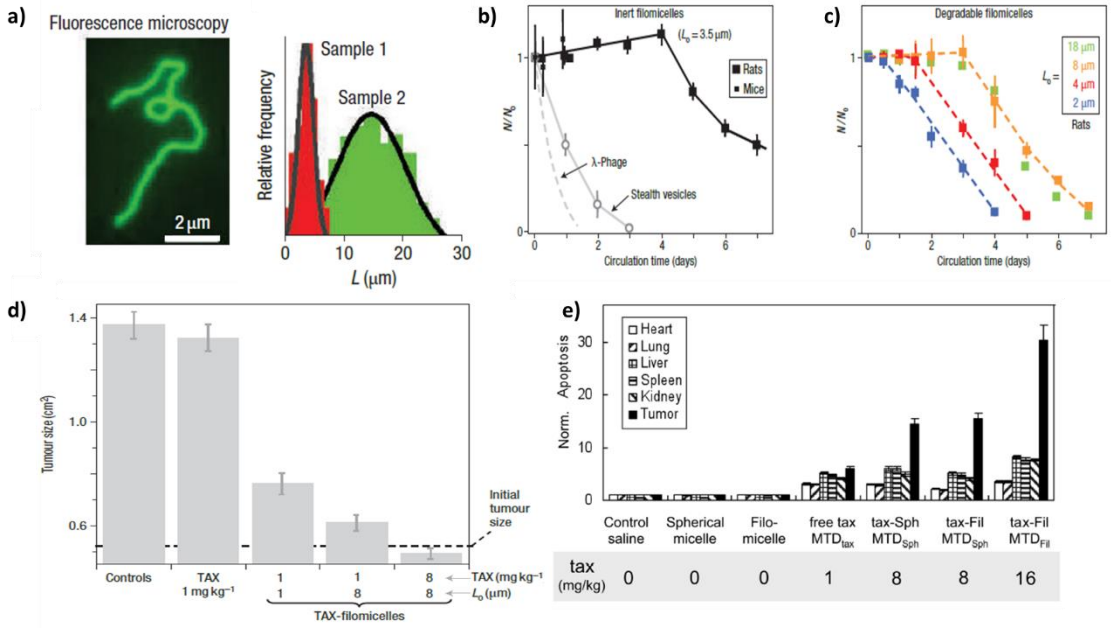

Figure 1-2: a) Image of the inert fluorescent filomicelle sample, as visualised by fluorescence microscopy, and length distribution of two distinct filomicelle samples. b) Relative numbers of filomicelles circulating in the rodent blood, compared to λ-phages and vesicles. c) Relative numbers of filomicelles circulating, comparing degradable filomicelles of different initial lengths. d) Tumour size after treatment with Paclitaxel (TAX) and TAX-loaded filomicelles.[46] e) Organ apoptosis measured for the main organs on A549 tumour-grafted mice after treatment with different morphologies, without and with TAX-loading at the maximum tolerable dose (MTD).[47] Adapted from the work of Discher and co-workers.[46, 47]

Other studies have looked at filomicelle creation and designed ways to attach cell-penetrating peptides efficiently to these structures before evaluating the effect on the *in vitro* properties.[48] In 2016, Zhao *et al.* synthesised sugar-containing diblock copolymers that self-assembled into cylindrical micelles; these polymers were composed of methyl methacrylate (MMA) and fructose methacrylate.[49, 50] The authors highlighted the complexity of morphology control, showing that the nanocylinders were not only sensitive to the polymer amphiphilicity but also to external factors such as the water content in the initial THF/water mix, as well as temperature and stirring rate variations during the self-assembly process.

In a first study, the cellular uptake in MCF-7 cells and in MCF-7 multicellular tumour spheroids (MCTS) models showed that the longer rods (>2000 nm) formed by these diblock copolymers were taken up to lower levels than their smaller (400 or 800 nm) counterparts.[49]

A following study demonstrated the importance of polymer stiffness, by comparing stiff fructose-containing cylindrical micelles with MMA in the hydrophobic block to softer butyl acrylate (BA). The stiffer polymer nanocylinders were taken up more than the softer ones in MCF-7 cells and MCTS (see **Figure 1-3**).[50]

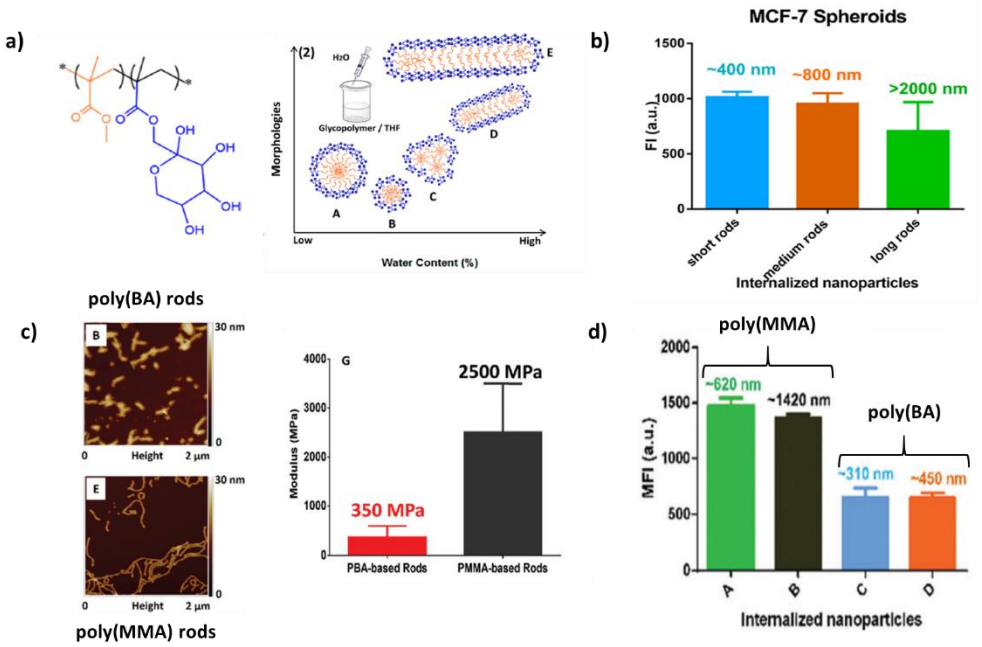

Figure 1-3: a) Fructose-based poly(MMA) diblock copolymer (left) and morphology phase diagram showing the variations observed with changes of the water content in the initial THF/water mixture. b) Mean fluorescence intensity in MCF-7 tumour spheroids after treatment with different sizes of fructose poly(MMA) nano-rods.[49] c) Atomic Force Microscopy profiles and Young's modulus estimation for fructose-containing poly(MMA) and poly(BA) rods. d) Mean fluorescence intensity in MCF-7 tumour spheroids after treatments with stiff (poly(MMA)) and soft (poly(BA)) filomicelles of different sizes.[50] Adapted from Zhao *et al.*[49, 50]

One of the main drawbacks of this nanocylinder generation technique is the lack of control over length of the obtained filomicelles, as most structures were over hundreds of nm long, with a non-uniform length distribution. Determining the appropriate preparation method for a new system can also be time-consuming; extreme care must be taken to control all external factors in the preparation technique to ensure satisfactory reproducibility.[49]

1.3.2 Polymerisation-Induced Self-Assembly (PISA)

1.3.2.1 Principles of PISA

Polymerisation-Induced Self-Assembly (PISA) is a technique based on living polymerisation, with the Reversible Addition Fragmentation chain Transfer (RAFT) radical polymerisation being one of the most commonly used synthetic methods. In the PISA process, a first polymer block is initially synthesised using solution polymerisation. It is then extended via dispersion or emulsion polymerisation with a second monomer in a solvent in which this growing polymer block slowly becomes insoluble, leading to the self-assembly of the block copolymer into nano-objects of diverse morphologies (see **Scheme 1-3**). The main appeal behind this technique is the possibility to tailor the self-assembly to the structure of interest by simply varying the degree of polymerisation of the "PISA monomer" in this second block.[51]

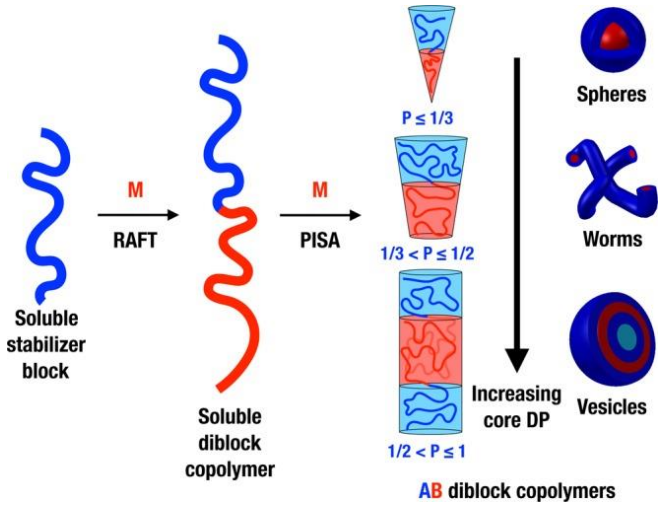

Scheme 1-3: Polymerisation Induced Self-Assembly (PISA) typical process, adapted from Canning *et al.*

It also allows for the synthesis of nanocylinders with additional properties via incorporation of adequate monomers: lectin-binding[52] (via the use of sugar monomers), thermo-responsiveness,[53] etc. However, there are a few limitations with the PISA process when aiming to synthesise nanocylinders. In order to generate worms or any desired morphology reproducibly with a new PISA system, a phase diagram needs to be plotted. It is also not ideal for the production of uniform populations of worms as the mean size may vary significantly within a population.[51] Nevertheless, PISA remains one of the most efficient ways to produce libraries of different morphologies of self-assembling nanoparticles in water, making it suitable for biological use.

1.3.2.2 Biological applications of PISA nanocylinders

As spherical, worm-like and vesicle nanoparticles can be obtained by simply changing the degree of polymerisation, PISA is extremely useful for systematic studies looking at the influence of self-assembling nanoparticle's size and shape on drug delivery. Karagoz *et al.* first reported the synthesis and biological testing of a library of doxorubicin (DOX) containing polymer morphologies in 2014. The monomers used were PEG methacrylate (PEGMA) in the first block and a statistical mixture of styrene (PISA monomer) and vinyl benzaldehyde in the second block; DOX was attached *via* imine formation on the aldehyde monomer. They found that structures of high aspect ratio, such as worms, entered MCF-7 breast cancer cells more readily than their spherical counterparts; their efficacy was also higher, with an IC50 seven times lower for worms compared to micelles.[54] A similar study published in 2016 by Qiu *et al.* using a different polymer system (DMAEMA / methacryloxyethoxybenzaldehyde MAEBA) with DOX and the same drug linkage strategy further confirmed previous observations. A higher potency of short rod-like structures (160 nm long), compared to spheres (70 nm diameter) and vesicles (180 nm diameter) was observed, the authors explaining it by suggesting differences in the cellular uptake mechanism from confocal imaging (see **Figure 1-4**). The addition of DOX to the pre-formed self-assemblies did not lead to any significant disruption, with the mean length maintained according to Transmission Electron Microscopy (TEM) imaging.[55]

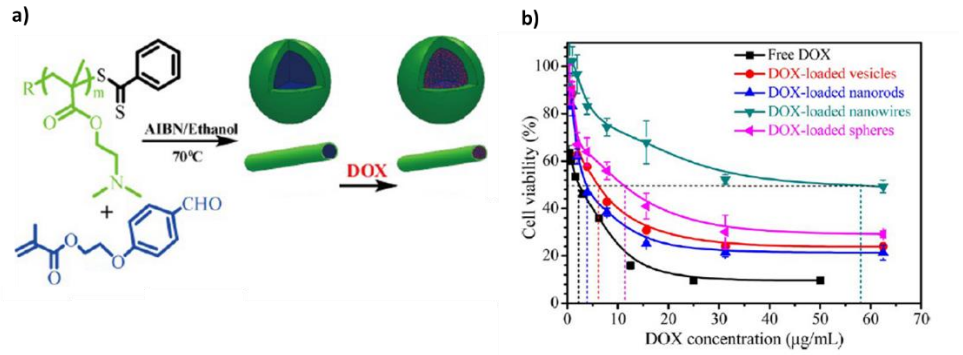

Figure 1-4: a) PISA system considered (DMAEMA/MAEBA) for the study and DOX attachment as reported by Qiu *et al.* b) Cell viability results for the different morphologies loaded with DOX. Adapted from Qiu *et al.*[55]

Similarly, Hinde *et al.* utilized the PISA approach to understand the relationship between nanoparticle shape and its intracellular behaviour, looking at the different barriers before reaching the nucleus. The system used was PEGMA/fluorescein methacrylate for the first block and styrene/benzaldehyde acrylate for the second block, to allow for DOX conjugation. The IC50 values, once again, correspond to what was initially found by Karagoz *et al.* with a higher efficiency for the rod-like structures. Using pair-correlation microscopy, the authors were able to identify that the most complex barrier to overcome for nanoparticles was the one formed by the nuclear pore complex. Only rod and worm-like morphologies were able to penetrate it (micelles and vesicles were detected in very low levels), with much more difficulty than they had when crossing the initial barrier (plasma membrane).[56]

Kaga *et al.* translated such a comparative study with PISA nanoparticles to *in vivo* models, determining the impact of morphology on biodistribution in tumour-grafted mice models. From their poly(glycidyl methacrylate-*b*-PEGMA-*b*-styrene) systems, they synthesised radiolabelled (tritiated ethanolamine reacted with the epoxide moieties) nano-objects of different morphologies. A higher tumour uptake was found for small spherical objects (21 or 33 nm) whilst nanorods (350-500 nm) and nanoworms (1-2 µm) were found in higher levels in other organs such as the liver and the spleen. Such results were attributed to the cross-section diameters of the nanocylinders (37-45 nm), which were larger than previously reported systems (e.g. those mentioned in 1.3.1.2, 5-25 nm).[57]

The formation of reversible worm gels has also been reported, allowing for applications of PISA worms to cell preservation. By using glycerolmonomethacrylate and 2-hydroxypropylmethacrylamide (HPMA) based polymers, Armes and co-workers successfully formed a thermoresponsive worm hydrogel. The gel structure was obtained above 22°C through entanglement between the worms; de-gelation occurred at lower temperatures due to a worm-to-sphere transition.[53] These worm gels were used for the preservation of pluripotent stem cells, inducing a state of reversible cellular stasis as demonstrated by the monitoring of key cell cycle biomarkers.[58] Efficient cryopreservation of red blood cells was also achieved with the same polymer system when combined with ice-recrystallisation inhibitor poly(vinylalcohol), the worm gel acting as a cryoprotectant (formation of a hydrated matrix around the cells, see **Figure 1-5**).[59]

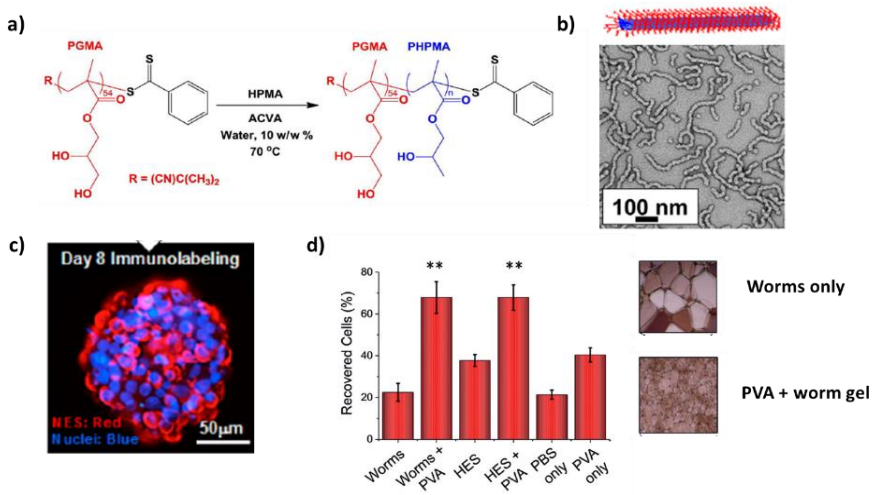

Figure 1-5: a) Representation of the polymer system poly(GMA-*b*-HPMA) used to form the worm gels. b) Schematic representation of worms and image acquired of a dried dispersion of worms by TEM at 21°C.[53] c) Five-day old embryo kept in worm gel for 8 days successfully stained for stasis using the Nuclear Envelope Statin (NES) marker.[58] d) Red blood cell recovery after 3 days storage in $N_{2\,(liq)}$ in the presence of different treatments with poly(vinylalcohol) (PVA), worm gels and hydroxyethyl starch (HES) ; on the right: ice-recrystallization inhibition for the worms and the worm gel with PVA.[59] Adapted from the work from Armes and coworkers.[53, 58, 59]

1.3.3 Crystallisation-Driven Self-Assembly (CDSA)

1.3.3.1 Principles of CDSA

Crystallisation-Driven Self-Assembly (CDSA) is a technique that allows for the formation of different morphologies, relying on the crystallisation of the polymer core.[60] Among the first examples reported was the work of Manners, Winnik and co-workers, who successfully synthesised a diblock copolymer made of a poly(ferrocenyldimethylsilane) (PFS) core and poly(2-vinylpyridine) (PVP) capable of undergoing a sphere to worm-transition in ethanol after a certain time. Using different characterisation techniques (TEM, X-ray scattering, Differential Scanning Calorimetry), they were able to correlate the arrangement into long and uniform cylindrical micelles to the formation of crystalline domains in the PFS core.[61] These observations, alongside further discoveries, led to the creation of the living CDSA process.[62] Briefly, a block copolymer with a crystalline core was dissolved in a solvent favouring self-assembling, before being sonicated to form smaller seed-micelles (crystallites). A certain amount of unimer solution of diblock copolymer, with the same polymer core, was then added slowly to the seeds to form cylindrical micelles of the desired size.[62]

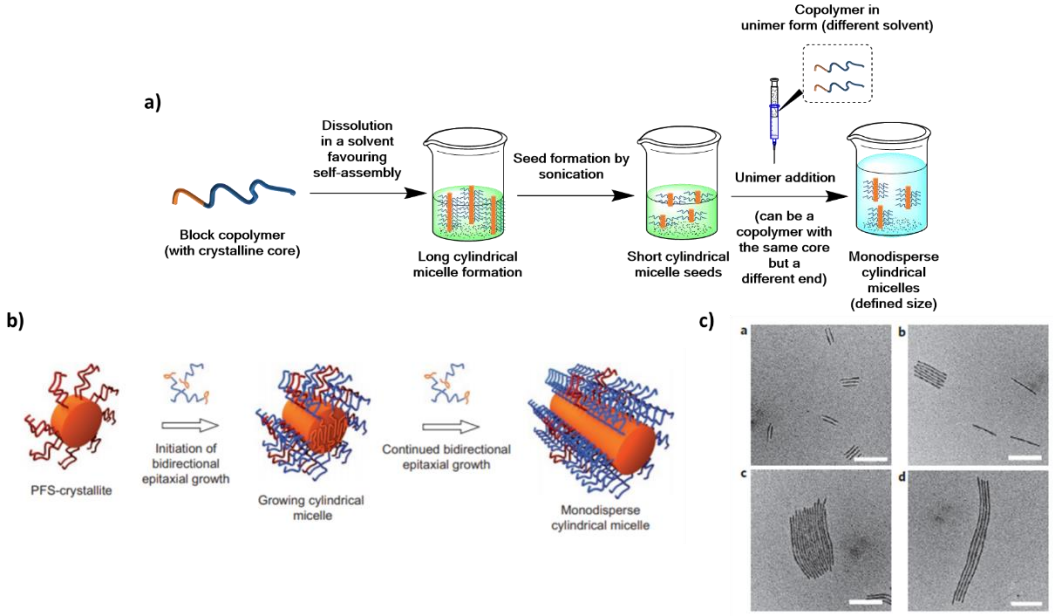

Scheme 1-4: a) and b) Typical preparation of uniform cylindrical micelles of defined size by living CDSA. c) Bright field TEM micrographs of monodisperse cylindrical micelles formed by living CDSA from PFS-*b*-PDMS seeds. Adapted from Gilroy *et al*.[62]

The use of living CDSA to generate cylindrical micelles allows for the formation of very well defined architectures that are difficult to replicate using other self-assembly techniques mentioned *vide supra*. A real challenge exists, however, to obtain nanocylinders that can be formed in or transferred to an aqueous environment, as the systems described earlier, based on a PFS core, were all formed in organic solvents.[60-62] Other CDSA systems, based on different semi-crystalline or crystalline biodegradable polymer cores have been developed over the past few years, such as PCL,[63, 64] polylactides (PLLA[65, 66] or PCL-*b*-PLLA[67] core). The attainment of stable and functional self-assemblies in water gave way to different biological applications.

1.3.3.2 Biological applications of CDSA

O'Reilly, Dove and co-workers have extensively studied CDSA nanocylinders systems based on the crystallisation of a poly(L-lactide) PLLA core and demonstrated their potential for applications in immunotherapy.[65, 66, 68-70] They reported in 2016 the synthesis of different sizes of mannose-functionalised cylindrical micelles, with a PLLA core and a protected poly(acrylic acid) (PAA) shell; mannose attachment occurred after deprotecting the PAA moieties via post-functionalisation (EDC coupling), with little impact on the nanocylinders' dimensions.[69]

Such nanocylinders were obtained by varying the amount of THF in the initial water/THF mixture. Spherical micelles of the same diameter (50 nm) were generated in parallel from a racemic poly(D,L-lactide) diblock copolymer of similar molecular weight. The authors established that the spherical nanoparticles were taken up significantly more than the nanocylinders in RAW 264.7 macrophages; studies of the endocytic mechanism inferred the presence of two different uptake mechanisms for spherical nanoparticles (clathrin and caveolin-mediated endocytosis) whilst only one seemed to occur for nanocylinders (clathrin-mediated endocytosis). The ability to trigger an immune response was also examined; the long mannose nanocylinders (215 nm) led to a higher IL-6 cytokine secretion in macrophages than when they were treated with the other morphologies, paving the way to potential applications in immunotherapy (see **Figure 1-6**).[69]

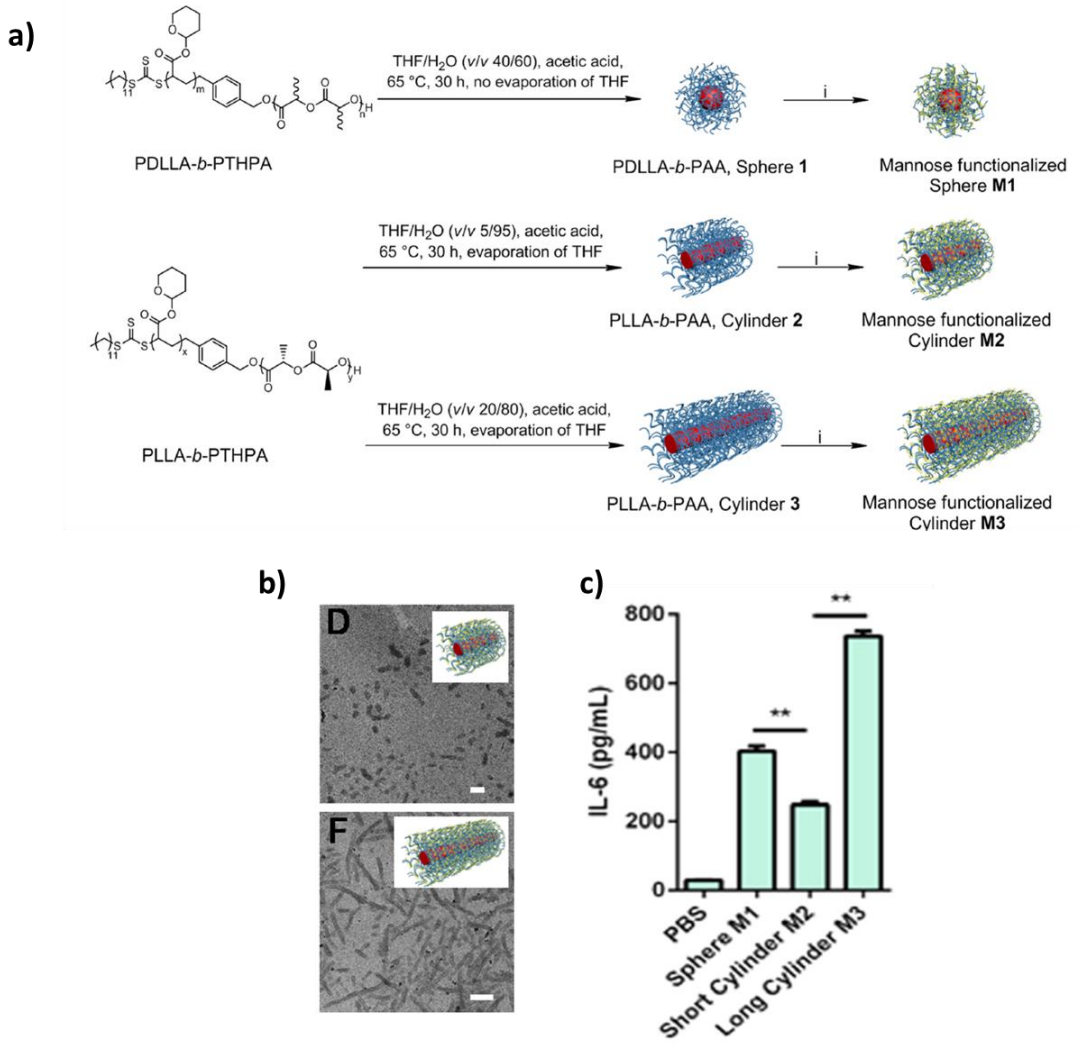

Figure 1-6: a) Representation of the mannose-functionalised PLLA-*b*-PAA used to form cylindrical micelles by CDSA. b) TEM micrographs of the mannose-functional cylindrical micelles (scale bar: 200 nm). c) Expression of the cytokine IL-6 (in pg/mL) in macrophages RAW 264.7 after treatment with the different mannosylated self-assemblies. Adapted from Li *et al*.[69]

The formation of nanoplatelets, in the presence of DMF as a co-solvent in the self-assembly process, was noticed in a follow-up study with shorter diblock copolymers of PLLA and mannose-functionalised PAA. The nanoplatelets were similarly tested for uptake and cytokine secretion, revealing that nanocylinders (120 nm long) were taken up more efficiently by macrophages whilst they were outperformed by the 2D architectures for cytokine secretion (showed on IL-1β, IL-12, and TNF-α).[70] As for living CDSA systems, few studies report their actual use for biological applications at present.[64, 71, 72] Arno *et al.* managed to perform living CDSA on PCL-based diblock copolymers in ethanol when combined with poly(dimethylacrylamide) (poly(DMA)) and in water for PCL-*b*-PMMA-*b*-PDMA. The 50 nm-long cylindrical micelles tested were found to be non-toxic on 3T3 (murine fibroblasts) and A549 in the range of concentrations tested (up to 5 mg/mL); the worm micelles (length above 2 μm) were also able to form worm gels in which the cells remained viable.[64] A novel polycarbonate core was employed by Finnegan *et al.* to form another variety of biodegradable cylindrical micelles formed by CDSA; they were also found to be non-toxic against HeLa and WI-38 cells up to 0.1 mg/mL (see **Figure 1-7**).[71]

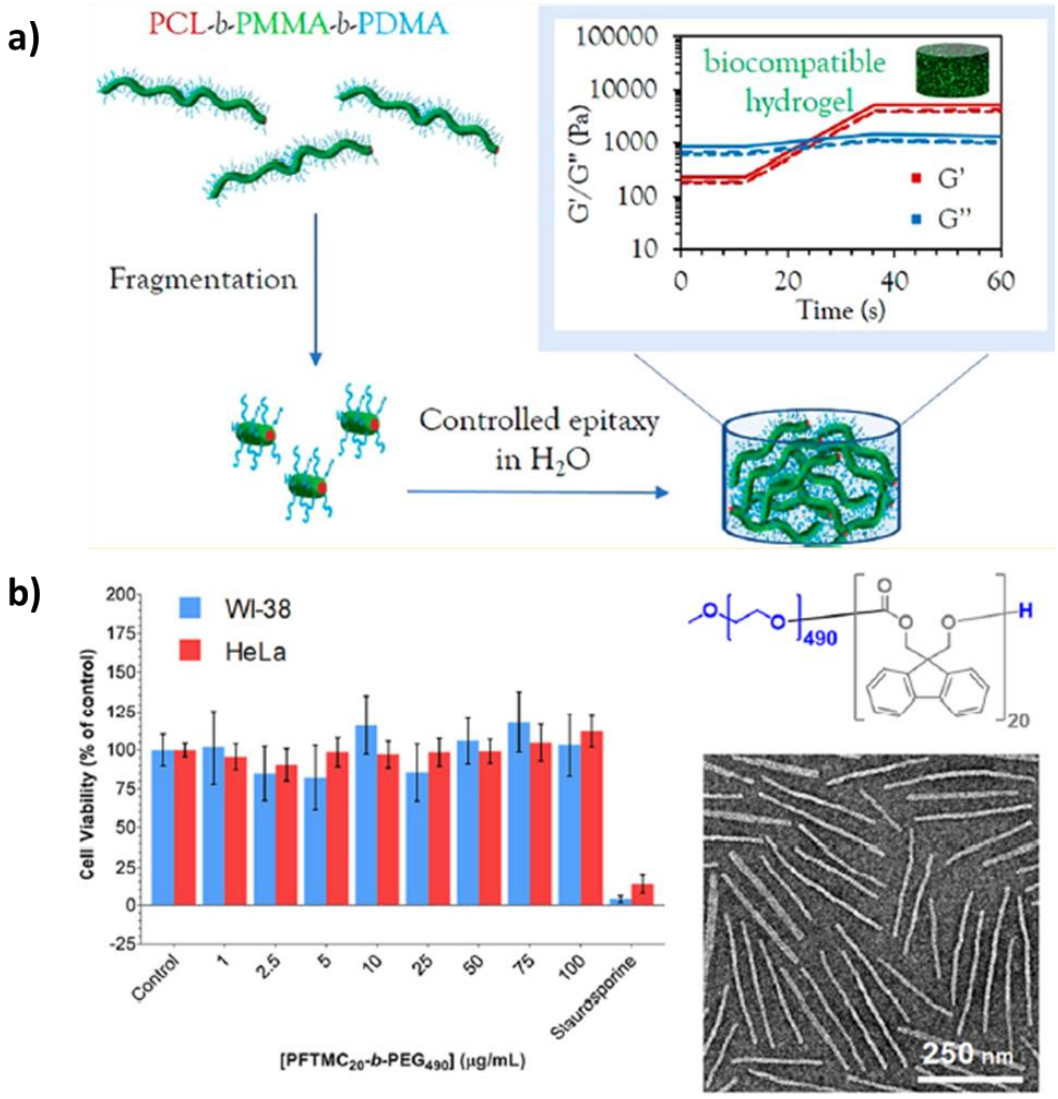

Figure 1-7: a) PCL-based polymer systems employed by Arno *et al.* to form cylindrical micelles by living CDSA, with the propensity to form biocompatible hydrogels.[64] b) Polycarbonate system developed by Finnegan *et al.*, with cell viability data on HeLa and WI-38 cells and a TEM micrograph of the morphologies formed by living CDSA.[71]

Finally, Manners, Winnik and co-workers described new biocompatible PFS-based systems using a complex PEG-based hydrophilic copolymer as a corona. The nanocylinders could be transferred into water and showed no toxicity (tested up to 0.1 mg/mL).[72] The synthesis of stable and functional (e.g.: drug-conjugated, fluorescent) cylindrical micelles by living CDSA is one of the main challenges with this technique. Living CDSA, when the right preparation conditions are found, yields well-defined and uniform populations of cylindrical micelles; the size window offered by existing living CDSA systems goes from tens to thousands of nanometers. This approach, given the morphology precision that can be achieved, will hopefully help understanding the importance of parameters such as size dispersity and size control. It is however important to notice that crystalline polymer cores might not be the ideal candidate for biological applications, given their rigidity. Their potential for disassembly in biological conditions also remains to be explored. Dynamic self-assembling systems, such as those formed by biocompatible cyclic peptide-polymer nanotubes (self-assembly directed by the cyclic peptide), are an interesting alternative to the conventional approaches previously described in this chapter.

1.4 Cyclic peptide-polymer nanotubes

1.4.1 A self-assembly process driven by the cyclic peptide core

Self-assembling peptides are increasingly popular in the field of nanomedicine, thanks to the structural diversity that can be achieved by varying the amino acid sequence and their excellent biocompatibility.[73, 74] Numerous peptide-based systems have been used to create new biocompatible nanomaterials. For instance, Stupp and co-workers reported the synthesis of nanofibers made from peptide amphiphiles (peptide sequences to which a long aliphatic chain is incorporated).[75] Peptide amphiphile-based nanomaterials have found direct applications in nanomedicine: enhanced growth factor signalling,[76] wound healing,[77] atherosclerosis therapy,[78] etc.[79] Another example of peptide-based self-assembly is the formation of gels from short peptide sequences such as di- and tri-peptides,[80, 81] which have found applications in tissue engineering.[82]

Among such systems, self-assembling cyclic peptides (CPs), comprising of an even number of alternating D- and L- amino-acids, exhibit biological properties, as they generally have a higher tolerance towards metabolic reactions (enzymatic or pH-induced cleavage) compared to linear peptide sequences.[83] Such cyclic peptides are able to self-assemble into tubular β-sheet-like structures. This assembly was first postulated in 1974 by De Santis *et al.*,[84] based on a theoretical study of the intermolecular hydrogen bonds and Van der Waals interaction in such systems. In 1993, this was shown experimentally by Ghadiri *et al.*, who first synthesised and characterised cyclic octapeptides able to stack into nanotubes.[85] These CP can adopt a disk-like structure in which the alignment of amide bonds (perpendicular to the axis of the ring) encourages hydrogen bonding, promoting stacking into functional nanotubes, where the amino acids residues (R-groups) point outwards (see **Figure 1-8**).[86] The average distance between each ring in a nanotube structure was found to be of 4.7 Å, according to X-ray crystallography measurements.[85] The internal diameter of α-amino acids based cyclic peptides (αCP) can be tailored by varying the ring size (from 4 to 12 residues) leading to diameters ranging from 2 to 13 Å (7 Å for the octapeptides based structures that will be extensively discussed throughout this thesis), as previously reviewed by Chapman *et al.*.[86]

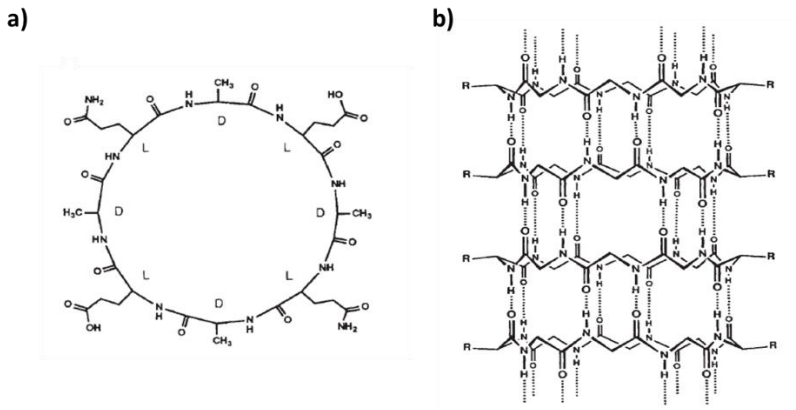

Figure 1-8: a) Two dimensional representation of the alternating D- and L- α amino acids cyclic octapeptide unit studied by Ghadiri *et al.*
b) Schematic representation of the self-assembly of CPs subunits in tubular configuration, showing antiparallel stacking and hydrogen-bonding interactions (from Ghadiri *et al.*[85])

Other self-assembling cyclic peptide systems have been designed, based on the use of β-amino acids[87] and on combinations of α and γ-amino acids[88], allowing for the generation of even wider nanotubes (up to 17 Å). The largest internal diameter CP nanotube has been recently reported by Granja and coworkers, who found that extremely wide cyclic peptides nanotubes could be made from α and δ-amino acids, generating structures with an internal diameter of 30 Å according to models; such systems were used to encapsulate C_{60} fullerene, widening the spectrum of existing applications for CP nanotubes.[89]

1.4.2 Biological applications of α-cyclic peptide nanotubes

α- Cyclic peptide nanotubes, thanks to their potential for structural versatility, have been used for a variety of applications in the life sciences, spanning from membrane disrupting activity (antibacterial, antiviral) to delivery roles.[86, 90]

1.4.2.1 Antibacterial and antiviral activity

There are quite a few examples of the use of CP nanotubes for antibacterial applications, which comes as little surprise since CP nanotubes are capable of interacting with lipid membranes, as shown by Ghadiri and coworkers who characterised this interaction by infrared spectroscopy in 1998.[91] The same group later reported the synthesis of antibacterial αCP with different amino acid sequences, with good selectivity against methicillin-resistant *S. Aureus* and high *in vivo* efficacy as they could increase survival rates in animals infected with this bacterial strain significantly (the pharmacokinetic aspect was, however, not fully explored).[92]

These properties were further explored by incorporating sugar modified Serine residues (mannose, glucose and galactose) inspired by existing mannopeptimycin; the toxicity against mammalian cells could be reduced 5-fold with a galactosylated αCP compared to the same sequence with just a Serine, with similar antibacterial activity against Gram-positive strains (see **Figure 1-9**).[93] A semi-systematic study by Danial *et al.* on Large Unilamellar Vesicles (LUV) and bacterial lipid extracts has shown that depending on the amount of charges, the degree of symmetry and the overall amphiphilicity, wider pores could be obtained in membranes, which corroborates with the results previously described.[94]

In parallel, antiviral activity of αCP nanotubes was evaluated on different viruses: adenovirus[95], Influenza A[95] and several forms of the Hepatitis C[96] virus. A positively charged amphiphilic αCP was found to be active against several adenoviruses strains and Influenza A; the authors suggested that the activity was linked to a disruption of the viral uptake process in HeLa cells causing a perturbation of endosomal pH upon which the virus relies to release its genetic material (see **Figure 1-9**).[95] Similarly, neutral amphiphilic αCP nanotubes were reported as specifically active against Hepatitis C strains, the activity being explained by interferences in viral uptake after binding the membrane and before RNA replication.[96]

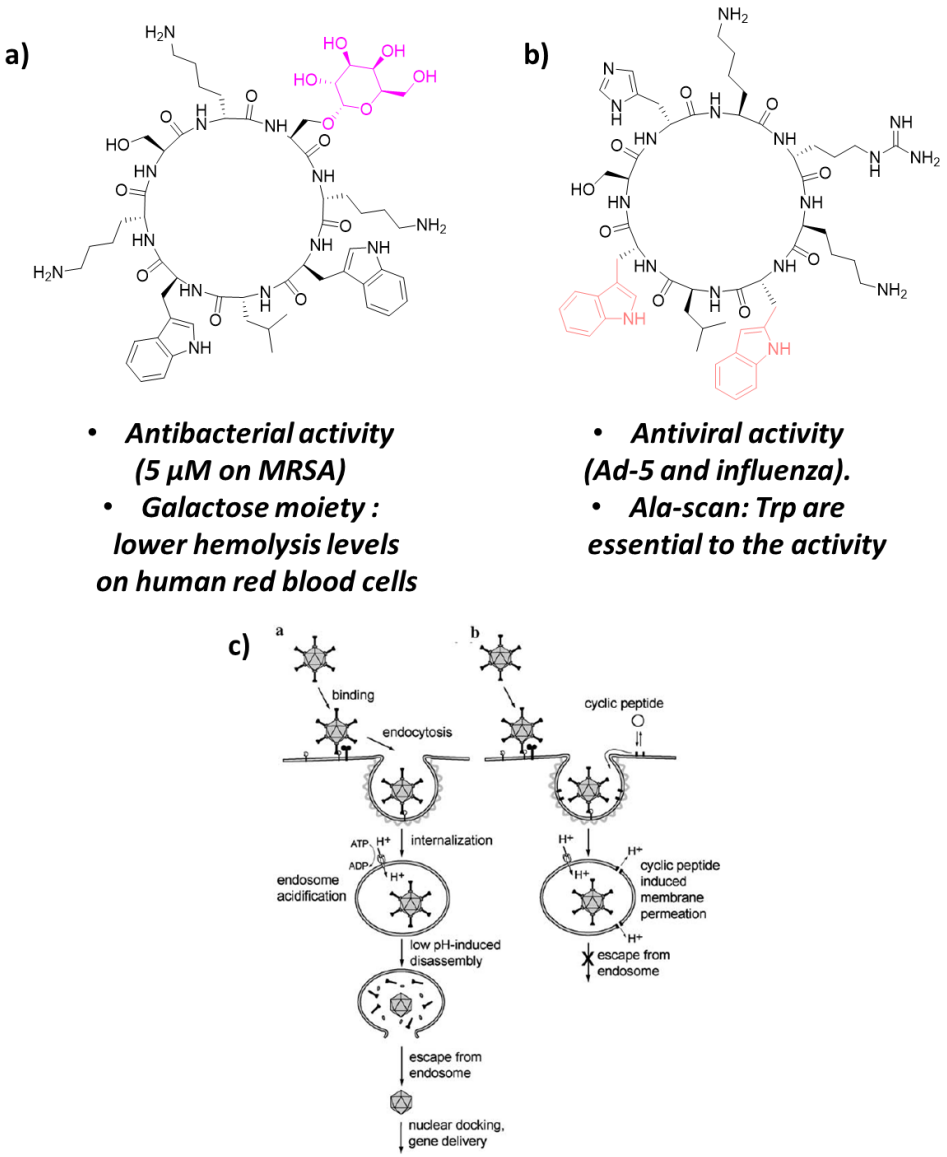

Figure 1-9: a) Lead cyclic peptide candidate from the systematic study from Ghadiri and co-workers for antibacterial applications.[93] b) Lead candidate for antiviral applications (Adenovirus 5 and influenza) from a systematic study from Ghadiri and co-workers, with the suggested action mechanism (disruption of endosome acidification).[95]

1.4.2.2 Gene and drug delivery

Few papers report the use of cyclic peptide nanotubes for gene delivery, most likely due to the inherent difficulty to combine nanotube self-assembly with a high level of cationic charges, usually necessary for gene complexation and transfection to an organism.[97, 98] Liaw and coworkers achieved successful oral delivery of CMV-plasmids containing *lacZ* (gene associated with βGal) and *hRluc* (humanised luciferase) on murine models by associating them with Tyrosine containing neutral αCP c-[D-Trp-L-Tyr]$_4$. The complexation phenomenon is due to electron transfer interactions between the phenolic alcohol function of Tyr and the A-T pairs in the DNA sequence. The same principle was used again for the intra-ocular delivery of plasmids containing anti-apoptotic Caspase3 silencing shRNA.[99] Another way to circumvent the challenge of balancing charge and self-assembly was found by Schmuck and coworkers, where one of the Lys groups on a c-[D-Ala-L-Lys]$_4$ CP was modified with a weakly basic guanidiniocarbonyl-pyrrole moiety.[97] This modified αCP was able to form nanotubes with calf thymus ctDNA and a GFP plasmid; successful transfection in HeLa cells was achieved, through a mechanism that differed from the usual endocytic pathway followed by polyethyleneimine (PEI) complexes (see **Figure 1-10**).[97]

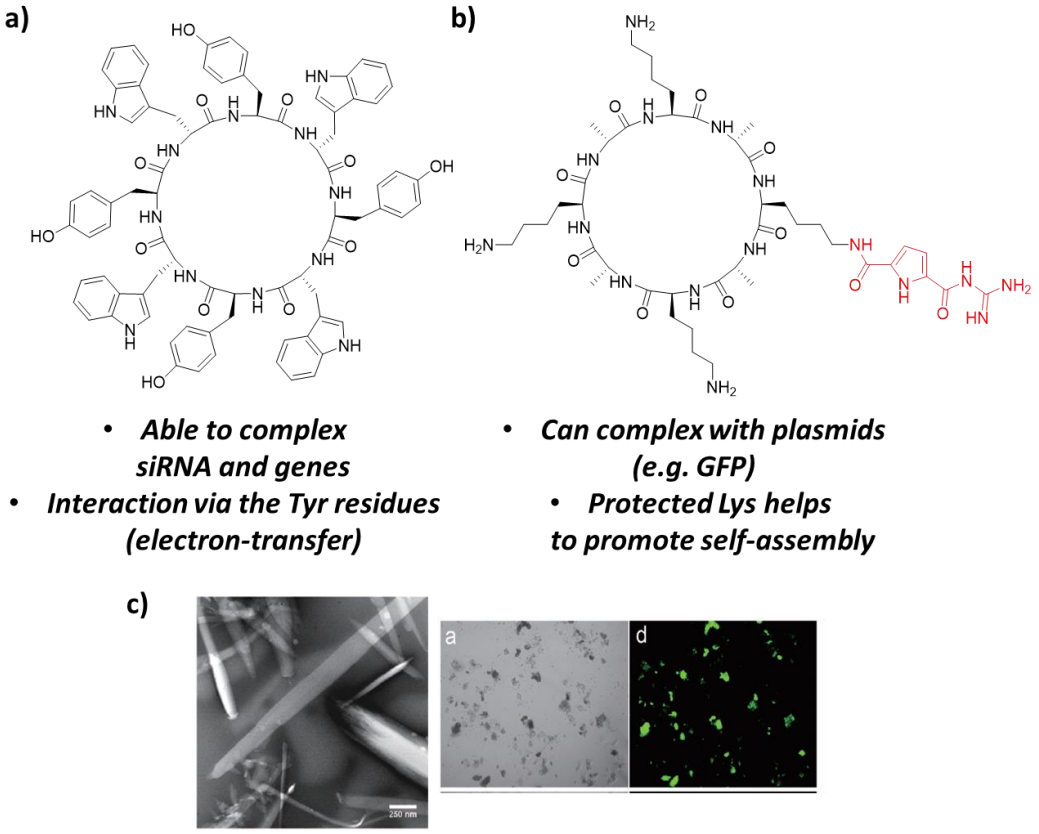

Figure 1-10: a) Cyclic peptide used for gene and siRNA delivery by Liaw and co-workers.[99] b) Cyclic peptide used for GFP plasmid transfection by Schmuck and co-workers. c) TEM micrograph of the nanofibers aggregates (top) and fluorescence microscopy of GFP-transfected cells after having complexed the CP to the plasmid (bottom).[97]

As for drug delivery, Chen *et al.* have utilised the potential of αCP (decapeptide used: c-[Gln-(D-Leu-L-Trp)$_4$-D-Leu], internal diameter of 10 Å) to interact with membranes in order to facilitate the delivery, and enhance the cytotoxic activity of, small anticancer drugs such as 5-FU.[100] The entry was found to be only effective for drugs smaller than the internal diameter of the nanotube, acting as a "tunnel" in BEL7402 cell membranes (hepatic cancer cells); tumour growth *in vivo* was also significantly reduced when treated with a combination of the αCP and 5-FU.[100] Other applications existing for αCP include ion channels, for the transport of cations (Na^+, Ca^{2+}) through lipid bilayer membranes, as well as in organic electronics.[90] Current molecular dynamics (MD) studies are ongoing to understand the self-assembly mechanism and its impact on interfaces further; for instance, Brotzakis *et al.* have recently run simulations, determining that certain sequences with the Thr-Ala-Thr motive, such as c-[(L-Lys-D-Ala)$_2$-(L-Thr-D-Ala)$_2$], could have some antifreeze properties.[101]

Despite showing promising results in many fields, αCP have some drawbacks, mostly in terms of solubility as they can require the use of non-negligible amounts of DMF or DMSO to be dissolved in aqueous medium (e.g.: 11% of DMF for the *in vivo* study led by Chen *et al.*).[100] There is also limited control over the NTs length (varying between 50 and hundreds of nm) as well as the non-uniform nature of these assemblies. They show a propensity to aggregate in aqueous solution, forming bundles of tubes. One of the solutions that have been considered to enhance the control of the self-assembly process and improve the solubility in aqueous solution is attaching hydrophilic polymer chains to the cyclic peptide core. In the rest of the chapter, all CP mentioned are αCP with a diameter of 7 Å.

1.4.3 Previous synthesis and characterisation of cyclic peptide-polymer nanotubes

1.4.3.1 Synthesis of cyclic peptide-polymer nanotubes

In 2005, Couet *et al.* reported the first synthesis of polymer CPNT, where a poly(*N*-isopropyl acrylamide) (NIPAAm) chain was grown directly from an ATRP-initiator functionalized CP that was pre-assembled into a nanotube.[102] A convergent approach for polymer attachment to a CP was investigated around the same time by Börner and coworkers, where two poly(*n*-butyl acrylate) arms were conjugated *via* amide coupling reaction to two L-lysine residues in the CP backbone.[103] Both groups showed the formation of smaller tubes compared to non-conjugates CPNT, with lengths varying from 50 to 300 nm and a width of around 5 nm, the variations being explained by the different nature of the initial CP and polymeric chains.[102, 103] Perrier and co-workers later described another CP-polymer conjugation technique, based on copper catalysed azide-alkyne cycloaddition (CuAAc).[104]

Different polymers (such as poly(*n*-butyl acrylate) (poly(BA)), poly(acrylic acid) (poly(AA)), poly(hydroxyethyl acrylate) etc.) synthesised *via* RAFT polymerisation, containing alkyne end-groups, were efficiently coupled to N_3-Lys CP.[105] Another method reported by Rho *et al.* described the use of an activated cyclooctyne, to avoid the use of copper salts in the conjugation.[106] Thiol-ene chemistry and amide coupling using activated esters also led to the synthesis of CP-polymer conjugates.[107, 108] Recently, redox-responsive architectures were also engineered using pyridyl disulfide functionalised polymers on cysteine-containing cyclic peptide (see summary in **Scheme 1-5**).[109]

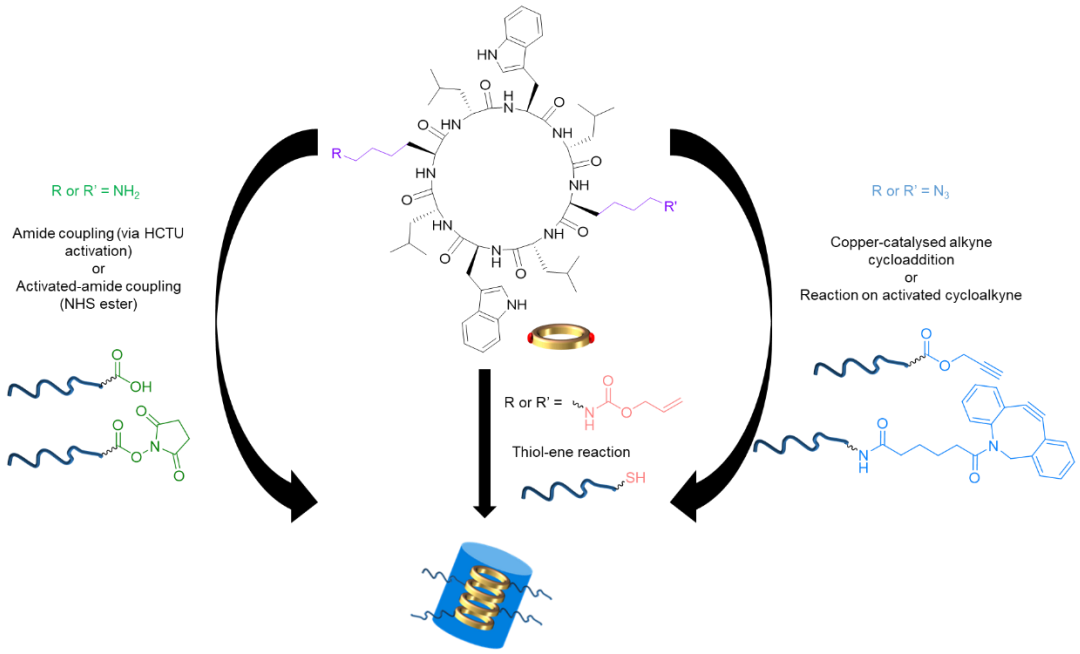

Scheme 1-5: Main synthetic paths explored by Perrier and co-workers for the polymer attachment to a cyclic peptide via a *grafting-to* approach.[105-108]

Polymers synthesised by Cationic Ring Opening Polymerisation (CROP) such as poly(2-ethyl-2-oxazolines) were also successfully attached to cyclic peptides via the functional end groups on the polymer chains.[110, 111] A systematic study published in 2016 by Larnaudie *et al.* directly compared the two main methods to synthesise conjugates, the *grafting-from* approach (the polymer is grown onto a cyclic peptide macro-chain transfer agent or macroCTA) and the *grafting-to* approach (the polymer is first synthesised then attached to the CP core).[112]

Each approach was found to have distinct benefits and drawbacks:

- The *grafting-from* approach, though allowing for the synthesis of pure conjugates, required large amounts of starting CP material and adequate conditions to maintain the solubility of the product.
- The *grafting-to* approach offered advantages in terms of molecular design (allowing conjugate libraries from CP and polymer stocks to be rapidly made), as well as an easier scalability process. Purification of unreacted polymer and CP is, however, a limiting factor, alongside with the use of functional polymers that require orthogonality with the conjugation reaction.[112]

Routes allowing for the synthesis of functional CP-polymer conjugates were developed by Barlow *et al.*, based on the post-modification of poly(bromoethylacrylate) units by nucleophilic substitutions.[113, 114] Charged (both positive and negative) and glycosylated conjugates could be obtained *via* this method, leading to a greater understanding of the self-assembly behaviour of such systems in aqueous environments.[113]

1.4.3.2 Self-assembly of cyclic peptide-polymer nanotubes

Self-assembly of different conjugates into tubular structures in different solvent systems was demonstrated using Small Angle Neutron Scattering (SANS) and Transmission Electron Microscopy (TEM), giving a better understanding of how polymer length, nature of the solvent considered, and temperature influence their core structure. [115, 116] Chapman *et al.* studied the behaviour of hydrophobic CP-[poly(BA)]$_2$, varying the length of the polymer chain and different sets of conditions (solvent, temperature) and proved that these parameters are key in the self-assembly process.[115] Studying the formation of CP(PEG) nanotubes in water, Mansfield *et al.* demonstrated the importance of different structural factors intervening in the self-assembly:

- the chain architecture (linear or brush polymer), with a noticeably lower assembly of brush conjugates (number of aggregation N_{agg} of 3 for CP-[poly(PEGA)]$_2$ and 22 for CP[PEG]$_2$, with the same overall molecular weight).
- the number of conjugated arms on the structure, showing that a lower number of polymer arms leads to higher numbers of aggregation.
- the solvent effect, with lower self-assemblies in solvent with strong hydrogen bonding capability such as DMF or DMSO (see **Figure 1-11**).[116]

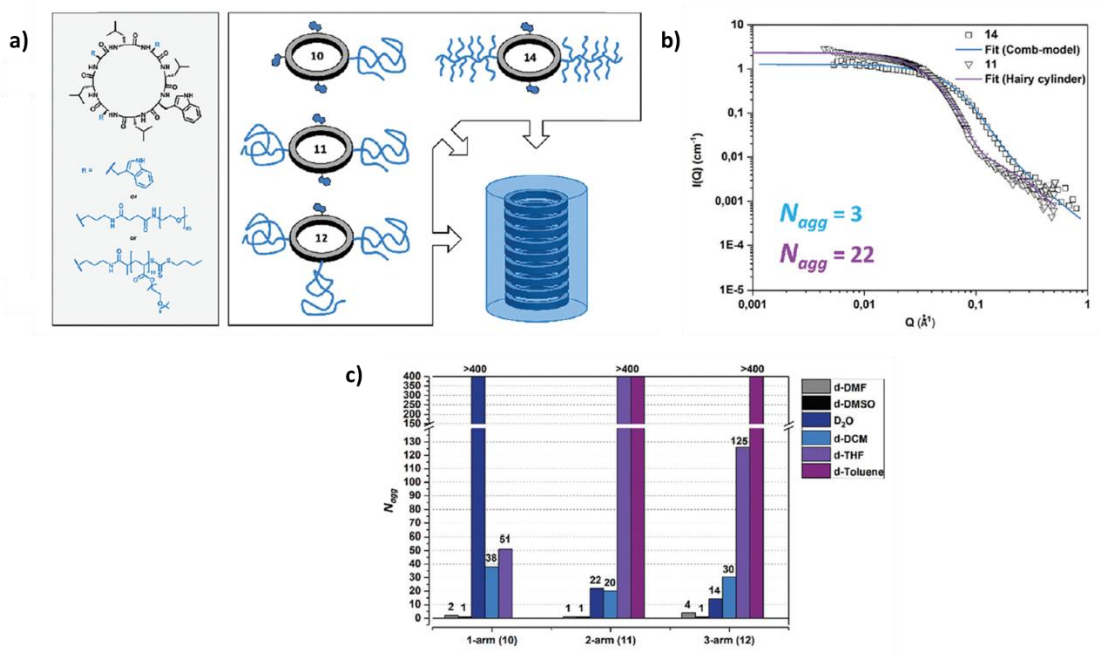

Figure 1-11: a) Structure of the different PEG-based CPNT systems investigated, varying the amount of polymer arms and the polymer morphology. b) SANS profiles comparing the self-assembly of CP[PEG]$_2$ with CP[poly(PEGA)]$_2$. c) Graph representing the number of aggregation determined by SANS in different solvents, with varying number of PEG arm on the CP.

The dynamic nature of these self-assemblies was also assessed by Rho *et al.*, checking the presence of a Förster Resonance Energy Transfer (FRET) between CP(PEG) conjugates labelled with FRET pair Cyanine 3 (Cy3) and Cyanine 5 (Cy5).[106] It was found that the self-assembly of these systems was highly dynamic, especially in aqueous systems, with the different CP-conjugates intermixing within the nanotube. Upon inclusion of a poly(BA) hydrophobic core, the self-assembly was stabilised resulting in structures with low exchange between the Cy3 and Cy5 CP-polymer unimers in the nanotube.[117]

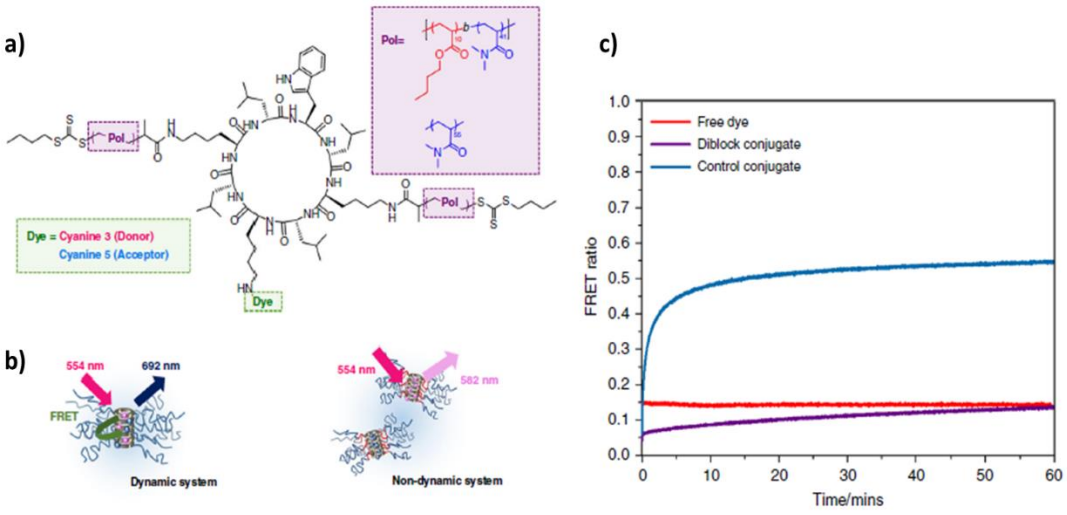

Figure 1-12: a) Structure of the cyclic peptide-polymer conjugate employed to generate structures with different dynamic behaviour (highly dynamic with poly(DMA), stabilised with poly(BA-*b*-DMA)). b) Scheme representing the FRET behaviour of dynamic (left) and non-dynamic (right) CPNT. c) Change of FRET ratio as for the Cy3/Cy5 FRET pair as studied by fluorescence spectroscopy. Adapted from Rho *et al.*[117]

1.4.3.3 Advanced CPNT based systems: responsiveness and Janus systems

Responsive cyclic peptide-polymer nanotubes were later designed, using different triggers to affect the self-assembly (pH,[118] redox conditions,[109, 111] host-guest chemistry[119]). Using the *grafting-from* approach to incorporate poly(2-(diisopropylamino)ethylmethacrylate–*b*-2-hydroxypropylmethacrylamide) (poly(DPAEMA-*b*-HPMA)) chains, Larnaudie *et al.* engineered pH-responsive CPNT where the poly(DPAEMA) block was protonated at pHs below 5. Short CPNT (around 11 nm) assembled upon a pH increase to 7.2.[118] Redox responsive CPNT developed by Song *et al.*, based on the use of pyridyl disulfide chemistry, saw their size dramatically increase (from 8.2 to over 200 nm, according to SANS) in the presence of reducing agents.[109] The use of cucurbit[n]uril CB-7 ability to engage in host-guest interactions with Phe moieties allowed for the disassembly of Phe-CPNT. This phenomenon was then reversed using 1-adamantanamine as a competitive guest molecule for CB-7, thus releasing the Phe moieties (see **Scheme 1-6**).[119]

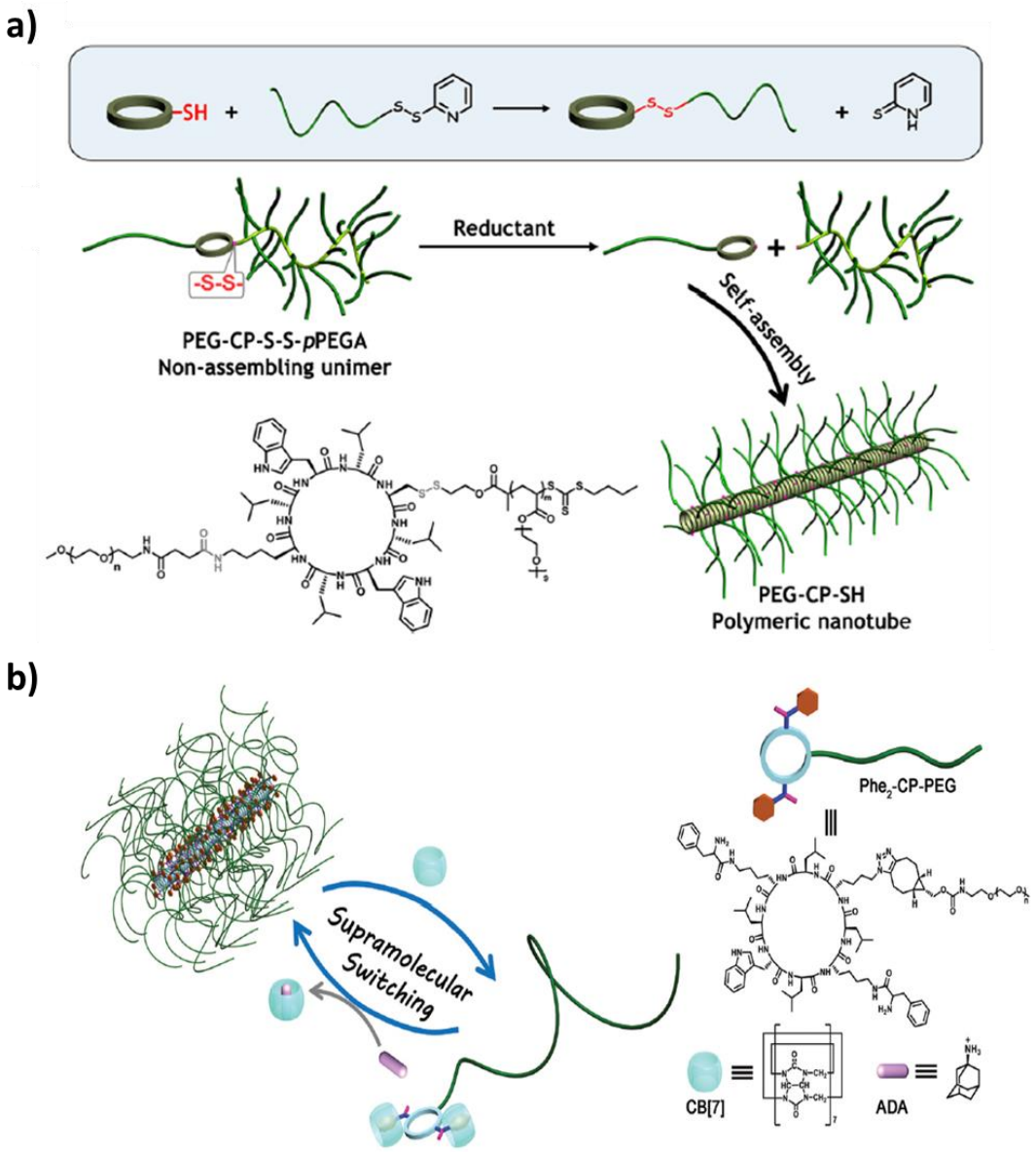

Scheme 1-6: Examples of responsive CPNT a) Redox responsiveness: scheme representing the pyridyl disulfide strategy employed to form redox responsive CPNT.[109] b) Host-guest chemistry: scheme representing CPNT with modified Phe moieties, capable of reversibly binding CB-7.[119]

Perrier and co-workers also investigated CPNT systems of higher complexity.[107, 120] Janus nanotubes, with a mixing or demixing polymer corona, were synthesised and have shown to interact with Large Unilamellar Vesicles (LUV) models, suggesting a membrane activity for such systems.[107] 250 nm-long CPNT with a wide diameter (16 nm), the so-called tubisomes, were formed using a similar approach to the aforementioned Janus CPNT. Each reactive Lys arm on the cyclic peptide was orthogonally functionalised with a different polymer: poly(BA) for the hydrophobic moiety and poly(PEGA) for its hydrophilic counterpart.[120]

1.5 Biological applications of cyclic peptide-polymer nanotubes

Given the relative recent development of these cyclic peptide-polymer nanotubes systems, few biological applications have been contemplated so far; their behaviour in biological systems has however started to be investigated.

1.5.1 Behaviour of cyclic peptide-polymer nanotubes in biological systems

The biocompatibility of several CPNT has been assessed over the past few years, thanks to the so-called MTT or XTT assays. Such assays evaluate the mitochondrial activity of mammalian cells by following the colour change in the cell culture media triggered by metabolic reactions on the incorporated tetrazolium dyes.[121] Most CP-polymer systems tested were found to be non-toxic according to this assay, to concentrations going up to 1 mg/mL, even for the charged conjugates previously described.[111, 113, 117, 120, 122] Following on from studies previously performed on cyclic peptide nanotubes and given their known propensity for membrane disruption (see 1.4.2), the membrane activity of CP-polymer nanotubes was investigated by Danial *et al.*[108] LUV dye leakage assays showed that hydrophobic CP-polymer conjugates were able to create more unimeric channels in vesicles compared to their hydrophilic counterparts. A thermoresponsive conjugate, based on poly(NIPAm) showed higher membrane interaction around 35°C, which is due to an increased lipophilicity of the CPNT (see **Figure 1-13**).[108] A similar study on LUV was performed on the redox responsive CPNT described by Hartlieb *et al*,, showing higher LUV disruption upon treatment with a reducing agent.[111] Tubisomes made from CPNT also showed membrane disruption properties, as they seem to be able to disrupt the lysosomal membrane.[120]

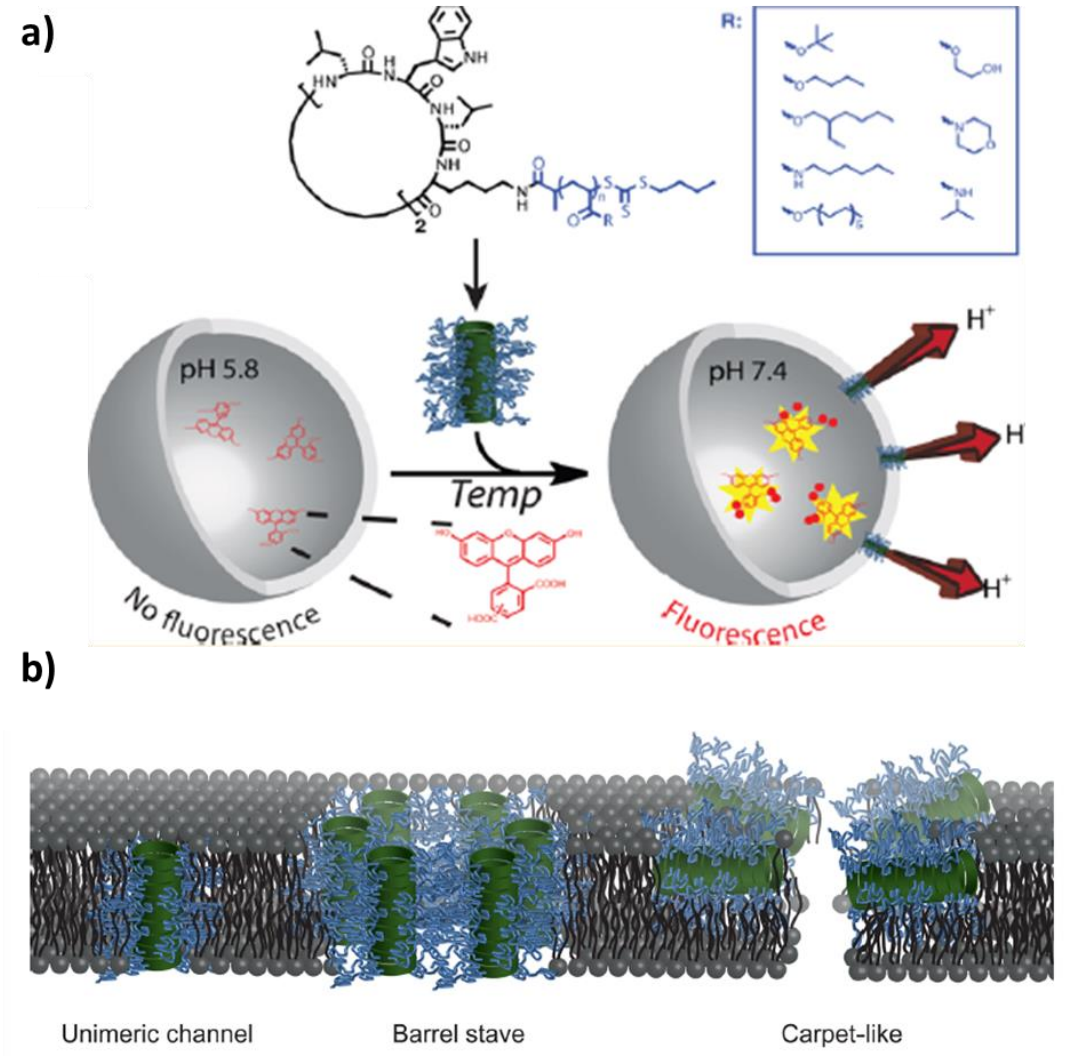

Figure 1-13: a) Scheme presenting the CPNT systems explored in this study on interactions with LUVs, with a focus on poly(NIPAm) thermoresponsive CPNT. b) Representation of the different modes of phospholipid bilayer disruption caused by cyclic peptide nanotubes and CP conjugates NTs. Adapted from Danial *et al.*[108]

1.5.2 Anticancer drug delivery applications

The main application explored for cyclic peptide-polymer nanotubes (CPNT) is in the delivery of anticancer drugs. Blunden *et al.* have found that in the case of antimetastatic Ru-based drug, RAPTA-C, the IC_{50} was reduced by a factor 18 on A2780 ovarian cancer cell line when attached to a CPNT.[123] The polymer used in this system was poly(2-hydroxyethylacrylate-*co*-2-chloroethylmethacrylate) (poly(HEA-co-CEMA)), the halogenated carbons in CEMA were substituted with RAPTA-C. The CPNT obtained were quite irregular in length (200-500 nm), with some aggregation into bundles that could be due to the destabilising presence of the drug.[123] More recently, the same anticancer activity was observed with a much more potent Ir complex.[124] The CPNT was this time made from poly(HPMA) copolymerised with some 2-(3-(Pyridin-4-ylmethyl)ureido)ethyl)methacrylate (PUEMA); this system was 20 nm long by static light scattering measurements (SLS). The IC_{50} of the drug-bearing CPNT was lower than the free drug and polymer conjugate on ovarian cancer cell line A2780. A better specificity of the nanotubes towards cancer cells was also noticed, as the toxicity of the Ir-containing CPNT was six times lower on healthy ovarian cells (HOF) than on A2780. Such changes were not correlated to a higher content of Ir in the cell, suggesting a more efficient mode of action for CPNT, in comparison to other systems considered in this study (see **Figure 1-14**).[124]

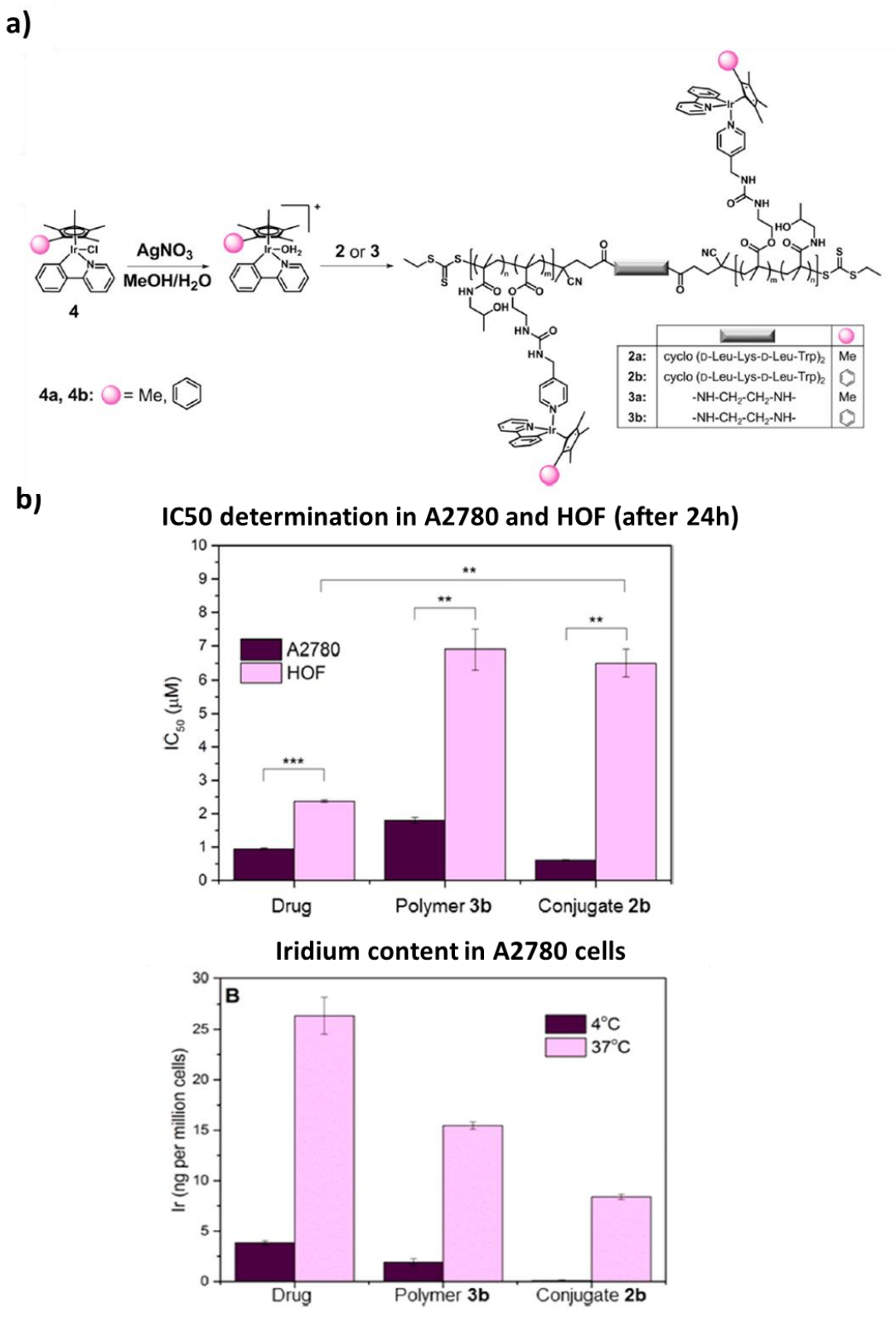

Figure 1-14: a) Ir-drug attachment strategy for the system designed by Larnaudie *et al.*, with the structure of the final conjugate tested. b) (top) IC50 determination for the free drug, the polymer-drug complex and the CPNT in ovarian cancer cells A2780 and healthy ovarian cells HOF. (bottom) Determination of the amount of Ir in cells after a 24 h exposure with the different systems tested.[124]

1.6 Motivation for this work

As previously demonstrated in this chapter, there is a wide scope of applications for polymer-based self-assembling nanocylinders in the life sciences. Cyclic peptide-polymer nanotubes, in particular, have been shown to be suitable drug delivery vectors and possess membrane-active properties that can be further exploited. It is, however, necessary to take a step back and try to comprehend fully the complexity of their behaviour on relevant biological models, as each of them has its own limitations and specificities to consider.

Better models need to be found to understand further the interaction at the lipid bilayer interface; results from LUV measurements do not deliver any information about the specificities of the interaction. The potential for adherence, the nanotube orientation in the bilayer as well as the differences in interaction in the presence of charges are all properties that demand further investigation. From what is already known on cyclic peptide nanotubes (see 1.4.2.1), such self-assemblies can have a use for antibacterial applications. Finding the right balance between solubility, membrane activity and self-assembly control could help develop the use of CP-polymer nanotubes for antibacterial purposes.

Such parameters are of equal importance when considering other applications, as they will directly affect cellular uptake. It is important to obtain a better understanding of the uptake phenomenon in different cell models to determine whether CPNT behave similarly to other classes of self-assembling polymer nanocylinders. The characteristics of tumour uptake of CPNT still requires special attention in order to pursue anticancer drug delivery applications.

The *in vivo* properties of these systems could be further investigated, especially in light of recent advances in controlling the dynamic nature of CPNT. Investigating the use of targeting moieties, both *in vitro* and *in vivo*, is an equally interesting research endeavour to delve into as they are commonly added to drug delivery vectors (see above).

The present work aims to provide answers to establish how CPNT behave in different biological models. It will also establish the key parameters of importance for the main applications being investigated, anticancer drug delivery and antibacterial action. The cellular interface will be the main focus of Chapter 2, wherein a library of fluorescent CPNT of differing lengths and containing a variety of polymers are tested against different cell lines. The uptake phenomenon will be further detailed, with an in-depth study of their fate in small tumour models (spheroids). The *in vivo* aspects will be discussed in Chapter 3, with a comparison of the pharmacokinetic and biodistribution profiles between stabilised and dynamic CPNT; integrin targeting CPNT and their activity will be presented for the first time in this chapter. Finally, the characteristics of the membrane activity of new charged and uncharged CPNT of different lengths will be examined on new bilayer models, using techniques such as Quartz Crystal Microbalance with Dissipation Effect (QCM-D) and neutron reflectivity in Chapter 4 (for an overall view of the models and parameters presented in this work, refer to **Scheme 1-7**).

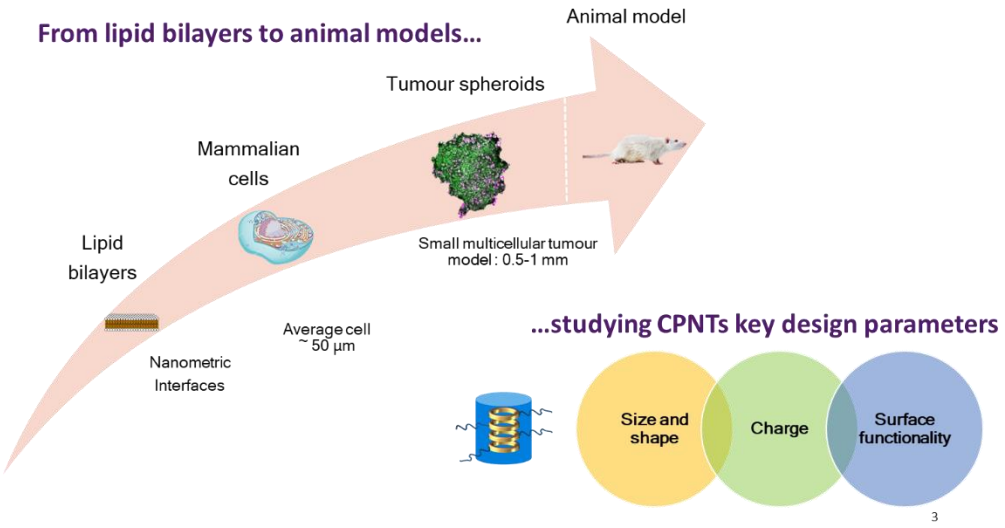

Scheme 1-7: Summary of the different biological models and CPNT' main design parameters covered in this thesis

1.7 References for Chapter 1

1. S. Friedrichs, *Report on statistics and indicators of biotechnology and nanotechnology*, OECD Science, Technology and Industry Working Papers, 2018.
2. B. Pelaz, C. Alexiou, R. A. Alvarez-Puebla, F. Alves, A. M. Andrews, S. Ashraf, L. P. Balogh, L. Ballerini, A. Bestetti, C. Brendel, *et al.*, *ACS Nano*, 2017, **11**, 2313.
3. J. A. Champion, Y. K. Katare and S. Mitragotri, *Journal of controlled release : official journal of the Controlled Release Society*, 2007, **121**, 3.
4. N. P. Truong, J. F. Quinn, M. R. Whittaker and T. P. Davis, *Polymer Chemistry*, 2016, **7**, 4295.
5. X. Zhu, C. Vo, M. Taylor and B. R. Smith, *Materials Horizons*, 2019, **6**, 1094.
6. X. Huang, L. Li, T. Liu, N. Hao, H. Liu, D. Chen and F. Tang, *ACS Nano*, 2011, **5**, 5390.
7. X. Huang, X. Teng, D. Chen, F. Tang and J. He, *Biomaterials*, 2010, **31**, 438.
8. Y. Qiu, Y. Liu, L. Wang, L. Xu, R. Bai, Y. Ji, X. Wu, Y. Zhao, Y. Li and C. Chen, *Biomaterials*, 2010, **31**, 7606.
9. S. J. Rosenthal, J. C. Chang, O. Kovtun, J. R. McBride and I. D. Tomlinson, *Chemistry & Biology*, 2011, **18**, 10.
10. Z. J. Han, A. E. Rider, C. Fisher, T. van der Laan, S. Kumar, I. Levchenko and K. Ostrikov, in *Carbon Nanotubes and Graphene (Second Edition)*, eds. K. Tanaka and S. Iijima, Elsevier, Oxford, 2014, pp. 279.
11. M. A. Bruckman, A. E. Czapar, A. VanMeter, L. N. Randolph and N. F. Steinmetz, *Journal of Controlled Release*, 2016, **231**, 103.
12. E. M. Plummer and M. Manchester, *WIREs Nanomedicine and Nanobiotechnology*, 2011, **3**, 174.
13. R. Heald and O. Cohen-Fix, *Current Opinion in Cell Biology*, 2014, **26**, 79.
14. Y. Shibata, G. K. Voeltz and T. A. Rapoport, *Cell*, 2006, **126**, 435.
15. G. M. Cooper, *The Cell: A molecular Approach (2nd edition)*, Sinauer Associates, Sunderland (MA), 2000.
16. H. Li, D. J. DeRosier, W. V. Nicholson, E. Nogales and K. H. Downing, *Structure*, 2002, **10**, 1317.
17. M. A. Jordan and L. Wilson, *Nature Reviews Cancer*, 2004, **4**, 253.
18. R. Dominguez and K. C. Holmes, *Annual Review of Biophysics*, 2011, **40**, 169.
19. A. Nürnberg, T. Kitzing and R. Grosse, *Nature Reviews Cancer*, 2011, **11**, 177.
20. J. Feher, in *Quantitative Human Physiology (Second Edition)*, ed. J. Feher, Academic Press, Boston, 2017, pp. 101.
21. L. Song, M. R. Hobaugh, C. Shustak, S. Cheley, H. Bayley and J. E. Gouaux, *Science*, 1996, **274**, 1859.
22. E. A. Merritt, S. Sarfaty, F. V. D. Akker, C. L'Hoir, J. A. Martial and W. G. J. Hol, *Protein Science*, 1994, **3**, 166.
23. R. Ketchem, W. Hu and T. Cross, *Science*, 1993, **261**, 1457.
24. M. Marsh and A. Helenius, *Cell*, 2006, **124**, 729.
25. J. Emanuel, A. Marzi and H. Feldmann, in *Advances in Virus Research*, eds. M. Kielian, T. C. Mettenleiter and M. J. Roossinck, Academic Press, 2018, vol. 100, pp. 189.
26. K. M. Johnson, J. V. Lange, P. A. Webb and F. A. Murphy, *The Lancet*, 1977, **309**, 569.
27. M. Zaitlin and P. Palukaitis, *Annual Review of Phytopathology* 2000, **38**, 117.
28. K. Namba, R. Pattanayek and G. Stubbs, *Journal of Molecular Biology*, 1989, **208**, 307.
29. J. A. Luckanagul, L. A. Lee, S. You, X. Yang and Q. Wang, *Journal of Biomedical Materials Research Part A*, 2015, **103**, 887.

30. S. Shukla, F. J. Eber, A. S. Nagarajan, N. A. DiFranco, N. Schmidt, A. M. Wen, S. Eiben, R. M. Twyman, C. Wege and N. F. Steinmetz, *Advanced Healthcare Materials* 2015, **4**, 874.
31. P. L. Chariou, K. L. Lee, J. K. Pokorski, G. M. Saidel and N. F. Steinmetz, *The Journal of Physical Chemistry B*, 2016, **120**, 6120.
32. S. Mukherjee, C. M. Pfeifer, J. M. Johnson, J. Liu and A. Zlotnick, *Journal of the American Chemical Society*, 2006, **128**, 2538.
33. M. A. Bruckman, L. N. Randolph, A. VanMeter, S. Hern, A. J. Shoffstall, R. E. Taurog and N. F. Steinmetz, *Virology*, 2014, **449**, 163.
34. F. Sainsbury, *Therapeutic Delivery*, 2017, **8**, 1019.
35. Z. Ahmad, A. Shah, M. Siddiq and H.-B. Kraatz, *RSC Advances*, 2014, **4**, 17028.
36. M. Müllner, *Macromolecular Chemistry and Physics*, 2016, **217**, 2209.
37. J. A. Champion, Y. K. Katare and S. Mitragotri, *Proceedings of the National Academy of Sciences* 2007, **104**, 11901.
38. J. L. Perry, K. P. Herlihy, M. E. Napier and J. M. DeSimone, *Accounts of Chemical Research*, 2011, **44**, 990.
39. H. Otsuka, Y. Nagasaki and K. Kataoka, *Materials Today*, 2001, **4**, 30.
40. L. Zhang and A. Eisenberg, *Science*, 1995, **268**, 1728.
41. Y.-Y. Won, H. T. Davis and F. S. Bates, *Science*, 1999, **283**, 960.
42. P. Dalhaimer, H. Bermudez and D. E. Discher, *Journal of Polymer Science Part B: Polymer Physics*, 2004, **42**, 168.
43. G. Srinivas, D. E. Discher and M. L. Klein, *Nature Materials*, 2004, **3**, 638.
44. Y. Geng and D. E. Discher, *Journal of the American Chemical Society*, 2005, **127**, 12780.
45. P. Dalhaimer, A. J. Engler, R. Parthasarathy and D. E. Discher, *Biomacromolecules*, 2004, **5**, 1714.
46. Y. Geng, P. Dalhaimer, S. Cai, R. Tsai, M. Tewari, T. Minko and D. E. Discher, *Nature Nanotechnology*, 2007, **2**, 249.
47. D. A. Christian, S. Cai, O. B. Garbuzenko, T. Harada, A. L. Zajac, T. Minko and D. E. Discher, *Molecular Pharmaceutics*, 2009, **6**, 1343.
48. K. Zhang, H. Fang, Z. Chen, J.-S. A. Taylor and K. L. Wooley, *Bioconjugate Chemistry*, 2008, **19**, 1880.
49. J. Zhao, H. Lu, P. Xiao and M. H. Stenzel, *ACS Applied Materials & Interfaces*, 2016, **8**, 16622.
50. J. Zhao, H. Lu, Y. Yao, S. Ganda and M. H. Stenzel, *Journal of Materials Chemistry B*, 2018, **6**, 4223.
51. S. L. Canning, G. N. Smith and S. P. Armes, *Macromolecules*, 2016, **49**, 1985.
52. V. Ladmiral, M. Semsarilar, I. Canton and S. P. Armes, *Journal of the American Chemical Society*, 2013, **135**, 13574.
53. A. Blanazs, R. Verber, O. O. Mykhaylyk, A. J. Ryan, J. Z. Heath, C. W. I. Douglas and S. P. Armes, *Journal of the American Chemical Society*, 2012, **134**, 9741.
54. B. Karagoz, L. Esser, H. T. Duong, J. S. Basuki, C. Boyer and T. P. Davis, *Polymer Chemistry*, 2014, **5**, 350.
55. L. Qiu, C.-R. Xu, F. Zhong, C.-Y. Hong and C.-Y. Pan, *ACS Applied Materials & Interfaces*, 2016, **8**, 18347.
56. E. Hinde, K. Thammasiraphop, H. T. T. Duong, J. Yeow, B. Karagoz, C. Boyer, J. J. Gooding and K. Gaus, *Nature Nanotechnology*, 2017, **12**, 81.
57. S. Kaga, N. P. Truong, L. Esser, D. Senyschyn, A. Sanyal, R. Sanyal, J. F. Quinn, T. P. Davis, L. M. Kaminskas and M. R. Whittaker, *Biomacromolecules*, 2017, **18**, 3963.
58. I. Canton, N. J. Warren, A. Chahal, K. Amps, A. Wood, R. Weightman, E. Wang, H. Moore and S. P. Armes, *ACS Central Science*, 2016, **2**, 65.
59. D. E. Mitchell, J. R. Lovett, S. P. Armes and M. I. Gibson, *Angewandte Chemie International Edition*, 2016, **55**, 2801.

60. J. A. Massey, K. Temple, L. Cao, Y. Rharbi, J. Raez, M. A. Winnik and I. Manners, *Journal of the American Chemical Society*, 2000, **122**, 11577.
61. L. Shen, H. Wang, G. Guerin, C. Wu, I. Manners and M. A. Winnik, *Macromolecules*, 2008, **41**, 4380.
62. J. B. Gilroy, T. Gädt, G. R. Whittell, L. Chabanne, J. M. Mitchels, R. M. Richardson, M. A. Winnik and I. Manners, *Nature Chemistry*, 2010, **2**, 566.
63. Z.-X. Du, J.-T. Xu and Z.-Q. Fan, *Macromolecules*, 2007, **40**, 7633.
64. M. C. Arno, M. Inam, Z. Coe, G. Cambridge, L. J. Macdougall, R. Keogh, A. P. Dove and R. K. O'Reilly, *Journal of the American Chemical Society*, 2017, **139**, 16980.
65. N. Petzetakis, A. P. Dove and R. K. O'Reilly, *Chemical Science*, 2011, **2**, 955.
66. N. Petzetakis, D. Walker, A. P. Dove and R. K. O'Reilly, *Soft Matter*, 2012, **8**, 7408.
67. J. Zhang, L.-Q. Wang, H. Wang and K. Tu, *Biomacromolecules*, 2006, **7**, 2492.
68. L. Sun, N. Petzetakis, A. Pitto-Barry, T. L. Schiller, N. Kirby, D. J. Keddie, B. J. Boyd, R. K. O'Reilly and A. P. Dove, *Macromolecules*, 2013, **46**, 9074.
69. Z. Li, L. Sun, Y. Zhang, A. P. Dove, R. K. O'Reilly and G. Chen, *ACS Macro Letters*, 2016, **5**, 1059.
70. Z. Li, Y. Zhang, L. Wu, W. Yu, T. R. Wilks, A. P. Dove, H.-m. Ding, R. K. O'Reilly, G. Chen and M. Jiang, *ACS Macro Letters*, 2019, **8**, 596.
71. J. R. Finnegan, X. He, S. T. G. Street, J. D. Garcia-Hernandez, D. W. Hayward, R. L. Harniman, R. M. Richardson, G. R. Whittell and I. Manners, *Journal of the American Chemical Society*, 2018, **140**, 17127.
72. Q. Yu, M. G. Roberts, S. Pearce, A. M. Oliver, H. Zhou, C. Allen, I. Manners and M. A. Winnik, *Macromolecules*, 2019, **52**, 5231.
73. L. Guyon, E. Lepeltier and C. Passirani, *Nano Research*, 2018, **11**, 2315.
74. D. Mandal, A. Nasrolahi Shirazi and K. Parang, *Organic & Biomolecular Chemistry*, 2014, **12**, 3544.
75. J. D. Hartgerink, E. Beniash and S. I. Stupp, *Proceedings of the National Academy of Sciences*, 2002, **99**, 5133.
76. C. J. Newcomb, S. Sur, S. S. Lee, J. M. Yu, Y. Zhou, M. L. Snead and S. I. Stupp, *Nano Letters*, 2016, **16**, 3042.
77. S. Zhou, A. Hokugo, M. McClendon, Z. Zhang, R. Bakshi, L. Wang, L. A. Segovia, K. Rezzadeh, S. I. Stupp and R. Jarrahy, *Burns*, 2019, **45**, 1112.
78. M. M. So, N. A. Mansukhani, E. B. Peters, M. S. Albaghdadi, Z. Wang, C. M. Rubert Pérez, M. R. Kibbe and S. I. Stupp, *Advanced Biosystems*, 2018, **2**, 1700123.
79. H. Cui, M. J. Webber and S. I. Stupp, *Peptide Science*, 2010, **94**, 1.
80. D. J. Adams, *Macromolecular Bioscience*, 2011, **11**, 160.
81. E. R. Draper, H. Su, C. Brasnett, R. J. Poole, S. Rogers, H. Cui, A. Seddon and D. J. Adams, *Angewandte Chemie International Edition*, 2017, **56**, 10467.
82. D. M. Ryan and B. L. Nilsson, *Polymer Chemistry*, 2012, **3**, 18.
83. D. S. Nielsen, N. E. Shepherd, W. Xu, A. J. Lucke, M. J. Stoermer and D. P. Fairlie, *Chemical Reviews*, 2017, **117**, 8094.
84. P. De Santis, S. Morosetti and R. Rizzo, *Macromolecules*, 1974, **7**, 52.
85. M. R. Ghadiri, J. R. Granja, R. A. Milligan, D. E. McRee and N. Khazanovich, *Nature*, 1993, **366**, 324.
86. R. Chapman, M. Danial, M. L. Koh, K. A. Jolliffe and S. Perrier, *Chemical Society Reviews*, 2012, **41**, 6023.
87. D. Seebach, J. L. Matthews, A. Meden, T. Wessels, C. Baerlocher and L. B. McCusker, *Helvetica Chemica Acta*, 1997, **80**, 173.
88. M. Amorín, L. Castedo and J. R. Granja, *Journal of the American Chemical Society*, 2003, **125**, 2844.
89. A. Lamas, A. Guerra, M. Amorín and J. R. Granja, *Chemical Science*, 2018, **9**, 8228.
90. W.-H. Hsieh and J. Liaw, *Journal of Food and Drug Analysis*, 2019, **27**, 32.

91. H. S. Kim, J. D. Hartgerink and M. R. Ghadiri, *Journal of the American Chemical Society*, 1998, **120**, 4417.
92. S. Fernandez-Lopez, H.-S. Kim, E. C. Choi, M. Delgado, J. R. Granja, A. Khasanov, K. Kraehenbuehl, G. Long, D. A. Weinberger, K. M. Wilcoxen, *et al.*, *Nature*, 2001, **412**, 452.
93. L. Motiei, S. Rahimipour, D. A. Thayer, C.-H. Wong and M. R. Ghadiri, *Chemical Communications*, 2009, 3693.
94. M. Danial, S. Perrier and K. A. Jolliffe, *Organic & Biomolecular Chemistry*, 2015, **13**, 2464.
95. W. S. Horne, C. M. Wiethoff, C. Cui, K. M. Wilcoxen, M. Amorin, M. R. Ghadiri and G. R. Nemerow, *Bioorganic & Medicinal Chemistry*, 2005, **13**, 5145.
96. A. Montero, P. Gastaminza, M. Law, G. Cheng, Francis V. Chisari and M. R. Ghadiri, *Chemistry & Biology*, 2011, **18**, 1453.
97. M. Li, M. Ehlers, S. Schlesiger, E. Zellermann, S. K. Knauer and C. Schmuck, *Angewandte Chemie International Edition*, 2015, **55**, 598.
98. J. Sanchez-Quesada, M. R. Ghadiri, H. Bayley and O. Braha, *Journal of the American Chemical Society*, 2000, **122**, 11757.
99. W.-H. Hsieh, S.-F. Chang, H.-M. Chen, J.-H. Chen and J. Liaw, *Molecular Pharmaceutics*, 2012, **9**, 1231.
100. J. Chen, B. Zhang, F. Xia, Y. Xie, S. Jiang, R. Su, Y. Lu and W. Wu, *Nanoscale*, 2016, **8**, 7127.
101. Z. F. Brotzakis, M. Gehre, I. K. Voets and P. G. Bolhuis, *Physical Chemistry Chemical Physics*, 2017, **19**, 19032.
102. J. Couet, J. D. J. S. Samuel, A. Kopyshev, S. Santer and M. Biesalski, *Angewandte Chemie International Edition*, 2005, **44**, 3297.
103. M. G. J. ten Cate, N. Severin and H. G. Börner, *Macromolecules*, 2006, **39**, 7831.
104. R. Chapman, K. A. Jolliffe and S. Perrier, *Australian Journal of Chemistry*, 2010, **63**, 1169.
105. R. Chapman, K. A. Jolliffe and S. Perrier, *Polymer Chemistry*, 2011, **2**, 1956.
106. J. Y. Rho, J. C. Brendel, L. R. MacFarlane, E. D. H. Mansfield, R. Peltier, S. Rogers, M. Hartlieb and S. Perrier, *Advanced Functional Materials*, 2018, **28**, 1704569.
107. M. Danial, C. My-Nhi Tran, P. G. Young, S. Perrier and K. A. Jolliffe, *Nature Communications*, 2013, **4**, 2780.
108. M. Danial, C. M. N. Tran, K. A. Jolliffe and S. Perrier, *Journal of the American Chemical Society*, 2014, **136**, 8018.
109. Q. Song, J. Yang, S. C. L. Hall, P. Gurnani and S. Perrier, *ACS Macro Letters*, 2019, **8**, 1347.
110. R. Chapman, P. J. M. Bouten, R. Hoogenboom, K. A. Jolliffe and S. Perrier, *Chemical Communications*, 2013, **49**, 6522.
111. M. Hartlieb, S. Catrouillet, A. Kuroki, C. Sanchez-Cano, R. Peltier and S. Perrier, *Chemical Science*, 2019, **10**, 5476.
112. S. C. Larnaudie, J. C. Brendel, K. A. Jolliffe and S. Perrier, *Journal of Polymer Science, Part A: Polymer Chemistry*, 2016, **54**, 1003.
113. T. R. Barlow, PhD thesis, University of Warwick, 2017.
114. T. R. Barlow, J. C. Brendel and S. Perrier, *Macromolecules*, 2016, **49**, 6203.
115. R. Chapman, M. L. Koh, G. G. Warr, K. A. Jolliffe and S. Perrier, *Chemical Science*, 2013, **4**, 2581.
116. E. D. H. Mansfield, M. Hartlieb, S. Catrouillet, J. Y. Rho, S. C. Larnaudie, S. E. Rogers, J. Sanchis, J. C. Brendel and S. Perrier, *Soft Matter*, 2018, **14**, 6320.
117. J. Y. Rho, H. Cox, E. D. H. Mansfield, S. H. Ellacott, R. Peltier, J. C. Brendel, M. Hartlieb, T. A. Waigh and S. Perrier, *Nature Communications*, 2019, **10**, 4708.
118. S. C. Larnaudie, J. C. Brendel, K. A. Jolliffe and S. Perrier, *ACS Macro Letters*, 2017, **6**, 1347.

119. Q. Song, J. Yang, J. Y. Rho and S. Perrier, *Chemical Communications*, 2019, **55**, 5291.
120. J. C. Brendel, J. Sanchis, S. Catrouillet, E. Czuba, M. Z. Chen, B. M. Long, C. Nowell, A. Johnston, K. A. Jolliffe and S. Perrier, *Angewandte Chemie International Edition*, 2018, **57**, 16678.
121. T. Mosmann, *Journal of Immunological Methods*, 1983, **65**, 55.
122. S. C. Larnaudie, J. Sanchis, T.-H. Nguyen, R. Peltier, S. Catrouillet, J. C. Brendel, C. J. H. Porter, K. A. Jolliffe and S. Perrier, *Biomaterials*, 2018, **178**, 570.
123. B. M. Blunden , R. Chapman, M. Danial, H. Lu, K. A. Jolliffe, S. Perrier and M. H. Stenzel, *Chemistry – A European Journal*, 2014, **20**, 12745.
124. S. C. Larnaudie, J. C. Brendel, I. Romero-Canelón, C. Sanchez-Cano, S. Catrouillet, J. Sanchis, J. P. C. Coverdale, J.-I. Song, A. Habtemariam, P. J. Sadler, *et al.*, *Biomacromolecules*, 2018, **19**, 239.

Chapter 2

Comparative Study of the Cellular Uptake and Intracellular Behaviour of a Library of Cyclic Peptide-Polymer Nanotubes with Different Self-Assembling Properties

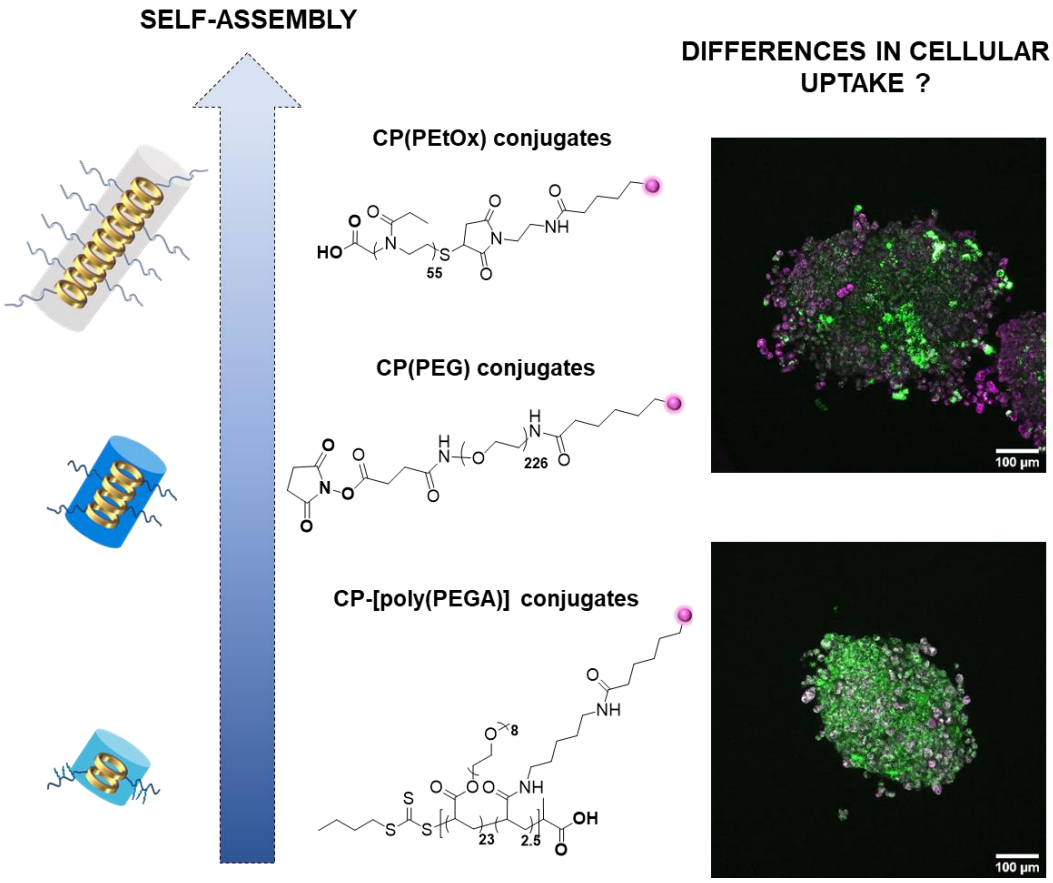

Chapter 2: Some repeats of the XTT cellular viability assay were carried out by Ji-Inn Song. The Transmission Electron Microscopy presented was acquired by Dr. Julia Y. Rho (University of Warwick).

2.1 Introduction

The design of novel nanomaterials for a diverse range of biological applications has gained great interest in recent years. The use of nanoparticle (NP) technologies, in particular for drug delivery, has allowed for enhanced bioavailability and increased efficacy of some drugs, as well as a reduction in the occurrence of side effects.[1] Different types of nanomaterials with various morphologies have been investigated for these purposes (e.g: polymeric micelles,[2] liposomes,[3] and nanogels)[4, 5]. Studying the stability and behaviour of drug-free nanoparticle systems *in vitro* and *in vivo* is essential to develop more efficient and biocompatible systems. Cellular uptake of NPs usually occurs *via* different pathways (endocytic or not), and understanding this is of vital importance for drug delivery systems. This process is known to be dependent on a variety of physico-chemical properties, including surface charge, hydrophobicity or presence of targeting moieties,[6] but is highly directed by the size and shape of the NPs.[7, 8] In particular, cylindrical or rod-like particles are known to have improved circulation times and cellular uptake when compared with their spherical counterparts.[9] For example, it has been observed that dextran-coated magnetic iron nanoworms, both labelled or not labelled with a targeting peptide sequence, were more efficient at targeting tumours selectively *in vivo* than their spherical equivalents.[10] Changing the aspect ratio of cylindrical polymer brushes also allows to tailor such systems to obtain improved uptake of the systems by tumours, both in spheroid and *in vivo* models.[11, 12] Remarkably, these changes in the cellular uptake efficiency between spheres and rods were attributed to differences on the membrane wrapping of the particles. Computational studies demonstrated that the mode of entry differs with the aspect ratio and the general morphology of the nanostructure, whilst also suggesting an orientation-dependence.[13] The importance of shape on intracellular behaviour was further highlighted in the work of Hinde *et al* where Polymerisation-Induced Self-Assembly (PISA) was employed to generate architectures of different size and shape.

The intranuclear uptake was studied by the authors using pair-correlation microscopy and surprisingly, it was found that despite adding a nuclear localisation signal (NLS) tag on spherical polymer nanoparticles, passage through the nuclear pore complex was still less efficient than with untagged rods or worms.[14]

Two of the most common challenges with previously described systems is to ensure their biodegradability and clearance from the body. The use of self-assembling materials, based on supramolecular interactions, could be a way to circumvent this issue for drug delivery.[15] Self-assembling organic nanotubes are then ideal systems for drug delivery, but also have potential applications in numerous fields, such as sensors, catalysis and ion channel mimics.[16] Amidst these self-assembling systems, cyclic octapeptides, comprising of alternating D- and L- amino-acids and able to self-assemble into tubular β-sheet-like structures, have been considered of interest for biological applications (see Chapter 1, section 1.4).[17, 18] These self-assemblies can lead to uncontrollable, insoluble aggregation; better control over the stacking process and improved solubility in water can be obtained through conjugation of hydrophilic polymers to the cyclic peptides (CP).[19-21] The potential for cyclic peptide-polymer nanotubes (CPNT) in the delivery of anticancer drugs has previously been explored, as mentioned in Chapter 1.[22,23] Despite these promising results, little is known on what design parameters are of importance to make optimal use of CPNT for biological applications. Very different polymer CPNT were considered in the aforementioned studies, hence the need for a more systematic study of the uptake of non-drug containing CPNT. Herein, we report the synthesis of a library of different fluorescently-labelled cyclic peptide-polymer conjugates. By varying the number of polymer chains, and the composition and morphology of the polymer used, we obtained systems with different self-assembling behaviour. Their cellular uptake was then evaluated on 2D cell models to establish patterns related to the propensity of the conjugates for self-assembly. Diffusion phenomena and intracellular behaviour were also investigated in 3D models with the help of confocal laser scanning microscopy (CLSM).

2.2 Results and discussion

2.2.1 Synthesis of the fluorescent cyclic peptide-polymer conjugates

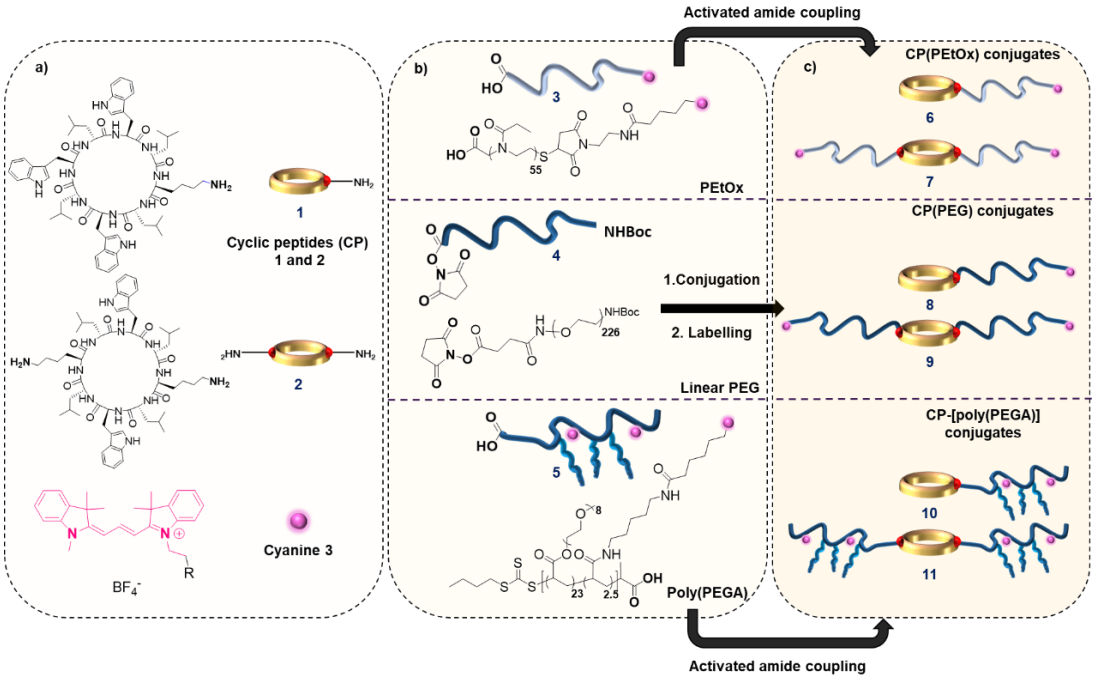

Scheme 2-1: Overview of the different fluorescent CP-polymer conjugates investigated. a) Cyclic peptides **1** and **2** and the dye molecule, Cyanine 3, b) different labelled hydrophilic polymers (**3**, **4** and **5**) and c) the final structures obtained by amide coupling onto cyclic peptides (**6**, **7**, **8**, **9**, **10**, **11**).

In order to study the effect of different design parameters on the cellular uptake of CP-polymer nanotubes, two cyclic peptides with different potential for polymer arm incorporation and three hydrophilic polymers with different composition and morphology were chosen. Cyclic peptides were synthesised by cyclising and deprotecting linear peptides obtained from automated solid phase peptide synthesis (SPPS), in a similar fashion than previously reported in the literature.[24] The amino-acid sequences considered herein are similar than the ones used in previous studies on the self-assembly of CPNT.[20] CP **1** and **2** contained four D-Leucine segments, essential for the self-assembly, in alternance with L-Lysine acting as the reactive arms (one or two depending on the peptide) and L-Tryptophan (2 or 3 units, acting as a UV chromophore and further stabilising the stacking process). Linear octapeptides, comprising of alternating D- and L- amino acids, were produced using an automated Solid Phase Peptide Synthesiser. Automation of the peptide synthesis is convenient for non-modified protected amino acids, as it allows for access to high yields of the final linear peptide in less than 24 h. Around 700 mg of the 1 arm Lys linear peptide and 475 mg of the 2 arm Lys linear peptide were obtained.

The cyclisation was performed using DMTMM.BF_4, reaching quantitative conversion after five days in both cases. Mass spectrometry was used to check the apparition of the cyclic species. DMTMM.BF_4, forms a "superactive triazine ester" during the reaction,[25] and was chosen to avoid epimerization side reactions so that the desired planar structure could be obtained. Highly dilute conditions were also required for this reaction in order to favour intramolecular cyclisation. Comparison of NMR spectra of the linear peptide and its protected cyclic counterpart showed a clear shift for the proton in alpha of the Lys group (see Appendix A, **Figure A-1** and **Figure A-2**), comforting observations made with mass spectrometry. After precipitation, the Boc-protected cyclic peptides were deprotected using a cleavage mix of TFA 9: Water 0.5: TIPS 0.5. The final cyclic peptides were characterised by NMR spectroscopy and mass spectrometry. The global yields obtained for the synthesis of CP **1** and CP **2** were 27% and 19%, respectively. It is likely that most losses of the compound occurred during the precipitation of the protected CPs. Other solvent mixtures or purification and isolation techniques could be considered to increase the global yield. The synthetic route is summarised on **Scheme 2-2**.

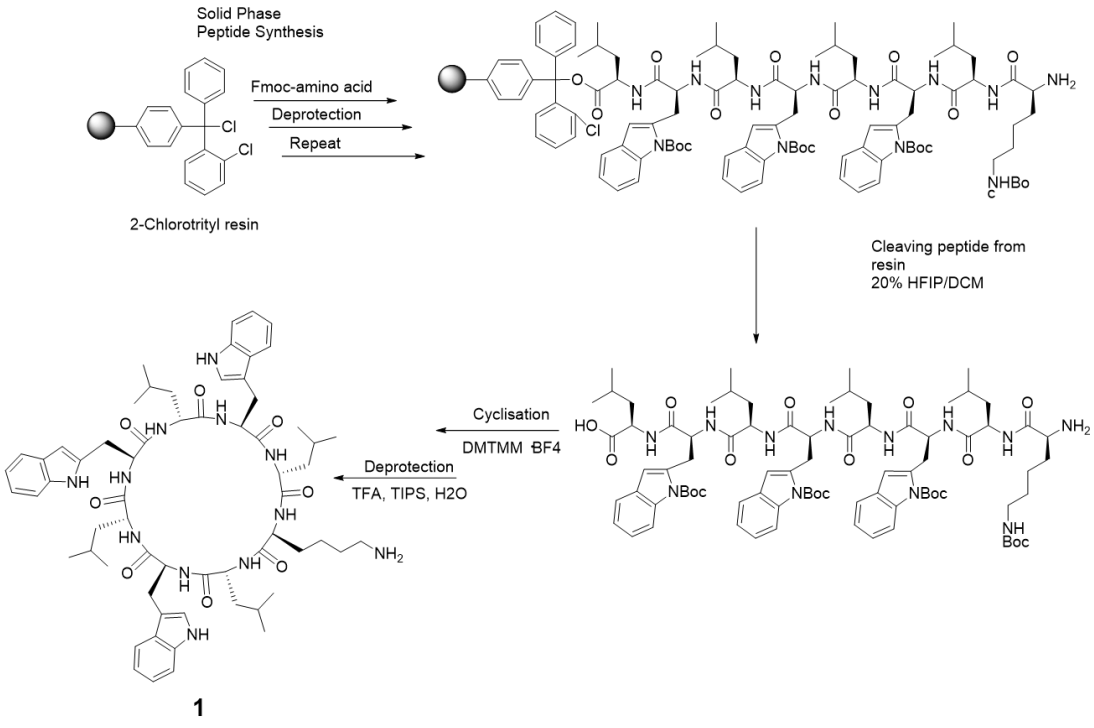

Scheme 2-2: Example of synthesis of a cyclic peptide (CP **1**), divided into three steps: automated linear peptide synthesis by solid phase peptide synthesis (SPPS); cyclisation in dilute conditions; deprotection of all functional groups (Boc removal).

A number of different systems were used to form the polymeric arms in this study. Linear poly(ethylene glycol) (PEG) was chosen as it is present in a high number of pharmaceutical preparations, given its biocompatibility and the large amount of information on its safety profile *in vivo*.[26] A brush copolymer of PEG-acrylate 480 (PEGA) was also synthesised for comparison, to evaluate the impact of morphology on both self-assembly and cellular uptake. Investigating alternatives to PEG are of interest, given rising concerns on the immunogenicity of PEG. As such, Poly-2-ethyl-2-oxazoline (PEtOx) was used as it is currently considered as a viable alternative to PEG given its biocompatibility, and allows easier access to diverse structures.[27, 28] Finally, all CP-polymer conjugates were labelled using Cyanine 3, as conjugates with this dye have already shown a good potential for biological imaging (**Scheme 2-1**). Non-labelled conjugates were synthesised for characterisation of the self-assemblies by scattering techniques.

To generate the PEtOx arms, Cationic Ring Opening Polymerisation (CROP) was performed in a microwave reactor using 2-ethyl-2 oxazoline as a monomer, adopting an end group functionalisation strategy with a tert-butyl protected carboxylic acid on the initiator end (**12**) and a xanthate group on the terminating agent end. This type of polymerisation requires the use of initiators with a good leaving group (here Br); in the case of 2-oxazolines, propagation occurs by successive nucleophilic addition of 2-oxazoline species on a covalent or ionic growing chain. The degree of polymerisation can be controlled and is equivalent to the number of equivalents of monomer compared to the initiator. The reaction is usually terminated by adding a nucleophilic species (here a xanthate salt) that will be the polymer end-group. Bifunctional poly(2-ethyl-2-oxazoline) **13** was formed by CROP of 2-ethyl-2-oxazoline, with good control over the polymerisation (M_n (NMR) = 5,700 g/mol, M_n (SEC) = 6,100 g/mol, $Đ$ = 1.16) and over end group fidelity, as determined by mass spectrometry and NMR (see Appendix A, **Figure A-4** and **Figure A-9**). Moreover, end groups were chosen to ensure the orthogonality of the reactions involved in the following modification (see **Scheme 2-3**). Both protecting groups were removed after treatment in basic conditions, allowing for further functionalisation with a maleimide-functionalised Cyanine 3 on the thiol-end prior to efficient attachment on the cyclic peptides.

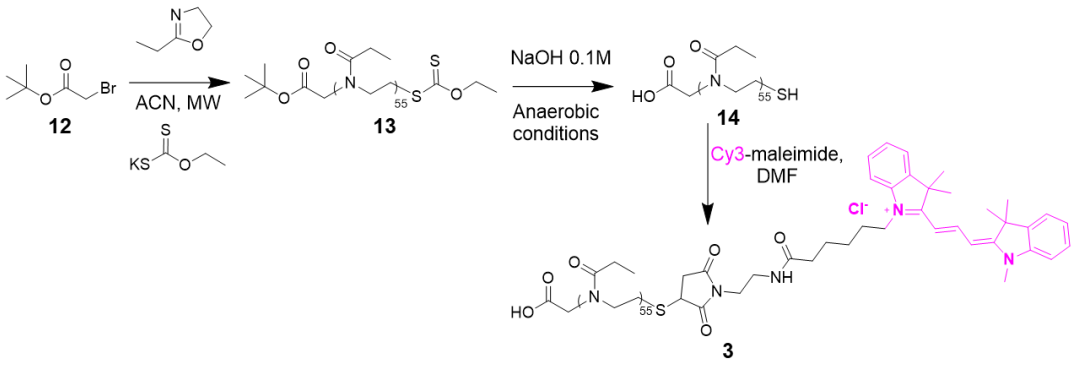

Scheme 2-3: Reaction scheme for the synthesis of bifunctional poly(2-ethyl-2-oxazoline) **3**.

A commercial N-hydroxysuccinimide (NHS) and Boc-protected amine bifunctional 10 kg/mol PEG was used to synthesise Cyanine 3-functionalised CP-PEG systems; these groups were chosen to allow for orthogonality without having to use copper-mediated alkyne cycloaddition or activated cyclooctyne coupling. The polymer was first conjugated onto the cyclic peptide using activated amide coupling, in the presence of DIPEA as a hindered base. Yields for this reaction were 65% for both cyclic peptides involved in this study, and dialysis against pure water allowed for an excellent recovery of the conjugate whilst removing the free unreacted polymer. The conjugates were then treated with a cleavage mixture of TFA:TIPS:water to deprotect the amine groups, prior to functionalisation of the pendant amine groups using NHS-tagged Cyanine 3, and purified to remove any free dye or fluorescent polymer using dialysis in water and preparative HPLC (see **Scheme 2-4**). A control fluorescent PEG of 20 kg/mol was also synthesised for biological studies.

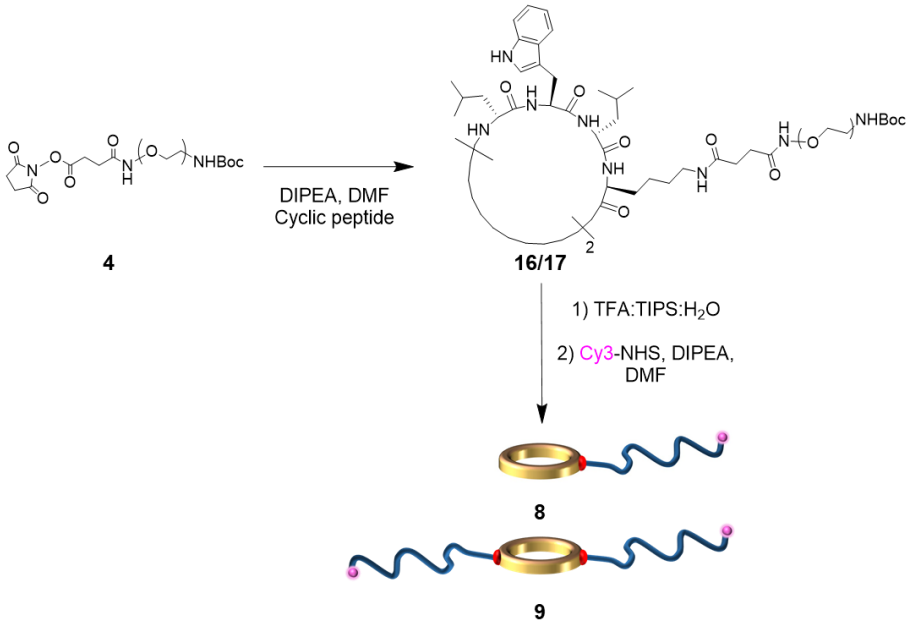

Scheme 2-4: Reaction scheme for the synthesis of fluorescent CP(PEG) and CP(PEG)$_2$.

Fluorescently labelled poly(PEGA) systems were produced using Reversible Addition-Fragmentation Chain Transfer (RAFT) polymerisation. RAFT polymerisation is a living radical polymerisation process, allowing excellent control over the molecular weight and dispersity of the polymer synthesised. It is based on the degenerative transfer of radicals between polymer chains *via* reversible addition to a chain transfer agent (CTA or RAFT agent), giving equal opportunities for all polymer chains to grow.[29] A statistical copolymer of PEGA and N-acryloxysuccinimide (NAS), a reactive monomer that can be used for post-functionalisation with amines, was first synthesised using (propanoic acid)yl butyl trithiocarbonate (PABTC) RAFT agent **18** given its compatibility with acrylates (the R group leading to the formation of a secondary radical). Brush copolymer **19** (M_n(SEC) = 8,400 g/mol, M_n(NMR) = 9,900 g/mol, $Đ$ = 1.14), containing 23 units of PEGA and 2.5 units of NAS as indicated by NMR, was obtained with excellent control over the polymerisation. Amine-functionalised Cyanine 3 was then used to label the copolymer; HPLC with fluorescence detection and NMR analysis (peaks in the aromatic regions) confirmed successful labelling. Both polymeric compounds were conjugated to the cyclic peptides using activated amide coupling (using NHS esters or HCTU/NMM as an activating agent) and then purified to remove any free dye or fluorescent polymer using dialysis in water and preparative HPLC.

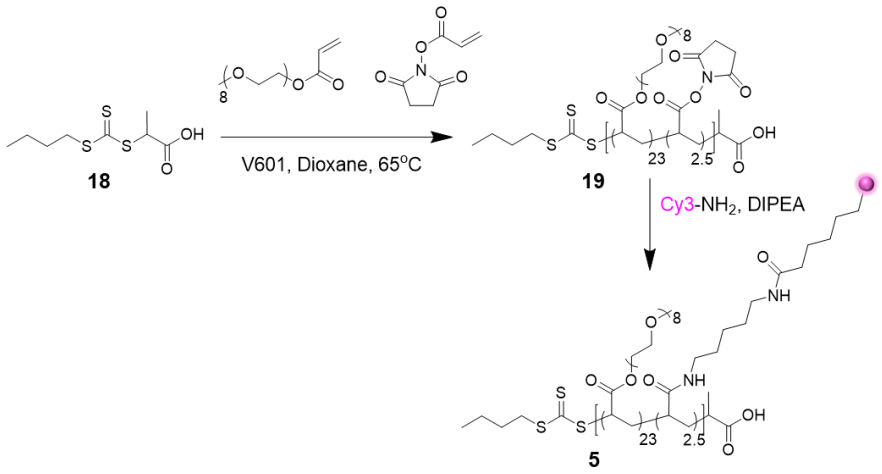

Scheme 2-5: Reaction scheme for the synthesis of fluorescent poly(PEGA) **5**.

The chromatograms showed little difference in retention time between the different conjugates, as all the compounds eluted around 80% MeOH content in the gradient tested, suggesting they were all of a similar lipophilicity. It is hypothesized that extensive self-assembly of CP(PEtOx) explains the peculiar chromatograms for this compound (**Figure 2-1**).

Table 2-1: Molecular weight (NMR, SEC) and dispersities of the polymers and CPNT synthesised (a: SEC in THF, PS calibration; b: SEC in DMF + LiBr, PMMA calibration).

Sample	M_n (NMR) (g/mol)	M_n (SEC)[a,b] (g/mol)	$Đ$
Protected PEtOx 1**3**	5,700	6,150[a]	1.16
Deprotected PEtOx **14**	5,500	4,500[a]	1.28
Fluorescent PEtOx **3**	6,100	6,200[a]	1.31
Poly(PEGA$_{22}$-*stat*-NAS$_{2.5}$) **19**	9,900	8,400[b]	1,14
Poly(PEGA-*stat*-Cy3Am) **5**	11,300	7,500[b]	1.28

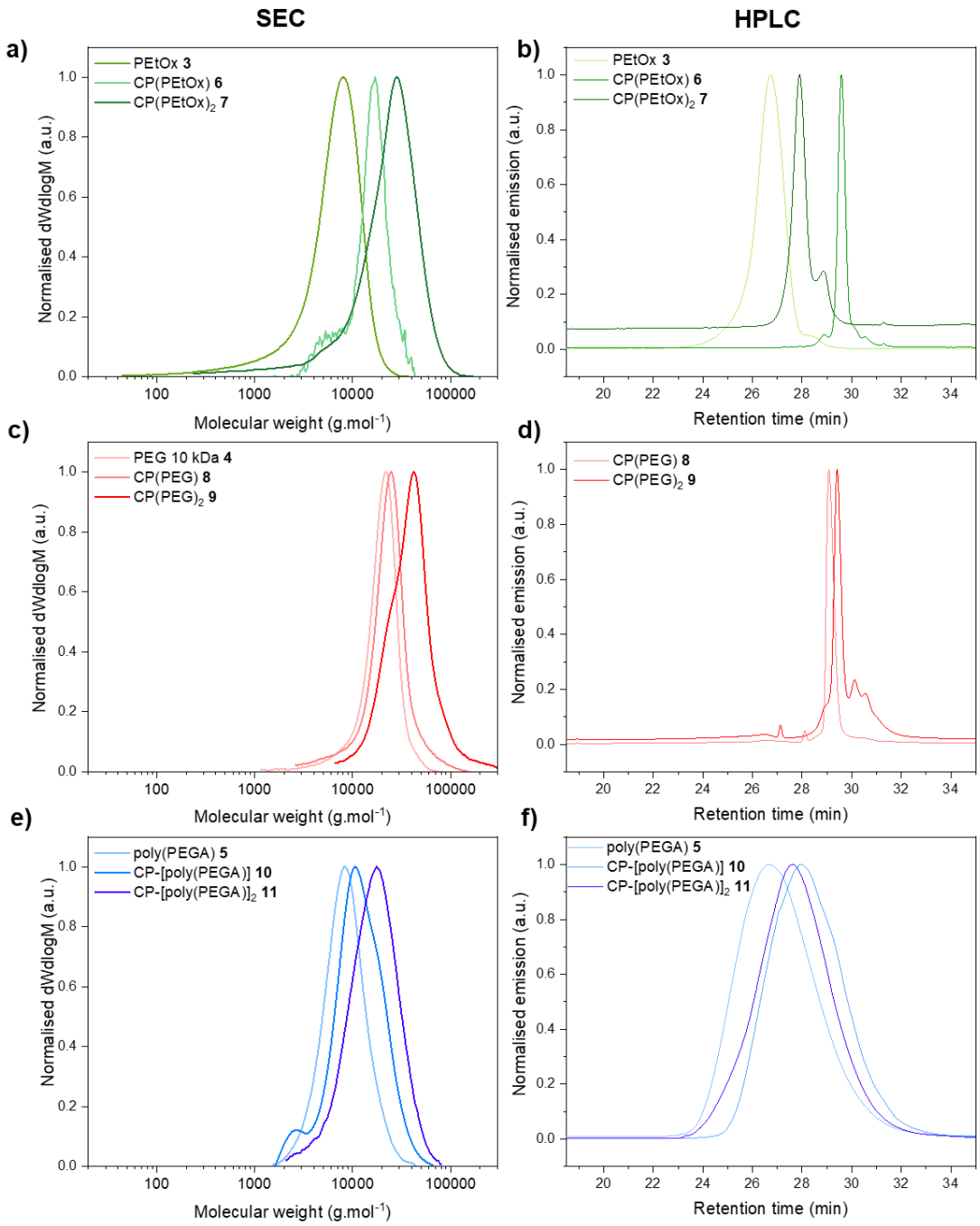

Figure 2-1: Chromatograms for the library of fluorescent polymers and CP-conjugates**.** (Left) SEC chromatograms in DMF + 0.1% LiBr of a) PEtOx, c) PEG and e) poly(PEGA) polymers and conjugates, RI detection. (Right) HPLC chromatograms for the polymers and the associated conjugates (b), d) and f)), acquired with a fluorescence detector (excitation: 554 nm, emission: 570 nm).

2.2.2 Characterisation of the supramolecular self-assemblies

2.2.2.1 Small Angle Neutron Scattering (SANS) and insights on data fitting

The size and shape of the self-assembled species formed by the previously synthesised CP-polymer conjugates in D_2O were evaluated using both SLS (Static Light Scattering) and SANS (Small Angle Neutron Scattering). SANS is a valuable technique to characterise supramolecular assemblies. It has been previously used on CP-polymer based systems, to determine the size and morphologies of the assemblies.[20] In a SANS experiment, the scattering from a collimated neutron beam is measured, from which a scattering cross section can be generated. By plotting the scattering intensity I(q) as a function of the wave vector q, it is possible to establish the size and shape of the scattering species. Here, SANS was used to establish how changes in the polymer corona on the CPNT affected the self-assembly process.

An estimation of the size and morphology of CP-polymer conjugates in aqueous solution can be obtained by fitting the data to appropriate models. The first step of the fitting process for all conjugates presented in this work was to use shape-independent fitting models, such as the Guinier-Porod model. The Guinier-Porod function is an empirical model and was used here to pre-assess the morphology of the nanostructures formed for all CP-polymer conjugates; a dimensional variable s was calculated in the fitting process.[30] After estimating the value of this parameter, different plausible models were tested as summarised and further explained in the Appendix (section A.3.1). The goodness of the fit was evaluated by a reduced chi-square statistic for each fitted model. Among the different models tested for a given CP-polymer conjugate, the chosen model was the one with the lowest Akaike information criterion (AIC) value.[31] AIC calculations were used to correct the chi-square value by including a penalty related to the numbers of parameters present in the fitting model therefore helping to determine the most appropriate fit.

2.2.2.2 Morphology and size of cyclic peptide-polymer self-assemblies

The structures studied here showed the best fits to the SASFit cylindrical micelle (with Gaussian polymer chains) form factor CYL+Chains(RW), with the exception of the CP-[poly(PEGA)] **10** which had the best fit to a Benoit polymer star form factor.[32, 33] CP-$[poly(PEGA)]_2$ **11** was not measured, as it has previously shown to give very little self-assembly.[20] For concentrations of 1.5 mg/mL, PEtOx conjugates **6** and **7** formed long tubular assemblies, as it could be seen in the scattering profiles; data could not be readily acquired at higher concentrations given the lack of solubility. At low q values, there was no plateau reached, suggesting that the overall size of the tube was outside the window of observation for this SANS experiment (150 nm) for CP(PEtOx) **6**.

An apparent length of 26.6 nm was found for CP(PEtOx)$_2$, in accordance to previous results demonstrating the effect of the number of polymer arms on a CP on self-assembly; data at lower q values is necessary to confirm this value given the lack of a clear plateau at the lowest q values measured.[20] SLS was used to further probe the SANS data, as it allows access to complimentary low q-values; the data was used to estimate the length of the self-assemblies at the working concentration used for cellular uptake experiments. The apparent length from SLS was obtained by evaluating the molecular weight of the self-assembly using Zimm plots; a number of unimer aggregation (N_{agg}) was determined and apparent lengths were obtained by multiplying it by the intermolecular distance between cyclic peptides in a self-assembly (0.47 nm) as previously established.[18] SLS of CP(PEtOx) confirmed lengths between 35 and 435 nm, in a range of concentrations varying between 0.3 and 2 mg/mL, which would explain why an accurate length could not be obtained from SANS at 2 mg/mL. Furthermore, Transmission Electron Microscopy (TEM) of CP(PEtOx)$_2$ showed the presence of some tubular structures that were on average 75 nm long (see **Figure 2-2**). However, as further discussed in Chapter 5, the use of dry state TEM might not be the most representative picture of the morphology of these systems as they exist in solution.

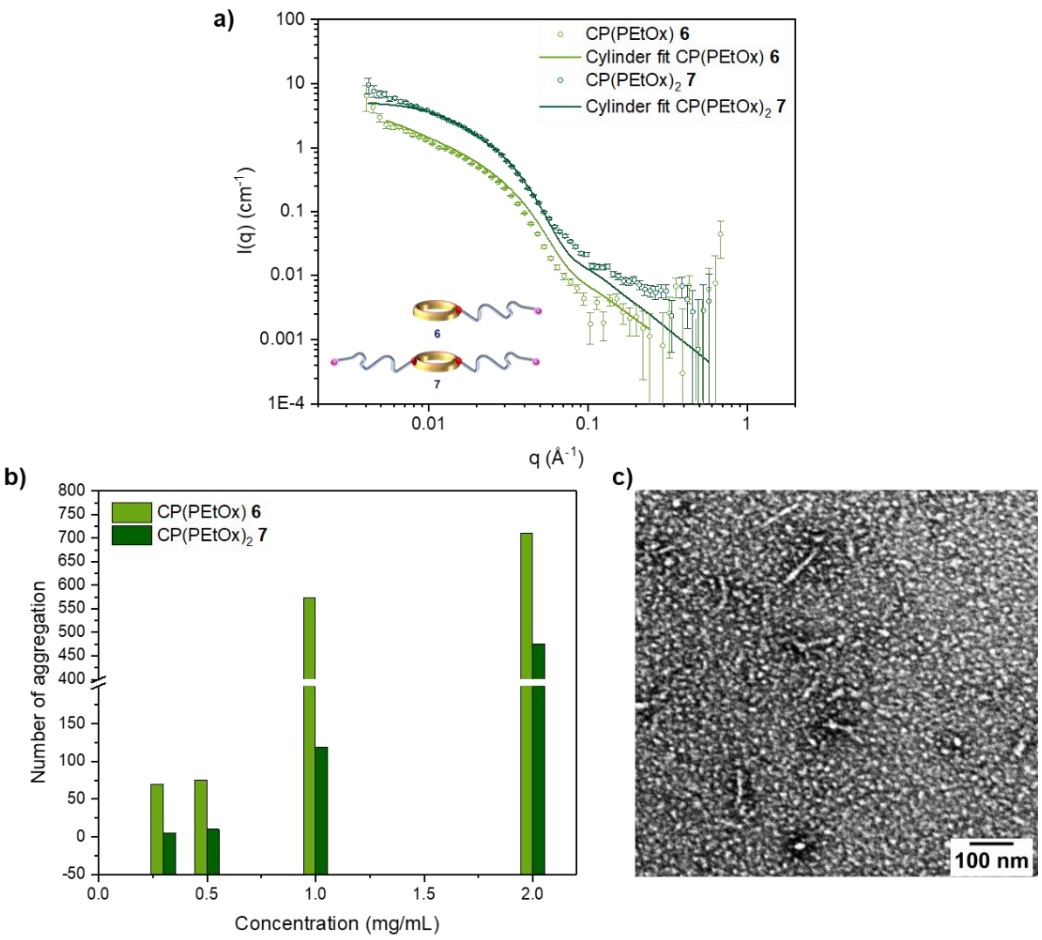

Figure 2-2: **S**elf-assembly of PEtOx CP-polymer conjugates**.** a) SANS cross section of the self-assembly of PEtOx conjugates **6** (light green) and **7** (dark green) at 1.5 mg/mL in D_2O. Hollow circles are used for the data plots, fits are plotted as lines; error bars are statistical. b) Evolution of the number of aggregation with concentration, determined by SLS for PEtOx conjugates (**6** and **7**, 0.3-2.0 mg/mL). Corresponding Zimm plots can be found in Appendix A on **Figure A-14**. c) TEM image representing $CP(PEtOx)_2$ nanotubes (stained with UOAc).

Microscopy results on such systems, where the concentration can affect the extent of the self-assembly process, need to be considered with great care as artefacts due to the sample preparation (e.g.: drying, staining) may appear. Such a strong self-assembly could be caused by hydrogen-bonding involving the polymer chains during the self-assembly process. The carbonyl group on EtOx can accept hydrogen bonds from the solvent therefore connecting different polymer chains together by hydrogen bonding with water.

As for linear PEGylated CPs, the SANS data (for a 5 mg/mL concentration) suggested the presence of tubular assemblies with a length of 16 nm (CP(PEG) **8**). There is still some uncertainty concerning the nature of these morphologies coming from the fitting process, as indicated by the relatively high chi-square value obtained for the best fit (cylindrical micelle, 45.8). The choice of the cylindrical micelle fitting model was supported by AIC calculations and by previous characterisation work on PEG CPNT where PEG chains of different molecular weight (2 and 20 kg/mol) were used.[20, 34] However, the model does not fully reflect the complex morphology of this system due to other contributions, such as the crystalline nature of PEG which was previously observed on extremely pure PEG oligomers.[35] The best fit for $CP(PEG)_2$ **9** was a very short cylindrical micelle (0.8 nm long) following the AIC calculation, the second best fit being an ellipsoid. SLS was used again to determine the length of PEG CPNT; the data was found to be quite consistent with the values from SANS for CP(PEG) whilst $CP(PEG)_2$ self-assemblies appeared to be longer (varying from 3.7 nm at low concentration to 13 nm at 2.5 mg/mL). The changes in aggregation with concentration were found to be relatively minor for CP(PEG) in comparison with PEtOx conjugates, which could be explained again by the polymer crystallinity potentially stabilising the self-assembly.

CP-polymer conjugates with a brush polymer poly(PEGA) had a different behaviour to the their linear counterparts. The SANS profile of CP-[poly(PEGA)] **10** was best fitted to a star polymer model, according to AIC calculations. A length *per se* could not be determined with the star polymer model; however, the N_{agg} was approximated from the scale factor and found to be around 8 (see more details in Appendix A, section A.3.1.6). The cylindrical micelle fit was the second best fit and indicated a length of 8 nm, which is in the same order of magnitude than the one that could be extrapolated from the star model (see **Figure 2-3**). Unfortunately, accurate Zimm plots of poly(PEGA) conjugates could not be obtained by SLS given the very low levels of self-assembly. The data for CP-$[poly(PEGA)]_2$ was directly taken from the work of Mansfield *et al.* who previously showed the lack of self-assembly for this system. The aspect ratio of each compound was calculated following the procedure detailed in Appendix A (section A.3.3), with values varying from 1 (CP-$[poly(PEGA)]_2$) to 25.3 (CP(PEtOx). All data related to self-assembly is summarised in **Table 2-2**.

Table 2-2: Summary of the self-assembly data collected using scattering techniques (SANS and SLS). CM: Cylindrical micelle (CYL+Chain(RW) model); SP: Benoit Star polymer. **: N_{agg} values.

Compound	Fit	Length (SANS, nm)	Concentration (mg/mL)	Nagg SLS at 0.1-0.3 mg/mL	Corresponding lengths (nm)	Aspect ratio (calculated from SANS data)
CP(PEtOx) **6**	CM	>150	1.5	75	35	25.3 (Length from SLS)
$CP(PEtOx)_2$ **7**	CM	27	1.5	5	2	3.5
CP(PEG) **8**	CM	16	5	32	15	1.8
$CP(PEG)_2$ **9**	CM	0.8	5	8	4	<1
CP-[poly(PEGA)] **10**	SP	8**	5	-	-	-
CP-[poly(PEGA)]2 **11**[20]	SP	2**	5	-	-	-

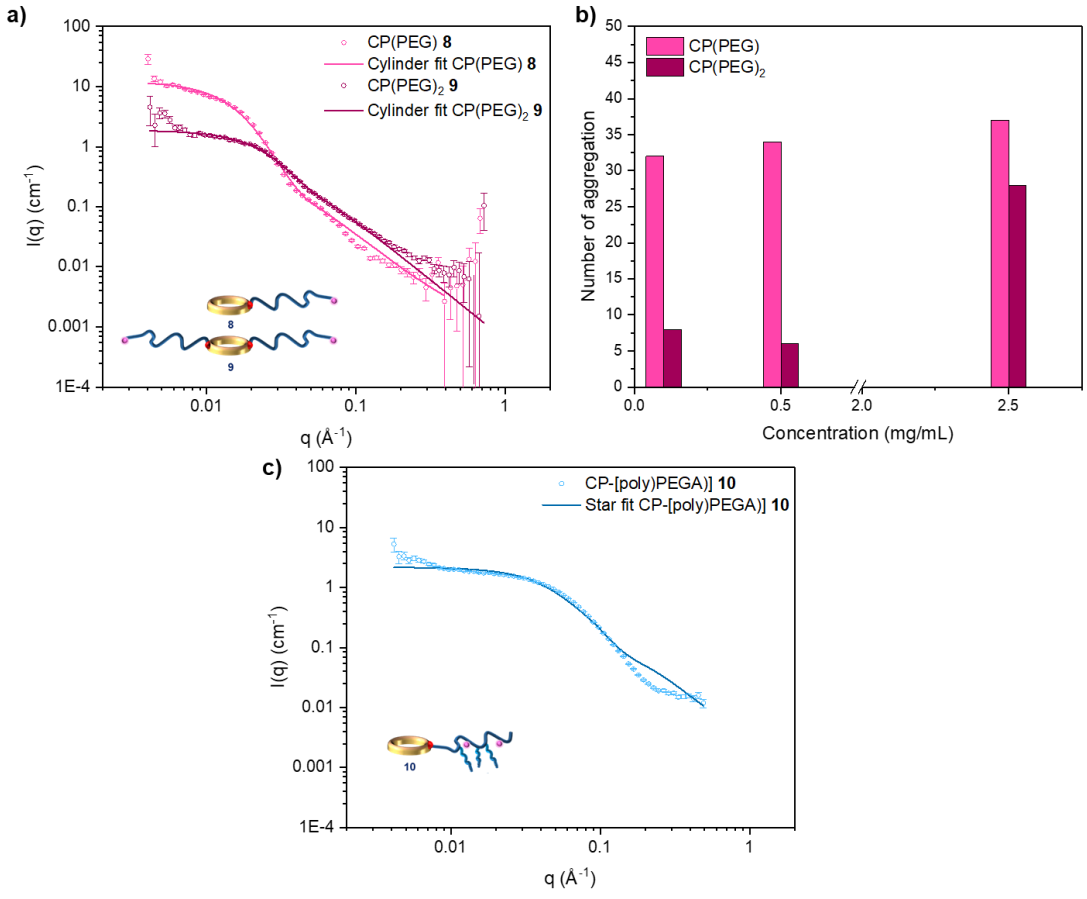

Figure 2-3: Self-assembly of PEG and poly(PEGA) conjugates. a) SANS cross section of the self-assembly of PEG conjugates **8** (pink) and **9** (purple) at 5 mg/mL in D_2O. b) Evolution of the number of aggregation with concentration, determined by SLS for PEG conjugates (**8** and **9**, 0.1-2.5 mg/mL). c) SANS cross section of the self-assembly of CP-[poly(PEGA]) **10** (blue). Hollow circles are used for the data plots, fits are plotted as lines; error bars are statistical.

2.2.3 Cellular uptake and evaluation of toxicity

The cellular uptake of the aforementioned labelled CP-polymer conjugates was evaluated on two different cell lines, breast cancer cell line MDA-MB 231 and murine fibroblasts NIH 3T3. The relative fluorescence within cells treated with each of the compounds was measured using the pictures acquired by fluorescence microscopy on a plate-reader. Images were corrected according to the intrinsic fluorescence of each of the compounds (details of image processing are presented in Appendix A, section A.4.2). The fluorescence per field of view was evaluated under four sets of conditions, varying the concentration as well as the incubation time, allowing for a relative comparison between the CPNT and polymers (**Figure 2-4**). As expected, both cells line showed a positive uptake of the compounds, with longer incubation time (24 h versus 2 h) and higher concentration (25 versus 5 μM) leading to higher cellular uptake in both cell lines, as did incubating cells with higher concentration of material.

Different trends can be extracted from the cellular uptake study of this library of CP-polymer conjugates. Variations in the intracellular fluorescence appeared to match the differences in self-assembly behaviour, as CPNT were not engineered to contain any charge or cell-uptake enhancing moiety. It appears that the extent of the self-assembly drove the rate of cellular uptake. The compounds have first been regrouped in subcategories, depending on the nature of the polymer considered (PEtOx, linear PEG or poly(PEGA)). Starting with PEtOx CP-polymer conjugates, it has been noticed that there was a significant preference in uptake for CP$(PEtOx)_2$, compared to CP(PEtOx) and the free polymer chain in both cell lines, for the highest concentration and incubation time. The mean fluorescence recorded was 1.4 and 1.8 times higher for CP$(PEtOx)_2$ compared to PEtOx and CP(PEtOx) (respectively) in NIH 3T3. The same differences can be extracted from the data on breast cancer cells MDA-MB 231, with an increase by a factor 1.9 (CP(PEtOx)) or 2.7 (PEtOx). We hypothesize that the size of the CP(PEtOx) nanotubes is most likely too high to be taken up efficiently in the timeframe studied. This phenomenon became more obvious when increasing the concentration of material, matching the concentration-dependent self-assembly of CP(PEtOx) nanotubes similarly to previously investigated systems.[34] CP$(PEtOx)_2$, forming smaller nanotubes than CP(PEtOx), was taken up more readily at higher concentrations. This was in accordance with previous observations that cylindrical structures of very high aspect ratio are taken up at a slower pace than lower aspect ratio nanotubes, as membrane-wrapping is more energetically challenging for longer nanotubes.[13]

In the case of linear PEG conjugates, there was a significantly higher uptake of CP(PEG) (~ 16 nm long) in both cell lines studied than for smaller assemblies formed by its two arm counterpart $CP(PEG)_2$, or a labelled PEG chain of 20,000 g/mol (equivalent in molecular weight to $CP(PEG)_2$). The uptake of CP(PEG) is between 3 (24 h, 25 µM) to 5 (2 h, 5 µM) times higher than $CP(PEG)_2$ in MDA, and 3 times higher on average for NIH 3T3. Similarly, $CP(PEG)_2$ had a significantly higher uptake than its linear polymer counterpart, suggesting again a beneficial impact of the self-assembly induced by the cyclic peptide core. Again, these differences between conjugates with 1 or 2 polymer arms can be attributed to difference in their propensity to self-assemble. It can also be linked to the presence of a bulky second polymer arm which makes it more challenging for the system to be taken up.

As for brush poly(PEGA) conjugates, no significant differences in uptake in MDA-MB-231 were noticed. Such variations could be observed in NIH 3T3 (with the exception of low concentration and short incubation time), with a better entry of CP-[poly(PEGA)] compared to the free polymer and CP-$(poly(PEGA))_2$. This increase in uptake is of a factor varying between 2.6 (24h, 25µM) and 4.5 (2 h, 25µM). Interestingly, poly(PEGA) was taken up more readily than CP-$[poly(PEGA)]_2$. Given that CP-$[poly(PEGA)]_2$ did not assemble and seemed to behave like a long unimeric polymer chain (~ 20 kDa), it did not benefit from the boost in cellular uptake previously observed for $CP(PEG)_2$ and $CP(PEtOx)_2$. Overall, self-assembly played an important role in the cellular uptake of CPNT, with slight variations between the cell lines. CPNT of a moderate length have the best uptake, compared to conjugates that self-assemble too readily (CP(PEtOx)) or that do not form nanotubes (CP-[poly(PEGA)]2). (**Figure 2-4**)

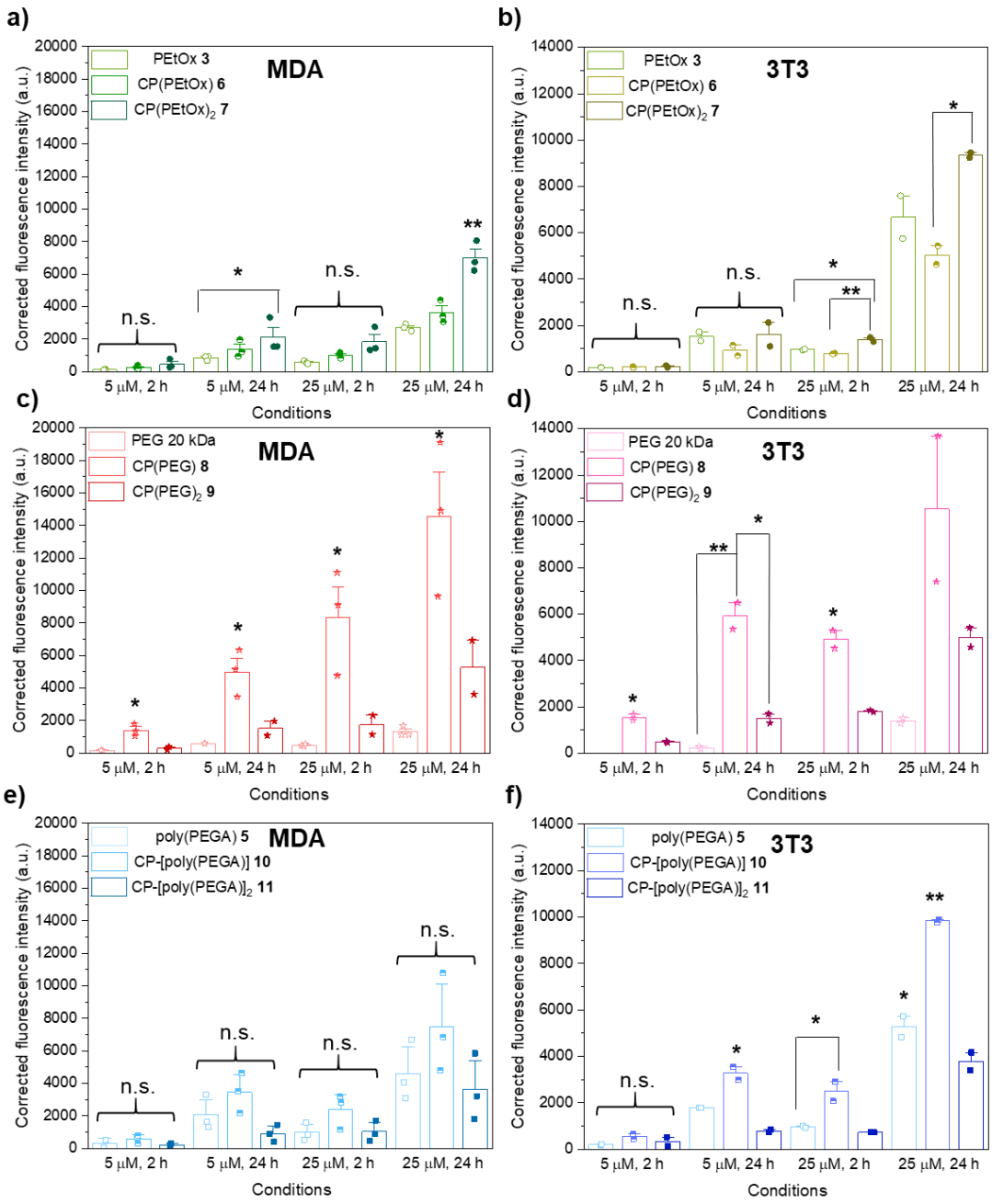

Figure 2-4: Evaluation of the cellular uptake of a library of CP-polymer conjugates. (Left) Cellular uptake in triple negative breast cancer cell line MDA-MB 231 following 2 or 24h incubation in the presence of; 5 or 25 µM of: a) PEtOx polymer and CP(PEtOx) conjugates (3,6 and 7); c) CP(PEG) conjugates (8 and 9) and PEG 20 kDa control; e) Poly(PEGA) and CP-[poly(PEGA)] conjugates (5, 10 and 11).

(Right) Cellular uptake in murine fibroblasts NIH 3T3 (same compounds and conditions).

The data was plotted as bar-charts (mean) with an overlap of all repeats. Error bars represent the standard error of the mean (n=3 or 2). Discrepancy in intrinsic fluorescence were corrected using fluorescence coefficient for each individual compound in PBS buffer (Appendix A, **Table A-8**). Statistical significance was assessed by an ANOVA + Tukey-Kramer post-hoc test. *: $p<0.05$, **: $p<0.005$.

Cellular uptake was also assessed at low temperature to understand the contribution of energy-dependent mechanisms to the uptake of compounds presented in this work. Overall, our study on PC-3 cells showed that there is less uptake at 4°C than at 37°C as it was expected (as energy-dependent pathways are being knocked out). Cellular viability was assessed for all these systems using the XTT/PMS assay, evaluating changes in mitochondrial metabolism. None of the compounds previously tested was found to be toxic after 24 h incubation with concentrations up to 100 μM, further highlighting the biocompatibility of CPNT (see **Figure 2-5**).

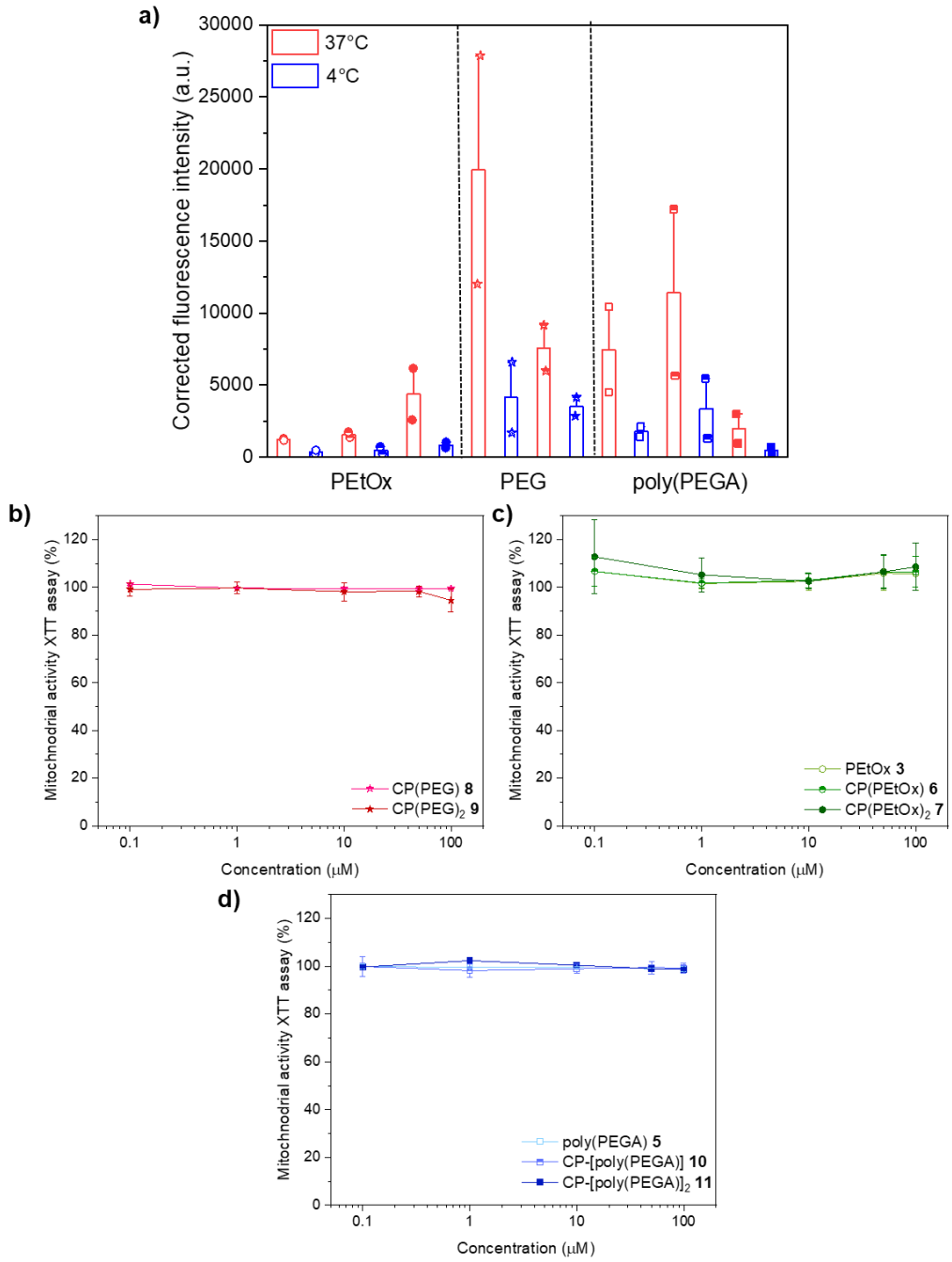

Figure 2-5: a) Comparison of the intracellular fluorescence for prostate cancer cell PC3 following 2h incubation with different polymers and conjugates (12.5 μM) after 2 h at 37°C (red) or 4°C (blue). (order: PEtOx, CP(PEtOx), $CP(PEtOx)_2$, CP(PEG), $CP(PEG)_2$, PEtOx, CP(PEtOx) and $CP(PEtOx)_2$) The data was plotted as bar-charts (mean) with an overlap of all repeats. Error bars represent the standard error of the mean (n = 2). Significance was found for all 37 vs 4°C plots (Student t-test). Evaluation of the cellular viability by measurement of mitochondrial activity (XTT assay) for the tested polymers and conjugates on MDA-MB 231: b) PEtOx polymer and CP(PEtOx) conjugates (**3**,**6** and **7**); c) CP(PEG) conjugates (**8** and **9**); d) Poly(PEGA) and CP-[poly(PEGA)] conjugates (**5**, **10** and **11**). Error bars represent the standard error of the mean on 2 independent biological replicates (n=2). There were no significant differences between any of the conjugates.

2.2.4 Study of the intracellular behaviour

2.2.4.1 Confocal microscopy on PC3 cells

Following on from our uptake and viability studies, the intracellular behaviour of the different CP conjugates was assessed using CLSM in both classic planar models (PC3 cells) and 3D models (PC3 Multicellular Tumor Spheroids or MCTS). In both cases, localisation studies were performed to determine where the conjugates could be found within a cell following 24 h.

Upon visual inspection of pictures from the 2D models it is clear that the conjugates (green channel) entered the cells and accumulated in the lysosomes (magenta channel), in charge of processing materials acquired through endocytic pathways. This was confirmed by mathematical analysis evaluating the correlation between the magenta (lysosomes) and green (CPNT) channels using the Pearson's Correlation Coefficients (PCC). PCC were measured using JACoP (Just Another Colocalisation Plugin)[36] on Fiji (ImageJ distribution)[37] for the channels of interest in an attempt to quantify the colocalisation of Cy3-labelled compounds with lysosomes in cells. Interestingly, the levels of lysosomal localisation of the different conjugates varied from 0.27 (CP(PEG)) to 0.59 (CP-[poly(PEGA)]$_2$), suggesting different intracellular behaviour depending on the self-assembly. Lysosomal pH being around 4 to 5, slow degradation of the conjugates by amide cleavage may occur over time; it was however not possible to assess whether or not the CPNT were kept intact or attached. A way to do so would be to use a responsive dye that would behave differently when it is no longer attached to the CPNT. Nevertheless, these results provide insights on the likelihood and speed of uptake via endocytic mechanisms depending on the self-assembly, which is key for further drug delivery applications.

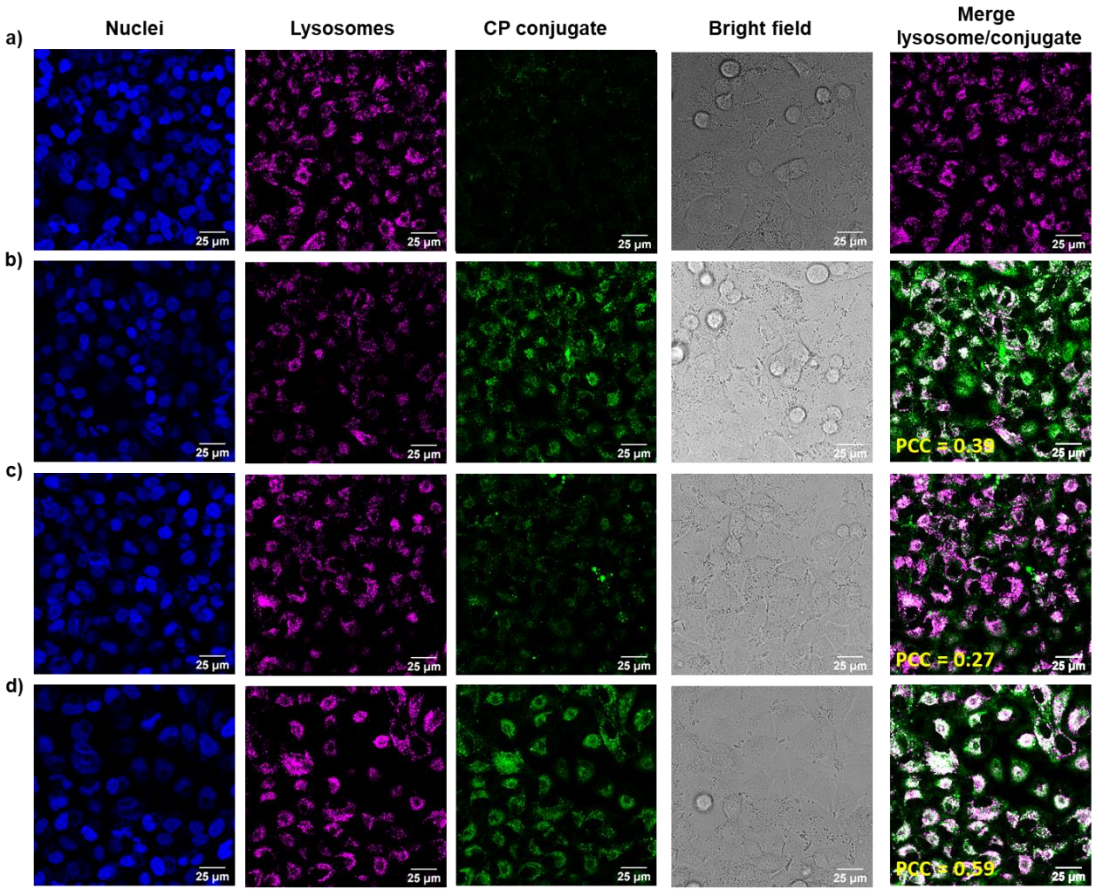

Figure 2-6: Intracellular behaviour of different CP conjugates in PC3 cells: a) Control, b) CP(PEtOx)$_2$ **7**, c) CP(PEG) **8**, d) CP-[poly(PEGA)]$_2$ **11**. Blue represents the DAPI channel, green represents the Cy3 channel of the conjugates, magenta is LysoTracker Deep Red™ and grey-white areas on the merge indicates colocalisation. The PCC value for the magenta/green channel colocalisation were 0.38, 0.27 and 0.59 for b), c) and d).

2.2.4.2 Confocal study on PC3 multicellular tumour spheroids (MCTS)

This phenomenon and the potential of the CPNT to achieve intratumoral penetration was extensively studied on PC3 spheroids. MCTS are a more accurate model of tumour behaviour than 2D models as they can be used to replicate different parameters such as the existence of intratumour gradients (oxygen, nutrients, pH, etc.) and cell-cell interactions.[38, 39] Penetration profiles for each compounds, based on the fluorescence intensity of each z-stack acquired, were plotted comparing the incubation times at 24 and 48 h. Efficient penetration was observed at 24 h, looking at the core of the spheroid (50 µm) for CP-polymer conjugates. Interestingly, the patterns observed are different between cylindrical micelle-like CPNT **6**, **7** and **8** and star-like poly(PEGA) conjugates **10** and **11**.

The intracellular behaviour also differed, with different apparent levels of colocalisation (**Figure 2-7**). It seems that compounds forming nanotubes (CP(PEtOx) **6**, CP(PEtOx)$_2$ **7** and CP(PEG) **8**) did not exhibit as much colocalisation, according to the values of the PCC recorded, by comparison with compounds with low self-assembly (poly(PEGA) conjugates) after 24 h. This can also be observed to some extent on the maximum projection for both channels (Cy3: green; LysoTracker: magenta) where more white areas can be observed in the case of poly(PEGA) conjugates.

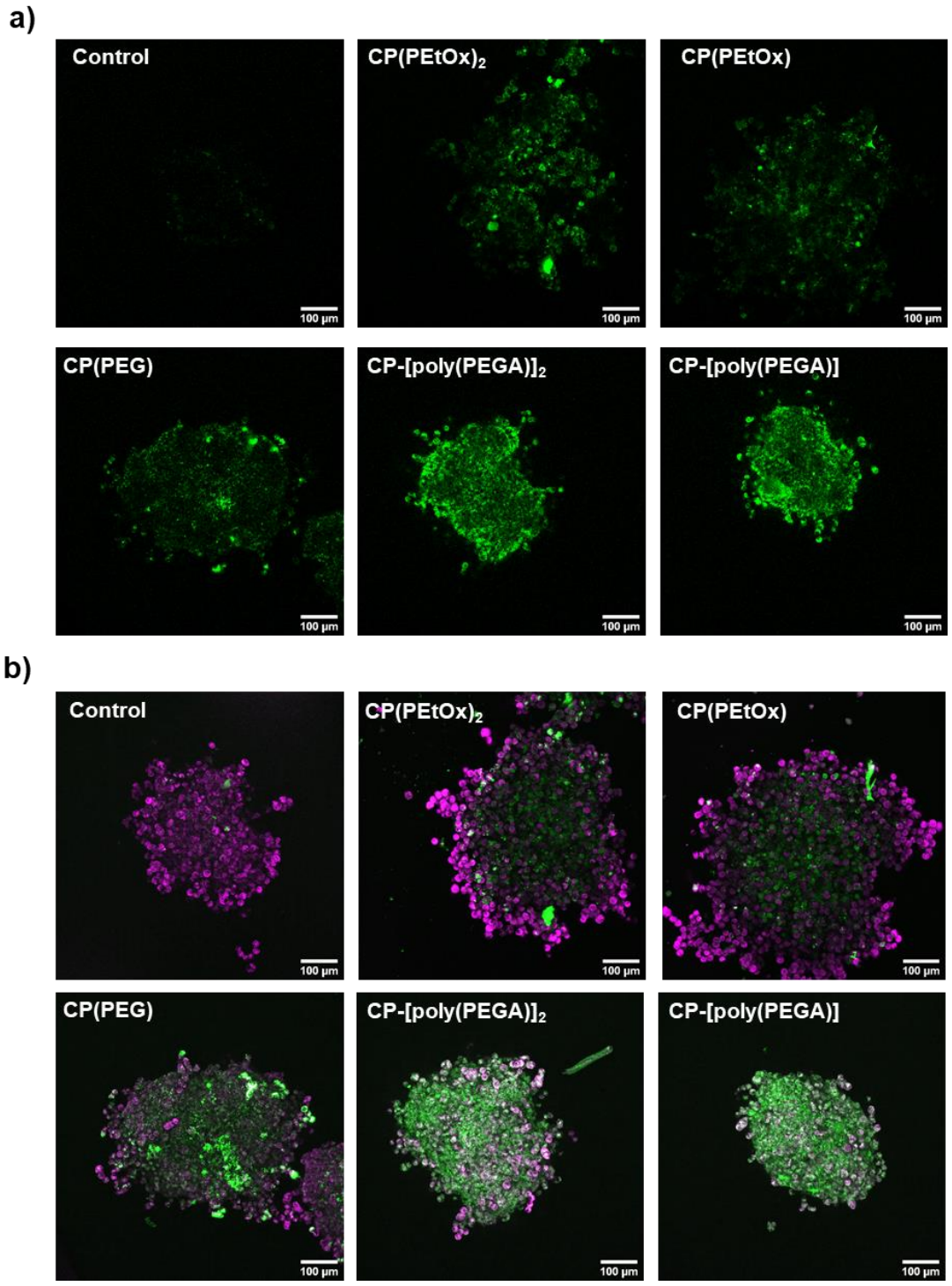

Figure 2-7: Intracellular behaviour of different CP conjugates in PC3 Multicellular Tumor Spheroids (MCTS). a) CLSM Penetration of CP-polymer conjugates (11, 10, 8, 7, 6) at z=50 µm in MCTS after 24 h incubation at 5 µM, Cy3 channel (green). The images were not corrected by the intrinsic fluorescence of each compound in buffer. b) Brightest point projection green/magenta overlay from 50 z-stacks (2 µm spacing) of PC3 MCTS after 24 h incubation with a series of CP-polymer conjugates (11, 10, 8, 7, 6). Green represents the Cy3 channel of the conjugates, magenta is LysoTracker Deep Red™, and grey-white areas indicate colocalisation).

The diffusion and uptake phenomena were both quantified after this initial analysis. In terms of relative fluorescence intensity (using the coefficients previously described in the uptake study, see **Table A-8** in Appendix A), CP(PEG) showed the highest fluorescence intensity overall in the spheroid, and a two-fold increase in the internalised quantity between 24 and 48 h. The trends are similar to what has been observed in the fluorescence microscopy study described *vide supra*, with CP(PEG) having the highest fluorescence throughout the spheroid. The fluorescence maximum was reached at a higher penetration depth between 24 and 48 h for all CP-polymer conjugates, suggesting that the diffusion through the core of the spheroid is time-dependent as observed for cylindrical viral nanoparticles by Steinmetz and co-workers.[40]

Pearson's Correlation Coefficients (PCC) were measured and averaged on 50 z-stacks using JACoP in spheroids. This can give us information on the mode of internalisation method used by the CPNT. Transcellular propagation would involve the conjugates to be internalised and excreted by cells on the spheroids. It would therefore lead to higher lysosomal correlation than paracellular propagation, which should happen throughout the intracellular matrix of the tumour model.

Overall, PCC values are on average two times lower for conjugates containing PEG and PEtOx than for poly(PEGA) conjugates. In terms of kinetics of the uptake phenomenon, it is interesting to notice that Pearson's coefficients for PEtOx and PEG conjugates are slightly higher after 48 h incubation, which supports the hypothesis of a delayed uptake via endocytosis for systems with higher aspect ratio. Such results seem to indicate that the transcellular uptake is the preferred mechanism for low aspect ratio poly(PEGA) conjugates (below 2). As for higher aspect ratio nanotubes (PEG and PEtOx based), the contribution of paracellular uptake seems to be more important, as the lysosomal correlation coefficients are lower. Lower levels of colocalisation for the CP(PEtOx) and CP(PEG) nanotubes tested could be explained by an accumulation of nanotubes in the cytosol, the intercellular spacing or in other vesicular compartments of the cell. Accumulation in non-lysosomal areas of the spheroid could also be due to the presence of anoxic regions, which might be more readily accessible and allow for higher uptake, following the known Enhanced Permeation and Retention (EPR) Effect (**Figure 2-7**). However, punctation present on 2D models for all labelled compounds suggest a compartmentalisation rather than an endosomal escape in the cytosol. The significant increase in colocalisation over time for PEG and PEtOx nanotubes could be explained by a delayed transcellular mechanism.

Overall, clear differences of behaviour in MCTS can be observed between CP-polymer conjugates of different nature. In terms of overall fluorescence intensity, similarities can be found with the study on the planar models with a predominance of CP(PEG) and CP-[poly(PEGA)]. Colocalisation studies showed a higher predisposition of non-assembling structures to accumulate within lysosomal compartments whilst self-assembling conjugates were present in different areas (probably intercellular regions, see **Figure 2-8**).

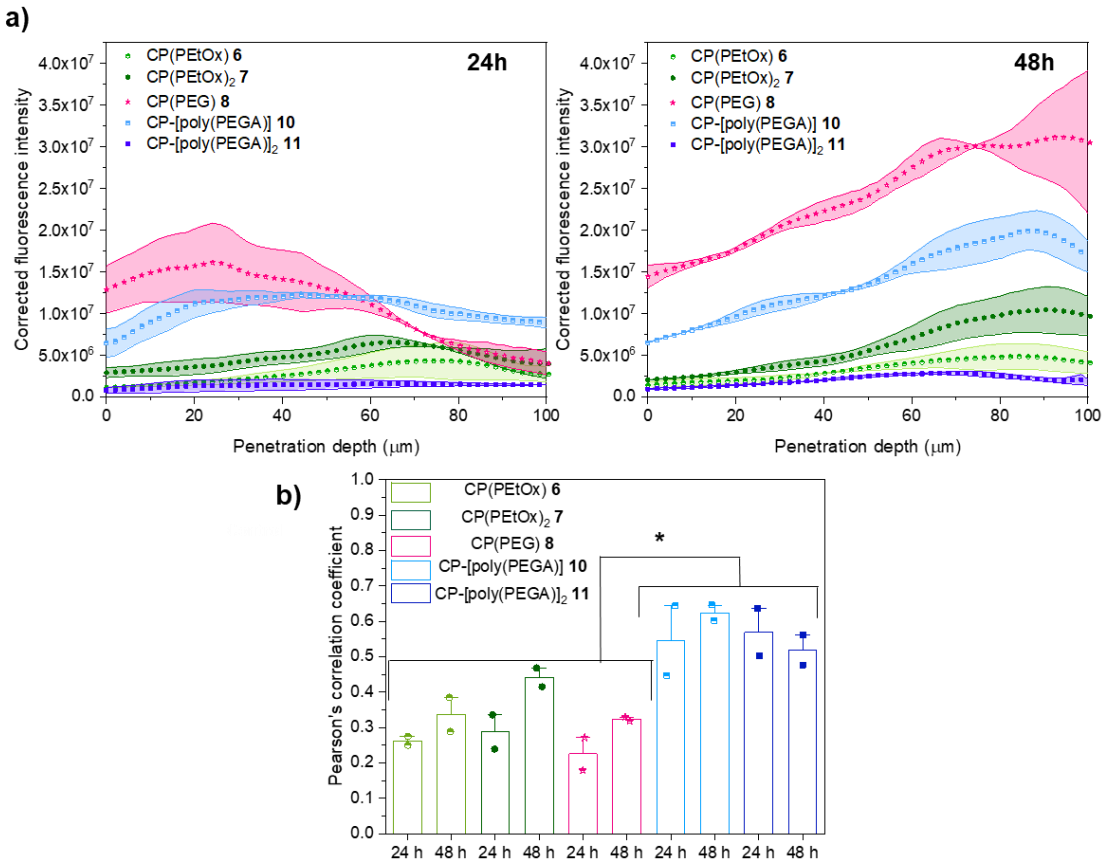

Figure 2-8: a) Penetration profiles at 24 (left) and 48 h (right) for a series of CP-polymer conjugates (11, 10, 8, 7, 6) over 100 µm. Each point represent the average relative fluorescence intensity recorded at a given z-stack in the spheroid, delimited by a Region of Interest. The envelope around each plot represents the standard error of the mean associated with each point (two replicates, n=2).) b) Evaluation of the overall level of colocalisation between the green (Cy3 CP-polymer conjugate) and magenta (LysoTracker Deep Red) channels, using an average of the Pearson's Correlation Coefficient (PCC) between two independent spheroids. Bar-charts represent the mean with an overlap of all repeats. Error bars are the standard error of the mean on two replicates (n=2). Statistical significance was assessed by an ANOVA + Tukey-Kramer post-hoc test. *: $p<0.05$, **: $p<0.005$.

2.3 Conclusions

In summary, a library of fluorescently-labelled CPNT with one or two hydrophilic polymer chains were synthesised. The impact over a range of design parameters (number of polymer arms, nature of the polymer, morphology) was studied, confirming their strong influence on the self-assembly process in water, allowing access to diverse nanostructures. The formation of self-assemblies of different size and shape, varying from a couple of nanometers star-like structures (CP-[poly(PEGA)]$_2$) to nanotubes with lengths over 100 nm (CP(PEtOx)), was linked to the variations in cellular uptake in mammalian cells. Overall, there is an optimal size range for efficient uptake of CPNT to be aimed for, around 10-20 nm as seen with CP(PEG) by comparison with shorter (poly(PEGA) based) or longer (PEtOx conjugates) self-assemblies. Further investigations on the intratumoural behaviour of the conjugates using MCTS models showed clear differences between the uptake of small and medium/large self-assembled structures. The maximal fluorescence intensity recorded increased quite significantly with time for CP(PEG), CP(PEtOx)$_2$ and CP-[poly(PEGA)], corroborating with the results from 2D models studies, showing a very efficient uptake of CP(PEG). As for lysosomal colocalisation studies, CPNT formed by poly(PEGA) conjugates showed higher colocalisation in lysosomes than PEG and PEtOx nanotubes, suggesting differences in the uptake mechanism with different contributions of paracellular and transcellular uptake. This excellent penetration of CPNT and the characteristics of this uptake phenomenon in 3D models are encouraging, suggesting that these systems are suitable for the delivery of small molecules in a tumour and should be further investigated *in vivo*.

2.4 Materials and methods

2.4.1 Materials

Protected amino acids (Fmoc-D-Leu-OH, Fmoc-L-Lys(Boc)-OH, Fmoc-L-Trp(Boc)-OH, Fmoc-L-Asp(OtBu), Fmoc-L-Arg(Pbf), Fmoc-Gly, Fmoc-D-Phe) and 2-(6-Chloro-1-H-benzotriazole-1-yl)-1,1,3,3-tetramethylaminium hexafluorophosphate (HCTU) were purchased from Iris Biotech GmbH (Germany). 4-(4,6-dimethoxy-1,3,5-triazin-2-yl)-4-methyl-morpholinium tetrafluoroborate (DMTMM.BF_4) was synthesised from DMTMM.Cl (Sigma Aldrich, UK) as previously described.[41] V-601 was purchased from Wako Chemicals (UK). NHS, maleimide, and amine functionalised Cyanine 3 were purchased from Lumiprobe (Germany). The RAFT agent (propanoic acid)yl butyl trithiocarbonate (PABTC) was synthesised according to a procedure described in the literature.[42] Functional PEG macromolecules were purchased from Rapp Polymere (Germany). 2-ethyl-2-oxazoline (99%, Sigma Aldrich, EtOx) was dried over barium oxide and distilled under reduced pressure then kept in a Schlenk flask prior to use. *tert*-Butyl bromoacetate (98%; Sigma Aldrich,), Amberlite™ IR120 resin (H form) ion exchange resin (Acros Organics™) and Potassium ethyl xanthogenate (96%, Sigma Aldrich) Acetonitrile Extra Dry (99.9%+, Fisher Scientific - Acros Organics, Loughborough, United Kingdom) were used as purchased. All other chemicals were purchased from Sigma-Aldrich (UK). All chemicals were used as received, except for the PEGA 480 monomer which was run through basic alumina to remove the inhibitor. All solvents were bought from commercial sources and used as received. Amicon Ultra-15 centrifuge tubes, with different molecular weight cut-offs MWCO, were purchased from Merck Milipore and used as received for purification in aqueous environment.

2.4.2 Characterisation

2.4.2.1 High Performance Liquid Chromatography

High performance liquid chromatograms (HPLC) was measured using an Agilent Technologies 1260 Infinity Series, equipped with an Eclipse 3.5 μm C18, 4.6 x 100 mm column and an absorption and fluorescence detector set at Cyanine 3 wavelengths (555 nm excitation, 575 nm emission). Solvent mixtures of Methanol/Water were used. All solvents contained 0.05 vol% TFA. The typical gradient used for all plots presented was 30% to 95% of MeOH (co-solvent: water) in 40 min.

2.4.2.2 Size Exclusion Chromatography

The size-exclusion chromatograms (SEC/GPC) were measured using an Agilent PL50 instrument with a differential refractive index (DRI) and UV detector set at 280 nm. The instrument contained two PolarGel H columns (300 x 7.5 mm) and a PolarGel 5μm guard column. DMF with 0.1% LiBr additive was used as the eluent. The system ran at 1mg/min (50ºC), with an injection volume of 100 μL. The samples were prepared by filtration through 0.22 μm pore size membranes, before injection. Agilent EasyVial poly (methyl methacrylate) standards Agilent Easy Vials (Agilent Technologies LDA UK, Cheadle, United Kingdom) were used to calibrate the instrument (550-1,568,000 g/mol) and output data was analysed using Agilent GPC/SEC software.

For the SEC measurements in tetrahydrofuran (THF), an Agilent 390-LC MDS instrument equipped with differential refractive index (DRI), viscometry (VS), dual angle light scatter (LS) and dual wavelength UV detectors was used. The system was equipped with 2 x PLgel Mixed C columns (300 x 7.5 mm, operating range between 200 to 2,000,000 g/mol) and a PLgel 5 μm guard column. The eluent is THF with 2 % TEA (triethylamine) and 0.01 % BHT (butylated hydroxytoluene) additives. Samples were run at 1ml/min at 30°C. Polystyrene standards (Agilent Easy Vials (Agilent Technologies LDA UK, Cheadle, United Kingdom) were used for calibration (150-350,000 g/mol).

Analyte samples were filtered through a GVHP membrane with 0.22 μm pore size before injection. Respectively, experimental molar mass (M_n, SEC) and dispersity ($Đ$) values of synthesized polymers were determined by conventional PMMA or PS calibration using Agilent GPC/SEC software.

2.4.2.3 Small Angle Neutron Scattering

SANS was performed on the SANS-2D instrument at the ISIS Pulsed Neutron Source (STFC Rutherford Appleton Laboratory, Didcot, U.K.). Samples were left to dissolve in deuterated water for 16 h prior to measurement, at a concentration of 5 (for compounds 6, 7 and 8) or 2 mg/mL (for 3 and 4) and transferred to 2 mm quartz Hellma cuvettes. The q-range, where the scattering wave vector q is defined as ($q = \frac{4\pi}{\lambda} sin\frac{\theta}{2}$, with θ being the scattered angle λ the incident neutron wavelength) for all measurements was 0.0040 - 0.73 $Å^{-1}$. The beam diameter was 8 mm, with an incident wavelength range varying between 1.75 and 16.5 Å. The small-angle detector was placed 4 m from the cuvette, offset vertically 60 mm and sideways 100 mm, following a previous protocol established for the study of CP-polymer nanotubes.[17] Temperature was set to 25°C. The raw data for each sample measurement was corrected for background, D2O, detector efficiency, sample transmission, and empty cuvette and reduced using instrument software Mantid resulting in a scattering cross-section for each sample, and placed on an absolute scale using a perdeuterated polystyrene.[43] The reduced data was fitted to different form factors using the SASfit software package.[32] Details about the form factors used and the different fitting parameters are provided in Appendix A, section A.3.1.

2.4.2.4 Static Light Scattering

Light scattering measurements presented here were acquired on the ALV-CGS3 system (ALV-GmBH, Langen, Germany), with a vertically polarised laser source at 632 nm. The measurements were taken at 25°C. Samples were prepared 16 h before measuring and filtered through a 200 μm GHP filter (Acrodisc, 13 mm diameter, VWR International, United Kingdom) into clean cylindrical glass cuvettes (inner diameter: 8mm; outer diameter: 10 mm; height: 75 mm; LS Instruments, Switzerland); the dn/dc was set at 0.1 during the measurement and corrected by its real value after measuring on a refractometer. The data was modelled to a Zimm equation and Zimm plots were drawn.[44] The molecular weight of the self-assemblies was then determined and a number of aggregation was obtained after dividing it by the molecular weight of the unimer constituting the self-assembly.

2.4.3 Synthesis

2.4.3.1 Cyclic peptide synthesis

2.4.3.1.1 Linear peptide synthesis (for 1 arm CP)

Solid phase peptide synthesis (SPPS) of H_2N-L-Lys(Boc)-D-Leu-L-Trp(Boc)-D-Leu-L-Trp(Boc)-D-Leu-L-Trp(Boc)-D-Leu-COOH was performed using a peptide synthesizer (Prelude – Protein Technologies), on a 2-chlorotrityl resin (6 x 60 mg, 1.1 $mmol.g^{-1}$ resin loading). 200 mM solutions of Fmoc-protected amino acids (D-Leu, L-Lys(Boc) and L-Trp(Boc)) in DMF were used. The following sequence was followed:

Loading the first AA on the resin:

Resin swollen in DCM for 30 min.

- Fmoc-Leu-OH solution and a solution of 0.4 M DIPEA in DMF (4 eq.) added to the resin after draining the DCM.
  Solution mixed for 2 h then DCM 17: MeOH 2: DIPEA 1 added to end-cap unreacted sites on the resin.
- Solution drained then resin washed with DCM, DMF and DCM (5 min per wash). Fmoc deprotection of the AA with a 20% vol. solution of piperidine in DCM, left for 5 min.
- Coupling of the next AA: DMF, DCM, DMF washes (5 min each). Fmoc-Trp-Boc (5 eq.) added with a HCTU (5eq.)/ NMM (10 eq.) solution in DMF for 3 h. New sequence of washes.

Building the peptide sequence:

Deprotection procedure 3) and coupling reaction 4) repeated, following the order of the amino acids in the sequence (L-W-L-X-L-W-L-X, where X is either K or W).

Cleaving the peptide from the resin:

3 x 10 mL of a 20% HFIP solution in DCM added, after deprotection of the last Fmoc-protected amino acid. 3 DCM washes.

The solid linear peptide was obtained after removing the solvent *in vacuo* (727 mg, >100% yield due to the presence of residual HFIP).

^{1}H-NMR (400 MHz, TFA-d, ppm): δ = 8.26-8.06 (m, 3H, Trp), 7.68-7.20 (m, 12H, Trp), 5.27-5.07 (m, 3H, H_α Trp), 4.77-4.41 (m, 4H, H_α Leu + HFIP), 4.37-4.21 (m, 1H, H_α Lys Nend), 3.45-3.08 (m, 8H, CH_2 Trp and CH_2-NH Lys), 2.18-2.01 (m, 2H, $CH_2CH_2C\mathbf{H_2}CH_2NHBoc$ Lys), 2.01-1.77 (m, 2H, $CH_2C\mathbf{H_2}CH_2CH_2NHBoc$ Lys), 1.73-1.47 (m, 42H, $C(C\mathbf{H_3})_3$ from 4Boc group + $C\mathbf{H}(CH_2)$ Leu + $C\mathbf{H_2}CH_2CH_2CH_2NHBoc$ Lys), 1.43-1.17 (m, 8H, Leu protons), 0.95-0.55 (m, 24H, CH_3 Leu), NH signals not observed

MS (ESI-ToF): $[M+H]^+$ calculated 1556.9 and found 1556.9

2.4.3.1.2 Cyclisation of the linear peptide

The linear peptide (727 mg, 0.45 mmol, 1.0 eq.) was dissolved in 70 mL of DMF in a round bottom flask. After placing the reaction mixture under a N_2 atmosphere, a solution of DMTMM.BF_4 (201 mg, 0.61 mmol, 1.35 eq.) in 30 mL DMF was prepared then added dropwise to the reaction mixture. The mixture was left stirring for 93 h at room temperature and the conversion of the linear peptide into the corresponding cyclic peptide was assessed using ESI-MicroTOF. The solvent was evaporated *in vacuo* before redissolving the cyclic peptide in 20 mL DMF. The compound was precipitated 3 times in a water 1: methanol 1 mixture in centrifuge tubes then dried for 16 h in a vacuum oven at 40°C, yielding **4** as a yellow solid (267 mg, 39%).

^{1}H-NMR (400 MHz, TFA-d, ppm): δ = 8.26-8.08 (m, 3H, Trp), 7.68-7.20 (m, 12H,Trp), 5.27-5.07 (m, 3H, H_α Trp), 4.95-4.85 (m, 1H, H_α Lys Nend), 4.77-4.41 (m, 4H H_α Leu), 3.45-3.08 (m, 8H, CH_2 Trp and CH_2-NH Lys), 2.05-1.17 (m, 54H, $C\mathbf{H_2}C\mathbf{H_2}C\mathbf{H_2}CH_2NHBoc$ Lys + $C(CH_3)_3$ Boc group + Leu protons), 0.95-0.55 (m, 24H, CH_3 Leu), NH signals not observed.

MS (ESI-ToF): $[M+Na]^+$ calculated 1561.8 and found 1561.8

2.4.3.1.3 Deprotection of the cyclic peptide

260 mg of the protected cyclic peptide were dissolved in 10 mL of the following solution: TFA 9: TIPS 0.5: water 0.5. The solution was left stirring for 3 h at room temperature. The deprotected cyclic peptide was then precipitated twice in cold diethyl ether. The solid was collected and dried in a vacuum oven at 40°C for 16 h, yielding **1** as a white solid (153 mg, 73%).

^{1}H-NMR (400 MHz, TFA-d, ppm): δ = 8.26-8.08 (m, 3H, Trp), 7.68-7.20 (m, 12H,Trp), 5.27-5.07 (m, 3H, H_α Trp), 4.95-4.85 (m, 1H, H_α Lys Nend), 4.77-4.41 (m, 4H H_α Leu), 3.45-3.08 (m, 8 H, CH_2 Trp and CH_2-NH Lys), 2.05-1.17 (m, 18H, C**H$_2$**C**H$_2$**C**H$_2$**CH_2NHBoc Lys + Leu protons), 0.95-0.55 (m, 24H, CH_3 Leu), NH signals not observed

MS (ESI-ToF): $[M+H]^+$ Calculated 1139.7, found 1139.7.

2.4.3.2 Poly(2-ethyl-2-oxazoline) (PEtOx) CP conjugates

2.4.3.2.1 Synthesis of a poly (2-ethyl-2-oxazoline) with tert-butyl protected carboxylic acid and ethyl xanthate groups **13**

tert-Butyl bromoacetate **12** (0.0350 g, 0.180 mmol), dry 2-ethyl-2-oxazoline (1.071 g, 10.8 mmol) and extra dry acetonitrile (1.88 mL) were added to a pre-dried Biotage® microwave vial, under a constant flux of nitrogen. The vial was sealed and immediately placed in the microwave synthesizer, stirred for 30 s then heated at 140 °C for 50 min. After being cooled down, a 2 mL solution of potassium ethyl xanthate (0.035 g, 0.216 mmol) in extra dry acetonitrile was added with a syringe to the polymer mixture for end-capping. The solution was left stirring at room temperature for 2 h. The vial was subsequently unsealed and 50 mL of chloroform were added. The organic phase was washed three times with a saturated solution of sodium hydrogen carbonate, with brine and dried on magnesium sulfate. The solvent was removed under reduced pressure and the polymer was redissolved in 10 mL of chloroform before being precipitated three times in diethyl ether. The precipitated polymer was left to dry overnight in a vacuum oven at 40 °C, yielding a white powder (**13**, 0.518 g obtained).

^{1}H NMR (400 MHz, $CDCl_3$) δ ppm: 3.75 – 3.35 (m, 220 H, backbone), 3.35 – 3.20 (m, 1 H, CH_2 xanthate), 2.55 – 2.13 (m, 110 H, C**H$_2$** side chain), 1.54 – 1.40 (m, 7.9 H, C(C**H$_3$**)$_3$ + C**H$_3$** xanthate), 1.23 – 0.98 (m, 165 H, C**H$_3$** side chain).

SEC (THF, triethylamine, PS calibration): M_n = 6,100 g mol^{-1}, $Đ$ = 1.16

2.4.3.2.2 Simultaneous deprotection of the carboxylic acid and of the thiol on poly (ethyl-2-oxazoline) **14**

Poly (2-ethyl-2-oxazoline) **13** (150 mg, 0.026 mmol) was dissolved in 2.6 mL of a solution of sodium hydroxide at 0.1 M and placed under an inert atmosphere of N_2. The solution was stirred for 16 h at room temperature then was treated with Amberlite™ IR120 resin (H form) ion exchange resin for 40 min, after a purge with N. The polymer was then purged again with N_2, then dialysed once in distilled water in an Amicon centrifuge tube then freeze-dried to afford a sticky white powder, kept under a nitrogen atmosphere. (**14**, 0.148 g)

^{1}H NMR (400 MHz, $CDCl_3$) δ ppm: 3.75 – 3.35 (m, 220 H, backbone), 2.55 – 2.13 (m, 110 H, CH_2 side chain), 1.23 – 0.98 (m, 165 H, CH_3 side chain).

SEC (THF, triethylamine, PS calibration): M_n = 4,500 g mol^{-1}, $Đ$ = 1.28.

2.4.3.2.3 Synthesis of a poly (2-ethyl-2-oxazoline) with carboxylic acid and maleimide-functionalised Cyanine 3 groups **3**

Thiol-functionalised poly(2-ethyl-2-oxazoline) **14** (50.2 mg, 0.0091 mmol) was dissolved in 2 mL of DMF and commercially available maleimide-functionalised Cyanine 3 (7.02 mg, 0.011 mmol) was added to the solution before purging it for 10 min with N_2. The solution was stirred for 16 h at room temperature, following the formation of fluorescent polymer by HPLC equipped with a fluorescence detection. The solvent was removed using a nitrogen flow, the residual crude redissolved in deionized water and dialysed in a 3 kDa-cut off dialysis centrifuge tube twice, until no free dye could be detected by HPLC. The aqueous solution of dialysed polymer was then freeze dried, giving a pink solid (**3**, 40 mg).

2.4.3.2.4 Synthesis of fluorescent CP(PEtOx) conjugates **6** *and* **7**

Cy3-functionalised poly-2-ethyl-2-oxazoline **3** (1.2 or 2.15 eq.) and HCTU (1.2 or 2.15 eq.) were dissolved in 1 mL of DMF and left stirring for 10 min. A solution of cyclic peptide (**1** or **2**, with 1 or 2 Lys arms, 1.0 eq.) with NMM (3.0 or 6.0 eq.) was prepared in DMF. This solution was added to the activated polymer, and the mixture was stirred at room temperature for 16 h. DMF was then removed with a flow of nitrogen and the crude was redissolved in deionized water, and dialysed three times in an adequate membrane cut-off centrifuge tube. The dialysed solution was then freeze-dried and the solid collected.

The efficiency of conjugation and the purity of the samples were assessed using SEC with DMF+LiBr and HPLC. The compounds were eventually purified using preparative HPLC (obtaining **6** and **7**). The same methodology has been used for the synthesis of non-fluorescent compounds, by reacting **1** or **2** with a carboxylic acid initiated and hydroxyl terminated poly(2-ethyl-2-oxazoline).

2.4.3.3 Polyethyleneglycol (PEG) CP conjugates

2.4.3.3.1 Conjugation of telechelic PEG **4** *to cyclic peptides*

Cyclic peptide (**1** or **2,** 1.0 eq.) and DIPEA (3 or 6 eq.) were dissolved in 1 mL of DMF. NHS-end functionalised PEG (**4**, 1.2 or 2.15 eq., 9,256 g/mol) was then added and the mixture was left stirring 16 h. DMF was then removed with a flow of nitrogen and the crude was redissolved in deionized water and dialysed three times in a 30 or 50 kDa membrane cut-off centrifuge tube. The dialysed solution was then freeze-dried and the solid collected. The efficiency of conjugation and the purity of the samples were assessed using SEC with DMF+LiBr and HPLC.

2.4.3.3.2 *Deprotection of BocHN-PEG-conjugates and synthesis of Cy3 CP(PEG) conjugates* **8** *and* **9**

Cyclic peptide-PEG-NHBoc (**16** or **17**) conjugate was dissolved in 1 mL of TFA and stirred for 30 min, following deprotection using HPLC. The TFA was removed with a nitrogen flow and the crude was redissolved in deionised water then dialysed in a 3 kDa-cut off dialysis centrifuge tube. The solution was then freeze-dried and the conjugate recollected.

Cyclic peptide-PEG-NH_2 and DIPEA were dissolved in 1 mL of DMF. NHS-functionalised Cy3 was then added, and the mixture was stirred for 16h, following the reaction using HPLC with a fluorescence detector. The solvent was removed using a nitrogen flow, the residual crude redissolved in deionized water, and filtered through a 0.2 µm GPC filter to remove excess of insoluble dye. The filtrate was dialysed in a 3 kDa-cut off dialysis centrifuge tube three times, until no free dye could be detected by HPLC. The aqueous solution of dialysed conjugate was freeze-dried, giving a bright pink solid (**8** or **9**, depending on the cyclic peptide that was first used).

2.4.3.4 Synthesis of poly(PEGA) conjugates

2.4.3.4.1 Synthesis of poly(PEGA-stat-NAS) **19**

The PABTC CTA **18** (20.5 mg, 0.085 mmol, 1.0 eq.), PEGA-480 (1.0 g, 2.1 mmol, 25 eq.), NAS (35.5 mg, 0.210 mmol, 2.5 eq.), V601 (1.29 mg, 0.0060 mmol, 0.066 eq.) and 1,4-dioxane (0.35 mL) were added to a 20 mL glass vial. The reaction mixture was sealed with a rubber septum and degassed for 10 min with a flow of nitrogen, before being heated at 65°C for 200 min in an oil bath. The polymer was then precipitated three times in cold diethyl ether and dried in a vacuum oven at 40°C for 16 h, affording poly-PEGA as a yellow viscous liquid (520 mg).

M_n (NMR) = 9,900 g/mol, M_n (SEC- DMF+LiBr) = 8,400 g/mol, $Đ$ = 1.14

^{1}H-NMR (400 MHz, $CDCl_3$, ppm, n = 22.5, n' = 2.5): 4.30-4.05 (br, 2 nH, C**H**$_2$CH$_2$(OCH$_2$CH$_2$)$_7$OCH$_3$), 3.72-3.60 (br, 14 nH, CH$_2$CH$_2$(OC**H**$_2$C**H**$_2$)$_7$OCH$_3$), 3.58-3.52 (br, 2nH, CH$_2$C**H**$_2$(OCH$_2$CH$_2$)$_7$OCH$_3$), 3.42-3.36 (br s, 3nH, PEG$_7$ OC**H**$_3$), 2.82 (s, 4n'H, succinimide), 2.50-2.20 (br, 2nH, S(CH(CO$_2$-PEG8)-C**H**$_2$)$_n$CH(CH$_3$)CH$_2$) 2.05-1.82 (br, nH, S(C**H**(CO$_2$-PEG8)-CH$_2$)$_n$CH(CH$_3$)CH$_2$), 0.94 (t, 3H, J = 7 Hz, C**H**$_3$-CH$_2$-CH$_2$-CH$_2$-SCS$_2$).

2.4.3.4.2 Post functionalisation into poly(PEGA-stat-Cy3Am) **5**

Poly(PEGA-*stat*-NAS) **18** (65 mg, 0.0065 mmol, 1.0 eq.), Cy3 amine (10.2 mg, 0.016, 2.5 eq.) and DIPEA (11.3 µL, 0.065 mmol, 10 eq.) were dissolved in 1 mL DMF in a 5 mL glass vial. The reaction was followed by HPLC, using a fluorescence detector. The solvent was removed using a nitrogen flow, and the residual crude was redissolved in deionized water, and filtered through a GPC filter to remove excess insoluble dye. The filtrate was dialysed in 3 kDa-cut off dialysis centrifuge tube three times, until no free dye could be detected on the HPLC. The aqueous solution of dialysed polymer was freeze-dried, giving a bright pink viscous liquid (63 mg).

M_n (SEC- DMF+LiBr) = 7,300 g/mol, $Đ$ = 1.28

^{1}H-NMR (400 MHz, $CDCl_3$, ppm): **Cy3 peaks** (br; 8.40, 7.39). Disappearance of the succinimide peaks at 2.82 ppm.

2.4.3.4.3 Synthesis of poly(PEGA-stat-Cy3Am) conjugates **10** and **11**

Poly-PEGA-*stat*-Cy3Am (1.0 or 2.15 eq.) and HCTU (1.0 or 2.15 eq.) were dissolved in DMF and left stirring for 15 min. A solution of cyclic peptide (with 1 or 2 Lys arms, 1.2 or 1.0 eq.) with NMM (3.0 or 6.0 eq.) was prepared in DMF. This solution was added to the activated polymer, and the mixture was stirred at room temperature for 16 h. DMF was then removed with a flow of nitrogen and the crude was redissolved in deionized water, and dialysed three times in an adequate membrane cut-off centrifuge tube. The dialysed solution was then freeze-dried and the solid collected. The efficiency of conjugation and the purity of the samples were assessed using SEC with DMF+LiBr and HPLC.

Table 2-3: Molecular weight (NMR, SEC) and dispersities of the polymers and CPNT synthesised

CPNT sample	Mn (NMR)	Mn (SEC – DMF + LiBr)	*Đ*
CP(PEtOx) **6**	7,200	9,200*	>2
$CP(PEtOx)_2$ **7**	13,300	12,900	1.45
Pro CP(PEG) **16**	-	19,100	1.05
Pro $CP(PEG)_2$ **17**	-	33,100	1.22
CP(PEG) **8**	11,000	18,000	1.10
$CP(PEG)_2$ **9**	20,800	NA	NA
CP-[poly(PEGA)] **10**	12,400	9,100	1.46
$CP\text{-}[poly(PEGA)]_2$ **11**	23,700	13,000	1.43

2.4.4 Cellular biology

2.4.4.1 Cell culture

MDA-MB-231 HM cells (epithelial metastatic breast cells) and PC-3 (epithelial prostate cancer cells) were grown in Dulbecco's modified Eagle's medium (DMEM) supplemented with 10% (v/v) fetal bovine serum (FBS) and 2 mM of L-glutamine and penicillin at 37°C in a humid 5% CO_2 environment. Cells were typically passaged at 80-90% confluence. NIH 3T3 cells (murine fibroblasts) were grown in Dulbecco's modified Eagle's medium (DMEM) supplemented with 10% (v/v) bovine calf serum (BCS) and 2 mM of L-glutamine and penicillin at 37°C in a humid 5% CO_2 environment.

2.4.4.2 Cytotoxicity assay (XTT/PMS)

Toxicity of the different non-fluorescent conjugates was assessed using a standard XTT protocol. The polymer and CP conjugates to be tested were dissolved in water with 0.5% DMSO in order to obtain solutions at 500 μM. These solutions were subsequently used to prepare dilutions in a mixture of culture media (DMEM) and PBS (50:50) at the following concentrations: 100, 50, 10, 1 and 0.1 μM. MDA-MB-231 cells were seeded in a transparent Greiner 96 well-plate at a density of 25,000 cells per well and incubated for 24 h. The culture media was then removed, and subsequently replaced by 100 μL of the prepared solutions. After 24 h incubation, the medium was replaced with fresh media supplemented with 25 μL of XTT solution (1 $mg \cdot mL^{-1}$) containing N-methyl dibenzopyrazine methyl sulfate (PMS) (25 $\mu mol.L^{-1}$). Cells were incubated for another 24 h. Absorbance was then directly measured using a BioTek™ Cytation™ 3 Cell Imaging Multi-Mode Reader at 450 nm and 650 nm (background).

2.4.4.3 Cell uptake study: microplate reading experiment

Solutions of Cy3-labelled polymer and CP conjugates at 5 and 25 μM were prepared in cell media. NIH 3T3 or MDA-MB-231 cells were seeded in a transparent Greiner 96 well-plate at a density of 10,000 or 15,000 cells per well and incubated for 24 h. The media was subsequently replaced by the prepared solutions of compounds and the cells were left incubating for a further 2 or 24 h. Hoechst 33342 (nuclei staining dye) was added and incubation proceeded for another 15 minutes before cells were washed with warm media twice. Cells were imaged in media using a Synergy HTX plate reader, set at absorption/emission detection of 350/450 nm for Hoechst 33342 and 555/575 nm for Cy3 (RFP filter). The average Cy3 fluorescence emission per well was then calculated, setting a cut-off of the cell limitations from the nuclei and excluding all fractions of cells expressing saturation (>10,000 A.U. of fluorescence intensity). The values were corrected using the values obtained from a fluorescence calibration study for all of the Cy3-labelled compounds. All data are reported as the means of 2 or 3 repeats, as scatterplots. Details on the processing of the images can be found in Appendix A, section A.4.1.

2.4.4.4 Cell uptake study: microplate reading experiment at 4°C

Solutions of Cy3-labelled polymer and CP conjugates at 12.5 μM were prepared in cell media. PC3 cells were seeded in a transparent Greiner 96 well-plate at a density of 10,000 cells per well and incubated for 48 h with 150 μL of cell media. For the 4°C assay itself, the plate was pre-incubated at 4°C before replacing with 50 μL of the prepared solutions of compounds and the cells were left incubating for a further 2 h, at 37 or 4°C. Hoechst 33342 (nuclei staining dye) was added and incubation proceeded for another 15 minutes before cells were washed with warm or cold medium (for the 4°C experiment) twice. 100 μL of fresh medium was eventually added. Cells were imaged using a Synergy HTX plate reader, set at absorption/emission detection of 350/450 nm for Hoechst 33342 and 555/575 nm for Cy3 (RFP filter). The average Cy3 fluorescence emission per well was then calculated, setting a cut-off of the cell limitations from the nuclei and excluding all fractions of cells expressing saturation (>7,000 A.U. of fluorescence intensity). The values were corrected using the values obtained from a fluorescence calibration study for all of the Cy3-labelled compounds. All data are reported as the means of 2 biological replicates. Details on the processing of the images are in Appendix A, section A.4.1.

2.4.4.5 Cell uptake study: confocal microscopy on 2D cell cultures

For confocal microscopy, PC-3 were seeded in a 10-well plate at a density of 20,000 cells per well, and allowed to grow for 48 h prior to the experiment. Cell media was then replaced by fresh media supplemented with the one of the four compounds of interest at 5 μM from stock solutions at 500 μM in water (2 wells were used for each compound) and were incubated for 24 h. LysoTracker™ Deep Red was added 2 h before imaging, Hoechst 33342 (nuclei stain) was then added and incubation proceeded for another 15 minutes before cells were washed with warm PBS twice. The cells were left in colourless media and imaged immediately. Confocal microscopy images were taken on a Leica TCS SP5 (Carl Zeiss, Germany) at a temperature of 37°C, using a x40 objective and sequential scanning for each channel. Excitation/Emission used for imaging are as follows: nucleus channel (405 / 406-459 nm), RFP channel for Cy3 compounds (561 / 557-598 nm), LysoTracker ™ Deep Red channel (633 / 646-698 nm).

2.4.4.6 Spheroid culture - Liquid overlay method

A suspension of PC-3 cells at a concentration of 104 cells/mL was prepared from a passage of 80-90% confluent PC-3 cells. 200 μL of cells (2 x 103 cells) were seeded in a Cellstar ® Cell-Repellent Surface 96 well plates. The plate was subsequently centrifuged for 5 min at 500 g and left incubating for 4 days at 37°C with 5% CO2 to form spheroids.

2.4.4.7 Confocal microscopy on spheroids

PC-3 spheroids were grown following the liquid overlay method. 100 μL of cell media were then taken off and replaced with 100 μL of solutions of the different compounds of interest at 10 μM (final concentration in wells: 5 μM). Spheroids were left to incubate at 37°C with 5% CO2 for 24 or 48 h. LysoTracker™ Deep Red and Hoechst 33342 (nuclei stain) were added 1 h before imaging. Media was subsequently removed and the spheroids were washed with warm PBS 3 times. Spheroids were eventually transferred into a 10 well confocal microscopy plate with colourless media for imaging. Confocal microscopy images were taken on a Leica TCS SP5 (Carl Zeiss, Germany) at a temperature of 37 °C, using a x20 objective and sequential scanning for each channel. Z-stacks were acquired over a length of 100 μm, with a step of 2 μm (50 steps overall). Excitation/Emission used for imaging are as follows: nucleus channel (405 / 406-459 nm), RFP channel for Cy3 compounds (561 / 557-598 nm), LysoTracker ™ Deep Red channel (633 / 646-698 nm). Colocalisation was measured using ImageJ to obtain Pearson's coefficients on a 3D projection of different spheroids. Details on the processing of the images can be found in the Appendix, section A.4.3.

2.5 References for Chapter 2

1. A. S. Hoffman, *Journal of Controlled Release*, 2008, **132**, 153.
2. Z. Ahmad, A. Shah, M. Siddiq and H.-B. Kraatz, *RSC Advances*, 2014, **4**, 17028.
3. L. Sercombe, T. Veerati, F. Moheimani, S. Y. Wu, A. K. Sood and S. Hua, *Frontiers in Pharmacology*, 2015, **6**, 286.
4. J. Li and D. J. Mooney, *Nature Reviews Materials*, 2016, **1**, 16071.
5. J. Zhou, J. Li, X. Du and B. Xu, *Biomaterials*, 2017, **129**, 1.
6. S. Behzadi, V. Serpooshan, W. Tao, M. A. Hamaly, M. Y. Alkawareek, E. C. Dreaden, D. Brown, A. M. Alkilany, O. C. Farokhzad and M. Mahmoudi, *Chemical Society Reviews*, 2017, **46**, 4218.
7. J. A. Champion, Y. K. Katare and S. Mitragotri, *Journal of controlled release : official journal of the Controlled Release Society*, 2007, **121**, 3.
8. J. Zhao, H. Lu, S. Wong, M. Lu, P. Xiao and M. H. Stenzel, *Polymer Chemistry*, 2017, **8**, 3317.
9. N. P. Truong, M. R. Whittaker, C. W. Mak and T. P. Davis, *Expert Opinion on Drug Delivery*, 2015, **12**, 129.
10. J.-H. Park, G. von Maltzahn, L. Zhang, M. P. Schwartz, E. Ruoslahti, S. N. Bhatia and M. J. Sailor, *Advanced Materials*, 2008, **20**, 1630.
11. M. Müllner, D. Mehta, C. J. Nowell and C. J. H. Porter, *Chemical Communications*, 2016, **52**, 9121.
12. M. Müllner, K. Yang, A. Kaur and E. J. New, *Polymer Chemistry*, 2018, **9**, 3461.
13. S. Dasgupta, T. Auth and G. Gompper, *Nano Letters*, 2014, **14**, 687.
14. E. Hinde, K. Thammasiraphop, H. T. T. Duong, J. Yeow, B. Karagoz, C. Boyer, J. J. Gooding and K. Gaus, *Nature Nanotechnology*, 2017, **12**, 81.
15. M. C. Branco and J. P. Schneider, *Acta Biomaterialia*, 2009, **5**, 817.
16. D. T. Bong, T. D. Clark, J. R. Granja and M. R. Ghadiri, *Angewandte Chemie International Edition*, 2001, **40**, 988.
17. P. De Santis, S. Morosetti and R. Rizzo, *Macromolecules*, 1974, **7**, 52.
18. M. R. Ghadiri, J. R. Granja, R. A. Milligan, D. E. McRee and N. Khazanovich, *Nature*, 1993, **366**, 324.
19. J. Couet, J. D. J. S. Samuel, A. Kopyshev, S. Santer and M. Biesalski, *Angewandte Chemie International Edition*, 2005, **44**, 3297.
20. E. D. H. Mansfield, M. Hartlieb, S. Catrouillet, J. Y. Rho, S. C. Larnaudie, S. E. Rogers, J. Sanchis, J. C. Brendel and S. Perrier, *Soft Matter*, 2018.
21. M. G. J. ten Cate, N. Severin and H. G. Börner, *Macromolecules*, 2006, **39**, 7831.
22. B. M. Blunden , R. Chapman, M. Danial, H. Lu, K. A. Jolliffe, S. Perrier and M. H. Stenzel, *Chemistry – A European Journal*, 2014, **20**, 12745.
23. S. C. Larnaudie, J. C. Brendel, I. Romero-Canelón, C. Sanchez-Cano, S. Catrouillet, J. Sanchis, J. P. C. Coverdale, J.-I. Song, A. Habtemariam, P. J. Sadler, *et al.*, *Biomacromolecules*, 2018, **19**, 239.
24. H. Shaikh, J. Y. Rho, L. J. Macdougall, P. Gurnani, A. M. Lunn, J. Yang, S. Huband, E. D. H. Mansfield, R. Peltier and S. Perrier, *Chemistry – A European Journal*, 2018, **24**, 19066.
25. Z. J. Kamiński, B. Kolesińska, J. Kolesińska, G. Sabatino, M. Chelli, P. Rovero, M. Błaszczyk, M. L. Główka and A. M. Papini, *Journal of the American Chemical Society*, 2005, **127**, 16912.
26. A. A. D'souza and R. Shegokar, *Expert Opinion on Drug Delivery*, 2016, **13**, 1257.
27. M. Bauer, C. Lautenschlaeger, K. Kempe, L. Tauhardt, U. S. Schubert and D. Fischer, *Macromolecular Bioscience*, 2012, **12**, 986.
28. T. X. Viegas, M. D. Bentley, J. M. Harris, Z. Fang, K. Yoon, B. Dizman, R. Weimer, A. Mero, G. Pasut and F. M. Veronese, *Bioconjugate Chemistry*, 2011, **22**, 976.
29. S. Perrier, *Macromolecules*, 2017, **50**, 7433.

30. B. Hammouda, *Journal of Applied Crystallography*, 2010, **43**, 716.
31. J. E. Cavanaugh and A. A. Neath, *WIREs Computational Statistics*, 2019, **11**, e1460.
32. I. Bressler, J. Kohlbrecher and A. F. Thunemann, *Journal of Applied Crystallography*, 2015, **48**, 1587.
33. H. Benoit, *Journal of Polymer Science*, 1953, **11**, 507.
34. J. Y. Rho, J. C. Brendel, L. R. MacFarlane, E. D. H. Mansfield, R. Peltier, S. Rogers, M. Hartlieb and S. Perrier, *Advanced Functional Materials*, 2018, **28**, 1704569.
35. A. C. French, A. L. Thompson and B. G. Davis, *Angewandte Chemie International Edition*, 2009, **48**, 1248.
36. S. Bolte and F. P. Cordelieres, *Journal of Microscopy*, 2006, **224**, 213.
37. J. Schindelin, I. Arganda-Carreras, E. Frise, V. Kaynig, M. Longair, T. Pietzsch, S. Preibisch, C. Rueden, S. Saalfeld, B. Schmid, *et al.*, *Nature Methods*, 2012, **9**, 676.
38. G. Lazzari, P. Couvreur and S. Mura, *Polymer Chemistry*, 2017, **8**, 4947.
39. S. Nath and G. R. Devi, *Pharmacology & therapeutics*, 2016, **163**, 94.
40. P. L. Chariou, K. L. Lee, J. K. Pokorski, G. M. Saidel and N. F. Steinmetz, *The Journal of Physical Chemistry B*, 2016, **120**, 6120.
41. S. A. Raw, *Tetrahedron Letters*, 2009, **50**, 946.
42. L. Martin, R. Peltier, A. Kuroki, J. S. Town and S. Perrier, *Biomacromolecules*, 2018, **19**, 3190.
43. O. Arnold, J. C. Bilheux, J. M. Borreguero, A. Buts, S. I. Campbell, L. Chapon, M. Doucet, N. Draper, R. Ferraz Leal, M. A. Gigg, *et al.*, *Nuclear Instruments and Methods in Physics Research Section A: Accelerators, Spectrometers, Detectors and Associated Equipment*, 2014, **764**, 156.
44. B. H. Zimm, *The Journal of Chemical Physics*, 1948, **16**, 1093.

Chapter 3

Investigating the Behaviour of Stabilised and Integrin-targeting Cyclic Peptide-Polymer Nanotubes on Cellular and Animal Models

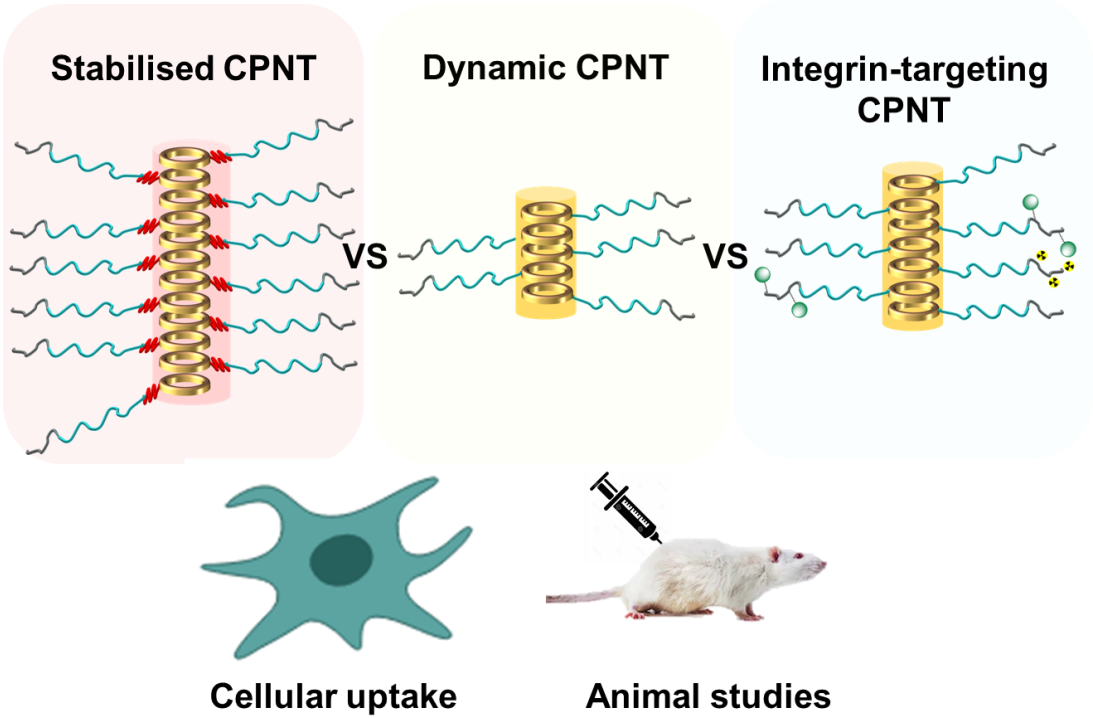

Gabby Han (1998-2020) – In memoriam

3.1 Introduction

Concomitantly with advances in chemistry, the field of drug delivery has witnessed major changes over the past sixty years. Drug delivery systems (DDS) have evolved from first being designed on the macroscopic scale to being made on the microscopic and nanoscopic scale.[1] In particular, anticancer drug delivery systems on the nanoscale have become extremely elaborate in order to face the challenges posed by highly cytotoxic agents: lack of specificity, secondary effects, poor pharmacokinetic profiles, etc. Such DDS now include advanced features such as specific morphologies, stimuli-responsiveness (allowing for triggered release) or cancer-cell targeting moieties.[2] Predicting the clinical fate of anticancer DDS is extremely difficult, hence why different models are currently being employed to pre-assess the performance of a new system. *In vitro* models are helpful in grasping a better understanding of the biomolecular interaction of a DDS with cells, as well as pre-evaluating their potency. Despite advances in the design of new biological systems to study DDS behaviour (e.g. spheroids as discussed in Chapter 2, section 2.2.4.2), the results obtained from studies on cells often fail to translate fully into animals or more advanced clinical models.[3, 4] The biological fate of a DDS nanocarrier in an animal model (e.g. rodent) is complex, with multiple new parameters to take into consideration as reviewed by Bertrand and Leroux: circulation time, interaction with the protein corona, organ distribution, metabolic stability and interaction with excretion organs (liver, kidney, spleen).[5] The nature of the surface of a nanoscale DDS can affect its propensity towards protein corona formation (as well as its composition), significantly affecting its biological fate (pharmacokinetics, biosafety).[6, 7] Studies have shown the possibility to take advantage of this protein corona to develop more effective nano DDS.[8, 9]

Oh *et al.* demonstrated that by cloaking mesoporous silica nanoparticles with a "protein corona shield" (based on the designed recombinant protein GST-HER2-Afb), it was possible to enhance the specificity of anticancer drug camptothecin delivery to tumour cells, both *in vitro* and *in vivo*, as blood proteins were less likely to adsorb on the nanoparticles.[8] A machine-learning algorithm developed by Lazarovits *et al.* managed to predict the accumulation of gold nanoparticles in organs just by analysing their protein corona composition; different organ accumulation patterns could be obtained by incubating Au nanoparticles in a rat and transferring the former to another rat.[9]

In the case of self-assembling polymer-based DDS systems, tailoring the shape to make cylindrical nanostructures has a clear impact on their circulation time and organ distribution, as previously discussed in Chapter 1.[10-13] Among such nanocylindrical structures, self-assembling cyclic peptide-polymer nanotubes (CPNT) are an emerging class of DDS with promising *in vitro* and *in vivo* properties. Their ability to deliver anticancer drugs was previously investigated, showing a higher potency and specificity of the drug on ovarian cancer cells (see Chapter 1, section 1.4).[14, 15] However, few reports of the biological fate of CPNT in animal models can be found in the literature.[16, 17] The *in vivo* behaviour of CPNT was first examined in 2018 by Larnaudie e*t al.*[16] The authors looked into the pharmacokinetics and biodistribution of poly(2-hydroxypropylmethacrylamide) (poly(HPMA)) based CPNT, with a small amount of 2-(3-(Pyridin-4-ylmethyl)ureido)ethyl)methacrylate (PUEMA) in the polymer chain, that system itself having previously been used for the delivery of an Ir anticancer drug *in vitro*.[15] This nanotube, containing a cyclic peptide with two polymer arms (the CP was identical to CP **2** mentioned in Chapter 2, visible on **Scheme 2-1**), was found to be 16 nm long and its behaviour was compared to a non-assembling polymer system made by linking the two polymer arms together. The CPNT showed longer blood circulation time and clearance 4 times lower than the free polymer in rats; a 2-fold higher liver uptake of the nanotube was also observed.[18] Very recently, a similar study compared a 36 nm-long poly(4-acryloyl morpholine) (poly(NAM)) CPNT (CP-[poly(NAM)$_{37}$]$_2$) to covalently grafted poly(NAM) brushes with a length of 40 and 133 nm (the radius in both cases being around 8-9 nm).[17]

The CPNT pharmacokinetic profile (half-life $t_{1/2}$ = 15 h) was at the crossroads between a linear polymer ($t_{1/2}$ = 5 h) and covalently bound poly(NAM) brushes ($t_{1/2} \geq$ 35 h). A similar trend was found for rats' urine excretion, with the CPNT showing 29% excretion of the initial dose whilst the linear poly(NAM) (51% of the dose) and the brushes (0.6% of the dose) were higher and lower, respectively. The biodistribution profiles showed high accumulation of the brushes in the liver, whilst the CPNT was mainly distributed between the kidneys and the liver, in similar proportions to what has been previously described by Larnaudie *et al* (see **Figure 3-1**). This behaviour of CPNT, allying high blood circulation to efficient excretion from the body, could be especially advantageous for the specific delivery of anticancer drug.

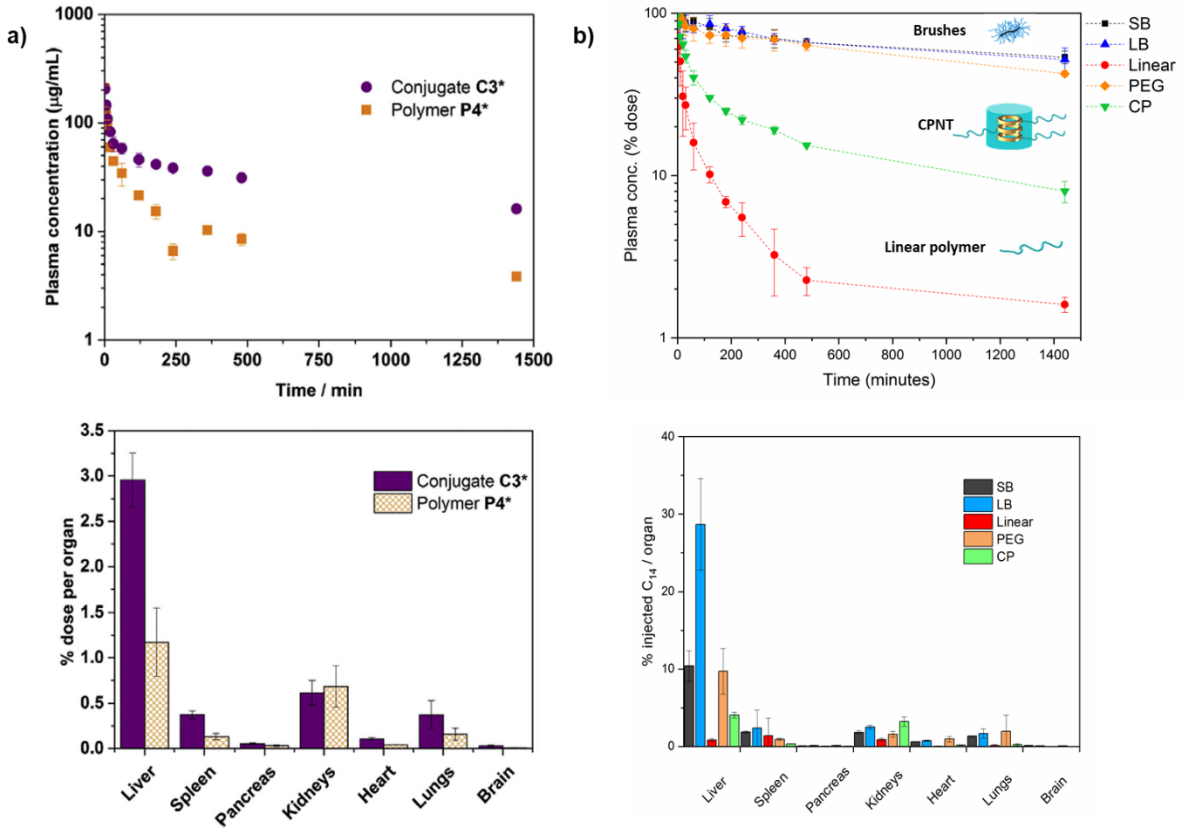

Figure 3-1: Pharmacokinetic (top) and biodistribution profiles (bottom) for the *in vivo* studies on rats performed by a) Larnaudie *et al.* comparing a poly(HPMA) CPNT C3*(16 nm long) to the free equivalent polymer P4*and by b) Kerr e*t al.* comparing a CPNT (CP, 36 nm long) to polymer brushes (short brush SB 40 nm long, long brush LB 133 nm long, PEG based short brush).[16, 17]

Passive accumulation in tumour tissue is possible *via* the Enhanced Permeation and Retention (EPR) effect, relying on the high vascular permeability in some solid tumours. Longer circulation times would effectively allow for higher likelihood of accumulation of CPNT into tumours.[19, 20]

Caution must however be taken when following this approach, as there is an ongoing paradigm shift in the field of nanomedicine concerning the EPR effect. Tee *et al.* have reviewed the current limitations of this approach, highlighting the diversity in tumours' "leakiness" (especially for immature tumours) and the complexity of the tumour microenvironment.[21] Sindwhani *et al.* also showed that the transport of solid nanoparticles inside solid tumours mostly relied on active mechanisms, relying on passage of the NP through endothelial cells instead of following a pattern passive accumulation through interendothelial gaps.[22]

Key aspects of the *in vivo* fate of CPNT remain unknown. So far, the CPNT tested were of relatively short lengths (below 40 nm) and only contained neutral hydrophilic polymers; the behaviour of longer and stabilised CPNT self-assemblies, less prone to dynamic exchange and disassembly, is yet to be determined. As previously discussed in Chapter 1 (section 1.3.3), stabilised CPNT in water were recently synthesised, with two poly(butyl acrylate-*b*-N-dimethylacrylamide) (poly(BA-*b*-DMA)) arms, the hydrophobic poly(BA) block helping with the stabilisation process. The hydrophobic core was aimed to exclude water molecules therefore avoiding any solvent interference with the cyclic peptide hydrogen-bonding mediated self-assembly. These poly(BA-*b*-DMA) CPNT showed less propensity towards dynamic exchange between nanotubes as well as a higher overall length (around 200 nm), compared to poly(DMA) CPNT, with the same amount of DMA units. These elongated CPNT were also shown to be biocompatible, according to cell viability assays.[23] The use of these elongated nanotubes could help in obtaining longer circulation times and better passive accumulation in tumours. Other systems could also be designed specifically for the active transport of drugs to the tumour; the use of targeting moieties, able to be recognised by receptors at the surface of tumour cells, may be of interest to maximise the chances of tumour accumulation.

The impact of targeting moieties on CPNT biological fate needs to be further explored, as cancer cells are known to overexpress certain receptors to maximise their growth. Different cancer-cell targeting motifs have been investigated in the nanomedicine literature. Antibodies are thought to be the most efficient targeting moieties, given their high specificity. Their use in nanomedicine has proven particularly promising but their cost, size and the scale at which they can be generated is often prohibitive.[24, 25] Smaller molecular entities, such as sugars (mannose,[26] glucose,[27] fructose[28, 29], etc.) and vitamins (biotin,[30, 31] folic acid[32], etc.) have been employed to target corresponding overexpressed receptors on specific cancer cells. Specific peptide sequences are also available for targeting different types of cells.[33] For instance, targeting integrins (cell adhesion receptors, involved in the cell cycle regulation), such as $\alpha_v\beta_3$ are a popular option as these tend to be overexpressed in angiogenic endothelial cells, which surround the tumour tissue and are therefore directly exposed to the flux of incoming blood.[34, 35] Different peptide sequences have been tested by Kapp *et al.* to target integrins overexpressed in cancer cells, with varying specificity. Among these the RGD motif (composed of arginine, glycine and aspartic acid) has been found to be particularly important in the integrin binding site, with an enhanced potency and specificity if contained within a cyclic peptide (e.g.: cRGDfK), given their higher stability and propensity to adopt more rigid conformations.[36]

Herein, we propose to investigate both of these aforementioned aspects (CPNT length and targeting). The synthesis and characterisation of the stabilised elongated CPNT and the integrin-targeting CPNT is reported here; their behaviour in different mammalian cell models has been investigated by confocal microscopy (CLSM) and flow cytometry. *In vivo* pharmacokinetic and biodistribution studies were also performed in rats using radiolabelled CPNT, to determine the effect of the previously proposed structural modifications (elongation, inclusion of cRGDfK integrin targeting moiety) on the circulation and organ targeting behaviour.

3.2 Results and discussion

3.2.1 Synthesis of stabilised and dynamic cyclic peptide-polymer nanotubes

The chemical design of stabilised and dynamic nanotubes for *in vitro* and *in vivo* study was inspired by previous work as described in the introduction of this chapter. Following on from promising *in vitro* results of self-assemblies of CPNT with one polymer arm discussed in Chapter 2 (length around 10-15 nm), it was decided to focus on such structures for the dynamic systems. The cyclic peptide (CP) **1** used is identical to the one described in Chapter 2; as for the polymer system, poly(NAM) was chosen as the hydrophilic polymer because of its biocompatibility and to match the nanotube and polymer brushes used *in vivo* by Kerr *et al.*[17] A diblock copolymer of BA and NAM was used to generate stabilised CPNT. These systems were optimised for facile post-functionalisation, in order to produce labelled and integrin-targeting CPNT suitable for both *in vitro* and *in vivo* studies (**Figure 3-2**). Similarly, to the work presented in Chapter 2, the polymers employed in this study were synthesised using the RAFT polymerisation technique. Advantages of RAFT include; retention of functional end groups, facile incorporation of multiple monomers and different functional groups, and good control over the polymer dispersity that can be obtained.

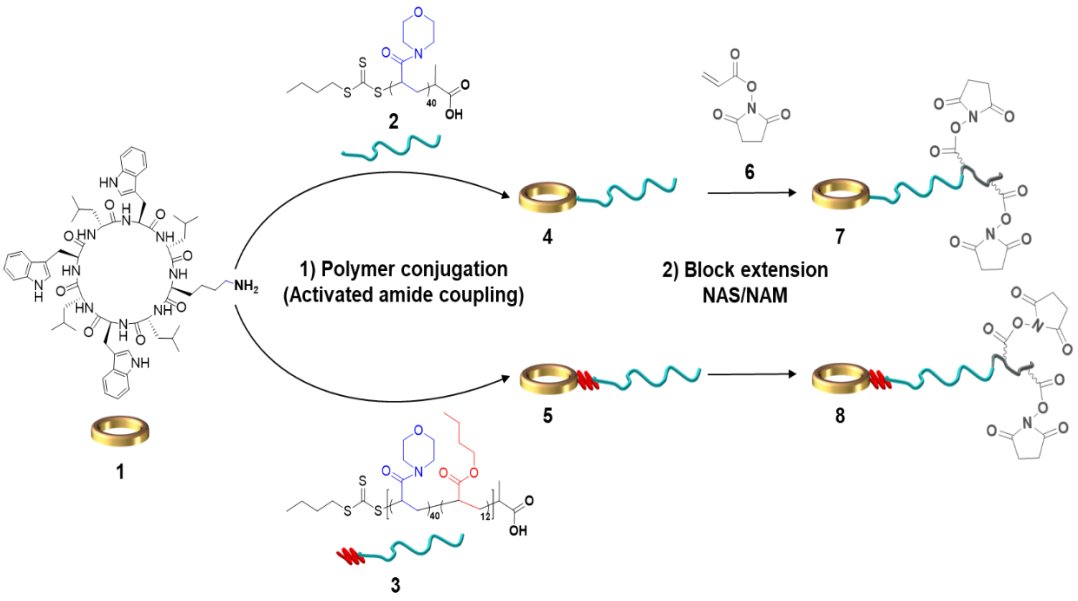

Figure 3-2: Synthetic route employed to generate NHS-functional dynamic **7** and stabilised **8** CP-polymer conjugates for post-functionalisation. Conditions for 1) were HCTU (1 eq. to polymer) /NMM (3 eq.) in DMF; for 2), a ratio of 60:40 NAS:NAM was used (DP target: 27) and the polymerisation was run using V-601 (0.1 eq. to macroCTA **4** or **5**) in DMF at 70°C overnight.

Two main polymers were first synthesised, homopolymer poly(NAM_{42}) **2** and diblock copolymer poly(BA_{12}-*b*-NAM_{42}) **3.** Polymers **2** (M_n (SEC) = 6,100 g/mol) and **3** (M_n(SEC) = 7,700 g/mol) had a low dispersity of 1.07 in both cases and good agreement with the theoretical molecular weights **2** (M_n (NMR) = 5,900 g/mol) and **3** (M_n (NMR) = 7,500 g/mol), indicating that good control over the polymerisation process had been achieved. The livingness for both blocks was also over 98%, suggesting near quantitative chain transfer, which is of interest for further extensions of the polymer chains. Conjugation of both polymers to cyclic peptide **1** was performed following a *grafting-to* approach, using HCTU-mediated activated amide coupling. Lower yields than the ones reported in Chapter 2 were obtained, most likely due to the purification process. Dialysis in aqueous media was not possible given the poor aqueous solubility of both compounds, therefore, purification was achieved by slow precipitation. SEC and NMR analysis were used to characterise the conjugation, showing a clear molecular weight shift and the presence of the cyclic peptide peaks in the material.

Exploiting the living nature of the RAFT process, CP-polymer conjugates **4** and **5** were block extended *via* a *grafting-from* approach, introducing a statistical copolymer of NAM and NHS-activated ester monomer NAS **6**.[37] The use of this approach was preferred to the *grafting-to* method, the former requiring perfect orthogonality between the CP-polymer conjugation and the polymer functionalisation. Constraints related to the use of radioactive materials (cost, safety procedures, etc.) were also a strong incentive to favour this approach for the synthesis of all functional nanotubes reported here; the amine-functional radiolabel can be directly reacted on the final material. After optimisation of the reaction conditions to reach higher monomer conversions, the polymerisation allowed for the efficient synthesis of CP-poly[NAM_{42}-*b*-(NAM_{10}-*stat*-NAS_{14})] **7** (M_n = 9,000 g/mol, Đ = 1.37) and CP-poly[BA_{12}-b-NAM_{42}-*b*-(NAM_{10}-*stat*-NAS_{14})] **8** (M_n = 13,200 g/mol, Đ = 1.18) with theoretical molecular weights (M_n (NMR) = 11,000 and M_n (NMR) = 12,200 g/mol for **7** and **8** respectively) in good agreement with the values obtained from SEC. A summary of all of the SEC data is available in **Table 3-1** and **Figure 3-3**. The partial loss of control can mainly be explained by the reaction scale and the low monomer concentrations used, as well as the complexity of the re-initiating group. NMR of the purified materials showed the presence of a clear peak for the succinimide protons at 2.83 ppm in d-DMSO from the 14 NHS moieties in the conjugates, confirming the potential for post-functionalisation of these materials (see Appendix B, section B.1).

Table 3-1: Molecular weight and dispersities of the polymers and CP-polymer conjugates synthesised in this work, as established by NMR and SEC in DMF.

	M_n (NMR) (g/mol)	M_n (GPC) (g/mol)	Đ
poly(NAM_{42}) **2**	6,200	6,100	1.03
poly(BA_{12}-*b*-NAM_{42}) **3**	7,700	7,700	1.03
CP- poly(NAM_{42}) **4**	7,300	8,450	1.10
CP-poly(BA_{12}-*b*-NAM_{42}) **5**	8,800	9,600	1.12
Dynamic NHS-functional CPNT **7**	11,000	9,050	1.37
Stabilised NHS-functional CPNT **8**	12,600	13,200	1.18

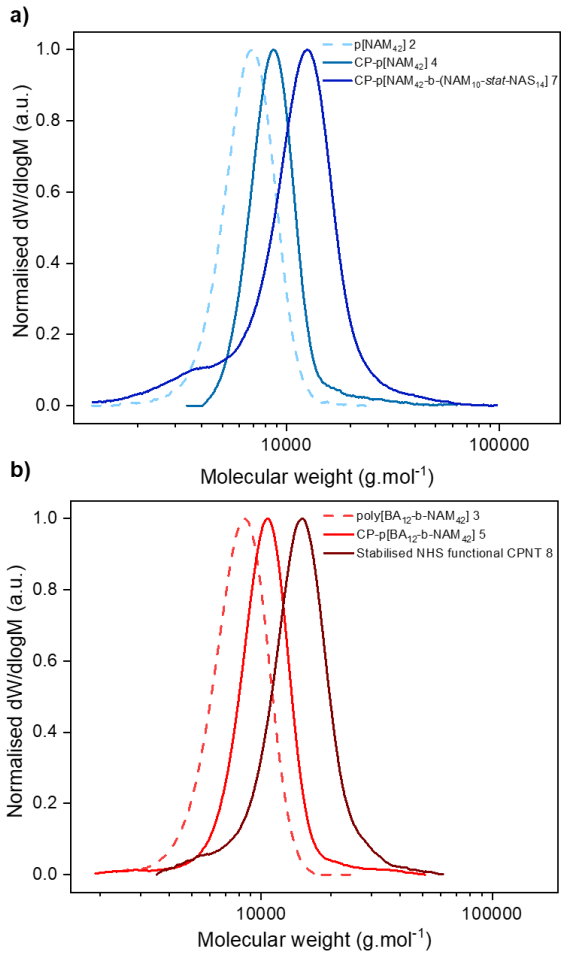

Figure 3-3: SEC chromatograms for: a) The synthesis of NHS-functional dynamic CPNT **7** (in blue; dashed light blue: poly(NAM_{42}) **2**, teal: CP-poly(NAM_{42}) **4** and royal blue: NHS functional CPNT **7**) and b) the synthesis of NHS-functional stabilised CPNT **8** (in red; dashed red: poly(BA_{12}-*b*-NAM_{42}) **3**, red: CP-poly(BA_{12}-*b*-NAM_{42}) **5** and dark red: NHS functional CPNT **8**).

3.2.2 Functionalisation of cyclic peptide-polymer nanotubes

3.2.2.1 Fluorescence and radiolabelling

CPNT **7** and **8** were post-functionalised using primary amines, as these react readily with NHS-activated esters to form amide bonds. Ethanolamine was used to form unlabelled (no fluorescent or radioactive tag) conjugates; these are the main constituent of the multifunctional assemblies that are discussed later in this chapter (see 3.2.3). The NAS-functional CPNT were treated with 11 eq. of ethanolamine in total (0.78 per NAS group) in the presence of hindered base DIPEA to form 2-Hydroyethyl acrylamide (HEAm) moieties; this reaction was performed following usual conditions employed for the reaction of amines onto reactive esters (see more examples in Chapter 2, section 2.2.1). Water was subsequently added with a supplementary amount of DIPEA to permit hydrolysis of the remaining NHS-activated esters to acrylic acid; the presence of negative charges in the system was found to be beneficial to the solubility in aqueous media, especially in the case of the stabilised CPNT **10** (dynamic CPNT **9** being already quite soluble). The disappearance of the NHS peak on the NMR spectrum is a clear indication of the success of this reaction (see **Figure 3-4**). The zeta-potential measurements, in 5% DMSO mixtures, were negative (-23.5 ± 5.4 and -14.8 ± 5.6 mV for **9** and **10** respectively), as expected given the acrylic acid groups present on CPNT **9** and **10**. These charges were not only incorporated to increase aqueous solubility but also to discourage the formation of a large protein corona *via* electrostatic repulsion with negatively charged proteins in the blood (see **Table 3-2**).[38, 39] A similar approach was used to form fluorescently labelled conjugates, 1 eq. of Cyanine 5.5 amine was introduced with some DIPEA before adding ethanolamine. Cy5.5 was chosen as it can be used both for *in vitro* and *in vivo* studies, given its emission in the far-red region; it also has the advantage of being quite similar to Cy3 or Cy5, which have been used extensively in the past for the study of CPNT (see Chapter 2).[23] Surprisingly, the introduction of Cy5.5 onto the stabilised self-assemblies led to a substantial loss of aqueous solubility.

For radiolabelling, 7.7 eq. of ^{14}C-ethanolamine were used, aiming for radioactive CPNT with high specific activity for *in vivo* studies; the labelling efficiency was characterised by SEC (with off-line scintillation counting). Interestingly, a higher molecular weight peak can be seen on the aqueous SEC for the stabilised CPNT **10***, which most likely corresponds to an aggregate as it self-assembles in aqueous media (see **Figure 3-4**). The specific activities were determined to be of 7.0 and 18.7 µCi/mg for **9***and **10*** respectively, which is satisfactory for *in vivo* studies in rodents. The difference in specific activity was explained by the fact that the reaction for **9*** was performed with radioactive ^{14}C-ethanolamine recycled from a previous unsuccessful attempt, given the prohibitive cost of the radiolabel.

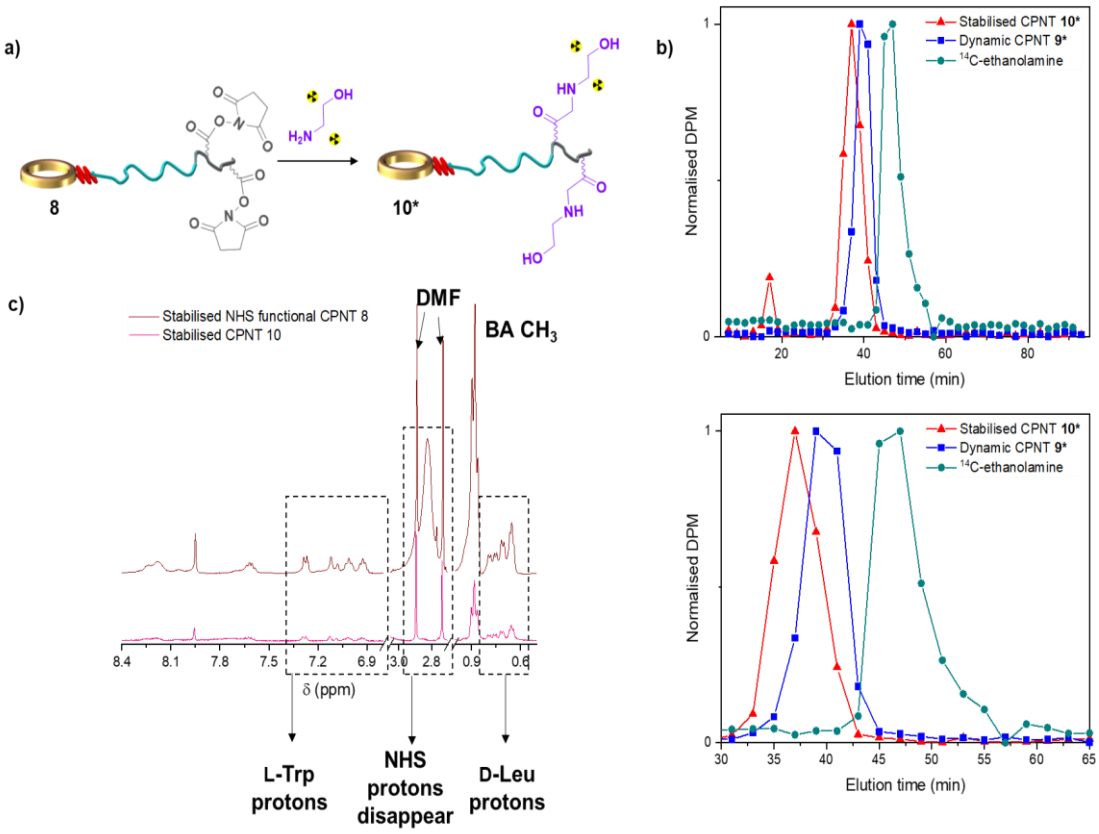

Figure 3-4: Post-functionalisation of CPNT with radioactive ^{14}C-ethanolamine. a) Reaction scheme for the post-functionalisation reaction (11 eq. ^{14}C-ethanolamine, Excess DIPEA, 3 eq. of ethanolamine).

b) SEC chromatograms for radioactive dynamic CPNT **9*** (blue), stabilised CPNT **10*** (red) and free ^{14}C-ethanolamine (green). The bottom graph is a zoomed version, focusing on the main peaks.

c) Comparison of the NMR profiles of NHS functional CPNT **8** (brown) and stabilised CPNT **10** (pink; product of the reaction with non-labelled ethanolamine). The NHS peak at 2.83 ppm disappears after treatment with ethanolamine; other peaks highlighting the presence of CP **1** are indicated (Trp, Leu).

3.2.2.2 Synthesis of integrin-targeting CPNT

Similarly, integrin-targeting dynamic CPNT **11** were synthesised by attaching 4 units of cRGDfK peptide onto the conjugate. cRGDfK was selected as a targeting moiety for the $\alpha_v\beta_3$ integrin, as it is one of the most selective and potent ligands for that receptor; it also has the added benefit of possessing a Phe moiety which is noticeable by NMR.[36] After adding ethanolamine and precipitating, the CPNT was dialysed against water to ensure the removal of any residual unreacted cRGDfK. NMR in DMSO after dialysis and lyophilisation of the sample showed the presence of the Phe groups in the 7.05-7.30 ppm region, as well as the disappearance of the NHS peak and the presence of D-Leu peaks from CP **1** (see **Figure 3-5**); the zeta-potential of CPNT **11** was found to be slightly positive (7.75 ± 3.38 mV), which would correlate with the presence of zwitterionic cRGDfK moieties. A shift towards higher molecular weight was also noticed on the SEC for the cRGDfK-labelled CPNT.

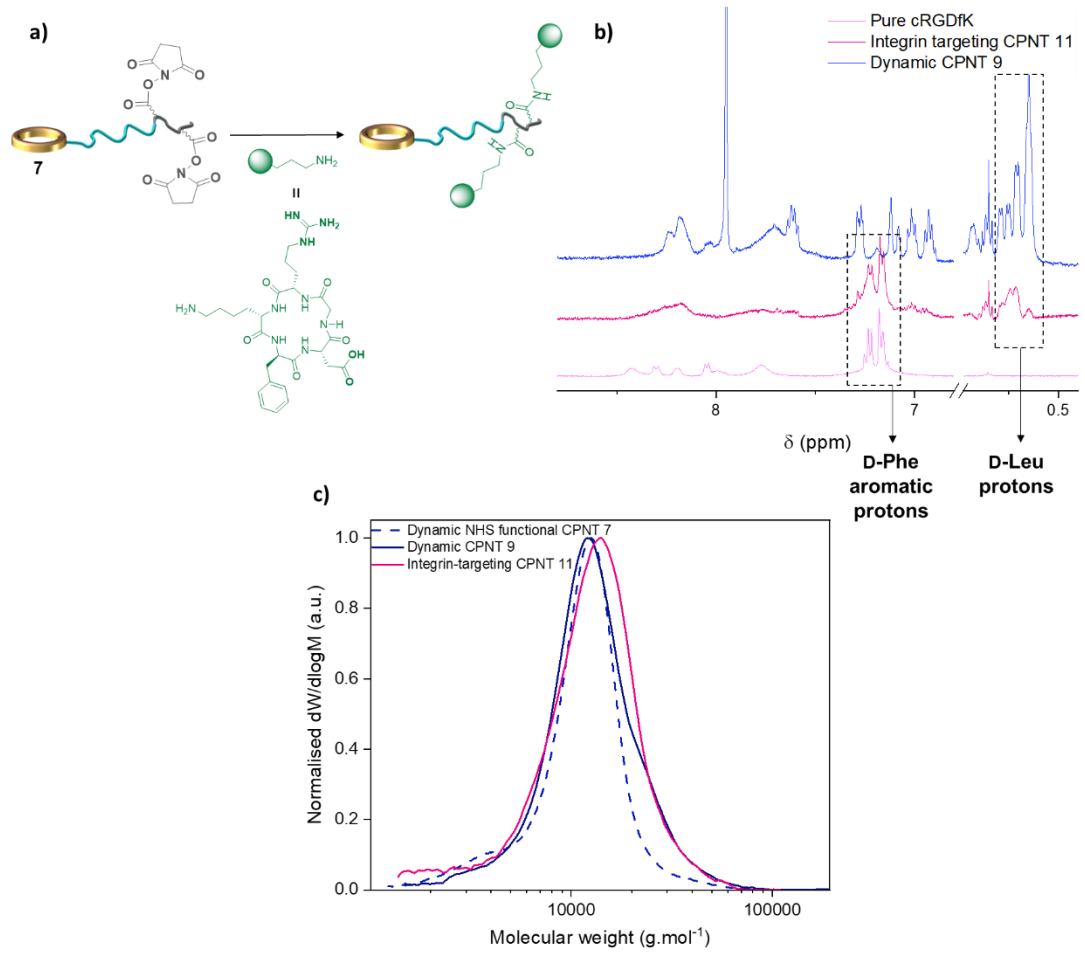

Figure 3-5: Post-functionalisation into integrin targeting CP-polymer conjugates. a) Reaction scheme for the post-functionalisation step in DMF (4 eq. of cRGDfK, Excess of DIPEA, final capping with ethanolamine).

b) Comparison of the NMR profiles of dynamic CPNT **9**, integrin-targeting CPNT **11** (pink-red) and pure cRGDfK (light pink), with a zoom on the D-Leu region showing the presence of cyclic peptide **1** in the structures of **9** and **11** and the D-Phe aromatic protons, clearly visible for **11** and cRGDfK. Full spectra are available in the Appendix B, section B.1.

c) SEC chromatograms representing: dynamic NHS functional CPNT (dashed royal blue), dynamic CPNT **9** and integrin-targeting CPNT **11** (red-pink).

3.2.3 Characterisation of the self-assemblies

The self-assembly of the different synthesised CPNT was studied in PBS buffer and in a 5% DMSO solution in PBS buffer, using Small Angle X-Ray Scattering (SAXS) at a concentration of 5 mg/mL The principle is similar to SANS (mentioned in Chapter 2), the main difference being the use of X-rays over neutrons. Differences of scattering length densities (SLD) in X-ray scattering depend on the number and the distribution of electrons in the structure whilst the variations in neutron scattering mostly depend on the coherent scattering length of each nucleus (example: deuterium is $6.6.10^{-13}$ cm whilst hydrogen is of $-3.7.10^{-13}$ cm, whilst they have the same value for X-rays). The sensitivity for these CPNT in water is therefore lower than in the case of SAXS, as the differences in SLD of water and the CPNT are small (1.2 times higher SLD for the CP core compared to pure water) compared to hydrogenated CPNT in D_2O exposed to neutrons (ca. 4 times lower SLD for the CP core compared to D_2O). Given the availability of the SAXS facility at the University of Warwick and in the absence of neutron beam time in the timeframe of this study, it was decided to use SAXS, which was able to give clear results. The data was fitted using the core-shell cylinder model; this model was chosen over the cylindrical micelle model as it was a better fit for stabilised structures, most likely given the more compact nature of the self-assembly (more "shell-like"). The loss of flexibility of the polymer chains could explain why the data did not properly fit the cylindrical micelle model described in Chapter 2, as the polymer chains are modelled as Gaussian chains. In hydrogenated PBS, it was found that dynamic CPNT **9** had a length of about 10 nm, as expected for this hydrophilic polymer. The stabilised CPNT **10** were found to be over 100 nm long; the lack of plateau and the aspect of the slope at low q indicates that the full size of this nanotube was outside of the window of observation for SAXS. The fit for this data was better considering a core of CP-poly(BA) and a shell of poly(NAM-*b*-(NAM-stat-HEAm)). All other attempts to determine the exact size of the self-assembly, including the use of Spin-Echo SANS (SESANS) or electron microscopy were unsuccessful. The presence of small amounts of DMSO seemed to affect the CPNT self-assembling behaviour significantly, as demonstrated by the SAXS profiles presented in Appendix B (**Figure B-10**). The fits showed nanotubes of a much smaller length, 5.5 nm and 9 nm for dynamic and stabilised CPNT respectively; the DMSO was removed by dialysis or highly diluted for all biological studies. The introduction of Cy 5.5 on dynamic CPNT did not have any significant effect as shown in the Appendix (**Figure B-11**).

The c(RGDfK)-labelled CPNT **11** were also analysed by SAXS, showing an intriguing behaviour as they were found to be much longer than anticipated (>100 nm, outside of the scope of observation for SAXS). Similar behaviour was previously observed by Larnaudie *et al.* when the hydrophilic polymer corona contained a few units of aromatic pyridine-based PUEMA units, which was attributed to enhanced π-π stacking between chains.[15, 16] It is suspected that the interactions involved here are of a different nature; the data was fitted using the core-shell cylinder model to which was added the contribution of a Power law at low q (q^{-4}), similarly to what has been employed in the literature for such profiles (see **Figure 3-6**).[40, 41] This behaviour was observed on polyelectrolyte CP-polymer conjugates and suggest the formation of higher order structures, probably due to interactions between the c(RGDfK) zwitterions (details of the fits can be obtained in **Table 3-2** and in Appendix B, **Table B-1**).[40]

Table 3-2: Summary of the CPNT characteristics obtained by acquiring SAXS profiles in PBS buffer (5 mg/mL) and zeta-potential in water (1 mg/mL) for pure CPNT **9**, **10** and **11.** CSC corresponds to the core-shell cylinder model from SasView.

	Dynamic CPNT **9**	Stabilised CPNT **10**	Integrin-targeting CPNT **11**
Fit	CSC	CSC	CSC + Power law
Length (nm)	10	>100	>100
Width (diameter core + shell thickness) (nm)	6	10	4.5
Aspect ratio	2	>10	>22
Zeta-Potential (mV)	-23.5 ± 5.4	-14.8 ± 5.6	7.75 ± 3.4

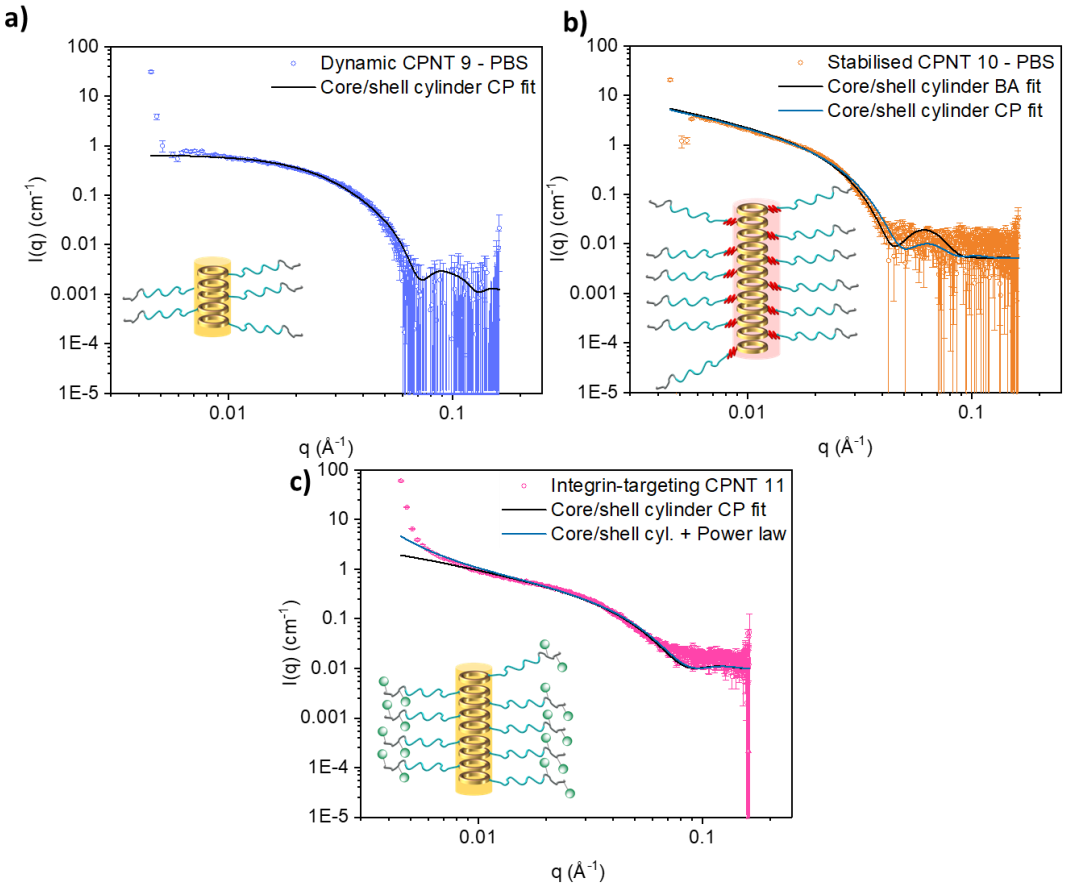

Figure 3-6: SAXS profiles for pure solutions of CPNT: a) **9** (blue), b) **10** (orange) and c) **11** (pink) in PBS buffer. Hollow circles are used for the data plots, fits are plotted as lines; error bars are statistical.

As for sample preparation for biological studies, a *mix-and-match* approach, based on our knowledge of the dynamics of cyclic peptide-polymer self-assembly was used to make multifunctional self-assemblies. This approach has the main advantage of avoiding the necessity of introducing all functionalities on a single CP-polymer conjugate, which could be detrimental to the self-assembly process. Different amounts of the functional conjugates were pre-mixed together in DMSO where they mainly exist in the unimer state before slowly adding PBS buffer, triggering the assembly into statistical CPNT for both stabilised and dynamic nanotubes.[17, 23] For fluorescence studies, the amount of fluorescently labelled conjugate was fixed at 10%; as for radioactive conjugates, different amounts were used depending on the specific activity, in order to target 1 μCi of radioactivity (to obtain a sufficient signal from plasma readings). The integrin-targeting CPNT were prepared by including 30 mol.% of cRGDfK-labelled CPNT **11**; the effect on self-assembly described *vide supra* was lessened as most of the mix is based on conjugate **9** (see schematic of the *mix-and-match* approach in **Scheme 3-1**). In order to alleviate the notation, the mixes containing fluorescent (*in vitro* studies) and radioactive conjugates are also referred to as dynamic CPNT **9**, stabilised CPNT **10** and integrin-targeting CPNT **11** for the rest of this chapter.

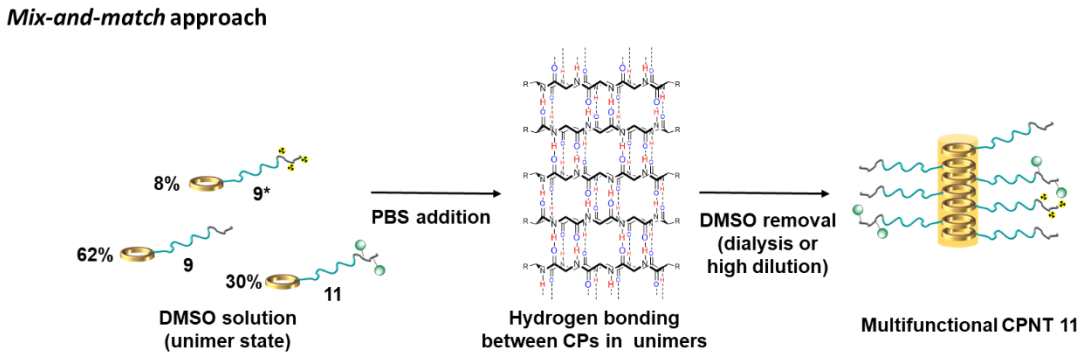

Scheme 3-1: Schematic representing the mix-and-match approach to generate multifunctional CPNT; example of radioactive integrin-targeting CPNT **11**.

3.2.4 Comparing stabilised and dynamic cyclic peptide-polymer nanotubes *in vitro*

3.2.4.1 Cell viability assays

The biocompatibility of the materials described above was first assessed using the tetrazolium-based MTT cell viability assay.[42] Dynamic and stabilised CPNT **9** and **10** were tested on three cell lines of interest: human breast cancer cells MDA-MB 231, similarly to our previous work (see Chapter 2); murine breast cancer cells 4T1, often used for tumour induction,[43,44] and murine fibroblasts NIH 3T3 (a murine "healthy" cell model). The concentration range considered was 0.001 to 1.0 mg/mL. Dynamic short CPNT **9** were shown to exhibit little toxicity on MDA-MB 231 and NIH 3T3 (mostly above 90%) and slight toxicity on 4T1 (~ 75% for most concentrations). Stabilised CPNT **10** demonstrated some effect on cell viability at concentrations above 0.25 mg/mL for all cell lines studied, with a more gradual decrease for MDA-MD 231 and NIH 3T3 where the cell viability varied from 69% to 46% and 90 to 60% respectively. The cell viability in 4T1 for **10** dramatically decreased, from 84% at 0.5 mg/mL down to 43% at 1 mg/mL or 85 µM (see **Figure 3-7**). Such a result could be explained by the relatively poor solubility of CPNT **10** at the highest concentrations. In order to minimise the impact of a decrease in cell viability, the working concentrations for the rest of the *in vitro* work was set to 0.3 mg/mL; pharmacokinetic (PK) studies were conducted in rats with a blood concentration of about 0.1 mg/mL or 5.0 mg/kg, to correspond to previous *in vivo* studies on CPNT.[17]

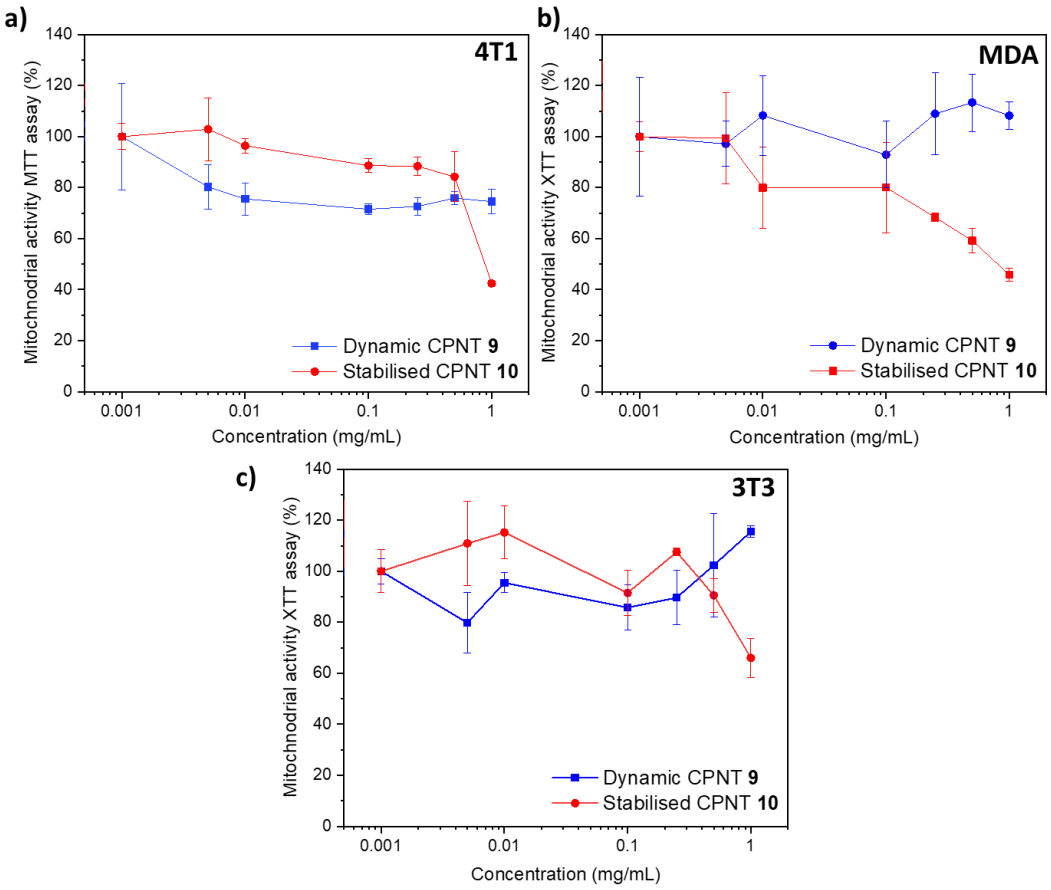

Figure 3-7: Cellular viability on the 0.001-1.0 mg/mL concentration range for dynamic CPNT **9** (blue) and stabilised CPNT **10** (red) for a) murine breast cancer cells 4T1, b) human triple negative breast cancer cell line MDA-MB 231 and c) murine fibroblasts 3T3, as evaluated by the MTT mitochondrial activity assay. Each point represents the mean mitochondrial activity detected by the assay, the error bars are the standard deviation for a measurement in triplicate (n=1, 3 technical replicates).

3.2.4.2 Flow cytometry

Fluorescent samples were prepared following the *mix-and-match* approach described above (**Scheme 3-1**). The cellular uptake of dynamic and stabilised CPNT **9** and **10** in the presence of Cy5.5-labelled conjugate was evaluated using flow cytometry on MDA-MB 231 and NIH 3T3 in three sets of conditions: 3 h at 4°C, 3 h at 37°C and 24 h at 37°C. The uptake at 4°C for both compounds in both cell lines was relatively low, as energy-dependent pathways are being knocked out, suggesting an energy-mediated uptake. Higher uptake levels over time were found comparing the two time points at 37°C. Interestingly, the difference between the two CPNT is more accentuated in MDA-MB 231 cells (1.7 and 1.9 times higher for 3 h and 24 h respectively), with dynamic CPNT **9** being taken up to the highest extent; in 3T3, the difference was only a factor of 1.2 (see **Figure 3-8**).

Such a result was expected, given previous results showing the CPNT cell-uptake dependence on self-assembly discussed in Chapter 2; stabilised CPNT **10** are over 100 nm long, hindering efficient uptake as discussed for poly(2-ethyl-2-oxazoline) CPNT (> 100 nm long for CP(PEtOx)). An analysis of the overall distribution of fluorescence across cells in this study also showed that most cells contained some fluorescent material for both compounds in comparison with the control as it can be seen on both **Figure B-12** and **Figure B-13** (the only exception being the experiments at 4 C, given the low levels of uptake).

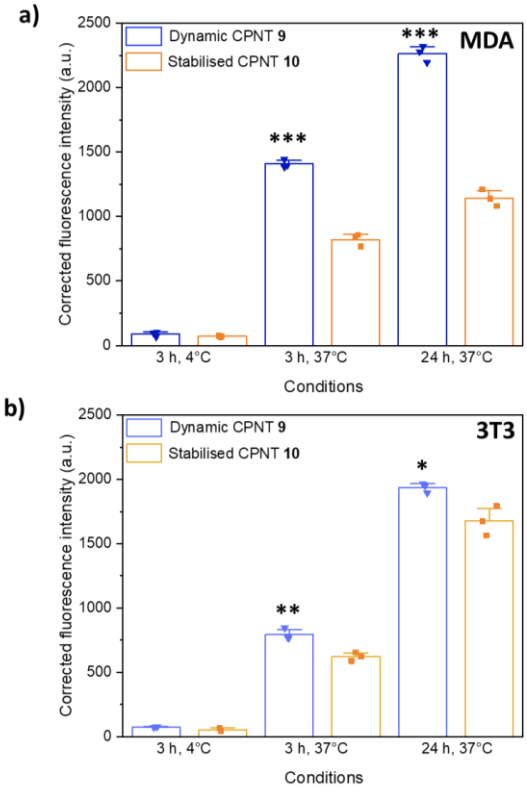

Figure 3-8: Mean cellular fluorescence intensity of Cy5.5-labelled dynamic CPNT **9** and stabilised CPNT **10** mixes after 3 h at 4°C, 3h at 37°C and 24 h at 37°C incubation in a) triple negative breast cancer cells (MDA-MB 231) and in b) murine fibroblasts (NIH 3T3), as measured by flow cytometry. Bar-charts in both cases represent the geometric mean of the fluorescence intensity with an overlap of the repeats, the error bars are the standard deviation for a measurement in triplicate. Statistical significance was assessed by a Student t-test assuming unequal variances. *: $p<0.05$, **: $p<0.005$, ***: $p<0.005$.

3.2.4.3 Confocal microscopy

Fluorescent mixes of the CPNT were also used for confocal microscopy, where their intracellular behaviour was studied on MDA-MB-231 and 3T3 cells. Their colocalisation with lysosomes was assessed in different pictures (n=2 repeats) across these two cell lines.

Overall, the cellular uptake mechanism is most likely endocytic as suggested by the energy-dependence presented *vide supra*, with average Pearson's coefficients of 0.44 and 0.31 in NIH 3T3 for CPNT 9 and 10 respectively; values of 0.20 and 0.23 were found in MDA cells.

These differences were not statistically significant which could be due to the fact that this experiment might not give an accurate depiction of the process of endocytosis. The dye used for lysosomes, LysoSensor DND189, was the best of all the dyes in the green region tested and despite an optimisation of the experimental conditions (dye concentration, incubation time, etc.), the fluorescence in the green region was still found to be relatively weak. This difference in fluorescence between the two channels could have negatively affected the colocalisation studies. The slight increase in colocalisation observed for stabilised CPNT in 3T3 cells could also be due to the presence of a hydrophobic core, aiding membrane penetration (see **Figure 3-9** and **Figure B-16** in Appendix B, section B.3.6 for the confocal images acquired on MDA-MB 231).

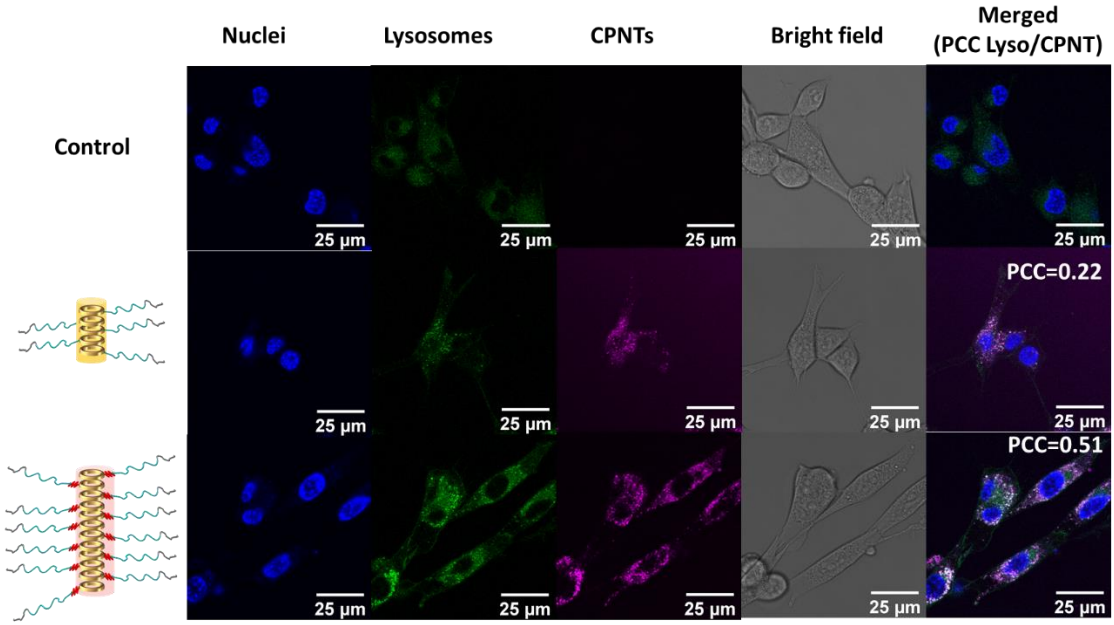

Figure 3-9: Confocal images acquired on NIH 3T3 cells on dynamic CPNT **9** (middle) and stabilised CPNT **10** (bottom). The Pearson's coefficient for the pictures shown here was calculated between the green and magenta channels and is indicated on the merge.

Channels: blue = Hoechst 33342, nucleus stain; magenta= 10% Cy5.5 CPNT **9** and **10**; green = LysoSensor DND189 green; grey = bright field; merge of blue, green and magenta with the Pearson's correlation coefficient.

3.2.5 Comparing targeting and non-targeting cyclic peptide-polymer nanotubes *in vitro*

3.2.5.1 Integrin expression in 4T1 and HUVEC cells

In order to assess the potential of our cRGDfK-labelled CPNT **11** to target the $\alpha_v\beta_3$ integrins, it was decided to work with cells that have been previously reported to overexpress them, murine breast cancer cells 4T1 and human endothelial cells from the umbilical vein (HUVEC).[45, 46] The integrin levels in these cell lines was determined by flow cytometry, in parallel to cellular uptake assays. A difference can be observed after treatment with FITC-labelled $\alpha_v\beta_3$ antibodies for the HUVEC cell line, which was expected; as for 4T1 cells, no difference was noticed (**Figure 3-10**). In terms of distribution of the fluorescence across cells, it can be noted that there is no change whatsoever for 4T1 cells upon treatment with the antibody whilst distribution in HUVEC still shows that a majority of the cells do not show fluorescence with a smaller second population with the label, in comparison to the control (**Figure B-14** and **Figure B-15**). These differences, compared to previously reported work, could be explained by the detachment method used. TryPLE solution, a milder alternative to trypsin, was used in this case for both cell lines, as EDTA treatment was not sufficient to obtain single cell suspensions for 4T1 cells. Previous work from Brown *et al.* showed that depending on the amount of trypsin utilised and the number of passages, integrin levels could significantly vary for HUVEC cells; the same likely being true for adherent 4T1 cells.[47]

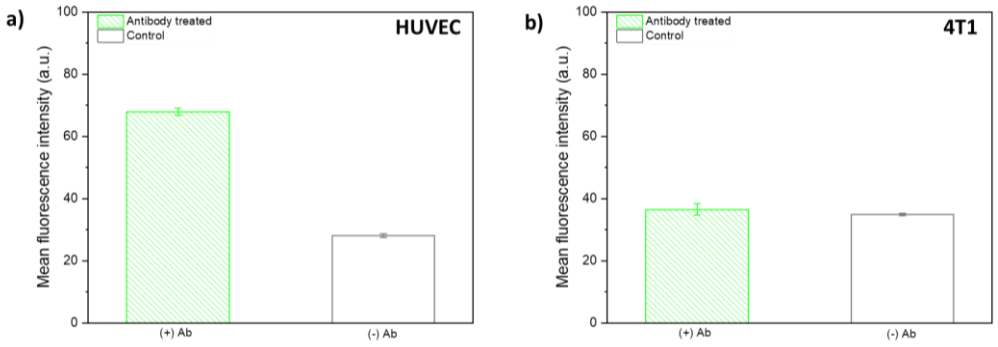

Figure 3-10: Expression of the $\alpha_v\beta_3$ integrin measured by flow cytometry using a FITC-labelled MAB1976X anti-αvβ3 antibody on a) human umbilical vein endothelial cells (HUVEC) and in b) murine breast cancer cells (4T1). Bar-charts represent the geometric mean of the fluorescence intensity, the error bars are the standard deviation for a measurement in triplicate.

3.2.5.2 Flow cytometry

The fluorescent samples were prepared, using 30% wt. of cRGDfK containing CPNT **11** in the mix, to ensure a 5% mol. content in cRGDfK in the final self-assembly. The cellular uptake in HUVEC and 4T1 cells was evaluated for three sets of conditions: 15 min at 37°C, 2 h at 37°C and finally 2 h at 37°C after a 30 min pre-treatment with an excess of cRGDfK to ensure saturation of the RGD-binding site on $\alpha_v\beta_3$ integrins.

The incubation times were shortened to be able to observe the difference over time (under the assumption that promoted uptake is faster). A slight increase of cellular uptake for cells treated with cRGDfK containing CPNT could be noticed for HUVEC cells at 2 h (factor of 1.16), compared to CPNT without the targeting motif; when pre-treating the cells with free cRGDfK, this difference was not observed, suggesting some contribution of integrin receptor-mediated endocytosis in the uptake of cRGDfK CPNT. This is reflected by a slight shift of the distribution upon pre-treatment with cRGDfK; the populations remain, however, extremely similar which shows that the effect is minimal (see **Figure B-15**). No remarkable changes upon treatment with cRGDfK-containing CPNT occurred in the case of 4T1 cells (**Figure 3-11**); this is most likely because of the lack of $\alpha_v\beta_3$ on the surface of 4T1 cells as discussed in paragraph 3.2.5.1. Those results were reflected on the distribution profiles as it can be observed on **Figure B-14**.

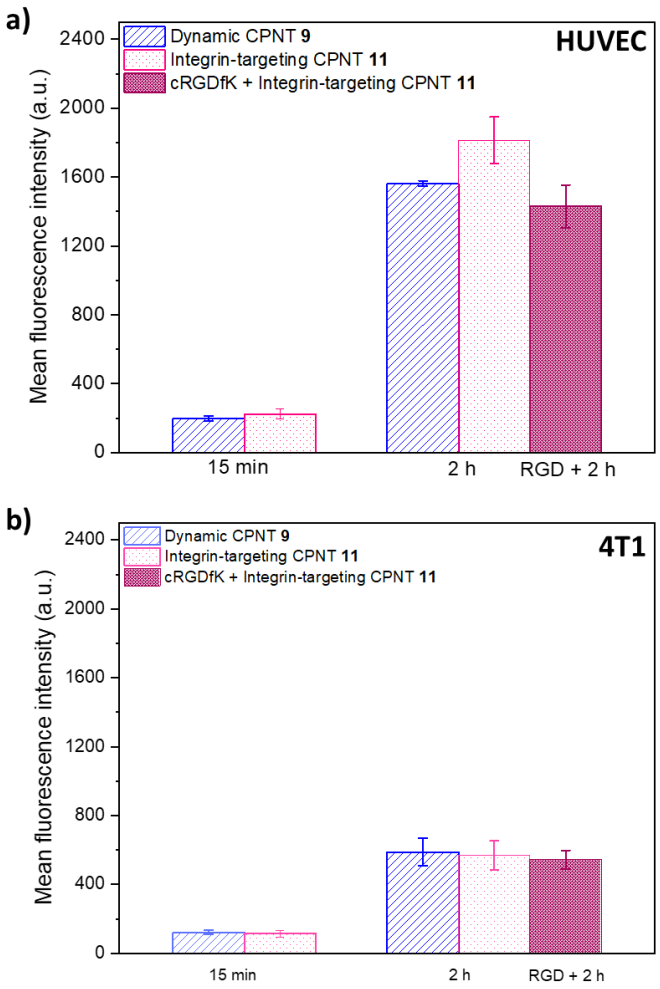

Figure 3-11: Mean cellular fluorescence intensity at 15 min, 2 h and after treatment with an excess of cRGDfK (1.5 mM) in (a) human umbilical vein endothelial cells (HUVEC) and in (b) murine breast cancer cells (4T1), as measured by flow cytometry, of Cy5.5-labelles non-integrin-targeting CPNT **9** and integrin-targeting CPNT **11** mixes (10% Cy5.5 labelled CPNT). Bar-charts represent the geometric mean of the fluorescence intensity, the error bars are the standard deviation for a measurement in triplicate.

It is worth mentioning that despite this lack of targeting-dependent response in flow cytometry experiments on 4T1 cells, tumour models *in vivo* might still present differences in uptake as the cells will not be subjected to treatment with detachment agents. Previous work from Eldar-Boock *et al.*, looking at the antitumoural activity of paclitaxel polymer conjugates labelled with integrin targeting peptide E-c(RGDfK)$_2$, demonstrated a clear decrease in 4T1 tumour size, compared to non-targeting materials, suggesting the potential of a tumour model based on 4T1 cells.[43, 44]

3.2.6 Pharmacokinetic properties and biodistribution of stabilised and dynamic cyclic peptide-polymer nanotubes

3.2.6.1 Pharmacokinetic study

The CPNT mixes containing the ^{14}C-ethanolamine radiolabels (**9*** and **10***) were prepared following the mix-and-match approach described *vide supra* (see **Scheme 3-1**). DMSO was dialysed out of the solutions to avoid any negative influence on the animal wellbeing, as well as on the self-assembly process. The radiolabelled materials (700 μL) were slowly injected to Sprague Dawley rats through the jugular vein cannula that had been inserted 12 h prior to the beginning of pharmacokinetic measurements. The doses were of 6.4 (solution of dynamic CPNT **9**) and 5.1 (for stabilised CPNT **10**) mg/kg, ensuring a radioactive dose of approximately 0.70 μCi.[17] The monitoring of the kinetics of circulation in blood was performed over 24 h by radioactive counting of the plasma samples collected *via* the carotid artery cannula (ca. 200 μL of blood was taken at each time point). Pharmacokinetic (PK) profiles were plotted relative to the initial dose; PK parameters were calculated using the non-compartmental (NC) analysis with intravenous bolus injection model from the PKSolver Microsoft Excel add-in.[48, 49]

The dynamic CPNT profile was first compared to data previously acquired on CP-poly(NAM)$_2$; despite the minor disparity in self-assembly length (35 nm for CP-poly(NAM)$_2$, 10 nm for **9**), the overall pharmacokinetic profiles were similar and were not statistically significantly different to each other. This result suggests that having two polymer chains instead of one, which would technically lead to a stealthier material, does not seem to affect the behaviour of dynamic CPNT *in vivo* (see in Appendix, **Figure B-17**).

The profiles of dynamic CPNT **9** and stabilised CPNT **10** showed clear differences for all time points after 30 min (with the exception of t = 4 h). The levels of stabilised CPNT in blood were found to be higher, reaching 30.4% of the initial dose after 24 h on average whilst there was only 5.8% of the initial dose of dynamic CPNT left at the same time point (see **Figure 3-12**).

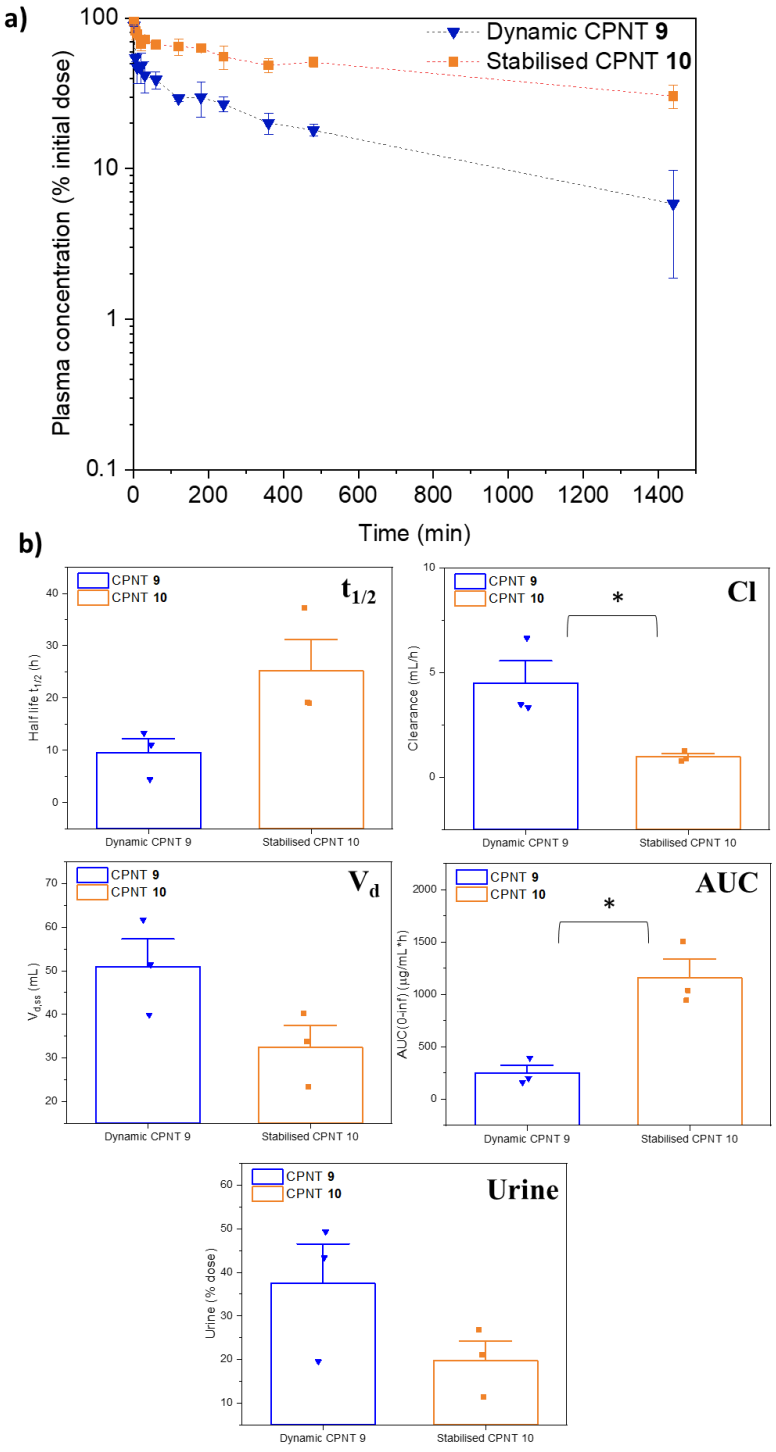

Figure 3-12: Animal studies comparing dynamic and stabilised CPNT. Error bars represent the standard deviation of the mean.

a) Pharmacokinetic profiles acquired for dynamic CPNT **9** (blue) and stabilised CPNT **10** (orange), representing the plasma concentration (% initial radioactive dose) in function of time. n=3 for CPNT **9** and n=3 for CPNT **10**.

b) Graphical representation of the pharmacokinetic parameters for CPNT **9** (blue) and **10** (orange), plotted as bar-charts with an overlap of all repeats.

The plasma exposure of stabilised CPNT **10**, which corresponds to the area under the plasma concentration curve (AUC), was higher than for dynamic CPNT. Given the inverse proportionality between this parameter and the clearance (Cl), it comes as little surprise that the clearance of CPNT **10** (0.97 ± 0.27 mL/h) is 77% lower than for CPNT **9** (4.49 ± 1.88 mL/h). This is reflected in the lower urine levels for stabilised CPNT (20%) compared to dynamic CPNT (37%), suggesting a good excretion for stabilised CPNT **10**, unlike long covalent polymer brushes that generally tend to have lower renal excretion rates.[17] The half-life ($t_{1/2}$), which corresponds to the time at which the plasma concentration reached half of the initial value, was found to be overall 2.6 times higher for stabilised CPNT. Additional replicates are necessary to confirm these trends; such results might suggest that decreased renal clearance occurs in the experiment timeframe for stabilised CPNT **10**. Similarly, it would help assessing variations of the steady-state volume of distribution (V_d), as no difference could be observed between the two compounds (see summary of the PK parameters in **Table 3-3** and a graphical representation in **Figure 3-12**).

Table 3-3: Summary of the calculated pharmacokinetic parameters obtained by NC analysis of the plasma concentration vs time profiles in rats for CPNT 9 and 10 (IV administration, dose: 6.4 and 5.1 mg/kg, mean ± SD, n = 3 rats). *: $p<0.05$ according to an unpaired Student test, using unequal variances.

	Dynamic CPNT **9**	Stabilised CPNT **10**
Half life $t_{1/2}$ (h)	9.57 ± 4.60	25.2 ± 10.4
Cl (mL/h)	4.49 ± 1.88	0.97 ± 0.27*
AUC (µg/mL*h)	251.4 ± 126	1161 ± 300*
V_d (mL)	51.0 ± 10.9	32.4 ± 8.52
Urine (%dose)	37.4 ± 15.8	19.8 ± 7.80

This propensity for longer blood circulation can be explained by the length increase for stabilised CPNT **10**, as described for self-assembling filomicelles in the literature by Discher and co-workers.[11] This observation needs, however, to be contrasted in the light of recent results obtained by Müllner *et al.* on covalent non-biodegradable cylindrical brushes, where an increase in their length seemed to lead to faster blood clearance. These differences were explained by the covalent nature of the nanoconstruct as the "steady attrition model" discussed by Discher and co-workers cannot be applied in this case.[50]

The decrease in clearance that is observed for CPNT can potentially be attributed to a better control over the dynamics of exchange and disassembly for stabilised CPNT **10**. An ideal way to validate this hypothesis would be to measure the persistent length of the self-assemblies in blood plasma at different time points, similarly to what has been described by Discher and co-workers on filomicelles.[11] Characterisation of the behaviour of CPNT (and self-assembled nanoparticles in general) in the presence of plasma proteins is, however, extremely complex. The size of the proteins is in the nanometer range, which is too close to the CPNT size to be distinguished by scattering techniques, hence why it has not been reported so far. A quick assessment of the change in molecular weight after incubation in plasma for both CPNT has been performed using SEC and scintillation counting, in order to examine the potential formation of a protein corona. In both cases, the CPNT were measured for the time point at which radioactivity levels in plasma could still be observed after dilution. The SEC chromatograms for both CPNT showed the presence of a higher molecular weight species, which is hypothesised to be CPNT interacting with a protein corona (the retention time is very similar after plasma incubation for both CPNT, see **Figure 3-13**). An incremental study of the X-ray or neutron scattering profiles in the presence of increasing amounts of protein, such as albumin, is necessary to obtain a better understanding of the biological stability of CPNT.

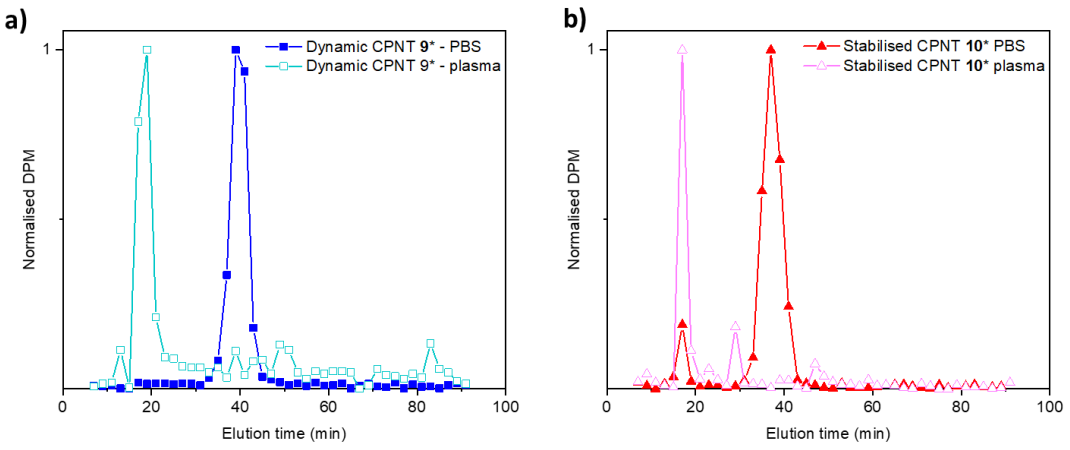

Figure 3-13: SEC chromatograms in PBS and for a specific timepoint from rat plasma for: a) radioactive dynamic CPNT **9*** (plasma at 3 h: light blue, PBS: dark blue) and b) stabilised CPNT **10*** (plasma at 6 h: pink, PBS: red).

3.2.6.2 Biodistribution study

The study of the biological fate of CPNT *in vivo* was complemented with biodistribution data for the major organs (excretion organs: liver, pancreas, kidneys, spleen and other essential organs: heart, lungs, brain) after 24 h of circulation by measuring the residual ^{14}C content in the *ex vivo* harvested tissues. **Figure 3-14** shows the percentage of injected ^{14}C dose recovered in each organ, with a cumulative % dose recovered of 12.7% for dynamic CPNT 9 and 10.4% for stabilised CPNT 10. The highest uptake was found in organs related to excretion (kidneys) and related to the mononuclear phagocyte system (MPS, liver and spleen). Dynamic CPNT **9** were mostly found in the kidney (8.6% dose) then in the liver (3.3% dose), with 4% of the kidney tissue containing radioactive material on average. This propensity for renal excretion was highlighted in previous work; high urine radioactive contents after 24 h also indicate that this pathway was favoured for dynamic CPNT.[16, 17] It is likely that the disassembly of the CPNT into small unimers, occurring alongside the formation of a negatively charged protein corona, allowed for efficient glomerular filtration and excretion by the kidneys over time. The kidney uptake was lower (2.3%) for stabilised CPNT, which are less likely to disassemble as readily, explaining the reduced renal excretion. Advances in characterisation of CPNT in complex media, such as urine or blood, could help validating this hypothesis. The partial liver accumulation is hypothesised to be due to uptake by the Kupfer cells whilst in the self-assembled state, probably directly from the first blood passages; examples in the literature show that nanocylinders have a propensity for liver uptake, most likely due to the orientation adopted when interacting with macrophages.[13, 51]. Spleen accumulation was higher for stabilised CPNT; this pattern of higher accumulation in MPS organs for structures of higher aspect ratio was also noticed for other nanocylindrical DDS,[13, 50] and could be harnessed for the development of immunogenic therapies.

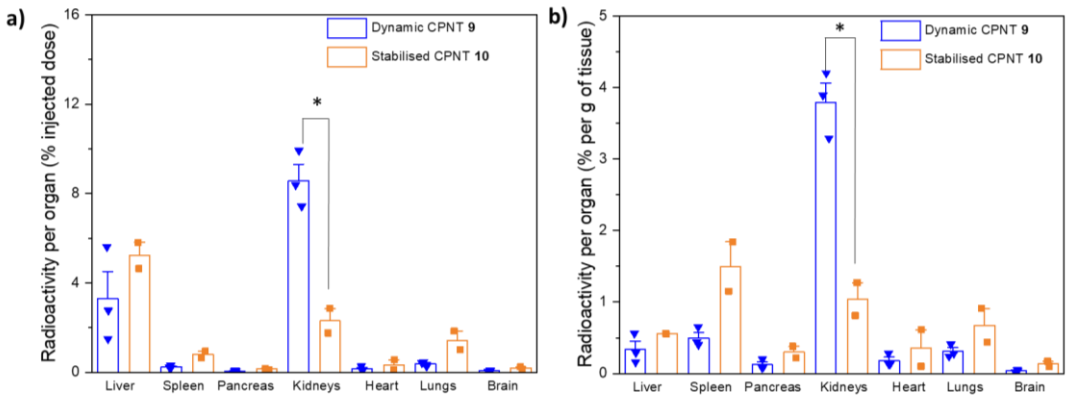

Figure 3-14: Biodistribution profiles in major organs for CPNT **9** (blue) and **10** (orange), plotted as radioactivity per organ in a) % initial dose and b) % found per g of tissue. The data was plotted as bar-charts with an overlap of all repeats. Error bars represent the standard deviation of the mean. *: $p<0.05$ according to an unpaired Student test, using unequal variances.

Higher uptake in lungs was found for stabilised CPNT **10** (see **Figure 3-14**). Structures of high aspect ratio were previously shown to have a better pulmonary accumulation due to the compatibility of their filamentous nature with the lung capillaries; long filomicelles were also compared by Discher and co-workers to *Filoviridiae* viruses capable of provoking lung infections.[11, 13] These *in vivo* results show that stabilised CPNT are promising drug carriers given their high blood persistence, balanced by a satisfactory elimination, compared to alternative systems such as cylindrical brushes.[17] Further studies are presently ongoing to determine their capability to penetrate tumours; their non-negligible cellular uptake, previously shown in 3.2.4, is encouraging and the attachment of a suitable drug is therefore being investigated.

3.2.7 Pharmacokinetic properties and biodistribution of targeting and non-targeting cyclic peptide-polymer nanotubes

3.2.7.1 Pharmacokinetic study

Another pharmacokinetic study was run in parallel to the experiment described in 3.2.6. It aimed to determine the *in vivo* effects of adding c(RGDfK), integrin-targeting moieties, onto dynamic CPNT **9**. Following the same experimental protocol as in section 3.2.6, the PK profile of a targeting CPNT **11** was established. First, significantly lower radioactivity levels were detected in the blood 3 h after injection for cRGDfK-labelled CPNT, compared to non-targeting CPNT **9**. Furthermore, the average half-life was of 5.5 h instead of 9.5 h, with an overlap of one of the repeats for CPNT **9**. The blood clearance was determined using NC analysis and found to be approximately 3.5 times higher for targeting CPNT. No difference in urine excretion at 24 h between CPNT **9** and **11** could be observed (see **Table 3-4** and **Figure 3-15**).

Table 3-4: Summary of the pharmacokinetic parameters obtained by NC analysis of the plasma concentration vs time profiles in rats for CPNT 9 and 11

	Dynamic CPNT **9**	Integrin-targeting CPNT **11**
Half life $t_{1/2}$ (h)	9.57 ± 4.60	5.49 ± 1.07
Cl (mL/h)	4.49 ± 1.88	15.6 ± 4.36*
AUC (µg/mL*h)	251.4 ± 126	96.4 ± 26.0
V_d (mL)	51.0 ± 10.9	79.4 ± 17.2
Urine (%dose)	37.4 ± 15.8	37.1 ± 3.63

This pattern suggests a faster and higher organ uptake for integrin-targeting CPNT. This effect is most likely linked to differences in biological recognition, as the amount of cRGDfK-labelled conjugate is only of 30%, unlikely to provoke a strong disruption of the self-assembly (besides, these systems are supposed to be dynamic).

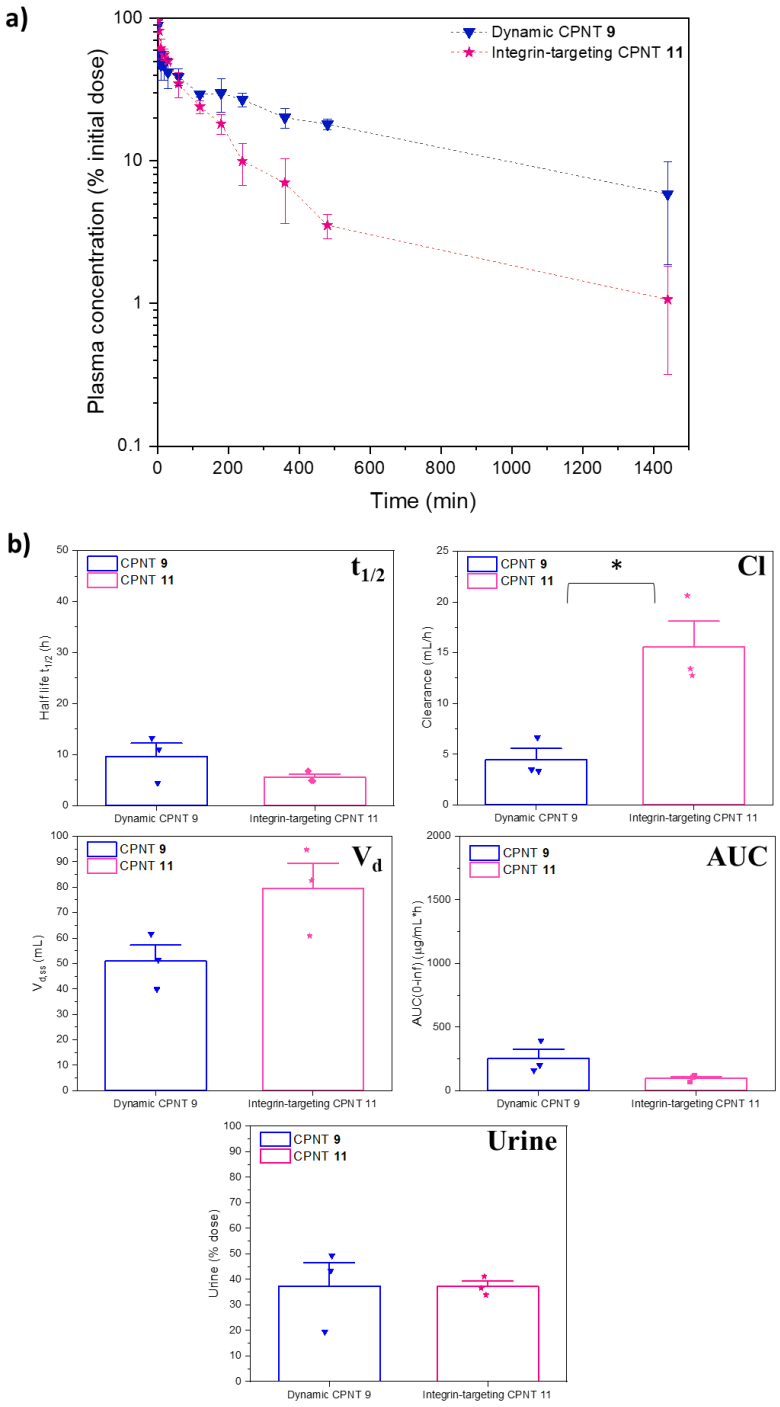

Figure 3-15: Animal studies comparing non-targeting and integrin-targeting dynamic CPNT. a) Pharmacokinetic profiles acquired for dynamic CPNT **9** (blue) and a integrin-targeting CPNT **11** (pink), representing the plasma concentration (% initial radioactive dose) in function of time. Error bars represent the standard deviation; n=3 for CPNT **9** and **11**.

b) Graphical representation of the pharmacokinetic parameters for CPNT **9** and **11**, plotted as bar-charts with an overlap of all repeats (error bars represent the standard deviation of the mean). *: $p<0.05$ according to an unpaired Student test, using unequal variances.

Previous studies directly compared the *in vivo* behaviour of drug-free nanocarriers after addition of targeting moieties.[52-55] In some instances, the presence of targeting moieties led to a higher blood clearance; these changes could be traced to higher tissue uptake by MPS organs (liver and spleen), intrinsically linked to the immune system.[54-56] Huang *et al.* observed this phenomenon for gold nanorods (50-100 nm long) decorated with antibody peptide fragments (EGFR, ATF) or the cRGDfK integrin-binding motif in healthy mice models. The blood half-life of cRGDfK gold nanorods was 25% lower than for non-targeting nanorods; this decrease was even more accentuated for the longer peptide fragments (32% for EGFR and 48% for ATF).[55] Chattopadhyay *et al.* have reported the same impact of adding targeting moieties on the pharmacokinetics of Au nanoparticles labelled with the HER-2 antibody in MDA-MB-361 (human breast cancer cells) tumour grafted mice; the half-life and tumour accumulation were effectively smaller for targeting Au nanoparticles.[54] The introduction of targeting moieties on nanoparticles, even when they are coated with a polymer for better stealth, seems to favour opsonisation and immunogenicity for nanomedicine administrated intravenously.[53, 57]

3.2.7.2 Biodistribution study

The biodistribution study performed on rats treated with integrin-targeting CPNT **11** confirmed the previous hypothesis of higher levels of uptake in MPS organs. After 24 h, the average liver and spleen uptake (in %initial dose) were found to be multiplied by a factor 3.2 and 5.4 respectively compared to non-targeting CPNT **9**. Uptake in kidneys did not change between the two samples, which matches previous observations on urine content at 24 h (see **Figure 3-16**).

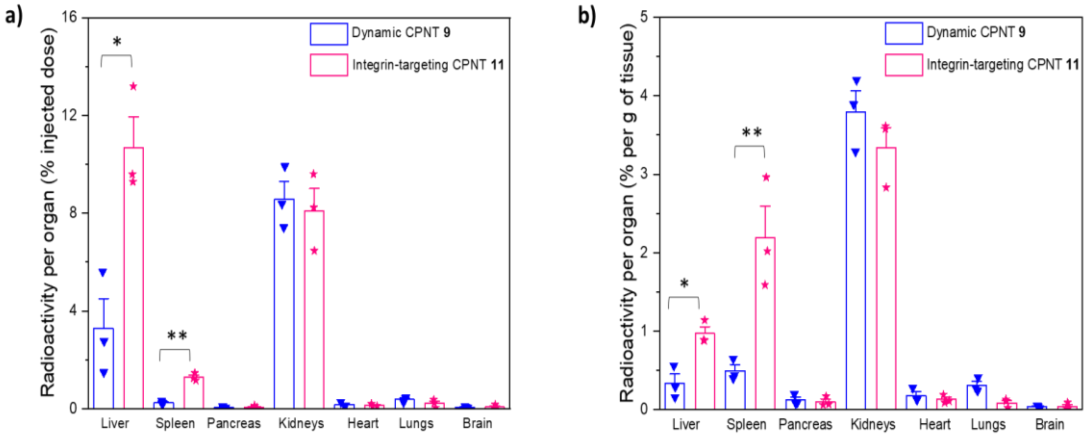

Figure 3-16: Biodistribution profiles in major organs for CPNT **9** and **11**, plotted as radioactivity per organ in a) % initial dose and b) % found per g of tissue. The data was plotted as bar-charts with an overlap of all repeats. Error bars represent the standard deviation of the mean. *, **: $p<0.05$ and $p<0.005$ according to an unpaired Student test, using unequal variances.

Such a behaviour could prove to be problematic for the use of these systems for anticancer drug delivery, as tumour uptake could be hindered. Previous studies on Au nanorods have clearly established that when liver and spleen accumulation of cRGDfK labelled systems significantly increased, tumour accumulation was divided by 2 in A549 xenograft tumour-grafted mice.[55] The MPS tissue localisation of targeting nanorods was relatively different to non-targeting systems, suggesting different uptake mechanisms.

Further insights on tumour accumulation kinetics for cRGDfK labelled polymer nanocarriers were obtained by Kunjachan *et al.* on two tumour models, CT26 (highly leaky) and BxPC3 (poorly leaky). In the poorly leaky tumour, a higher and faster uptake of integrin-targeting polymer was found after 1 h, compared to the non-targeting controls; however, this trend was reversed over time, with higher accumulation of non-targeting control in both cases after 24, 48 and 72 h in both models.[53] It should also be noted that the non-targeting control in some publications contained a non-targeting peptide fragment (e.g. cRAD) that could also result in higher opsonisation.[43, 45]

3.3 Conclusions and perspectives

Stabilised and elongated cyclic peptide-polymer nanotubes (>100 nm long), comprising of a hydrophobic poly(BA) core, were successfully synthesised and characterised; their biological relevance was studied using *in vitro* cell and *in vivo* rodent models, and subsequently compared to dynamic CPNT (10 nm long). Stabilised CPNT were found to have less propensity for cellular uptake than their dynamic counterparts in breast cancer cells and fibroblasts. A study of their behaviour *in vivo* in rats revealed that stabilised CPNT circulated for longer and had a lower clearance than their dynamic counterparts. Biodistribution profiles and evaluation of urine content after 24 h suggest lower levels of renal excretion, possibly due to a more complex or slower disassembly process for stabilised CPNT. Their high blood persistence, similar to long cylindrical polymer brushes, combined with their potential for gradual elimination over time by slowly disassembling, make stabilised CPNT promising anticancer drug delivery systems. Drug attachment should be investigated in future work, ensuring that the selected drug does not interfere significantly with CPNT solubility and self-assembly in an aqueous environment.

Dynamic integrin-targeting CPNT, containing cRGDfK peptide moieties in the polymer corona were also prepared and investigated for the first time, using a *mix-and-match* approach. Their self-assembling behaviour was found to be similar to non-targeting counterparts. As expected, a higher uptake in cells overexpressing $\alpha_v\beta_3$ integrins (HUVEC model) was observed for integrin-targeting CPNT using flow cytometry. These cRGDfK labelled CPNT had different pharmacokinetic and biodistribution profiles to non-targeting CPNT. The increase in blood clearance was linked to higher distribution of targeting CPNT into MPS organs, suggesting a better recognition by the immune system. These results show that our approach to active targeting using CPNT should be reconsidered, by employing a more holistic approach as preconized by Cheng *et al.* This approach strongly suggests to determine the most appropriate route of administration for a given molecular composition of the nanocarrier, in addition to biological timing considerations (i.e. the stage at which treatment would be the most efficient).[58] Furthermore, a better understanding of the interaction of the protein corona with CPNT systems is essential, as the corona can hinder cellular recognition as it did on transferrin-coated silica nanoparticles described by Salvati *et al.*.[59]

3.4 Experimental

3.4.1 Materials

Protected amino acids (Fmoc-D-Leu-OH, Fmoc-L-Lys(Boc)-OH, Fmoc-L-Trp(Boc)-OH, Fmoc-L-Asp(OtBu), Fmoc-L-Arg(Pbf), Fmoc-Gly, Fmoc-D-Phe) and 2-(6-Chloro-1-H-benzotriazole-1-yl)-1,1,3,3-tetramethylaminium hexafluorophosphate (HCTU) were purchased from Iris Biotech GmbH (Germany). 4-(4,6-dimethoxy-1,3,5-triazin-2-yl)-4-methyl-morpholinium tetrafluoroborate (DMTMM.BF_4) was synthesised from DMTMM.Cl (Sigma Aldrich, UK) as previously described.[60] Initiators Dimethyl 2,2'-azobis(2-methylpropionate) (V-601) and 4,4′-azobis(4-cyanovaleric acid) (ACVA) were obtained from Wako Chemicals (UK). The RAFT agent (propanoic acid)yl butyl trithiocarbonate (PABTC) was synthesised according to a procedure described in the literature.[61] 4-acryloylmorpholine (NAM), and butyl acrylate (BA), were purchased from Sigma Aldrich (UK) and were deinhibited with basic aluminium oxide prior to polymerisation reactions. N-Acryloxysuccinimide (NAS) was purchased from Fischer Scientific (UK) and used directly. Anhydrous dimethylformamide was purchased from VWR Chemicals (UK).

Cyanine 5.5 amine was purchased from Lumiprobe GmbH (Germany). Radiolabelled 14C-ethanolamine (50-60 μCi/mmol) was obtained from American Radiolabeled Chemicals (ARC, USA). The AlexaFluor488™ MAB1976-anti $\alpha_v\beta_3$ murine antibody was supplied by Merck (Australia). The Slide-A-Lyser™ cassettes used for dialysis were obtained from ThermoFisher Scientific (Australia). All other chemicals were obtained from Sigma Aldrich and used directly.

3.4.2 Characterisation techniques

3.4.2.1 Nuclear magnetic resonance

^{1}H NMR spectrum were measured using a Bruker DPX-300 or DPX-400 NMR spectrometer that operated at 300.13 and 400.05 MHz respectively. The residual solvent peaks were used as internal references. Deuterated dimethylsufoxide (d-DMSO) (δH = 7.27 ppm) was used to record spectral data for the polymers and cyclic peptide-polymer conjugates tested.

3.4.2.2 Size exclusion chromatography

Two different systems were used for SEC:

- Agilent Infinity II MDS instrument equipped with differential refractive index (DRI), viscometry (VS), dual angle light scatter (LS) and variable wavelength UV detectors. The system was equipped with 2 x PLgel Mixed D columns (300 x 7.5 mm) and a PLgel 5 μm guard column. The eluent is DMF with 5 mmol NH_4BF_4 additive.

Samples were run at 1ml/min at 50'C. Poly(methyl methacrylate) standards (Agilent EasyVials) were used for calibration between 955,000 – 550 gmol-1. Analyte samples were filtered through a nylon membrane with 0.22 μm pore size before injection. Respectively, experimental molar mass (M_n, SEC) and dispersity (Đ) values of synthesized polymers were determined by conventional PMMA calibration using Agilent GPC/SEC software.

- Monash SEC: The system was equipped with a Sephadex G25 column. Samples were run at 0.5 mL/min and fractions were collected in scintillation vials every two minutes between 5 and 95 min. The scintillation of each fraction was counted after adding UltimaGold™ scintillation liquid (3 mL).

3.4.2.3 Scintillation counting

All radioactive samples were counted on a Packard Tri-Carb 2000CA liquid scintillation analyzer (Meriden, CT) after being immersed in UltimaGold™ scintillation liquid. The program used was set to count for ^{14}C disintegration, with a 2 min run length per sample.

3.4.2.4 Zeta potential measurements

Zeta potential measurements were carried out on a Malvern Zetasizer in pure water in a DTS1070 folded capillary zeta cell at a concentration of 1 mg/mL (3 independent measurements, between 10 and 100 runs).

3.4.2.5 Small Angle X-ray Scattering (SAXS)

Small Angle X-ray scattering (SAXS) was performed by Dr Steven Huband at the University of Warwick X-ray Diffraction facility. The instrument was a 5 m Xenocs Xeuss 2.0 SAXS instrument, equipped with a micro-focus Cu Kα (λ = 1.54189 Å) source collimated with Scatterless slits with a beam diameter of 0.8 mm. The scattering was measured using a Pilatus 300k detector with a pixel size of 0.172 mm x 0.172 mm. The distance between the detector and the sample was calibrated using silver behenate ($AgC_{22}H_{43}O_2$), giving a value of 2.481 (5) m. The samples were dissolved in in PBS buffer or 5% DMSO solution in PBS buffer and transferred to a capillary. The q-range, where the scattering wave vector q is defined as ($q = \frac{4\pi}{\lambda} sin\frac{\theta}{2}$, with θ being the scattered angle, λ the incident X-rays wavelength) for all measurements was 0.0054 - 0.16 $Å^{-1}$. A radial integration of the 2D scattering profile was performed using FOXTROT software and the resulting data corrected for the absorption, sample thickness and background.[62] Finally, the scattering intensity was then rescaled to absolute intensity using glassy carbon as a standard. SAXS pattern were collected at 25°C for 4 hours.[63] The reduced data was fitted to different form factors using the SASview software package.[64] Details about the fitting parameters and the form factors employed can be found in the Appendix to this chapter (section B.2).

3.4.3 Synthesis

3.4.3.1 Cyclic peptide synthesis

The cyclic peptide **1** synthesis and characterisation is identical to the one reported in Chapter 2 (section 2.4.3.1). The synthesis of cRGDfK is detailed in Appendix B, section B.1.8.

3.4.3.2 Synthesis of poly(NAM_{42}) **2**

The PABTC CTA (40.2 mg, 0.169 mmol, 1.0 eq.), NAM (1.0 g, 7.80 mmol, 42 eq.), V601 (0.652 mg, 2.83 µmol, 0.0168 eq.) and 1,4-dioxane (1.47 mL) were added to a 20 mL glass vial. The reaction mixture was sealed with a rubber septum and degassed for 10 min with a flow of nitrogen, before being heated at 65°C for 2.5 h in an oil bath, to reach quasi-quantitative monomer conversion. The polymer was then precipitated three times in cold diethyl ether and dried in a vacuum oven at 40°C for 16 h, affording poly(NAM_{42}) **2** as a yellow-white powder (936 mg).

M_n (NMR) = 6,200 g/mol, M_n (SEC- DMF) = 6,100 g/mol, Đ = 1.07

^{1}H-NMR (300 MHz, $CDCl_3$, ppm, n = 42): 3.9 – 3.1 (8nH, (OC**H$_2$**C**H$_2$**N)$_2$), 2.8 -2.2 (1nH, CH_2C**H**C=O), 2.1 – 1.5 (2nH, C**H$_2$**CH backbone), 0.94 (t, 3H, C**H$_3$**-CH_2-CH_2-CH_2-SCS_2).

3.4.3.3 Synthesis of poly(BA_{12}-b-NAM_{42}) **3**

The PABTC CTA (155 mg, 0.650 mmol, 1.0 eq.), BA (1.0 g, 7.80 mmol, 12 eq.), V601 (2.99 mg, 13.0 µmol, 0.020 eq.) and 1,4-dioxane (1.47 mL) were added to a 20 mL glass vial. The reaction mixture was sealed with a rubber septum and degassed for 10 min with a flow of nitrogen, before being heated at 65°C for 16 h in an oil bath, to reach quasi-quantitative monomer conversion. The second monomer, NAM (3855 mg, 27 mmol, 42 eq.) was subsequently added alongside V601 (2.94 mg, 13.0 µmol, 0.020 eq.) and 1,4-dioxane (3.07 mL); the polymerisation was left to react for 3 h, to reach 98% monomer conversion. The polymer was then precipitated three times in cold diethyl ether and dried in a vacuum oven at 40°C for 16 h, affording poly(BA_{12}-*b*-NAM_{42}) **3** as a yellow-white powder (2150 mg).

M_n (NMR) = 7,700 g/mol, M_n (SEC- DMF) = 7,700 g/mol, Đ = 1.07

^{1}H-NMR (300 MHz, $CDCl_3$, ppm, n = 42 (NAM), n'=12 (BA)): 4.1 – 3.9 (2n'H CH_3-CH_2-CH_2-C**H$_2$**-O from BA), 3.9 – 3.1 (8nH, (OC**H$_2$**C**H$_2$**N)$_2$), 2.8 – 2.2 (1nH, 1n'H, CH_2C**H**C=O), 2.1 – 1.5 (2nH and 2n'H, C**H$_2$**CH backbone + 2n'H CH_3-CH_2-C**H$_2$**-CH_2-O from BA), 1.5 – 1.3 (2n'H CH_3-C**H$_2$**-CH_2-CH_2-O from BA), 1.0 – 0.89, (3n'H C**H$_3$**-CH_2-CH_2-CH_2-O from BA+ 3H C**H3**-CH_2-CH_2-CH_2-SCS_2 from CTA).

3.4.3.4 Synthesis of CP-poly(NAM_{42}) **4**

Poly(NAM42) (93.0 mg, 15 µmol, 1.15 eq.) and HCTU (6.26 mg, 15 µmol, 1.15 eq.) were dissolved in 1 mL of DMF and left stirring for 10 min. A solution of cyclic peptide (15 mg, 13 µmol, 1.0 eq.) with NMM (4.00 mg, 40 µmol, 3.0 eq.) was prepared in DMF. This solution was added to the activated polymer, and the mixture was stirred at room temperature for 16 h. The conjugate was then precipitated in diethyl ether once then redissolved in DCM before slow addition of diethyl ether, to reach a final ratio of 60 DCM: 40 ether allowing for selective precipitation of the conjugate (and removal of the free polymer). The precipitated solid was then dried in the vacuum oven at 40°C overnight, affording CP-poly(NAM_{42}) **4** (57%, 55 mg).

M_n (NMR) = 7,300 g/mol, M_n (SEC - DMF) = 8,500 g/mol, Đ = 1.10

^{1}H-NMR (400 MHz, DMSO-d6, ppm, n = 42 (NAM)) (only indicating distinctive CP peaks):

8.3 – 7.6 (L-Trp protons), 7.3 – 6.9 (L-Trp aromatic protons), 4.6 – 4.2 (H_α, amino acids), 3.9 – 3.0 (8nH, (OC**H$_2$**C**H$_2$**N)$_2$), 2.7 – 2.3 (1nH, CH_2C**H**C=O), 1.8 – 1.3 (2nH, C**H$_2$**CH backbone), 0.87 (3H, C**H$_3$**-CH_2-CH_2-CH_2-SCS_2), 0.80 – 0.60 (D-Leu isopropyl protons).

3.4.3.5 Synthesis of CP- poly(BA_{12}-b-NAM_{42}) **5**

Poly(BA_{12}-*b*-NAM_{42}) (116 mg, 15 µmol, 1.15 eq.) and HCTU (6.26 mg, 15 µmol, 1.15 eq.) were dissolved in 1 mL of DMF and left stirring for 10 min. A solution of cyclic peptide (15 mg, 13 µmol, 1.0 eq.) with NMM (4.00 mg, 40 µmol, 3.0 eq.) was prepared in DMF. This solution was added to the activated polymer, and the mixture was stirred at room temperature for 16 h. The conjugate was then precipitated in diethyl ether once then redissolved in DCM before slow addition of diethyl ether, to reach a final ratio of 70 DCM: 30 ether allowing for selective precipitation of the conjugate (and removal of the free polymer). The precipitated solid was then dried in the vacuum oven at 40°C overnight, affording CP-poly(BA_{12}-*b*-NAM_{42})) **5** (39%, 45 mg).

M_n(NMR) = 8,800 g/mol, M_n(SEC - DMF) = 9,600 g/mol, Đ = 1.12

^{1}H-NMR (400 MHz, DMSO-d6, ppm, n = 42 (NAM), n'=12 (BA)) (only indicating distinctive CP peaks):

8.3 – 7.6 (L-Trp protons), 7.33 – 7.25+ 7.15 – 6.9 (L-Trp aromatic protons), 4.1 – 3.9 (2n'H CH_3-CH_2-CH_2-C**H$_2$**-O from BA), 3.9 – 3.0 (8nH, (OC**H$_2$**C**H$_2$**N)$_2$), 2.7 – 2.3 (1nH and 1n'H, CH_2C**H**C=O), 1.8 – 1.5 (2nH and 2n'H, C**H$_2$**CH backbone + 2n'H CH_3-CH_2-C**H$_2$**-CH_2-O from BA) 1.4 –1.2 (2n'H CH_3-C**H$_2$**-CH_2-CH_2-O from BA), 1.0 – 0.83 (3n'H C**H$_3$**-CH_2-CH_2-CH_2-O from BA+ 3H C**H$_3$**-CH_2-CH_2-CH_2-SCS_2 from CTA), 0.80 – 0.60 (D-Leu isopropyl protons).

3.4.3.6 Synthesis of CP-poly[NAM_{42}-b-(NAM_{10}-stat-NAS_{14})] **7**

The block extension was performed using a NAS:NAM ratio of 60:40, following similar procedures from the literature.[17] The macroCTA CP-poly(NAM_{42}) (55 mg, 7.60 µmol, 1.0 eq.), NAM (11.5 mg, 81.6 µmol, 11 eq.), NAS (20.7 mg, 122 µmol, 16 eq.), ACVA (0.221 mg, 0.789 µmol, 0.010 eq.) and anhydrous DMF (1.25 mL) were added to a 8 mL glass vial. An internal standard for conversion calculations, 1,3,5-trioxane (30.2 µmol), was added to the mixture. The reaction mixture was sealed with a rubber septum and degassed for 10 min with a flow of nitrogen, before being heated at 70°C for 16 h in an oil bath, to reach 85% NAS and 93% NAM conversion. The polymer was then precipitated twice in cold diethyl ether and dried in a vacuum oven at 40°C for 16 h, affording CP-poly[NAM_{42}-*b*-(NAM_{10}-*stat*-NAS_{14})] **7** as a yellow-white powder (50 mg).

M_n (NMR) = 11,000 g/mol, M_n (SEC- DMF) = 9,000 g/mol, Đ = 1.37

^{1}H-NMR (400 MHz, $CDCl_3$, ppm, n = 42, n''=14): See NMR for compound **4**, with an additional peak at 2.89 – 2.80 (4n''H, succinimide group).

3.4.3.7 Synthesis of CP-poly[BA_{12}-b-NAM_{42}-b-(NAM_{10}-stat-NAS_{14})] **8**

The block extension was performed using a NAS:NAM ratio of 60:40. The macroCTA CP-poly(BA_{12}-b-NAM42) (50 mg, 5.70 µmol, 1.0 eq.), NAM (8.67 mg, 61.4 µmol, 11 eq.), NAS (15.5 mg, 92.2 µmol, 16 eq.), ACVA (0.166 mg, 0.594 µmol, 0.010 eq.) and anhydrous DMF (0.95 mL) were added to a 8 mL glass vial. An internal standard for conversion calculations, 1,3,5-trioxane (22.8 µmol), was added to the mixture. The reaction mixture was sealed with a rubber septum and degassed for 10 min with a flow of nitrogen, before being heated at 70°C for 16 h in an oil bath, to reach 85% NAS and 93% NAM conversion. The polymer was then precipitated twice in cold diethyl ether and dried in a vacuum oven at 40°C for 16 h, affording CP-poly[BA_{12}-b-NAM_{42}-*b*-(NAM_{10}-*stat*-NAS_{14})] **8** as a yellow-white powder (45 mg).

M_n (NMR) = 12,600 g/mol, M_n (SEC- DMF) = 13,200 g/mol, Đ = 1.18

^{1}H-NMR (400 MHz, $CDCl_3$, ppm, n = 42, n'=12, n''=14): See NMR for compound **5**, with an additional peak at 2.89 – 2.80 (4n''H, succinimide group).

3.4.3.8 Summary of the polymerisation conditions

Table 3-5: Summary of the conditions used for RAFT polymerisations, to synthesise **2**, **3**, **7** and **8**.

	Monomer concentration (M)	Temperature (°C)	CTA:initiator	Conversion (%) (NMR)	Estimated cumulative livingness (%)
poly(NAM_{42}) **2**	3	65	50	98	99.8
poly(BA_{12}-*b*-NAM_{42}) **3**	3	65	50	>99	98.4
Dynamic NHS-functional CPNT **7**	0.15	70	10	NAS: 85 NAM: 93	92.3
Stabilised NHS-functional CPNT **8**	0.15	70	10	NAS: 85 NAM: 93	91

3.4.3.9 Postfunctionalisations

3.4.3.9.1 Labelling with ethanolamine (example with CP-poly[NAM_{42}-b-(NAM_{10}-stat-NAS_{14})] **9**

CP-poly[NAM_{42}-b-(NAM_{10}-stat-NAS_{14})] (40 mg, 3.61 µmol, 1 eq.), ethanolamine (2.43 mg, 39.8 µmol, 11 eq.) and DIPEA (6.10 mg, 47.0 µmol, 13 eq.) were dissolved in dry DMF (0.60 mL). The reaction mixture was left to react for 16 h before adding milliQ water (10 µL, excess) and left to stir for another 16 h. The polymer was then precipitated twice in cold diethyl ether and dried in a vacuum oven at 40°C for 16 h, affording CP-poly[NAM_{42}-*b*-(NAM_{10}-*stat*-$HEAm_{11}$-*stat*-AA_3)].

NMR: see compound **4** and check the disappearance of the succinimide peak from NAS at 2.89 – 2.80 ppm.

3.4.3.9.2 Labelling with Cy5.5 (example with CP-poly[NAM42-b-(NAM_{10}-stat-NAS_{14})]

CP-poly[NAM42-b-(NAM_{10}-stat-NAS_{14})] (5.0 mg, 0.452 µmol, 1 eq.), Cy5.5 amine (0.341 mg, 0.452 µmol, 1 eq.) and DIPEA (0.20 mg, 1.81 µmol, 4 eq.) were dissolved in dry DMF (0.30 mL). The reaction mixture was left to react for 16 h before adding ethanolamine (0.28 mg, 4.52 µmol, 10 eq.) and a supplementary amount of DIPEA (0.70 mg, 5.43 µmol, 12 eq.) and left to stir for another 16 h. MilliQ water (10 uL, excess) was subsequently added and the reaction left to stir for another 16 h. The polymer was then precipitated twice in cold diethyl ether and dried in a vacuum oven at 40°C for 16 h, affording CP-poly[NAM42-*b*-(NAM_{10}-*stat*-Cy5.5Am-*stat*-$HEAm_{10}$-*stat*-AA_3)].

NMR: see compound **5** and check the disappearance of the succinimide peak from NAS at 2.89 – 2.80 ppm.

3.4.3.9.3 Labelling with cRGDfK of CP-poly[NAM42-b-(NAM$_{10}$-stat-NAS$_{14}$)]- synthesis of an integrin targeting CP-polymer conjugate **11**

CP-poly[NAM42-b-(NAM$_{10}$-stat-NAS$_{14}$)] (7.0 mg, 0.633 µmol, 1 eq.), cRGDfK (1.53 mg, 2.54 µmol, 4 eq.) and DIPEA (0.655 mg, 5.07 µmol, 8 eq.) were dissolved in dry DMF (0.30 mL). The reaction mixture was left to react for 16 h before adding ethanolamine (0.27 mg, 4.43 µmol, 6 eq.) and a supplementary amount of DIPEA (0.737 mg, 5.70 µmol, 9 eq.) and left to stir for another 16 h. MilliQ water (10 uL, excess) was subsequently added and the reaction left to stir for another 16 h. The polymer was then precipitated twice in cold diethyl ether and dried in a vacuum oven at 40°C for 16 h. To ensure full removal of any residual cRGDfK, the sample was dissolved in water and left to dialyse against water in a 3.5 cutoff kDa Float-A-Lyser device overnight. The sample was then freeze-dried, affording CP-poly[NAM42-*b*-(NAM$_{10}$-*stat*-cRGDfKAm$_4$-*stat*-HEAm$_6$-*stat*-AA$_3$)].

NMR: see compound **4** and check the disappearance of the succinimide peak from NAS at 2.89 – 2.80 ppm and the appearance of the amino acids H_α and the D-Phe peaks (overlap with L-Trp, 7.50 – 7.15 ppm).

3.4.3.10 Radiolabelling

Prior to radiolabelling, a known amount of ^{14}C- ethanolamine solution in ethanol:water was evaporated under a constant flux of compressed air. The ^{14}C- ethanolamine residue was then redissolved in dry DMF for further use.

CP-poly[NAM_{42}-b-(NAM_{10}-stat-NAS_{14})] (3.0 mg, 0.271 µmol, 1 eq.), ^{14}C- ethanolamine (0.128 mg, 2.09 µmol, 7.7 eq.) and DIPEA (0.351 mg, 2.71 µmol, 10 eq.) were dissolved in dry DMF (0.30 mL). The reaction mixture was left to react for 16 h before adding ethanolamine (0.055 mg, 0.896 µmol, 3.3 eq.) and a supplementary amount of DIPEA (0.210 mg, 1.63 µmol, 12 eq.) and left to stir for another 16 h. MilliQ water (10 uL, excess) was subsequently added and the reaction left to stir for another 16 h. The radioactive conjugate was then precipitated twice in cold diethyl ether and left to dry at room temperature. The conjugate was then dissolved in milliQ water and ran through a PD10 column, collecting 22 fractions of ca. 400 µL. Fractions were analysed by scintillation counting, assembling the first radioactive samples and drying under a flux of compressed air, to afford the pure radioactive conjugate, as confirmed by aqueous SEC (4.6 mg).

Specific activity of CPNT **9***: 7.0 µCi/mg

A similar procedure was employed for the radiolabelling of CP-poly[BA_{12}-b-NAM42-*b*-(NAM_{10}-*stat*-NAS_{14})], with the main differences being the addition of 5% DMSO prior to purification in a PD10 column. After the PD10, the radioactive conjugate was further purified by dialysis against water in a dialysis cassette (Slide-A-Lyzer™ regenerated cellulose cassettes, 0.5-3 mL, 2 kDa Mw cut-off). The radioactive conjugate was then dried and its purity confirmed by aqueous SEC (2.0 mg).

Specific activity of CPNT **10***: 18.7 µCi/mg

3.4.4 Cellular biology

3.4.4.1 Cell culture

The following cells were all regenerated from frozen stocks available at Monash University (original source: ATCC). MDA-MB-231 HM cells (epithelial metastatic breast cells) and 4T1 (murine epithelial breast cancer cells) were grown in Dulbecco's modified Eagle's medium (DMEM) supplemented with 10% (v/v) fetal bovine serum (FBS) at 37°C in a humid 5% CO2 environment. Cells were typically passaged at 80-90% confluence with a Trypsin/EDTA solution. NIH 3T3 cells (murine fibroblasts) were grown in Dulbecco's modified Eagle's medium (DMEM) supplemented with 20% (v/v) fetal bovine serum (FBS) and penicillin-spreptomycin/Funginzone ® at 37°C in a humid 5% CO2 environment and were typically passaged at 80-90% confluence with a Trypsin/EDTA solution. HUVEC cells (human umbilical vein endothelial cells) were provided by Mr Scott Peng and were grown in F-12K Medium (ATCC) supplemented with FBS, heparin and endothelial cell growth supplement (ECGS). The cells were typically grown to 80-90% confluence at 37°C in a humid 5% CO2 environment and passaged up to P+5 after treatment with a Trypsin/EDTA solution.

3.4.4.2 Cell viability assessment on 4T1, MDA-MB 231 and NIH 3T3 (MTT assay)

Cell viability of the two CP-polymer conjugates was tested on 4T1, MDA-MB 231 and NIH 3T3 cells using the MTT assay, measuring mitochondrial activity. The cells were seeded at a density of 5,000 cells per well in a transparent Greiner 96 well-plate (150 µL of the appropriate culture media) and incubated for 24 h prior to adding the compounds. Solutions of the CP-polymer conjugates in cell culture media were prepared by serial dilutions of a stock solution at 10 mg/mL in media (1.5% DMSO was first added to help solubilise the stabilised CP-diblock). The prepared solutions were added (75 µL) to the corresponding wells and left to incubate for 72 h. The MTT reagent was then added (12 mM in PBS, 10 µL) and left to incubate for 4 h. The media was subsequently removed by aspiration and DMSO (50 µL) was added to dissolve the purple crystals formed upon reaction of the MTT reagent. Absorbance at 540 nm was measured with a multi-mode microplate reader (FlexStation 3, Molecular Devices) to evaluate the cell viability by assessing the mitochondrial activity of the cells. This experiment was performed in triplicate for each cell line.

3.4.4.3 Sample preparation for fluorescent materials

The CP-polymer nanotubes solutions were prepared following mixing procedures outlined in publications highlighting the dynamics of CP-polymer nanotubes from Rho *et al.*[21, 63] The compounds (dynamic CPNT **9** or stabilised CPNT **10**) and their fluorescent Cy5.5 counterparts were weighed to obtain 10% wt. fluorescent material in the final mix. The solids (labelled and unlabelled) were dissolved in DMSO and left for 1 h. PBS was then added slowly to reach a final concentration of material of 16 mg/mL (with 5% DMSO). This solution was then used to prepare stock solutions in cell culture media at 1.6 mg/mL for use in confocal microscopy and flow cytometry experiments. As for integrin-targeting nanotubes, cRGDfK-containing conjugate (30% wt. overall) was weighed alongside the Cy5.5 conjugate (10% wt.) and the unlabelled material before following the same preparation procedure.

3.4.4.4 Confocal microscopy

For confocal microscopy, MDA-MB 231 and NIH 3T3 cells were seeded in a 10-well plate at a density of 20,000 cells per well in 200 µL of media, and allowed to grow for 24 h prior to the experiment. The cells were then treated with solutions of the Cy5.5 labelled CP-polymer nanotubes (44 µL of solutions at 1.6 mg/mL, final conc.: 0.3 mg/mL) in duplicate and were incubated for 24 h. Half of the media was removed from each well and LysoSensor Green DND 189 (36 µL at 10 µM, final concentration: 2.3 µM) was added 30 min before imaging, Hoechst 33342 (1.5 µL at 1 mg/ml, final conc.: 1 µg/mL) was then added and incubation proceeded for another 10 minutes. The cell media was removed and the cells washed once with warm phenol-red free DMEM media (with 10% FBS). The cells were left in colourless media and imaged immediately. Confocal microscopy images were taken on a Leica TCS SP8 (Carl Zeiss, Germany) at a temperature of 37°C, using a HCX PL APO 40x (NA 1.30) oil objective and sequential scanning for each channel. Excitation/Emission used for imaging are as follows: nucleus channel (405 / 415 – 467 nm), green channel for LysoSensor Green DND 189 (458 / 480 – 607 nm), Cy5.5 channel (633 / 650 -– 734 nm). The images were then processed using Fiji (scale bar and merges performed).

3.4.4.5 *Flow cytometry*

3.4.4.5.1 Comparison between dynamic and stabilised CP-polymer nanotubes.

MDA-MB 231 (200,000 cells) and NIH 3T3 (100,000 cells) were seeded in a standard transparent Greiner 24-well plate (500 µL of cell media). After a 24 h incubation, the cells were treated with the CP-polymer nanotubes solutions (75 µL at 1.6 mg/mL, final conc.: 0.3 mg/mL) under three sets of experimental conditions: 3 h at 37°C, 3 h at 4°C and 24 h at 37°C. For the experiments at 4°C, the cells were pre-incubated for 30 min at 4°C and then dosed with cold solutions. After incubation, the cell culture media was removed and the cells washed with cold PBS once.

Trypsin/EDTA solution (50 µL) was added to each well to detach the cells; 1% wt. BSA solution (200 µL) was subsequently used to transfer the cells to a 96-well plate with V-shaped bottoms. The 96-well plate was then centrifuged for 7 min at 500 g; the supernatant solution was removed for each well and the cell pellets redispersed in 200 µL of cell fixation solution (1.6% formaldehyde). Propidium iodide (PI) was added to some wells to allow for gating of the living cells population. Samples were analysed using a S100EXi flow cytometer (Stratedigm), equipped with 405, 488, 552 and 640 nm solid-state lasers. A gate narrowing the measurement to living cells was used, excluding all cells that were showing a fluorescence above 150 a.u. in the PI emission (see Appendix, sections B.3.2 and B.3.3). The number of events recorded per sample was set to 10,000 within the gate. The geometric mean fluorescence intensity in the Cy5.5 region (642/ 647-705 nm) was then extracted from each histogram using FlowJo v 8.0. Each measurement was performed in triplicate.

3.4.4.5.2 Determination of the $\alpha_v\beta_3$ integrin content in HUVEC and 4T1 cells

HUVEC (200,000 cells) and 4T1 (100,000 cells) were seeded in a standard transparent Greiner 12-well plate (500 µL of cell media). After a 24 h incubation, the cells were detached in mild conditions using a TrypLE solution and then resuspended in serum-free medium. The cells were then resuspended and incubated on ice in a PBS solution containing AlexaFluor© 488 labelled MAB1976 anti-$\alpha_v\beta_3$ integrin antibody for 30 min. The cells were subsequently centrifuged, washed with 1% BSA solution once and fixed. Samples were analysed using a S100EXi flow cytometer (Stratedigm), equipped with 405, 488, 552 and 640 nm solid-state lasers. A gate narrowing the measurement to living cells was used, excluding all cells that were showing a fluorescence above 150 a.u. in the PI emission (see Appendix, sections B.3.4 and B.3.5). The number of events recorded per sample was set to 10,000 within the gate. The geometric mean fluorescence intensity in the AlexaFluor 488 region (488/ 500-560 nm) was then extracted from each histogram using FlowJo v 8.0. Each measurement was performed in triplicate.

3.4.4.5.3 Comparison between targeting and non-targeting CP-polymer nanotubes.

HUVEC (200,000 cells) were seeded in a 12-well plate; 4T1 (100,000 cells) were seeded in a standard transparent Greiner 24-well plate (500 µL of cell media). After a 24 h incubation, the cells were treated with targeting and non-targeting CP-polymer nanotubes solutions (75 µL at 1.6 mg/mL, final conc.: 0.3 mg/mL) under three sets of experimental conditions: 15 min at 37°C, 2 h at 37°C and 2 h at 37°C following a 30 min pre-treatment with excess cRGDfK (2 mM) to saturate the integrin receptors. After incubation, the cell culture media was removed and the cells washed with cold PBS once. Trypsin/EDTA solution (50 µL) was added to each well to detach the cells; 1% wt. BSA solution (200 µL) was subsequently used to transfer the cells to a 96-well plate with V-shaped bottoms.

The 96-well plate was then centrifuged for 7 min at 500 g; the supernatant solution was removed for each well and the cell pellets redispersed in 200 µL of cell fixation solution (1.6% formaldehyde). Propidium iodide (PI) was added to some wells to allow for gating of the living cells population. Samples were analysed using a S100EXi flow cytometer (Stratedigm), equipped with 405, 488, 552 and 640 nm solid-state lasers.

A gate narrowing the measurement to living cells was used, excluding all cells that were showing a fluorescence above 150 a.u. in the PI emission (see Appendix). The number of events recorded per sample was set to 10,000 within the gate. The geometric mean fluorescence intensity in the Cy5.5 region (642/ 647-705 nm) was then extracted from each histogram using FlowJo v 8.0. Each measurement was performed in triplicate.

3.4.5 Pharmacokinetics and biodistribution studies

3.4.5.1 Animals

All animal experiments carried out in this work were approved by the Monash Institute of Pharmaceutical Sciences Animal Ethics Committee, Monash University, Parkville, VIC. Male Sprague Dawley rats (250-350 g) were provided by the Monash Animal Research Platform husbandry (Clayton campus). Animals were transported to the Parkville campus and left to acclimatize for seven days before use for i*n vivo* studies. Animal were maintained on a 12 h light/dark cycle at all times.

3.4.5.2 Sample preparation

The CP-polymer nanotubes solutions were prepared following mixing procedures outlined in publications highlighting the dynamics of CP-polymer nanotubes from Rho *et al.*[23, 65] Stock solutions of radioactive CP-diblock (746 µCi/mL) and CP-pNAM (709 µCi/mL) were prepared in DMSO. The compounds (dynamic CPNT **9** and stabilised CPNT **10**) were weighed and dissolved in DMSO. The radioactive solutions were added in order to obtain 3.5% and 8% wt. radioactive material in the final mix (corresponding to 4 µCi for these solutions, with a total volume of DMSO of 100 µL). The solutions were left to stabilise for 1 h. PBS (1.9 mL) was then added slowly to reach radioactive concentrations of material of 2 µCi/mL (with 5% DMSO). The solutions were dialysed against Phosphate Buffer Saline (PBS) in dialysis cassettes (Slide-A-Lyzer™ regenerated cellulose cassettes, 0.5-3 mL, 2 kDa Mw cut-off) to remove the DMSO prior to injection. Samples were then filtered through a 0.45 µm diameter Nylon filter and their radioactivity measured *via* scintillation counting prior to injection.

3.4.5.3 Pharmacokinetic study protocol

Cannulations: A day prior to the compound administration, rats were anaesthesised in an isoflurane (2-5%) induction chamber and cannulas (polyethylene tubing 0.96 x 0.58 mm, Paton Scientific, Victor Harbour, Australia) were surgically inserted into the right jugular vein and carotid artery, to facilitate dose injection and blood sample collection respectively.

The rats were then moved to individual metabolic cages (to allow separate collection of urine and feces) and allowed to recover overnight prior to dosing. The procedure followed was previously described by Larnaudie *et al.*[16] Each animal was fasted up to 14 h prior to and up to 8 h after administration of the IV dose with water provided *ad libitum*. The surgery was performed by Dr. Estelle Suys and Erny Sagita (Monash University).

Dose administration and blood sampling: Samples were prepared according to the method described *vide supra*. Pre-injection (blank) blood samples were collected from the carotid artery. The compound solutions (700 µL, 0.7 µCi) were injected as a slow bolus intravenous injection *via* the jugular cannula, at doses of 5.1 and 6.4 mg/kg for stabilised and dynamic/targeting nanotubes respectively. The cannula was subsequently flushed with heparinised saline solution (500 µL) to ensure complete infusion of the dose.

Blood samples (200 µL) were taken over 24 h, at the following time points: 1, 5, 10, 20, 30, 60, 120, 180, 240, 360, 480 and 1440 min after dose administration. The samples were placed in Eppendorf tubes filled with 10 IU of heparin and centrifuged for 5 min at 3,500 g. Plasma (50 µL) was collected for each time point and transferred to scintillation vials containing Ultima Gold scintillation liquid (4 mL). The samples radioactivity was counted on a Packard Tri-Carb 2000CA liquid scintillation analyzer (Meriden, CT). Each compound was tested on three rats, with the exception of stabilised CPNT **10** (the third injection was unsuccessful).

Data processing: The pharmacokinetic parameters were calculated from the profiles using the Microsoft Excel software PKSOLVER add-in (model: Non Compartmental Analysis after Intravenous Bolus/linear trapezoidal method). The half life ($t_{1/2}$ in h), the area under the curve or plasma exposure (AUC_{0-t} in µg/mL*h), the volume of distribution (V_d in mL) and the clearance (Cl in mL/h) were determined and averaged over the repeats performed.

Statistical analysis (stabilised vs dynamic): The statistical analysis for the comparison of each PK parameter between the two samples (dynamic CPNT **9** and stabilised CPNT **10**) was performed using an unpaired Student test with the Welch correction, accounting for heteroscedasticity of the variance (n=3 for dynamic CPNT **9** and n=3 for stabilised CPNT **10**). The same statistical test was used to compare each timepoint plasma concentration between samples. The p-value for significance was set at 0.05, following usual standards for significance (95% confidence interval).

Statistical analysis (integrin-targeting study): The same statistical analysis was performed for the study comparing integrin-targeting compounds and their non-targeting counterparts.

3.4.5.4 SEC analysis of radioactive CPNT in plasma (plasma stability study)

Radioactive plasma samples were taken from the pharmacokinetic studies mentioned above and were run on the aqueous SEC. Briefly, the plasma from two or three rats (at a given time point and for a given compound) were mixed and diluted in PBS by a factor 2. The diluted sample was then filtered through a 0.45 µm Nylon filter before injection on the SEC.

3.4.5.5 Biodistribution

After completion of the pharmacokinetic study (24 h after injection), animals were exsanguinated by cardiac puncture (to minimise the presence of residual blood in organs) under isoflurane (2-5% v/v) and humanely killed by injection of a lethal dose of sodium pentobarbital (via the jugular vein cannula). The following organs were then immediately harvested: liver, spleen, pancreas, heart, kidneys, lungs and brain and rinsed with PBS. The organ samples were homogenised in MilliQ water (5 mL) using a gentle MACS Dissociator (Milteny Biotech). Tissue homogenates for each organ were split into six scintillation vials, three of which were spiked with a known dose of radioactive ^{14}C-ethanolamine for processing efficiency calculations; all samples were treated with Solvable (2 mL) and incubated at 60°C overnight to facilitate tissue digestion. Hydrogen peroxide (200 µl, 30% w/v) was added once the samples had cooled down to room temperature, followed by Ultima Gold™ scintillation liquid (10 mL). Samples were vortexed before storage at 4°C in the dark, without agitation, for at least 24 h prior to scintillation counting. Blank organs were also treated following the same procedure to determine the organ background signal. After being stored at 4°C in the dark for 24 h, all samples were counted on a Packard Tri-Carb 2000CA liquid scintillation analyzer (Meriden, CT). The processing efficiency for each organ, was calculated using equation (1), to account for any losses of radioactivity in the procedure detailed above:

$$(1)\ efficiency = \frac{spiked\ tissue\ dpm - tissue\ dpm}{spike\ solution\ dpm}$$

The first term of this equation is the difference between the number of desintegrations per minute (dpm) counted for the spiked tissue and the one for unspiked tissue (both mass-corrected). This is then divided by known activityfor the amount of spike solution added. The efficiency value determined was then used to calculate the real ^{14}C content in the tissue samples, as shown in equation (2):

$$tissue\ dpm\ corr = \frac{tissue\ dpm}{efficiency}$$

The organ total radioactive content was finally determined by accounting for the organ mass measured before processing. Organ collection was performed with the help of Dr. Joaquin Sanchis Martinez and Erny Sagita.

Urine collection: Urine samples were first collected prior to compound administration (blank) in a pre-weighed 50 mL centrifuge cube connected to the metabolic cage. Another tube was immediately used after administration and the urine was collected over 24 h (with an intermediate reading at 6 h). Urine samples (50 µL) were then transferred to scintillation vials containing Ultima Gold scintillation liquid (4 mL). The samples radioactivity was counted on a Packard Tri-Carb 2000CA liquid scintillation analyzer (Meriden, CT).

Statistical analysis (stabilised vs dynamic): The statistical analysis for the comparison of each organ radioactive content between the two samples (dynamic CPNT **9** and stabilised CPNT **10**) was performed using an unpaired Student test with the Welch correction, accounting for heteroscedasticity of the variance (n=3 for dynamic CPNT **9** and n=2 for stabilised CPNT **10**). A comparison between all organs for a given CP-polymer nanotube sample was also performed using an ANOVA analysis accounting for heteroscedasticity, followed by a Games-Howell post-hoc test. The p-value for significance was set to 0.05, following usual standards for significance (95% confidence interval).

Statistical analysis (integrin-targeting study): The same statistical analysis was performed for the study comparing integrin-targeting compounds and their non-targeting counterparts.

3.5 References for Chapter 3

1. A. S. Hoffman, *Journal of Controlled Release*, 2008, **132**, 153.
2. S. Senapati, A. K. Mahanta, S. Kumar and P. Maiti, *Signal Transduction and Targeted Therapy*, 2018, **3**, 7.
3. M. Björnmalm, K. J. Thurecht, M. Michael, A. M. Scott and F. Caruso, *ACS Nano*, 2017, **11**, 9594.
4. P. Jain, R. S. Pawar, R. S. Pandey, J. Madan, S. Pawar, P. K. Lakshmi and M. S. Sudheesh, *Biotechnology Advances*, 2017, **35**, 889.
5. N. Bertrand and J.-C. Leroux, *Journal of Controlled Release*, 2012, **161**, 152.
6. R. Cai and C. Chen, *Advanced Materials*, 2019, **31**, 1805740.
7. P. C. Ke, S. Lin, W. J. Parak, T. P. Davis and F. Caruso, *ACS Nano*, 2017, **11**, 11773.
8. J. Y. Oh, H. S. Kim, L. Palanikumar, E. M. Go, B. Jana, S. A. Park, H. Y. Kim, K. Kim, J. K. Seo, S. K. Kwak, *et al.*, *Nature Communications*, 2018, **9**, 4548.
9. J. Lazarovits, S. Sindhwani, A. J. Tavares, Y. Zhang, F. Song, J. Audet, J. R. Krieger, A. M. Syed, B. Stordy and W. C. W. Chan, *ACS Nano*, 2019, **13**, 8023.
10. S. Cai, K. Vijayan, D. Cheng, E. M. Lima and D. E. Discher, *Pharmaceutical Research*, 2007, **24**, 2099.
11. Y. Geng, P. Dalhaimer, S. Cai, R. Tsai, M. Tewari, T. Minko and D. E. Discher, *Nature Nanotechnology*, 2007, **2**, 249.
12. D. A. Christian, S. Cai, O. B. Garbuzenko, T. Harada, A. L. Zajac, T. Minko and D. E. Discher, *Molecular Pharmaceutics*, 2009, **6**, 1343.
13. S. Kaga, N. P. Truong, L. Esser, D. Senyschyn, A. Sanyal, R. Sanyal, J. F. Quinn, T. P. Davis, L. M. Kaminskas and M. R. Whittaker, *Biomacromolecules*, 2017, **18**, 3963.
14. B. M. Blunden , R. Chapman, M. Danial, H. Lu, K. A. Jolliffe, S. Perrier and M. H. Stenzel, *Chemistry – A European Journal*, 2014, **20**, 12745.
15. S. C. Larnaudie, J. C. Brendel, I. Romero-Canelón, C. Sanchez-Cano, S. Catrouillet, J. Sanchis, J. P. C. Coverdale, J.-I. Song, A. Habtemariam, P. J. Sadler, *et al.*, *Biomacromolecules*, 2018, **19**, 239.
16. S. C. Larnaudie, J. Sanchis, T.-H. Nguyen, R. Peltier, S. Catrouillet, J. C. Brendel, C. J. H. Porter, K. A. Jolliffe and S. Perrier, *Biomaterials*, 2018, **178**, 570.
17. A. Kerr, PhD thesis, University of Warwick, 2019.
18. S. C. Larnaudie, J. Sanchis, T.-H. Nguyen, R. Peltier, S. Catrouillet, J. C. Brendel, C. J. H. Porter, K. A. Jolliffe and S. Perrier, *Biomaterials*, 2018.
19. J. Fang, H. Nakamura and H. Maeda, *Advanced drug delivery reviews*, 2011, **63**, 136.
20. Y. Matsumura and H. Maeda, *Cancer Research*, 1986, **46**, 6387.
21. J. K. Tee, L. X. Yip, E. S. Tan, S. Santitewagun, A. Prasath, P. C. Ke, H. K. Ho and D. T. Leong, *Chemical Society Reviews*, 2019, **48**, 5381.
22. S. Sindhwani, A. M. Syed, J. Ngai, B. R. Kingston, L. Maiorino, J. Rothschild, P. MacMillan, Y. Zhang, N. U. Rajesh, T. Hoang, *et al.*, *Nature Materials*, 2020, **19**, 566.
23. J. Y. Rho, H. Cox, E. D. H. Mansfield, S. H. Ellacott, R. Peltier, J. C. Brendel, M. Hartlieb, T. A. Waigh and S. Perrier, *Nature Communications*, 2019, **10**, 4708.
24. G. Farahavar, S. S. Abolmaali, N. Gholijani and F. Nejatollahi, *Biomaterials Science*, 2019, **7**, 4000.
25. A. J. Sivaram, A. Wardiana, C. B. Howard, S. M. Mahler and K. J. Thurecht, *Advanced Healthcare Materials*, 2018, **7**, 1700607.
26. E. Dalle Vedove, G. Costabile and O. M. Merkel, *Advanced Healthcare Materials*, 2018, **7**, 1701398.
27. E. C. Calvaresi and P. J. Hergenrother, *Chemical Science*, 2013, **4**, 2319.

28. J. Zhao, H. Lu, P. Xiao and M. H. Stenzel, *ACS Applied Materials & Interfaces*, 2016, **8**, 16622.
29. J. Zhao, H. Lu, Y. Yao, S. Ganda and M. H. Stenzel, *Journal of Materials Chemistry B*, 2018, **6**, 4223.
30. P. Dalhaimer, A. J. Engler, R. Parthasarathy and D. E. Discher, *Biomacromolecules*, 2004, **5**, 1714.
31. G. Russell-Jones, K. McTavish, J. McEwan, J. Rice and D. Nowotnik, *Journal of Inorganic Biochemistry*, 2004, **98**, 1625.
32. S. A. Kularatne and P. S. Low, in *Cancer Nanotechnology: Methods and Protocols*, eds. S. R. Grobmyer and B. M. Moudgil, Humana Press, Totowa, NJ, 2010, pp. 249.
33. M. Ahmed, *Biomaterials Science*, 2017, **5**, 2188.
34. C. J. Avraamides, B. Garmy-Susini and J. A. Varner, *Nature Reviews Cancer*, 2008, **8**, 604.
35. P. Brooks, R. Clark and D. Cheresh, *Science*, 1994, **264**, 569.
36. T. G. Kapp, F. Rechenmacher, S. Neubauer, O. V. Maltsev, E. A. Cavalcanti-Adam, R. Zarka, U. Reuning, J. Notni, H.-J. Wester, C. Mas-Moruno, *et al.*, *Scientific Reports*, 2017, **7**, 39805.
37. F. D'Agosto, M.-T. Charreyre, L. Veron, M.-F. Llauro and C. Pichot, *Macromolecular Chemistry and Physics*, 2001, **202**, 1689.
38. K. Xiao, Y. Li, J. Luo, J. S. Lee, W. Xiao, A. M. Gonik, R. G. Agarwal and K. S. Lam, *Biomaterials*, 2011, **32**, 3435.
39. Y. Xue, L. Tao, Y. Zhou, J. Liu, B. Yu, S. Long, S. Huang and F. Yu, *Advanced Engineering Materials*, 2018, **20**, 1701151.
40. T. R. Barlow, PhD thesis, University of Warwick, 2017.
41. A. Z. Cardoso, L. L. E. Mears, B. N. Cattoz, P. C. Griffiths, R. Schweins and D. J. Adams, *Soft Matter*, 2016, **12**, 3612.
42. T. Mosmann, *Journal of Immunological Methods*, 1983, **65**, 55.
43. A. Eldar-Boock, K. Miller, J. Sanchis, R. Lupu, M. J. Vicent and R. Satchi-Fainaro, *Biomaterials*, 2011, **32**, 3862.
44. A. Eldar-Boock, R. Blau, C. Ryppa, H. Baabur-Cohen, A. Many, M. J. Vicent, F. Kratz, J. Sanchis and R. Satchi-Fainaro, *Journal of Drug Targeting*, 2017, **25**, 829.
45. D. G. Vartak, B.-S. Lee and R. A. Gemeinhart, *Molecular Pharmaceutics*, 2009, **6**, 1856.
46. E. K. Sloan, N. Pouliot, K. L. Stanley, J. Chia, J. M. Moseley, D. K. Hards and R. L. Anderson, *Breast Cancer Research*, 2006, **8**, R20.
47. M. A. Brown, C. S. Wallace, C. C. Anamelechi, E. Clermont, W. M. Reichert and G. A. Truskey, *Biomaterials*, 2007, **28**, 3928.
48. E. B. Nakashima, L.Z., *Journal of Pharmacokinetics and Biopharmaceutics*, 1989, **17**, 673.
49. Y. Zhang, M. Huo, J. Zhou and S. Xie, *Computer Methods and Programs in Biomedicine*, 2010, **99**, 306.
50. M. Müllner, S. J. Dodds, T.-H. Nguyen, D. Senyschyn, C. J. H. Porter, B. J. Boyd and F. Caruso, *ACS Nano*, 2015, **9**, 1294.
51. P. Decuzzi, B. Godin, T. Tanaka, S. Y. Lee, C. Chiappini, X. Liu and M. Ferrari, *Journal of Controlled Release*, 2010, **141**, 320.
52. Z. Chen, J. Deng, Y. Zhao and T. Tao, *Int J Nanomedicine*, 2012, **7**, 3803.
53. S. Kunjachan, R. Pola, F. Gremse, B. Theek, J. Ehling, D. Moeckel, B. Hermanns-Sachweh, M. Pechar, K. Ulbrich, W. E. Hennink, *et al.*, *Nano Letters*, 2014, **14**, 972.
54. N. Chattopadhyay, H. Fonge, Z. Cai, D. Scollard, E. Lechtman, S. J. Done, J.-P. Pignol and R. M. Reilly, *Molecular Pharmaceutics*, 2012, **9**, 2168.
55. X. Huang, X. Peng, Y. Wang, Y. Wang, D. M. Shin, M. A. El-Sayed and S. Nie, *ACS Nano*, 2010, **4**, 5887.
56. K. M. McNeeley, A. Annapragada and R. V. Bellamkonda, *Nanotechnology*, 2007, **18**, 385101.

57. T. Lammers, F. Kiessling, W. E. Hennink and G. Storm, *Journal of Controlled Release*, 2012, **161**, 175.
58. C. J. Cheng, G. T. Tietjen, J. K. Saucier-Sawyer and W. M. Saltzman, *Nature Reviews Drug Discovery*, 2015, **14**, 239.
59. A. Salvati, A. S. Pitek, M. P. Monopoli, K. Prapainop, F. B. Bombelli, D. R. Hristov, P. M. Kelly, C. Åberg, E. Mahon and K. A. Dawson, *Nature Nanotechnology*, 2013, **8**, 137.
60. S. A. Raw, *Tetrahedron Letters*, 2009, **50**, 946.
61. L. Martin, R. Peltier, A. Kuroki, J. S. Town and S. Perrier, *Biomacromolecules*, 2018, **19**, 3190.
62. www.synchrotron-soleil.fr/en/beamlines/swing.
63. F. Zhang, J. Ilavsky, G. G. Long, J. P. G. Quintana, A. J. Allen and P. R. Jemian, *Metallurgical and Materials Transactions A*, 2010, **41**, 1151.
64. www.sasview.org.
65. J. Y. Rho, J. C. Brendel, L. R. MacFarlane, E. D. H. Mansfield, R. Peltier, S. Rogers, M. Hartlieb and S. Perrier, *Advanced Functional Materials*, 2018, **28**, 1704569.

Chapter 4

Understanding the Membrane Interaction of Cyclic Peptide-Polymer Nanotubes with Model Lipid Bilayers

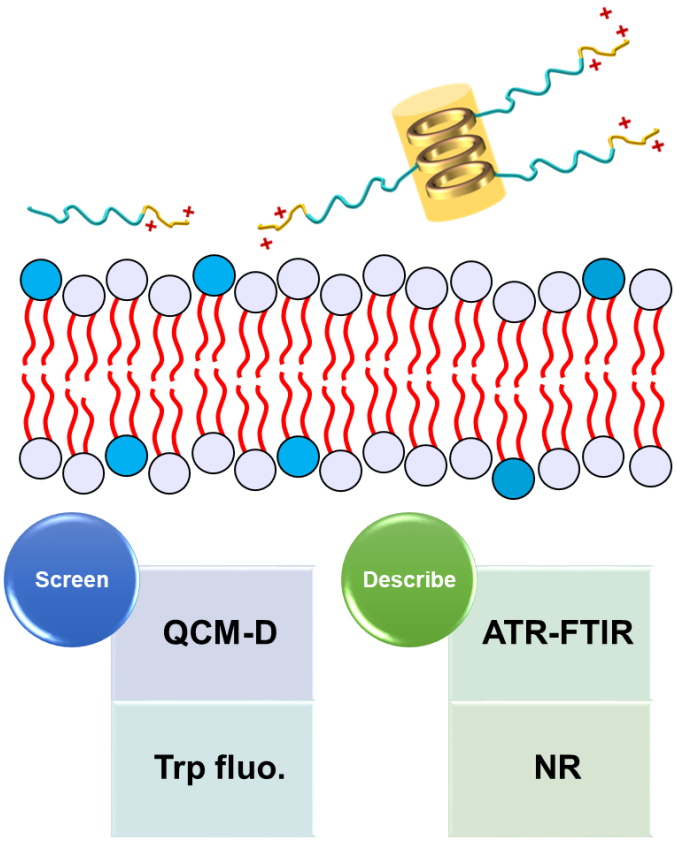

Chapter 4: The script for the model used to fit the neutron reflectivity data was written by Dr. Stephen C.L. Hall, who also performed the ATR-FTIR spectroscopy experiments at ISIS-Neutron Muon Source and one of the QCM presented. Antibacterial assays were performed by Dr Agnes Kuroki and Ramon Garcia-Maset (University of Warwick).

4.1 Introduction

Biological membranes are present in all type of cells, be it prokaryotic (e.g.: bacteria, archea, etc.) or eukaryotic (e.g.: plant and mammalian cells, fungi) organisms. The cellular membrane is an essential component of the cell, acting as a responsive interface in constant communication with its external environment and safeguarding the integrity of the organism.[1] It is composed of a complex molecular network combining lipids, arranged in bilayers, with proteins and sugars. Singer and Nicolson described this structure in 1972 and developed the "fluid mosaic model", which remains the standard employed by biologists.[2, 3] The membrane composition and architecture is strongly dependent on the cell type (eukaryotic cell, Gram-positive and Gram-negative bacteria, etc.) and important differences exist in the biomolecular interaction between cells and macromolecular objects such as nanoparticles.

Understanding the nature of the interaction of nanoparticles with the cellular membrane is essential when considering biological applications. For instance, the predominant cellular uptake phenomenon for nanoparticles in mammalian cells is endocytosis, as mentioned in Chapter 2 and 3. Certain design parameters of nanoparticles, such as surface functionality, shape and charge can influence the preferred cellular uptake mechanism.[4, 5] Non-endocytic cellular uptake pathways, such as direct translocation, have been reported. For instance, nanoparticle shape can influence passive membrane penetration, as it was shown by Hinde *et al*, with higher levels of penetration for rod and worm-like nanoparticles compared to other polymer nanoparticles of different morphologies formed by Polymerisation Induced Self-Assembly (PISA, refer to Chapter 1 for more details).[6] The addition of lysine or arginine-rich cell-penetrating peptides (e.g. TAT peptide, penetratin, etc.), able to disrupt cellular membranes, was found to lead to accelerated nanoparticle cellular uptake and was linked to some level of direct translocation.[7, 8] Divita and co-workers reported that by complexing siRNA with amphipathic peptide CADY, small nanoparticles could be formed and used to obtain high levels of intracellular delivery of siRNA. The mechanism of uptake was elucidated and found to rely primarily on direct translocation, without leading to any decrease in cellular viability, which is a common concern for membrane interacting nanomaterials.[9, 10]

Given their ability to avoid normal endocytic pathways and directly translocate into cells, such systems are garnering interest in order to limit entrapment of drug in the endo-lysosomal system. Additional insights on nanoparticle endosomal escape can be found in a recent review by Selby *et al.* where current strategies to engineer nanoparticles able to avoid treatment by the endo-lysosomal system are detailed (pH responsiveness, lipid-mediated membrane fusion, drug-induced escape, peptide-mediated escape).[11]

The study of membrane interactions is also important in the search for new antimicrobial treatment. Antibiotic resistance is one of the main challenges faced by modern societies, with an estimated 2.4 million deaths around the world in the next thirty years due to resistant micro-organisms.[12, 13] Different approaches have been adopted to face this challenge: small molecules,[14] peptides,[15] phage therapy,[16] antimicrobial polymers[17] and antimicrobial nanoparticles (as antibiotic drug carrier or with an intrinsic antimicrobial activity).[18, 19] Antimicrobial polymer nanoparticles, either formed by polymer self-assembly or star polymers, have recently garnered interest given their potential for multivalency (e.g.: clusters of charged moieties), encapsulation of antibiotic agents and the possibility to access different morphologies which may boost their antimicrobial efficacy. The polymers employed were designed taking inspiration from existing antimicrobial peptides, containing both hydrophobic moieties and cationic charges.[19] Yao *et al.* developed nanoparticles of different morphology based on the self-assembly of cross-linked diblock copolymers of quaternised poly(2-(dimethylamino)ethylmethacrylate)-block-poly(3-(triethoxysilyl)propyl methacrylate) (poly(DMAEMA-*b*-PTEPM)); they found that the MIC (minimum inhibitory concentration) was lower for cylinders than for sheets, outperforming the activity of free poly(DMAEMA).[20] Current polymer nanoparticles face similar challenges to those faced by antimicrobial peptides, such as selectively targeting bacterial membranes without damaging mammalian cell membranes. Additional data is necessary concerning the *in vivo* behaviour of antimicrobial polymer nanoparticles, as positive charges encourage the formation of substantial protein coronas, leading to higher immunogenicity.[21, 22]

Among existing membrane-interacting systems, self-assembling cyclic octapeptides (CP), comprising of D- and L- α amino acids, have recently garnered interest. As previously discussed in Chapter 1 (paragraph 1.3.2), CP are able to interact with lipid bilayers and were shown to be of interest for antibacterial and antiviral applications.[23-26] The CP-bilayer interaction was found to depend on the hydrophilicity of the amino acids and required the CP to be capable of self-assembly *via* hydrogen bonding.[26]

An in-depth characterisation of the interaction of cyclo[(L-Trp-D-Leu)$_3$- L -Gln- D -Leu] with dimyristoyl phosphatidylcholine (DMPC) was performed by Kim *et al.* in 1998 using infrared (IR) spectroscopy; the CP was found to be orientated perpendicularly to the lipid bilayer, thus confirming membrane interaction and highlighting a potential use of CP as transmembrane channels.[27]

The formation of transmembrane channels through a lipid bilayer was later modelled using coarse grained molecular dynamics simulation by Fu *et al.*, who determined the influence of the peptide sequence and of the extent of self-assembly (or oligomeric state) in this process.[28]

The exact nature of the interaction at stake in the case of cyclic peptide-polymer nanotubes (CPNT) is yet to be determined. Danial *et al.* demonstrated that CPNT with different polymer coronas interact differently, depending on the lipophilicity of the polymer chains; increasing the hydrophobicity of the polymer chains led to higher release of 5(6)-carboxyfluorescein from Large Unilamellar Vesicles (LUVs) made from egg phosphatidylcholine (EggPC); the leakage from calcein or 5(6)-carboxyfluorescein was used to infer the structures of the pores formed (barrel-stave/carpet-like and unimeric channels respectively).[29] Another similar study, based on EggPC vesicle dye leakage assays, showed that hydrophobic Janus CPNT, comprising of one poly(styrene) (PS) chain and one poly(butyl acrylate) chain (poly(BA)), could undergo phase separation within a lipid bilayer.[30] Hartlieb *et al.* recently reported the membrane disrupting potential of redox responsive CPNT based on poly(2-ethyl-2-oxazoline) linked through a disulfide bond. Calcein-entrapped vesicles made from phosphatidylethanolamine (PE) and phosphatidylglycerol (PG) were used to mimic the plasma membrane of *E. Coli.* bacteria. The combination of the responsive CPNT and reducing agent 1,4-dithiothreitol (DTT) allowed for cleavage of the polymer group thus favouring the interaction between the regenerated CP and the lipid bilayer.[31] Tubisomes made from the secondary self-assembly of amphiphilic Janus CPNT were found to give a similar response on calcein-entrapped 1-palmitoyl-2-oleoyl-sn-glycero-3-phosphocholine (POPC) vesicles. A qualitative study performed using confocal microscopy, looking at the differences in uptake of lysosomal dyes and of calcein release, showed that CPNT tubisomes seem to compromise the integrity of the lysosomal compartment.[32]

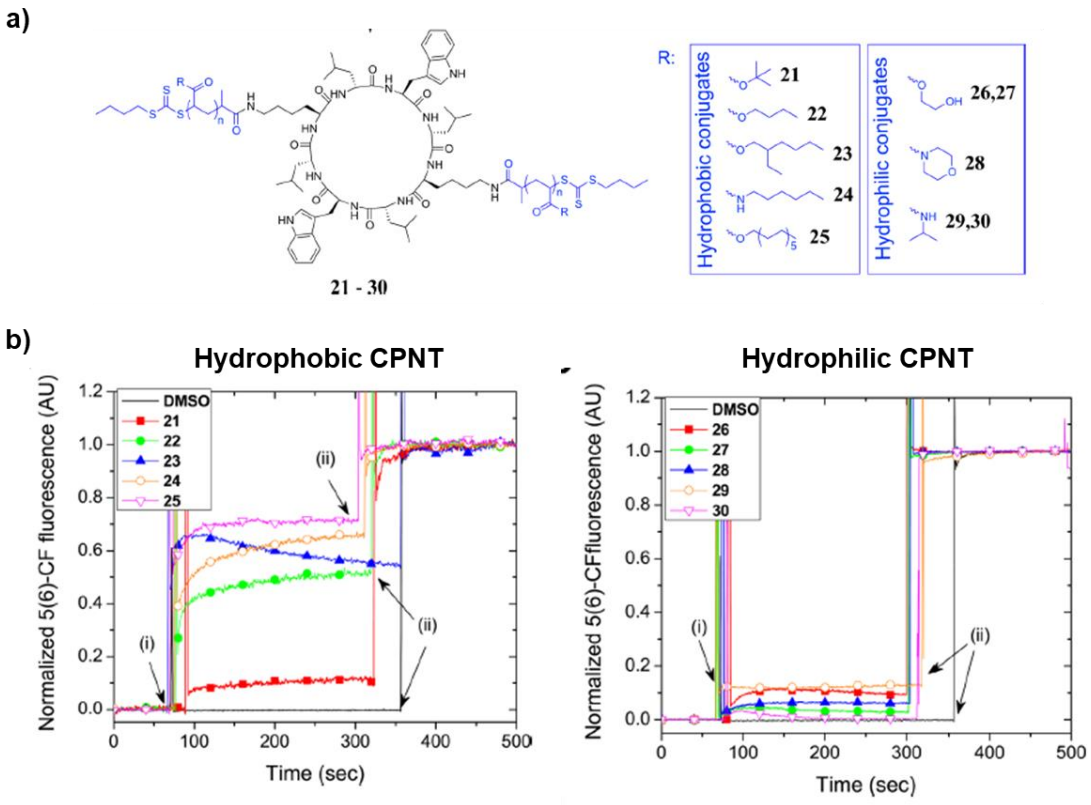

Figure 4-1: Interaction of CPNT of varying hydrophilicity with 5-carboxyfluorescein-entrapped Egg PC vesicles, as described by Danial *et al.*[29] a) Representation of the CPNT considered in the study (hydrophobic polymer: 21-25, hydrophilic: 26-30). b) Evolution of 5-carboxyfluorescein fluorescence intensity in the used buffer after treating dye-entrapped Egg PC vesicles with i) CPNT (or DMSO control) and ii) Triton solution (detergent to ensure full recovery of the dye). Hydrophobic CPNT are represented on the left side whilst hydrophilic CPNT interactions are displayed on right side. An increase after treatment with i) was considered to be an interaction.

These studies established the potential of CPNT for membrane interactions; however, the exact nature of this interaction is yet to be characterised, vesicle dye leakage assays remaining mostly qualitative (besides the relative fragility of dye-encapsulated vesicles).[33] The contribution of each component of cyclic peptide-polymer conjugate to this interaction remains unclear, especially the nature of the physical and chemical interactions involved. Moreover, the impact of having charges on the polymer corona of the CPNT on the interaction with lipid bilayers still needs to be explored as cationic charges are essential components of usual antimicrobial peptide and polymer systems.[15, 17]

Herein, we report the synthesis and characterisation of a library of new water-soluble polymer and cyclic peptide-polymer conjugates, with an incremental addition of positively charged and hydrophobic moieties to the structures. The interaction of these compounds with lipid vesicles and supported lipid bilayers (SLB) was studied extensively, using complementary analytical techniques (Quartz-Crystal Microbalance with Dissipation monitoring, infrared and fluorescence spectroscopy) to assess the effect of each component; the influence of the model lipid bilayer chosen was also briefly investigated. Finally, neutron reflectivity (NR) measurements were performed to obtain a better understanding of the mode of interaction with lipid bilayers.

4.2 Results and discussion

4.2.1 Design and synthesis of cyclic peptide-polymer nanotubes for membrane interaction studies

A library of different polymers and CPNT, charged and uncharged, was designed rationally by incorporating different moieties (charged, hydrophobic) in successive order (see **Scheme 4-1**).

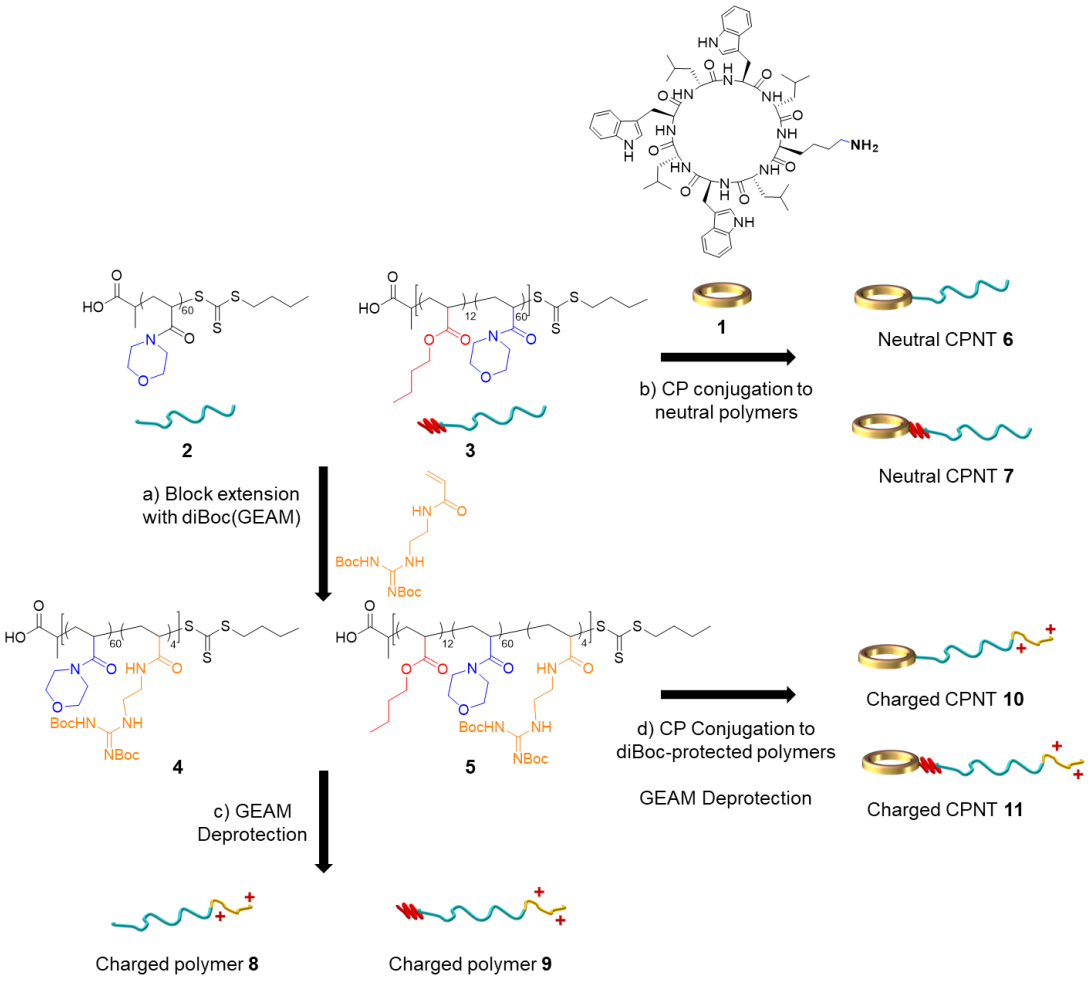

Scheme 4-1: Synthetic route employed to generate a library of charged and neutral polymers and CPNT. Polymers **2** and **3** were synthesised by RAFT polymerisation. The block extension a) with diBoc(GEAM) was performed using VA-044 (0.05 eq. to macroCTA **2** and **3**) at 46°C overnight in dioxane. Conjugation of polymers to CP **1** b) and d) was run with HCTU (1 eq. to polymer) and NMM (3 eq.) in DMF. Deprotection of the guanidinium units of GEAM were performed using a cleavage cocktail composed of TFA: TIPS: H_2O (9.5: 0.5: 0.5).

The cyclic peptide CP **1** used in this work is the same than the one in Chapter 3. Following previous work on the synthesis of stabilised and dynamic CPNT (see Chapter 3 and the work from Rho *et al.*),[34] a hydrophilic polymer poly(4-acryloylmorpholine) (poly(NAM_{60}) **2**) and a diblock copolymer comprising a poly(butyl acrylate) (poly(BA)) component, poly(BA_{12}-*b*-NAM_{60}) **3**, were synthesised using RAFT polymerisation. The RAFT agent (propanoic acid)yl butyl trithiocarbonate (PABTC) used was the same than in Chapter 2 and 3, given its versatility and its compatibility with acrylamides.[35] A good control over the polymer dispersity and over the molecular weight were obtained for polymer **2** (M_n (NMR) = 9,500 g/mol, M_n (SEC) = 9,200 g/mol, Đ = 1.09) and **3** (M_n (NMR) = 11,100 g/mol, M_n (SEC) = 12,200 g/mol, $Đ$ = 1.07). The polymers were block extended with Boc-protected monomer diBoc guanidine-ethylacrylamide (diBocGEAM), as positively charged guanidium moieties (GEAM being an arginine mimic monomer) were shown to be efficient in increasing the membrane interaction and antibacterial efficacy of polymers.[36, 37] The block extension was performed at 46°C with VA-044 overnight, to avoid any loss of control over the polymerisation as it was previously observed by Kuroki *et al.*[38] The monomer reached full conversion (4 units inserted), leading to well-defined polymers **4** (M_n (NMR) = 10,820 g/mol, M_n (SEC) = 10,600 g/mol, $Đ$ = 1.09) and **5** (M_n (NMR) = 12,800 g/mol, M_n (SEC) = 13,200 g/mol, $Đ$ = 1.09). Polymers **2** and **3** were conjugated to CP **1** using HCTU-mediated activated amide coupling; neutral hydrophilic CPNT **6** and amphiphilic CPNT **7** were obtained. NMR spectroscopy showed the presence of both D-Leu alkyl peaks and L-Trp aromatic protons as expected; a slight shift towards higher molecular weights was also observed on the SEC profiles after conjugation. Charged polymers **8** and **9** were generated by deprotecting the guanidinium moieties on intermediate polymers **4** and **5** in an acidic TFA: TIPS: H_2O cleavage cocktail; the disappearance of the Boc *tert*-butyl (*t*Bu) protons at 1.39 and 1.47 ppm on the NMR spectrum after purification, associated with an increased solubility were good indicators of the success of this reaction (see **Figure 4-2**).

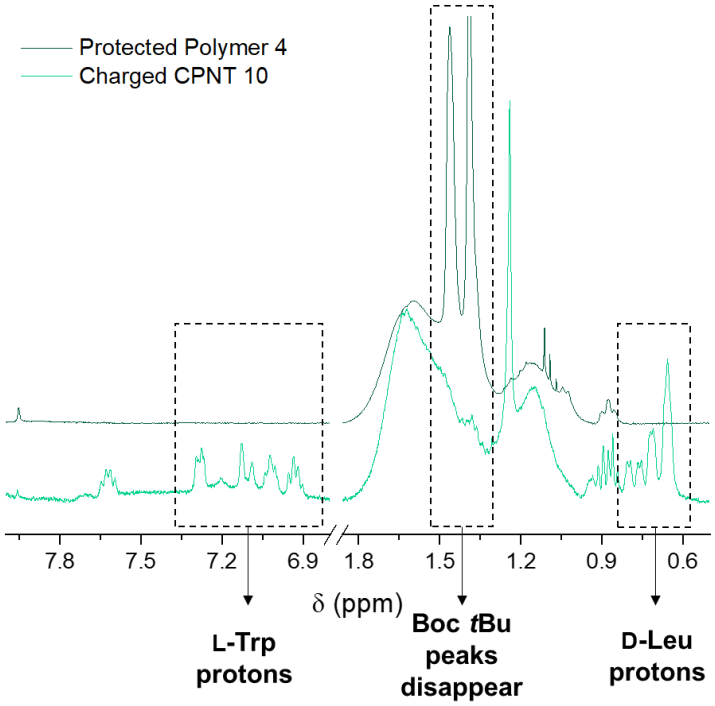

Figure 4-2: Comparison of the NMR profiles of diBoc protected polymer **4** (dark green) and charged CPNT **10** (water green). The tBu peaks from the Boc groups at 1.39 and 1.47 ppm disappear after deprotection; other peaks highlighting the presence of CP **1** are indicated (Trp, Leu). Full NMR spectra are present in Appendix C, section C.1.

The SEC profiles for the deprotected polymers showed an increase in dispersity in both cases, which was attributed to interactions of the charged moieties with the column used for analysis, given the low molecular weight tailing observed. Finally, charged hydrophilic CPNT **10** and charged amphiphilic CPNT **11** were obtained by successive conjugation of **4** and **5** using activated amide coupling and deprotection of the guanidinium moieties. NMR analysis showed the aforementioned characteristic CP peaks (D-Leu, L-Trp), as well as the disappearance of the Boc *t*Bu groups (see **Figure 4-2** and Appendix C, section C.1). Similarly to charged polymers, the dispersities of the charged conjugates were higher because of interactions with the SEC column. The higher molecular weight shoulder for charged amphiphilic CPNT **11** is probably due to partial aggregation in the system (see **Figure 4-3**). The zeta-potential of all CPNT was also compared, providing complementary data to check for the efficiency of the deprotection reaction. As expected, values corresponding to relatively neutral entities were found for CPNT **6** (8.54 ± 4.9 mV) and **7** (-1.23 ± 3.2 mV) whilst more positive values were determined for charged CPNT **10** (24.8 ± 4.3 mV) and **11** (19.4 ± 4.9 mV) (see summary in **Table 4-2**).

Table 4-1: Molecular weight (NMR, SEC) and dispersities of the polymers and CPNT synthesised.

Sample	M_n (NMR) (g/mol)	M_n (SEC) (g/mol)	$Đ$
poly(NAM_{65}) **2**	9,500	9,200	1.09
poly(BA_{12}-*b*-NAM_{65}) **3**	11,100	12,200	1.07
Boc-protected polymer **4**	10,820	10,600	1.09
Boc-protected polymer **5**	12,800	13,200	1.09

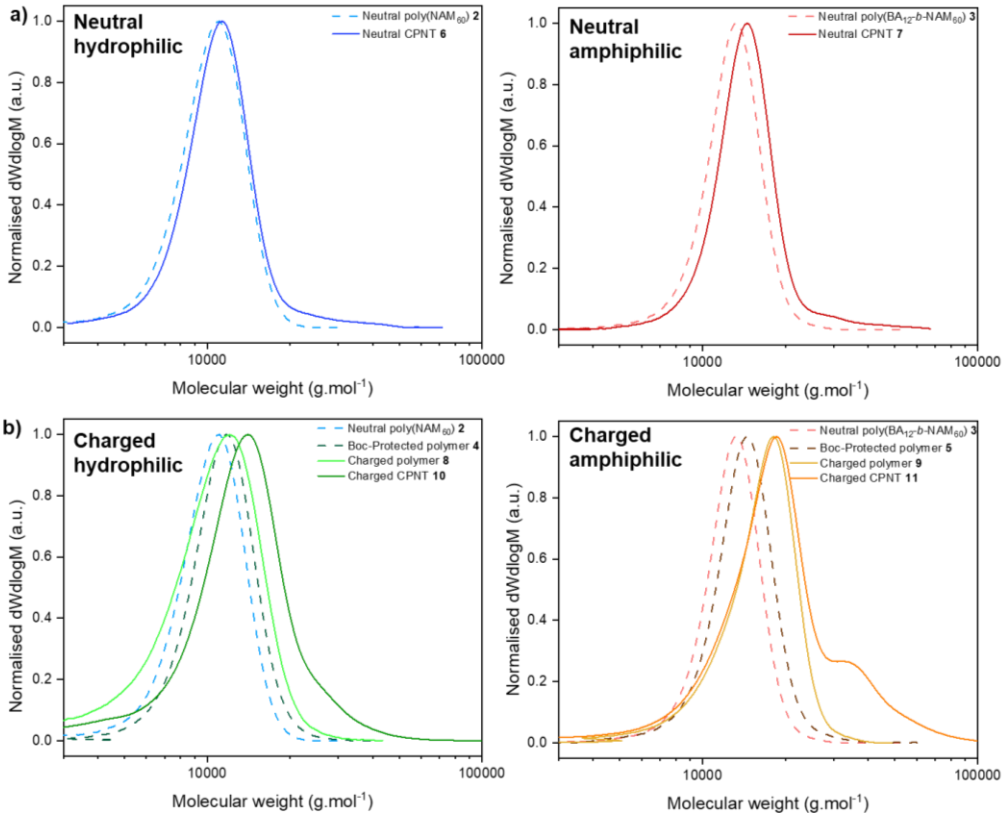

Figure 4-3: SEC chromatograms for: a) the synthesis of neutral hydrophilic polymer **2** (dashed blue) and CPNT **6** (blue) and of neutral amphiphilic polymer **3** (dashed red) and CPNT **7** (red). b) the synthesis of charged hydrophilic polymer **8** (light green) and CPNT **10** (green) and of charged amphiphilic polymer **9** (yellow) and CPNT **11** (orange). Protected polymers **4** (green dash) and **5** (brown dash) are also represented.

4.2.2 Characterisation of the self-assemblies

The CPNT self-assembly was assessed by Small Angle X-Ray Scattering (SAXS) in D_2O HEPES buffer (20 mM, pD = 7.2), to match the conditions used for neutron reflectivity studies (see 4.2.5) and to account for any potential differences in hydrogen bonding self-assembly in a deuterated solvent. The data was fit to a core-shell cylinder model within SasView as it was a better fit for structures containing poly(BA) segments, as discussed in Chapter 3 (section 3.1.3).[39] In D_2O HEPES buffer, it was found that neutral CPNT **6** and **7** fitted well to the core-shell cylinder model and were both relatively short nanotubes (9.8 and 8.3 nm respectively); their shell thickness corresponded to what was expected for the polymer lengths employed, according to previous results (see Chapter 2 and 3). Amphiphilic CPNT **7** was fitted considering the core to be solely constituted of the CP and the corona being the diblock copolymer as the data did not fit as well when adding a poly(BA) contribution to the core. Amphiphilic CPNT **7** did not form self-assemblies as long as the stabilised CPNT mentioned in Chapter 3, which was attributed to the different hydrophilic polymer corona length (60 NAM units versus 42 for previously studied stabilised CPNT). This result suggests that a very fine balance between hydrophobic content, surface charge and steric considerations needs to be found to obtain elongated structures. The impact on the dynamic nature of the self-assembly process for such shorter diblock copolymer-based CPNT remains unstudied.

Positively charged CPNT **10** and **11** were fit to the same core-shell cylinder model, with again better fits in the high q region for amphiphilic CPNT **11** when considering the CP alone as the core. As expected, charged hydrophilic CPNT **10** was found to be slightly shorter (6.8 nm) than its neutral counterpart (9.8 nm); a slight increase at low q could suggest aggregation, characteristic of charged structures but more datapoints in this area are necessary to validate this hypothesis.[40] Charged amphiphilic CPNT **11** was longer than all previous architectures (21.3 nm); a power law contribution could not be identified from the combined fitting therefore the data is only represented with the core-shell cylinder fits (for a summary of the SAXS data, refer to **Table 4-2** and **Figure 4-4** and to Appendix C, **Table C-1** for the fit parameters). The presence of longer CPNT in solution in that case was expected, as the presence of hydrophobic groups stabilised the charged self-assemblies.

Table 4-2: Summary of the CPNT characteristics obtained by acquiring SAXS profiles in D_2O HEPES buffer (5 mg/mL) and zeta-potential in water (1 mg/mL) for pure CPNT **6**, **7**, **10** and **11,** using the core-shell (CS) cylinder model**.** The CPNT width was defined as the diameter of the core combined with the shell thickness.

	Neutral CPNT **6**	Neutral CPNT **7**	Charged CPNT **10**	Charged CPNT **11**
Fit	CS cylinder	CS cylinder	CS cylinder	CS cylinder
Length (nm)	9.8	8.3	6.8	21
Width* (nm)	5.7	7.6	5.3	8.2
Aspect ratio	1.7	1.1	1.3	2.6
Zeta-Potential (mV)	8.54 ± 4.9	-1.23 ± 3.2	24.8 ± 4.3	19.4 ± 4.9

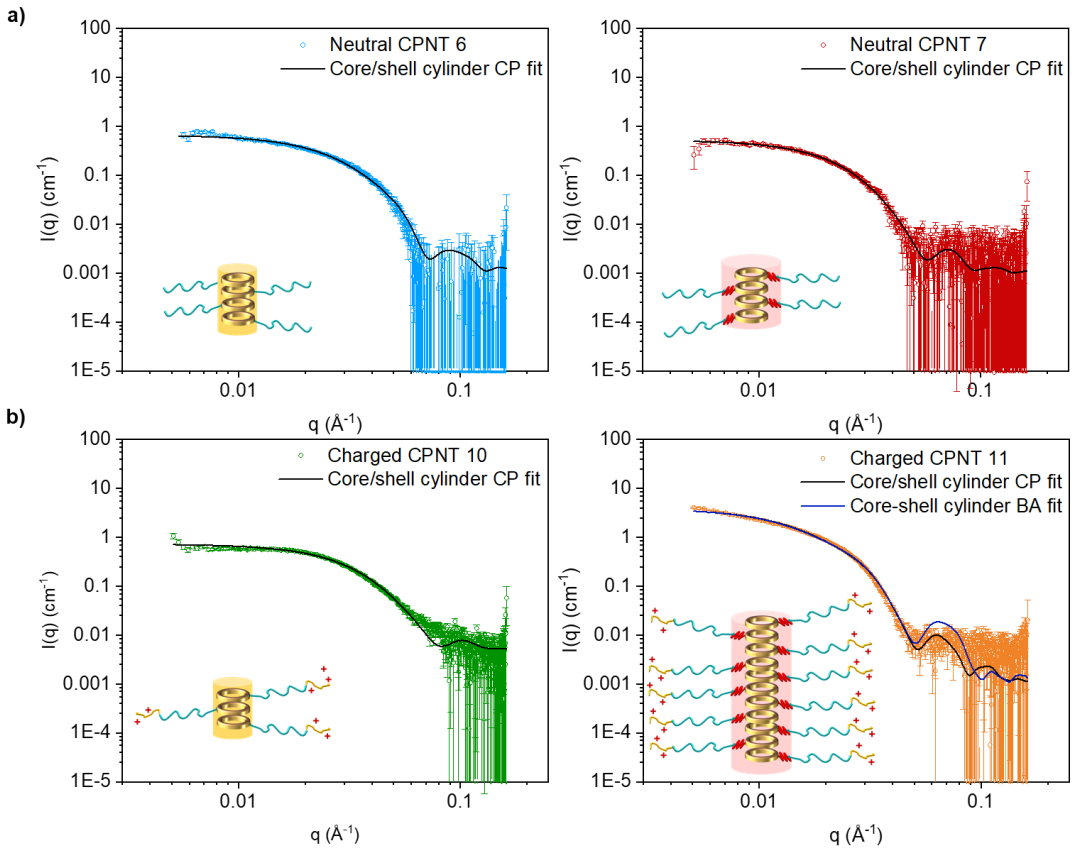

Figure 4-4: SAXS profiles for pure solutions of a) neutral CPNT **6** (blue) and **7** (red) and b) charged CPNT **10** (green) and **11** (orange) and in D_2O HEPES buffer. Hollow circles are used for the data plots, fits are plotted as lines; error bars are statistical.

4.2.3 Assessment of the lipid bilayer interaction with Quartz Crystal Microbalance with Dissipation Monitoring (QCM-D)

4.2.3.1 Model lipid bilayer and QCM-D

The interaction of the different polymers and CPNT with biological membranes was investigated using solid-supported lipid bilayers (SLB) models formed by vesicle fusion. Although biological membranes are much more complex than phospholipids alone, SLB models are robust and have shown to generate reproducible data. Unlike dye-encapsulated vesicles which are prone to dye leaking and for which encapsulation can be challenging, there is less uncertainty related to the extent of the interaction measured on SLB models.[33, 41] The SLB model employed in this study relied on the fusion of unilamellar vesicles once flushed over an appropriate substrate (silicon dioxide SiO_2 here). This method allows for a facile bilayer deposition and mostly leads to the generation of symmetric lipid bilayers composition between the two leaflets when using mixtures of lipids (examples of asymmetric bilayers were also reported, as discussed in section 4.2.5.1). Given its accessibility and relative versatility, SLB formation by vesicle fusion is an ideal model for both exploratory screening studies and to deconvolute the role of individual components. Other more complex SLB models are capable of recreating the asymmetry existing in natural cellular membranes, using Langmuir-Blodgett and Langmuir-Schaeffer deposition techniques or more advanced methods (*e.g.* lipid tethering to the substrate, floating bilayers, etc.), as reviewed by Clifton *et al.*[41] As this membrane interaction study is relatively novel, it was preferred to use a more accessible model SLB (using vesicle fusion).

Quartz-Crystal Microbalance with Dissipation Monitoring (QCM-D) is a sensitive method to screen for interaction of nanoparticles with lipid bilayers, as demonstrated by its growing traction among biomolecular scientists.[42] It can also be employed to elucidate complex biochemical mechanisms. For example, it was used to study the formation of protein corona on amyloid polypeptides; [40] similarly QCM-D helped elucidating the parameters influencing the phospholipid export by a protein, showing again the true versatility of this technique.[41] Variations of mass adsorbed onto a substrate can be extracted by QCM-D by measuring the frequency oscillation changes of a resonant piezoelectric single quartz crystal using the Sauerbrey equation and visco-elastic modelling. The energy dissipation can also be measured, providing information on the viscoelastic properties of films formed at a given interface.

4.2.3.2 Effect of the lipid composition on the CPNT-bilayer interaction

QCM-D was first used to determine the effect of variations in lipid composition in the studied SLB on the interaction with an interacting polymer or CPNT. The QCM-D experiment is divided in multiple steps that have been summarised on **Figure 4-5**.

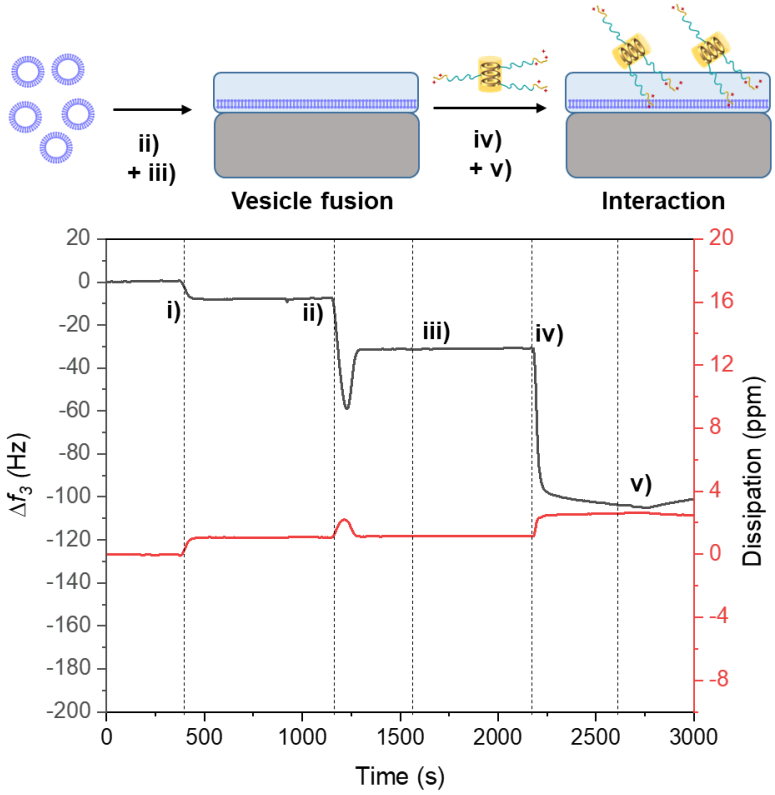

Figure 4-5: The different steps of the assessment of the interaction strength between polymers and CPNT with lipid bilayers by QCM-D. i) Initial equilibration with water and buffer; ii) Lipid bilayer formation by vesicle fusion, followed by iii) Flushing with buffer to remove any unfused vesicles; iv) Compound injection and v) Buffer wash, to evaluate the strength and stability of the interaction between the bilayer and the compound.

Initially, a study was performed to establish a behavioural pattern in relationship with the amount of free negative charges present in the bilayer. The initial bilayer was formed of the zwitterionic DMPC lipid, mostly present in mammalian cells. Other lipids with one (1,2-Dimyristoyl-sn-glycero-3-phosphorylglycerol or DMPG) or two (1,3-bis(sn-3'-phosphatidyl)-sn-glycerol or cardiolipin CL) negatively charged phosphate head groups were incorporated in different ratios in a mixture with DMPC, with the hypothesis that increasing the charge density on the surface of the lipid bilayer would lead to increased electrostatic interaction with charged CPNT. The different lipid bilayers compositions are represented in **Scheme 4-2**. The transition temperature of 14:0 DMPG (Tm = 24°C) was quite similar to 14:0 DMPC (Tm = 23°C) therefore it was preferred to use it instead of 14:0 cardiolipin (Tm = 46°C) in the rest of this work.[43] This model lipid bilayer is also quite interesting to consider potential antibacterial applications as phosphatidylglycerols enter in the bacterial membrane composition of a few species of bacteria, in similar ratios (e.g.: *E. Coli.*, *S. Epidermidis*.).[44]

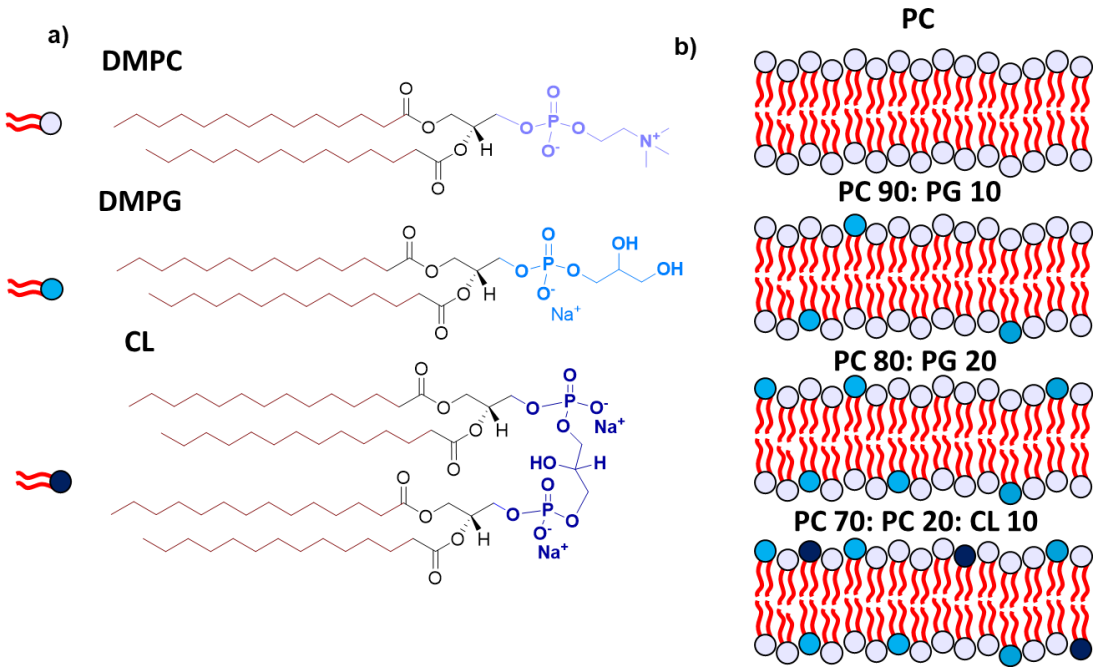

Scheme 4-2: a) Chemical structure of the lipids (DMPC or PC, DMPG or PG, CL) used in this study, distinguishing the head group (shade of blue) and the tail group (brown). b) Structure of the bilayers generated during the screening study.

The lipid bilayer formation by vesicle fusion followed the usual QCM-D pattern, with a decrease in frequency to around -60 Hz (vesicle adsorption) and an increase in dissipation to 2 ppm (formation of viscoelastic vesicle films); this is followed by an increase of frequency (loss of water) and stabilisation around -25 Hz (vesicle fusion and rupture), as well as a decrease in dissipation (the films are more rigid). Initial measurements showed that CPNT **10** could interact with anionic lipid bilayers. The interaction of charged CPNT **10** in the 4 bilayer models was tested on a SiO_2 sensor and was found to increase with the amount of negative charges incorporated in the lipid bilayer, when evaluating variations in frequency and dissipation. The QCM-D profiles were ranging from no visible interaction in pure PC bilayers to very high frequency (Δf_3 = -185 Hz) and energy dissipation (ΔD = 18.9 ppm) shifts in the PC: PG: CL 70: 20: 10 bilayers (40 mol. % of free negative charges, given that cardiolipin is doubly charged). In all cases here, the changes in dissipation mirrored the variations of frequency with higher increases of dissipation, due to the accumulation of CPNT and water in the film making it more viscoelastic (this can also be seen in the splitting of the overtones).

These results suggest that electrostatic interaction plays an important role in the adsorption of charged CPNT **10** on the lipid bilayer. Given the good reproducibility in bilayer formation and the possibility to see interaction, the PC: PG 80: 20 model was chosen as a model lipid bilayer for the rest of this study (see **Figure 4-6**, **Table 4-3** and **Figure 4-7** below for a summary of the data obtained).

Table 4-3: Values for the frequency and dissipation shifts for the third overtone observed after interaction of CPNT **10** on 4 model bilayers, with increasing levels of negative charges. The shift was measured between the stable lipid bilayer and after stabilisation of the interaction.

Lipid composition	Frequency shift (Hz)	*Dissipation shift (ppm)*
PC	0	0
PC:PG 90:10	-74	1.49
PC:PG 80:20	-141	10.8
PC:PG:CL 70:20:10	-185	18.9

Other model lipid bilayers could have been considered for this study to mimic bacterial membranes. Åkesson *et al.* reported the used of unsaturated lipids palmitoyl-2-oleoyl-sn-glycero-3-phosphocholine (POPC) and 1-palmitoyl-2-oleoyl-sn-glycero-3-phospho-(1′-rac-glycerol) (POPG) in a similar study looking at the interaction of charged dendrimers with bilayers of varying membrane charge density.[45] Lind *et al.* described the formation of bilayers by vesicle fusion from 1-palmitoyl-2-oleoyl-sn-glycero-3-phosphoethanolamine (POPE) and POPG, as PE head groups are quite common in the composition of bacterial membranes; the main limitations with this model are the high temperature required for optimal bilayer formation (50°C) and the lipid packing parameter.[46]

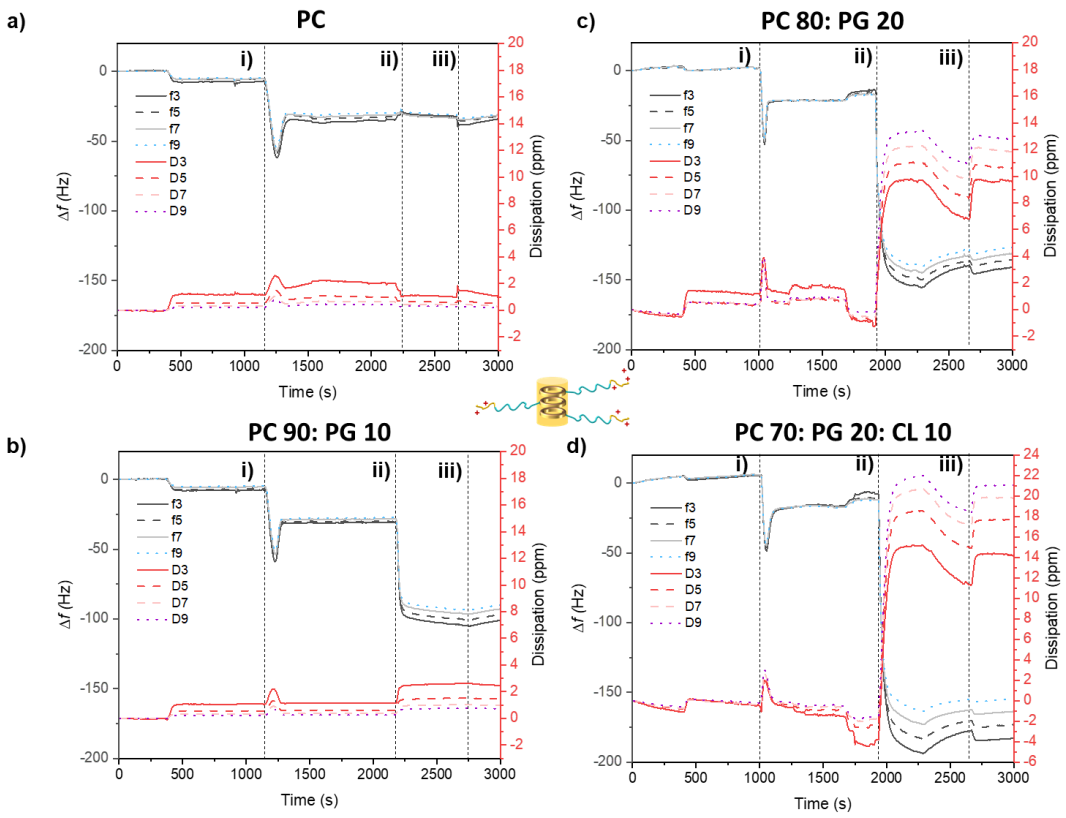

Figure 4-6: QCM-D profiles showing the frequency Δf (Hz, in shades of grey-black) and dissipation (ppm, in shades of red) variations with time (s) for charged CPNT **10** in 4 different model lipid bilayers, with a varying amount of free negative charges: a) DMPC (0%) b) DMPC:DMPG 90:10 (10%), c) DMPC:DMPG 80:20 (20%), d) DMPC:DMPG:CL 70:20:10 (40%). The substrate used was SiO_2 in all cases; dashed lines represent vesicle deposition and subsequent fusion (i) followed by compound injection (ii)) and buffer wash (iii)). Data is shown for the 3rd, 5th, 7th and 9th overtones.

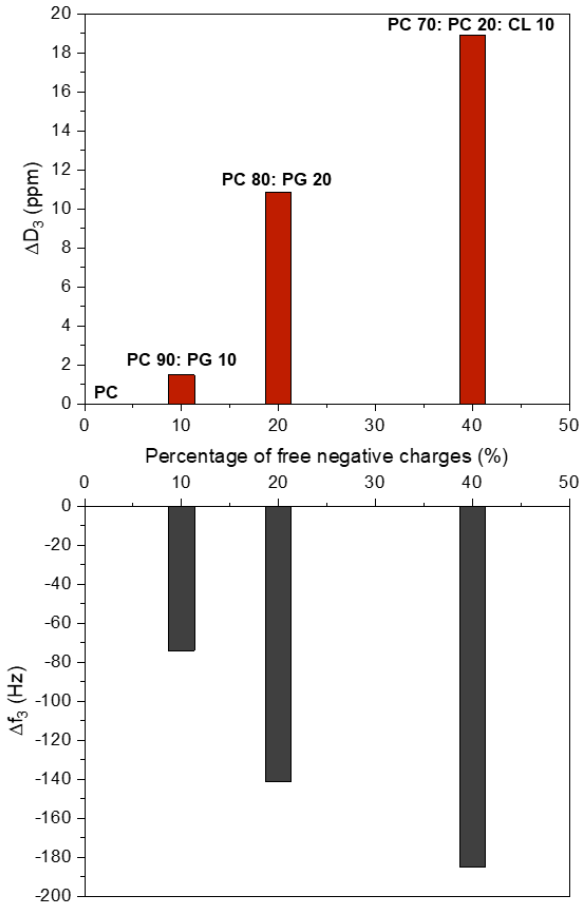

Figure 4-7: Summary of the variations in dissipation (red, top) and frequency (black, bottom) before and after injection of CPNT **10** on lipid bilayers with different amount of "free" negative charges.

4.2.3.3 Structure-Activity Relationships on the DMPC: DMPG model

The interaction of synthesised polymers and CPNT was assessed on the PC: PG 80: 20 model lipid bilayer. Neutral CPNT **6** was found not to interact with the lipid bilayer as indicated by the absence of changes upon addition of the compound, which suggests that the presence of a hydrophilic polymer chain stopped the cyclic peptide from embedding in the SLB as previously observed by Danial *et al.* on dye-loaded lipid vesicles.[29] Charged polymer **8** showed little interaction with the bilayer (Δf_3 = - 17 Hz, ΔD = 2.12 ppm), by comparison with charged CPNT **10** (Δf_3 = - 128 Hz, ΔD = 10.4 ppm), where frequency and dissipation variations upon interaction were stronger. The dissipation change for polymer **8** is minimal as observed on **Figure 4-8**, with a return to the value corresponding to a rigid bilayer (the decrease observed was probably due to the bilayer stabilisation process). The presence of a cyclic peptide in the structure led to a higher interaction; this result was hypothesised to be due to the nanotube formation, generating small clusters of positive charges that can synergistically interact with the bilayer. The interaction of CPNT **11** (length of 21.3 nm) was slightly stronger than for CPNT **9** (length of 6.8 nm) (see **Figure 4-8, Figure 4-9** and **Table 4-4)**. These results need however to be confirmed by further repeats, as the dissipation profile for CPNT **11** shows a number of variations between 1000 and 1800 s that could be due to a faulty detector on the instrument. It is also worth noticing that the final buffer washing step led to an increase in dissipation, that was more remarkable for CPNT **11**, which could be due to additional solvent penetration making the bilayer more viscoelastic (the splitting of the overtones also indicates such a phenomenon). Current work is investigating this phenomenon, using neutron reflectometry (similarly to what is described in paragraph 4.2.5) to have a better understanding of the underlying mechanisms. This importance in self-assembly in interaction was observed directly on bacteria by Nederberg *et al.* on self-assembling polycarbonate micelles bearing quaternary ammonium groups. The MIC was found to decrease significantly for multiple bacterial strains when treated above the critical micellar concentration (CMC) of the polymers. The formation of micelles was hypothesised to enhance antimicrobial activity by stronger electrostatic interaction (higher local charge concentration) and because of the higher steric hindrance that compromised cell wall synthesis.[47] Similarly, cationic peptide-based nanoparticles designed by Liu *et al.* were much more active against bacteria once self-assembled.[48]

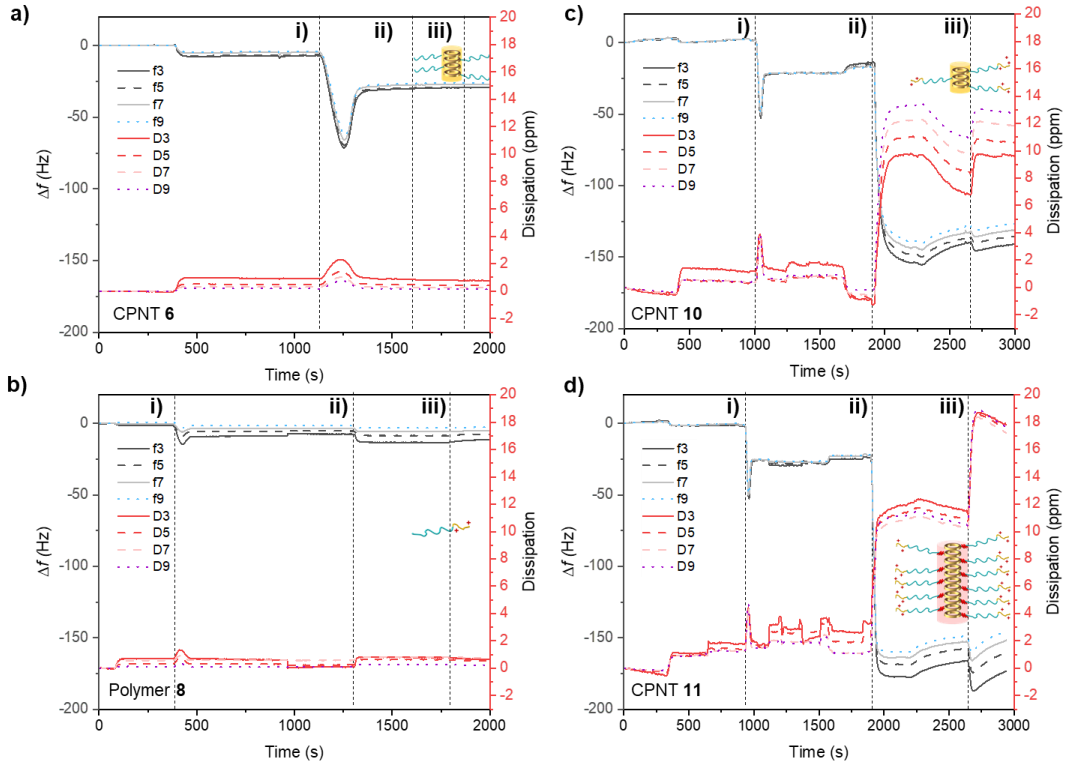

Figure 4-8: QCM-D profiles showing the frequency Δf (Hz, in shades of grey-black) and dissipation (ppm, in shades of red) variations with time (s) for different compounds on the DMPC:DMPG 80:20 model lipid bilayer: a) CPNT **6**; b) charged polymer **8**; c) CPNT **10** and d) CPNT **11**. Dashed lines represent, from left to right: vesicle deposition and subsequent fusion (i) followed by compound injection (ii)) and buffer wash (iii)).)). Data is shown for the 3rd, 5th, 7th and 9th overtones.

Table 4-4: Values for the frequency and dissipation shifts for the third overtone observed after interaction on the DMPC:DMPG 80:20 model lipid bilayer with different compounds. The shift was measured between the stable lipid bilayer and after stabilisation of the interaction.

Sample	Frequency shift (Hz)	*Dissipation shift (ppm)*
CPNT **6**	0	0
Polymer **8**	-17	2.12
CPNT **10**	-128	10.4
CPNT **11**	-153	9.37

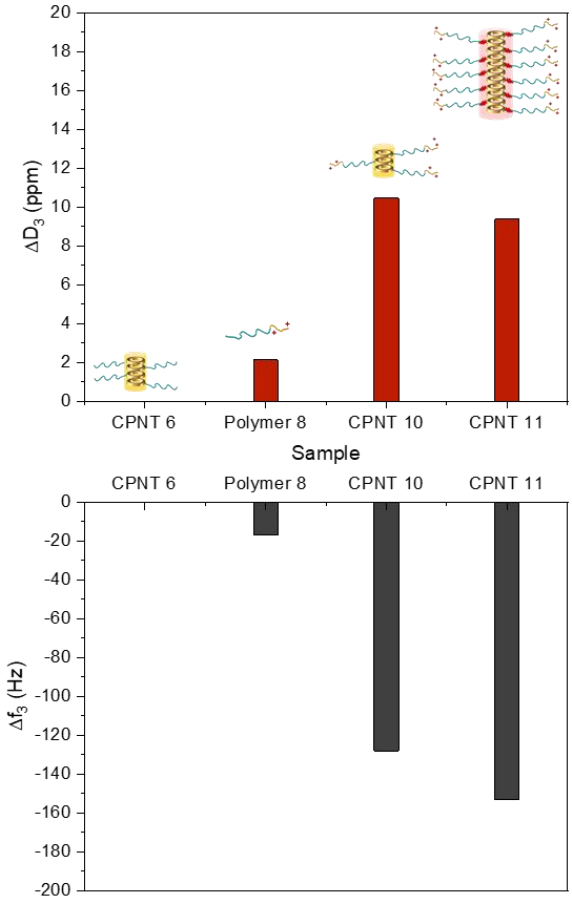

Figure 4-9: Summary of the variations in dissipation (red, top) and frequency (black, bottom) before and after injection of different compounds on the lipid bilayer

4.2.4 Chemical characterisation of the interaction (fluorescence spectroscopy and infrared spectroscopy kinetics)

4.2.4.1 Contribution of the cyclic peptide moiety: tryptophan fluorescence study

In order to validate the hypothesis of improved membrane binding by clustering due to the nanotube morphology of CPNT, the contribution of the cyclic peptide to the interaction was assessed using fluorescence spectroscopy. The cyclic peptide CP **1**, present in all CPNT tested, is composed of three L-Trp amino acids which have a strong emission between 300 and 420 nm when excited at 280 nm (expected maximum: 350 nm). The fluorescence of L-Trp is dependent on the environment in which it is found; when interacting with a lipid bilayer, the emission maximum is expected to go through a "blue shift" towards lower values in the presence of a hydrophobic environment.[49, 50] The study of Trp fluorescence in peptides can provide insights on the location of Trp residues in interaction. For instance, Christiaens *et al.* established the importance of the position of each Trp residue in the sequence of penetratin peptides for interaction with different lipid vesicle models.[50] Here, the Trp fluorescence of free CP **1**, CPNT **10** and **11** was studied in the presence of DMPC:DMPG 80:20 vesicles. Upon addition of vesicles, the fluorescence intensity decreased for both CPNT **10** and **11** whilst it significantly increased for CP **1**. No blue shift could be noticed after 20 min of equilibration for CPNT **10** and **11**, suggesting that the CP Trp residues were not embedded within the lipid bilayer hydrophobic environment. Surprisingly, the fluorescence spectra for CPNT **11** showed the presence of two local maximas at 365 and 461 nm, with negligible variation upon treatment with vesicles. The presence of the peak at 461 nm was attributed to the potential formation of Trp excimers as the value obtained corresponds to the one observed for this amino acid at high concentrations (see **Figure 4-10**, a) and b)).[51]

The fluorescence of Trp residues on CP **1** shifted significantly after treatment with lipid vesicles, going from 351 to 335 nm. This comes with little surprise as CP with hydrophobic residues, such as L-Trp, were shown to partition within lipid bilayers therefore surrounding Trp in a hydrophobic environment and causing here a shift in the emission maximum.[26, 27] This behaviour of CP **1** was further confirmed by acrylamide collisional quenching assays where CP **1** was treated with aliquots of acrylamide, in the presence or absence of vesicles. Acrylamide quenching experiments provide information on the level of accessibility of the Trp in solution. The quenching is less pronounced if the Trp moieties are buried in the bilayer.[50] The Stern Vollmer plots, representing the ratio F_0/F between initial fluorescence (F_0) and fluorescence at a concentration of quencher (F) showed that the slope was much higher in the presence of vesicles, therefore making the Trp less accessible for collisional quenching.

When Trp are freely accessible in solution, quenching already took place at lower concentration in comparison to Trp embedded within a protective lipid bilayer (see **Figure 4-10**, c) and d)). The results from the aforementioned fluorescence study strongly suggest that the CP did not embed in the hydrophobic leaflets of the lipid bilayer, which corroborates the hypothesis of a stronger interaction due to the formation of charge clusters.

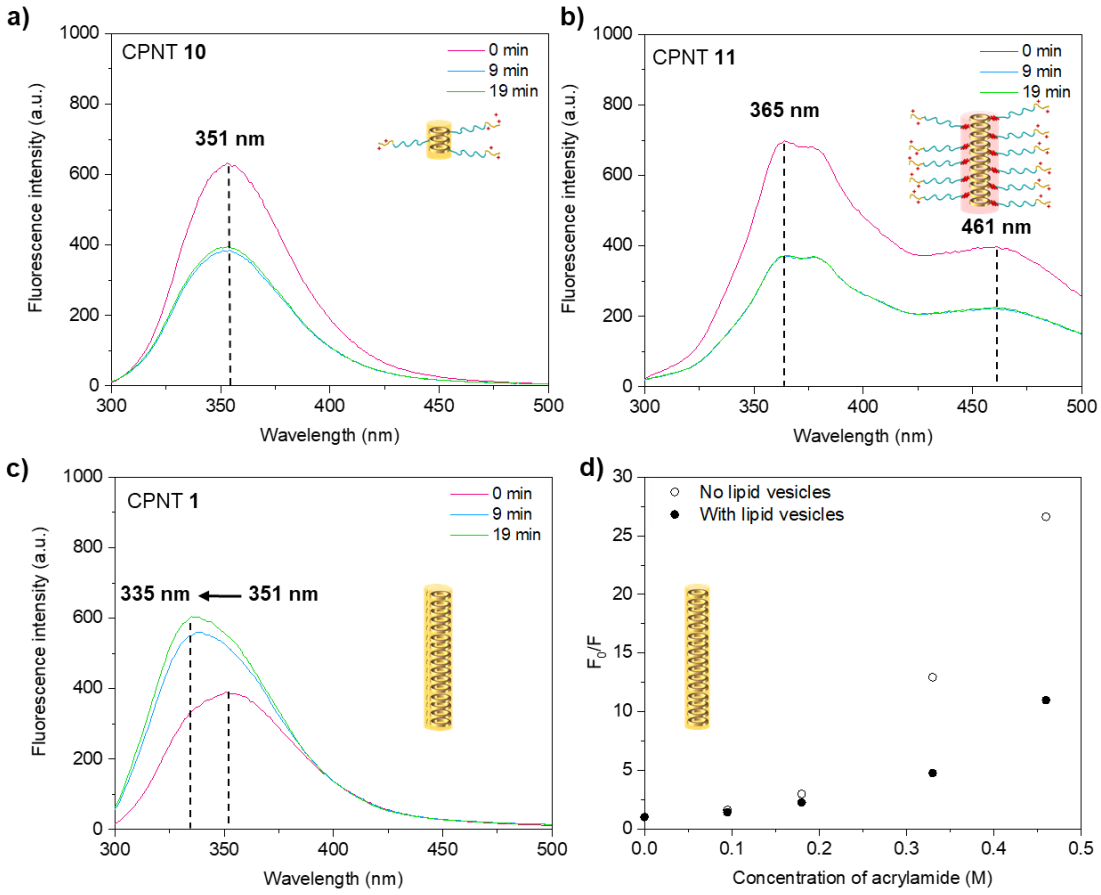

Figure 4-10: Study of the fluorescence of L-Trp present on the CP core in the presence of DMPC:DMPG 80:20 lipid vesicles for: a) charged hydrophilic CPNT **10**, b) charged amphiphilic CPNT **11** and c) nanotubes formed by CP **1**. The fluorescence emission spectra at three time points are represented for t = 0 (pink), 9 (blue) and 19 (green) min, with the excitation set at 280 nm. d) Stern-Vollmer plot representing the ratio between initial fluorescence (F_0) and fluorescence at a concentration of quencher (F), F_0/F, in the presence of increasing amounts of acrylamide quencher.

4.2.4.2 Interaction kinetics from infrared spectroscopy (ATR-FTIR)

QCM-D and fluorescence spectroscopy provided key information on the interaction strength and on the role played by the cyclic peptide moieties of CPNT on lipid bilayers. Aspects related to the effect of each component and to the kinetics of the interaction and the nature of the disruption (lipid removal, etc.) could, however, not be obtained using these techniques.

Therefore, Attenuated Total Reflection Fourier Transform Infrared (ATR-FTIR) spectroscopy was performed to investigate the chemical changes occurring at the Si-water interface. This method allowed for deconvolution between changes in lipid mass and CPNT adsorption, which is not possible solely using QCM-D.

The interaction between a SiO_2 supported dDMPC: hDMPG 80:20 bilayer and CPNT **10** was characterised by observing variations in specific ATR-FTIR peak integrations upon treatment with the nanomaterial. The use of deuterated dDMPC allowed for easy detection of any variation in lipid content at the bilayer surface as the C-D_n stretches (2,230 – 2,050 cm^{-1}) from the deuterated aliphatic tails is in a different spectral region than the aliphatic hydrogenated stretches C-H_n (2,990 – 2,810 cm^{-1}) from the hDMPG tails and the CPNT polymer backbone. No consistent changes were detected for the C-D_n region over time after treatment with CPNT **10** which suggest that there is little to no removal of dDMPC lipid. The C-H_n data seemed to show a gradual increase of signal intensity after incubation with CPNT **10**. These changes in C-H_n intensities were, however, not used for any kinetic considerations of the interaction phenomenon as the lipid bilayer initially contained hDMPG lipids, which would also contribute to the aliphatic hydrogenated stretches observed. The ATR-FTIR integrations for the amide stretch HNC=O peak (present in the cyclic peptide and the acrylamide monomers) clearly increased over time, most likely because of the adsorption or embedding of the polymer acrylamide moieties (in particular from the GEAM pendant groups). It was unfortunately not possible to extract any information from the C=N asymmetrical vibrations (1,586 and 1,608 cm^{-1} from the guanidinium moieties) given the predominance of the amide stretch signal in that region (see **Figure 4-11**).

The kinetics of interaction were extracted from the amide stretch HNC=O and C-D_n peak integrations and the data was modelled to a single phase first-order rate equation (with an initial I_0 intensity of 0, given the absence of amide stretches before addition of CPNT **10**). The absence of change in C-D_n peak integrations was clearly visible as the slope was quasi-null for this fit. Overall, the results from the QCM-D, Trp fluorescence and ATR-FTIR experiments suggest that the interaction observed was either due to an insertion of the conjugate within the lipid bilayer or to carpet-like coating of the surface, both hypotheses relying on anchoring of the charged GEAM moieties to anionic head groups. The assumption of a surfactant-like membrane disruption through lipid solubilisation was excluded given that no lipid removal was observed.

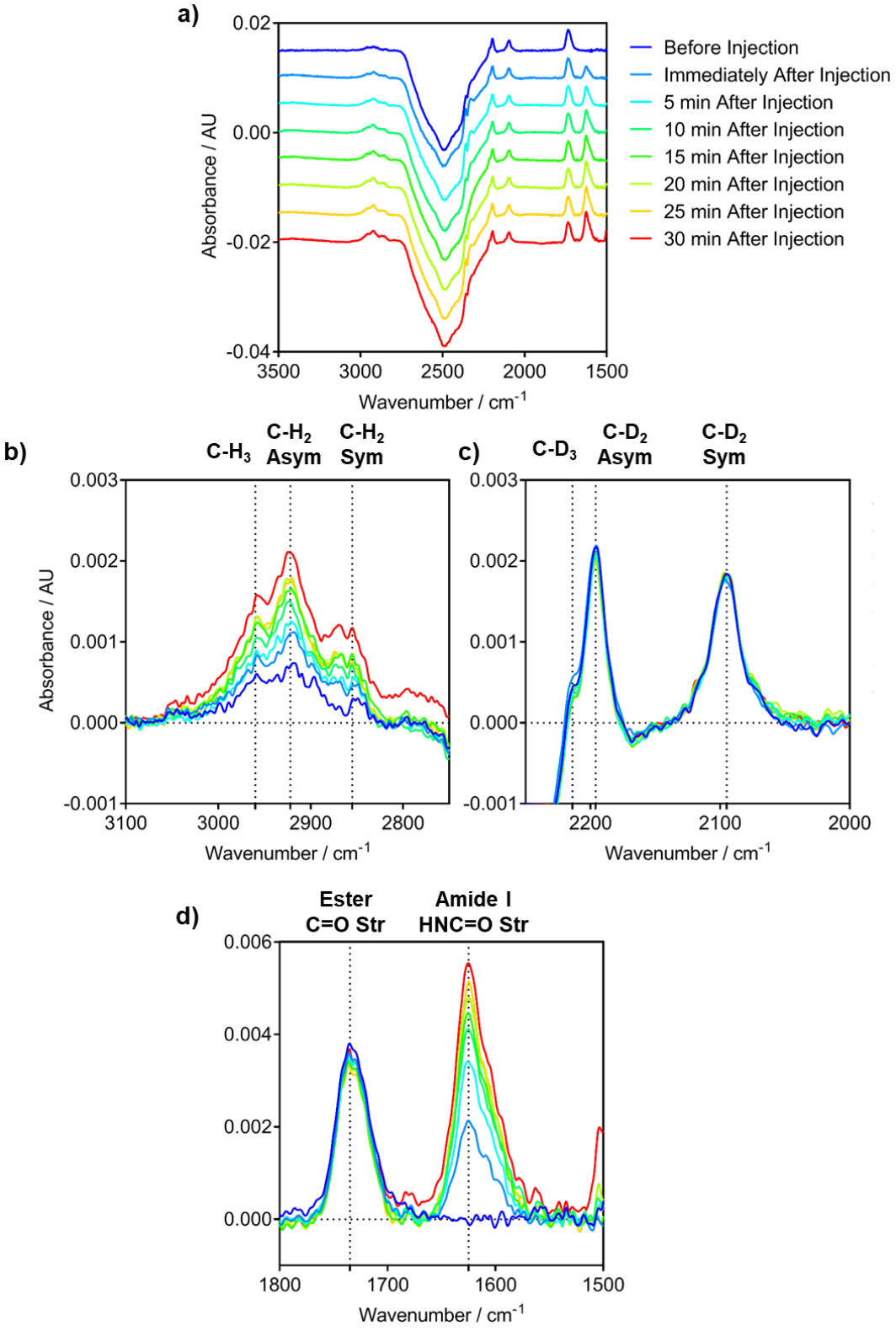

Figure 4-11: a) ATR-FTIR spectra collected on a 8:2 dDMPC:hDMPG silicon-supported lipid bilayer and during incubation with CPNT **10**. b)-d) Excerpts of ATR-FTIR spectra a), showing spectral changes in regions assigned to aliphatic C-H_n stretches, aliphatic C-D_n stretches and carbonyl stretches, respectively.

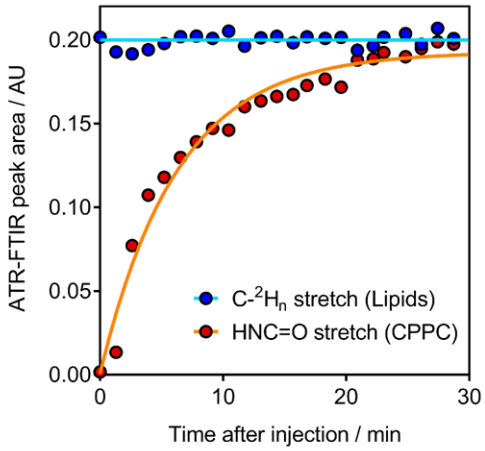

Figure 4-12: Peak areas from ATR-FTIR spectra corresponding to C-D_n stretches (corresponding to phospholipid, in blue) and HNC=O stretches (corresponding to CPNT **10**, in red) plotted with respect to incubation time. Solid lines represent fits to a single-phase first order rate equation.

Table 4-5: Parameters and associated values for the single-phase first-order fits represented on **Figure 4-12**.

$$I_t = I_0 + (I_{eq} - I_0) \cdot (1 - e^{-kt})$$

Parameter	Value
I_0	0
I_{eq}	0.19 ± 0.004
K (min^{-1})	0.16 ± 0.01

4.2.5 In-depth study of structural changes after interaction of CPNT with lipid bilayers by neutron reflectivity

In order to obtain more information on the interactions between CPNT and anionic lipid bilayers, the structural changes on a 80 dDMPC: 20 hDMPG SLB were studied upon addition of CPNT using neutron reflectivity. Neutron reflectivity is a powerful technique which consists in illuminating a planar sample with a collimated neutron beam at grazing incidence and measuring the specular reflected intensity as a function of the scattering vector, ***Q***. The advantage of using neutrons is the possibility to obtain a higher sensitivity in detection, as deuterated and hydrogenated materials have different scattering length densities (SLD).

Neutron reflectivity has been extensively used for the characterisation of thin films, such as lipid bilayers, as well as their response to various stimuli; it is a valuable technique to obtain structural insights on the lipid bilayer after incubating nanomaterials.[52, 53]

4.2.5.1 Lipid bilayer characterisation by NR and interaction of neutral CPNT **6**

The Si crystal substrates were first characterised in H_2O and D_2O contrasts in order to determine the surface roughness and define the thin SiO_2 oxide layer which spontaneously forms at the surface. Following initial characterisation, a 80 dDMPC: 20 hDMPG SLB was deposited using the vesicle fusion approach, similarly to QCM-D and ATR-FTIR. Throughout this work, the data were analysed using multilayer 'slab' models describing homogenous layers of a given scattering length density corresponding to: a pure Si layer, a thin hydrated SiO_2 oxide layer , a thin solvent layer (present because of electrostatic repulsion), the inner leaflet headgroups, two phospholipid tail layers (inner and outer) and the outer leaflet headgroups. The model employed was constrained by implementing physically realistic limits for each fitting parameter (e.g.: thickness, roughness, etc.) and constraining the model such that the final SLD profile represents a chemically consistent structure constrained by the mean molecular area of each lipid (for details see Appendix C, section C.3.1). According to the best fit obtained, the bilayer formed from PC:PG vesicles was found to have a high coverage, defined by low hydration in the tail area (4.2%) in agreement to previous studies investigating DMPC bilayers.[54] Best fits to the experimental data were obtained when including a small water gap (3.1 Å) between the inner leaflet and the Si crystal. The bilayer composition was found to deviate from the desired ratio of 80 PC: 20 PG (mol %) as indicated by the amount of deuterated DMPC tails in the tail region (64 or 68 vol %). Attempts to analyse the data using a model assuming a symmetrical bilayer with identical chemical composition in each leaflet led to poor agreement with the experimental data. Instead, the approach was taken to allow asymmetry between the two leaflets. Due to the differential isotopic labelling of dDMPC and hDMPG, this appears as a change in SLD of the tail layer of each leaflet. Coverage and thickness of each tail layer was constrained to be equal. Based on the proportion of dDMPC and hDMPG in each leaflet (defined by the tail SLD) the thickness of the headgroups and, therefore, their hydration, was permitted to vary based on the different partial molecular volumes of the PC vs PG headgroup. The obtention of a slightly asymmetric lipid bilayer by vesicle fusion is interesting as biological membranes also tend to show some degree of asymmetry, which is usually replicated on SLB models using laborious alternative deposition techniques (e.g.: Langmuir troughs). An recent example of asymmetric bilayers obtained by vesicle fusion is the work of Rondelli *et al.*, who reported the generation of bilayers with GM1 gangliosid enriched microdomains in DMPC:GM1 mixes.[55]

Similarly, Stanglmaier *et al.* demonstrated that asymmetric POPC: POPS bilayers could be made by vesicle fusion by inducing osmotic shock, which is of interest for the study of lipid protein interactions.[56] Wacklin showed that the conditions of vesicle deposition had a significant effect on the level of asymmetry in PC bilayer mixtures, mixing PC lipids with different tail groups (*e.g.* DOPC-DPPC, DMPC-DPPC, etc.).[57]

Neutral CPNT **6** was subsequently incubated with the lipid bilayer, and the interfacial structure determined by fitting to the same model, with only the Si substrate and SiO_2 layer constrained to remain the same than the structure prior to CPNT incubation. No significant changes of the lipid bilayer structure were observed, according to the Bayesian statistical analysis showing a clear overlap of the confidence intervals for most parameters. Furthermore, the absence of any additional peripheral layers required to achieve satisfactory fits to the experimental data suggests that no embedding or carpet-like adsorption is occurring for CPNT **6**. Similarly, due to the similarity in SLD and hydration in all layers before and after CPNT incubation, no CPNT penetration into the bilayer could be observed. Based on the QCM-D results discussed in section 4.2.3, this was an expected result. It is hypothesised that adsorption and embedding on the bilayer were not achievable given the lack of positively charged moieties in this short nanotube system (see data in **Figure 4-13** and a summary of all fitting parameters in **Table 4-6**).

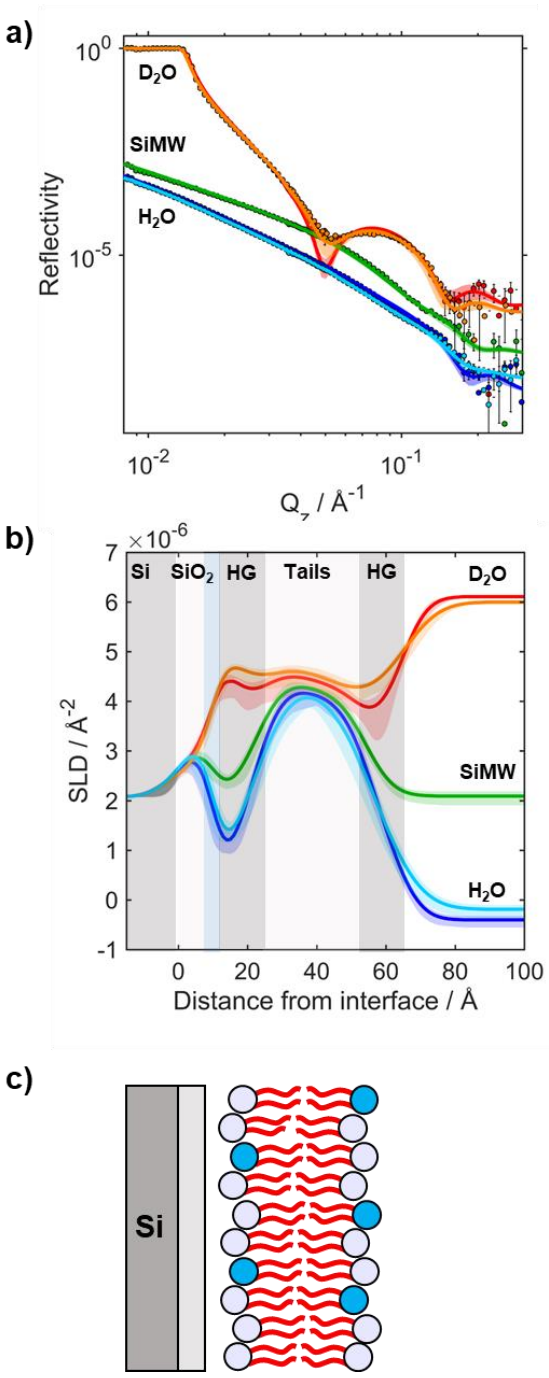

Figure 4-13: Neutron reflectometry data and best fits a) with corresponding SLD profiles b), collected using the FIGARO instrument at the Institut Laue Langevin, for a silicon SLB containing 8:2 dDMPC:hDMPG. The initial bilayer was measured in three solution contrasts; D_2O, silicon-matched water (SiMW) and H_2O, corresponding to red, green and blue data, respectively. The same bilayer was subsequently incubated with neutral CPNT **6** and characterised in D_2O and H_2O, corresponding to orange and cyan data, respectively. Grey shaded areas represent the layer covered by the profile (HG: lipid head groups). c) A schematic representation of the interfacial structure described by the SLD profile in b). Throughout, experimental data are shown as points with best fits to the experimental data shown as lines. Coloured shaded regions represent the 95% confidence interval associated with the fit determined by Bayesian MCMC error estimation.

Table 4-6: Structural parameters obtained by fitting NR data of dDMPC: hDMPG (80:20) bilayers at the Si-water interface to a multi-layer model before and after incubation with CPNT **6**. Values in brackets correspond to the 95% confidence intervals estimated from Bayesian MCMC error estimation. Parameters with * were held as a constant throughout the fitting procedure; χ_{dDMPC} is the volume fraction of dDMPC lipid in a leaflet.

Layer	Parameter	Initial bilayer	Bilayer after incubation with neutral CPNT 6
Si	SLD / $\times 10^{-6}$ Å^{-2}	2.07*	
	Roughness / Å	7 (4.9, 8.0)	
SiO_2	Thickness / Å	8 (7.0, 9.9)	
	SLD / $\times 10^{-6}$ Å^{-2}	3.41*	
	$\chi_{Solvent}$	0.028 (0.001, 0.074)	
	Roughness / Å	4 (3.0, 4.6)	
Water gap	Thickness / Å	3 (3.0, 3.4)	4 (3.0, 6.5)
	Roughness / Å	6 (4.9, 7.4)	9 (7.9, 9.0)
Inner Headgroups	Thickness / Å	9 (8.6, 10.3)	9 (6.9, 10.7)
	SLD / $\times 10^{-6}$ Å^{-2}	2.12 (2.09, 2.15)	2.09 (2.06, 2.12)
	$\chi_{Solvent}$	0.378 (0.360, 0.395)	0.375 (0.257, 0.417)
	Roughness / Å	6 (4.9, 7.4)	9 (7.9, 9.0)
Inner Tails	Thickness / Å	16 (15.3, 16.0)	16 (14.7, 16.0)
	χ_{dDMPC}	0.68 (0.64, 0.72)	0.72 (0.67, 0.76)
	SLD / $\times 10^{-6}$ Å^{-2}	4.52 (4.26, 4.78)	4.82 (4.46, 5.13)
	$\chi_{Solvent}$	0.042 (0.04, 0.087)	0.052 (0.011, 0.10)
	Area per lipid / Å^2	51.7 (49.1, 55.1)	53.0 (58.7, 49.5)
	Roughness / Å	6 (4.9, 7.4)	9 (7.9, 9.0)

Outer Tails	Thickness / Å	16 (15.3, 16.0)	16 (14.7, 16.0)
	χ_{dDMPC}	0.64 (0.60, 0.68)	0.64 (0.59, 0.72)
	SLD / $\times 10^{-6}$ Å^{-2}	4.24 (3.94, 4.55)	4.25 (3.86, 4.78)
	$\chi_{Solvent}$	0.042 (0.04, 0.087)	0.052 (0.011, 0.10)
	Area per lipid / Å^2	51.7 (49.1, 55.1)	53.0 (58.7, 49.5)
	Roughness / Å	6 (4.9, 7.4)	9 (7.9, 9.0)
Outer Headgroups	Thickness / Å	8 (6.1, 9.7)	9 (6.2, 11.8)
	SLD / $\times 10^{-6}$ Å^{-2}	2.15 (2.12, 2.18)	2.15 (2.09, 2.19)
	$\chi_{Solvent}$	0.233 (0.111, 0.359)	0.365 (0.180, 0.475)
	Roughness / Å	6 (4.9, 7.4)	9 (7.9, 9.0)
Bulk Solvent	SLD (D_2O) / $\times 10^{-6}$ Å^{-2}	6.06 (5.81, 6.34)	6.00 (5.98, 6.01)
	SLD (SiMW) / $\times 10^{-6}$ Å^{-2}	2.09 (1.98, 2.20)	-
	SLD (H_2O) / $\times 10^{-6}$ Å^{-2}	-0.40 (-0.50, -0.31)	-0.19 (-0.29, -0.08)

4.2.5.2 Studying the interaction of charged CPNT **10** *by NR*

Similarly to the aforementioned NR study, charged CPNT **10** was incubated with a 80 dDMPC: 20 hDMPG bilayer model. An extra "polymer" layer was added to the previous model to describe any polymer adsorption on the bilayer. Additional contributions to the lipid bilayer composition coming from the CPNT were also implemented in the model, to explain variations in the SLD and hydration of each layer. The lipid bilayer formed had an even more pronounced asymmetry, with the outer leaflet containing significantly more PG (~34%) than the inner leaflet (~19%); such a difference could be attributed to differences in the substrate. The reflectivity profile showed clear differences upon interaction with CPNT **10**, which is in agreement to the data previously acquired on QCM-D and ATR-FTIR. The much steeper drop of intensity after the critical edge in the D_2O and 4MW contrasts were indicative of a thicker interfacial structure. The absence of well-defined fringes indicated intrinsically high roughness or lateral inhomogeneities in the interfacial structure, neither of which are unexpected for this system. Satisfactory fits were obtained by allowing the SLD of each lipid model layer to decrease after incubation with CPNT 10.

The SLD went down from $5.47.10^{-6}$ to $4.46.10^{-6}$ $Å^{-2}$ in the inner tail region; the outer tail region SLD decreased from $4.39.10^{-6}$ to $3.63.10^{-6}$ $Å^{-2}$. This decrease in SLD was hypothesised to be due to polymer insertion of hydrogenated CPNT moieties.

The volume fraction of CPNT found in the inner head groups (27%) was lower than in the outer head groups (39%), most likely because of the different local lipid composition and of the steric restriction due to the presence of the Si substrate. This could be explained by a higher likelihood for electrostatic interaction as the PG content on the outer leaflet was higher. Concomitantly to this phenomenon, a thinning of the tail region, from 14.7 to 10.6 Å was observed, further corroborating the hypothesis of lipid bilayer insertion. In addition to this insertion, an adsorbed "polymer" layer in this model was included and its thickness was estimated to be 136.4 Å, with a high hydration (>80 %) (for a summary of the data, see **Figure 4-14** and **Table 4-7**).

Overall, the data was best fitted to a model describing the interaction as a combination of insertion within the bilayer (pore formation) and adsorption on the bilayer surface. The decrease in SLD within the bilayer was an indication of potential insertion. According to the Trp fluorescence study in section 4.2.4.1, the cyclic peptide moieties on CPNT **10** did not seem to embed in the bilayer; the current hypothesis is that the polymer triggered large scale disruption thanks to electrostatic interaction with head groups, leading to potential pore formation. If this hypothesis is correct, then the apparent change in SLD of the tails will also be contributed to by lipid headgroups, as well as CPNT within the tail region. Therefore the volume fraction of CPNT present within the tails in our model is likely an overestimation. The same mechanism also allowed for the formation of a highly solvated polymer layer on top of the bilayer. Additional neutron reflectometry studies are currently ongoing to evaluate differences due to the CPNT size.

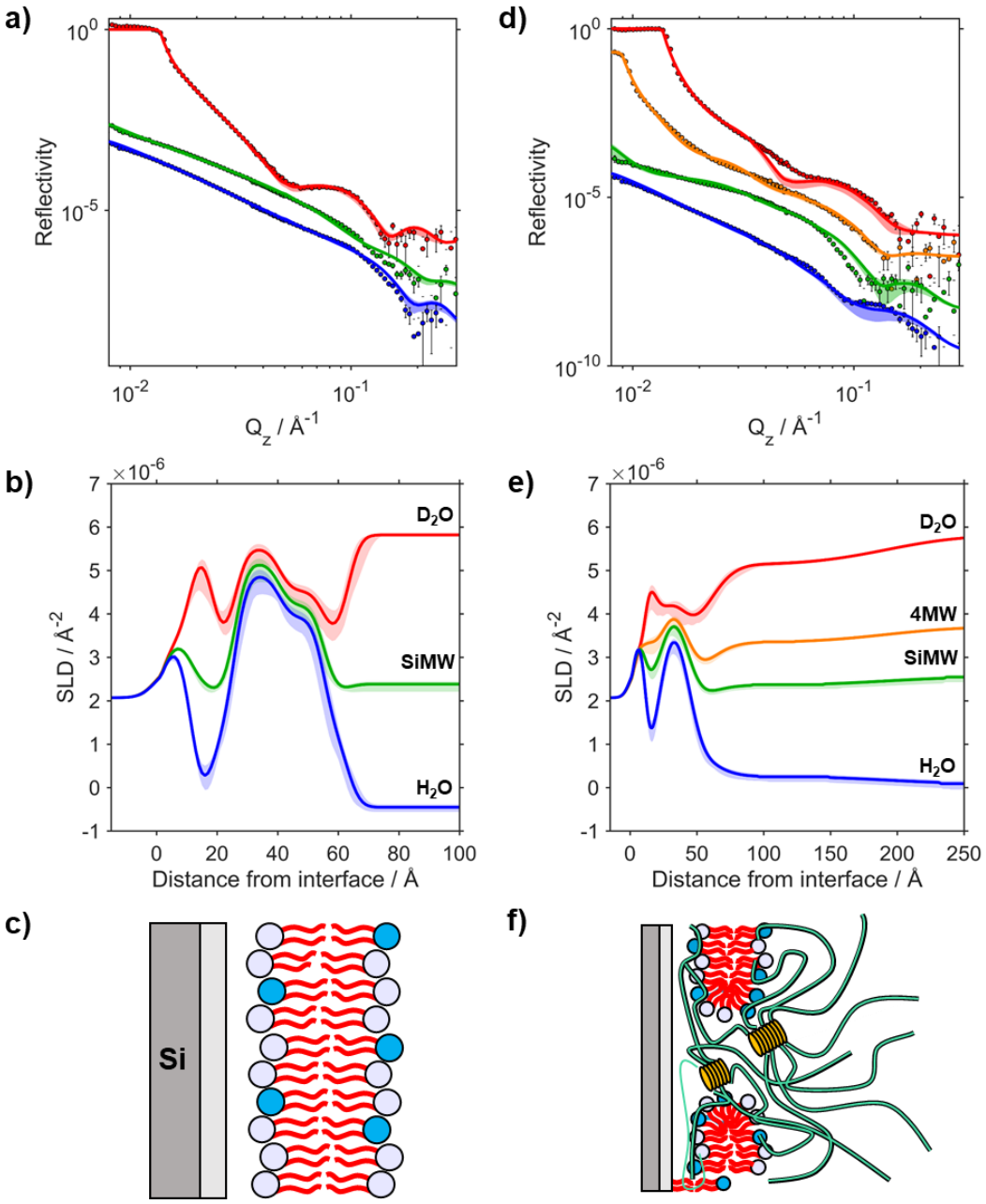

Figure 4-14: Neutron reflectometry data and best fits a) with corresponding SLD profiles b), collected using the FIGARO instrument at the Institut Laue Langevin, for a silicon SLB containing 8:2 dDMPC: hDMPG. The initial bilayer was measured in three solution contrasts; D_2O, silicon-matched water and H_2O, corresponding to red, green and blue data, respectively. c) A schematic representation of the interfacial structure described by the SLD profile in b). Neutron reflectometry data and best fits d) and corresponding SLD profile e) collected for the same bilayer after incubation with CPNT **10**. Due to the anticipated structural complexity resulting from the interactions an additional contrast was collected (66:34 D_2O:H2O, 4-matched water 4MW) corresponding to orange coloured data. f) A schematic representation of the interfacial structure described by the SLD profile in e). Throughout, experimental data are shown as points with best-fits to the experimental data shown as lines. Shaded regions represent the 95% confidence interval associated with the fit determined by Bayesian MCMC error estimation.

Table 4-7: Structural parameters obtained by fitting NR data of dDMPC: hDMPG (8:2) bilayers at the Si-water interface to a multi-layer model before and after incubation with CPNT **10**. Values in brackets correspond to the 95% confidence intervals estimated from Bayesian MCMC error estimation. Parameters with * were held as a constant throughout the fitting procedure. χ_{dDMPC} is the volume fraction of dDMPC lipid in a leaflet.

Layer	Parameter	Initial bilayer	Bilayer after incubation with CPNT 10
Si	SLD / $\times 10^{-6}$ Å^{-2}	2.07 *	
	Roughness / Å	4 (3.5, 4.5)	
SiO_2	Thickness / Å	11 (10.8, 11.3)	
	SLD / $\times 10^{-6}$ Å^{-2}	3.41*	
	Hydration / %	1.1 (0.1, 2.0)	
	Roughness / Å	3 (3.0, 3.4)	
Water gap	Thickness / Å	7 (4.2, 8.3)	5 (3.1, 6.8)
	Roughness / Å	3 (3.0, 3.8)	8 (6.3, 9.3)
Inner Headgroups	Thickness / Å	8 (6.1, 10.4)	8 (6.1, 9.9)
	χ_{dDMPC}	0.813 (0.781, 0.843)	
	χ_{CPNT}	0*	0.27 (0.06, 0.53)
	$\chi_{Solvent}$	0.31 (0.19, 0.49)	0.32 (0.06, 0.56)
	SLD / $\times 10^{-6}$ Å^{-2}	2.02 (2.00, 2.05)	1.72 (1.58, 1.94)
	Roughness / Å	3 (3.0, 3.8)	8 (6.3, 9.3)
Inner Tails	Thickness / Å	15 (14.2, 15.2)	11 (9.2, 12.0)
	χ_{dDMPC}	0.813 (0.781, 0.843)	
	χ_{CPNT}	0*	0.23 (0.15, 0.22)
	$\chi_{Solvent}$	0.10 (0.07, 0.13)	0.03 (0.14, 0.00)
	SLD / $\times 10^{-6}$ Å^{-2}	5.47 (5.24, 5.69)	4.46 (4.21, 5.01)
	Area per lipid / Å^2	58.9 (55.3, 62.7)	100.7 (134.0, 76.8)
	Roughness / Å	3 (3.0, 3.8)	8 (6.3, 9.3)
Outer Tails	Thickness / Å	15 (14.2, 15.2)	11 (9.2, 12.0)
	χ_{dDMPC}	0.662 (0.640, 0.687)	
	χ_{CPNT}	0*	0.23 (0.15, 0.22)
	$\chi_{Solvent}$	0.10 (0.07, 0.13)	0.03 (0.14, 0.00)
	SLD / $\times 10^{-6}$ Å^{-2}	4.39 (4.23, 4.57)	3.63 (3.46, 4.07)
	Area per lipid / Å^2	58.9 (55.3, 62.7)	100.7 (134.0, 76.8)
	Roughness / Å	3 (3.0, 3.8)	8 (6.3, 9.3)

Outer Headgroups	Thickness / Å	8 (6.1, 10.7)	10 (7.3, 11.9)
	χ_{dDMPC}	0.662 (0.640, 0.687)	
	χ_{CPNT}	0*	0.39 (0.26, 0.52)
	$\chi_{Solvent}$	0.35 (0.21, 0.48)	0.32 (0.15, 0.43)
	SLD / $\times 10^{-6}$ Å^{-2}	2.13 (2.11, 2.15)	1.64 (1.59, 1.74)
	Roughness / Å	3 (3.0, 3.8)	8 (6.3, 9.3)
Polymer	Thickness / Å	-	136 (129.1, 144.0)
	SLD / $\times 10^{-6}$ Å^{-2}	-	1.26*
	$\chi_{Solvent}$	-	0.85 (0.84, 0.86)
	Roughness / Å	-	44 (43.3, 45.0)
Bulk Solvent	SLD (D_2O) / $\times 10^{-6}$ Å^{-2}	5.82 (5.80, 5.84)	5.81 (5.80, 5.84)
	SLD (4MW) / $\times 10^{-6}$ Å^{-2}	-	3.70 (3.69, 3.72)
	SLD (SiMW) / $\times 10^{-6}$ Å^{-2}	2.38 (2.29, 2.46)	2.55 (2.48, 2.60)
	SLD (H_2O) / $\times 10^{-6}$ Å^{-2}	-0.45 (-0.53, -0.38)	0.09 (0.01, 0.17)

Previous work in the literature described similar studies of the interaction of cationic polymers or nanoparticles on SLB using neutron reflectivity, where models including adsorption, embedding or more complex structural changes were employed.[45, 58-60] For example, Åkesson *et al.* investigated the membrane translocation of positively charged poly(amidoamine) dendrimers in POPC:POPG bilayers. Their NR study concluded that a mixed model where bilayer patches were "sandwiched" in between dendrimer molecules (with modification of the lipid bilayer curvature) was the most appropriate. Translocation and formation of dendrisomes alone did not provide a satisfactory fit to the data acquired on POPC:POPG bilayers.[45] Tatur *et al.* compared the interaction of positively and negatively charged gold nanoparticles with 1,2-distearoyl-sn-glycero-3-phosphocholine (DSPC) floating bilayer models, looking at their effect on the SLB in different lipid phases. The positively charged AuNP were found to embed in the bilayer whilst their negative counterparts only had a superficial interaction, which corresponds to what was observed here comparing neutral and charged CPNT.[58] In recent work, Di Silvio *et al.* evaluated the effect of protein corona formation on nanoparticle-membrane interaction, using 1,2-Dioleoyl-sn-glycero-3-phosphocholine (DOPC) bilayer models. The authors observed that the presence of a protein corona on polystyrene nanoparticles could induce changes in the SLB thickness and hydration.[59] Such an exploration of the effect of protein corona formation on membrane activity could be beneficial to CPNT, be it for drug delivery purposes (as mentioned in Chapter 2 and 3) or to predict *in vivo* antibacterial applications. Additional NR studies looking into the simultaneous influence of nanoparticle shape, stability and charge on lipid bilayers would also be welcome.

4.2.6 Biological relevance: assessment of antibacterial properties

Given the potential of CPNT for membrane adsorption and pore formation on anionic membrane models, the antibacterial activity of neutral CPNT 6 and charged polymers **8** and CPNT **10** and **11** was assessed on different bacterial strains. The bacterial membrane of the strains considered is net anionic, which was expected to be favourable for interaction with charged CPNT. Gram-positive (*S. Aureus*, *S. Epidermidis*) and Gram-negative (*P. Aeruginosa*, *E. Coli*) bacterial strains were chosen for this assay. The bacterial strains spanned across different membranes types and lipid composition (in particular, the percentage of negatively charged lipid in the plasma membrane). For Gram-positive bacteria, *S. Aureus* usually contain around 60 mol% of negatively charged lipids (40% PG, 20% CL) and around 40% of zwitterionic Lysyl-PG; *S. Epidermidis* is composed of around 70% of lipids with PG head groups and 20% of neutral diglycoside diglycerides, according to the literature.[61, 62] As for Gram-negative strains, *E. Coli.* bacteria lipid membrane composition was reported to be zwitterionic PE (75%) and anionic PG (20%) and CL (5%); *P. Aeruginosa* has a similar lipid composition, with PE (70%), PG (12%) and other neutral lipids.[63, 64] Across all compounds tested and all strains, only one positive result could be found, for CPNT **10** on *S. Epidermidis*, a strain present in the skin flora that can cause serious infections to immuno-compromised patients (see **Table 4-8**).[65]

Table 4-8: Summary of the antibacterial testing performed with CPNT 6, polymer 8, CPNT 10 and CPNT 11 on four bacterial strains, up to 1024 µg/mL (85-100 nM, depending on the compound). +: active at 1024 µg/mL (n = 2 independent repeats).

Bacterial strain	CPNT **6**	Charged polymer **8**	CPNT **10**	CPNT **11**
E. Coli.	-	-	-	**NA**
P. Aeruginosa	-	-	-	-
S. Aureus	-	-	-	-
S. Epidermidis	-	-	+	**NA**

The antibacterial activity was only observed at a relatively high concentration of material (1024 μg/mL); the difference between free polymer **8** and CPNT **10** was probably caused by an enhanced interaction of the self-assembling material with the lipid membrane. As mentioned *vide supra*, *S. Epidermidis* has more negatively charged lipids in its bilayer composition than *S. Aureus*, explaining the presence of a MIC for CPNT **10** due to a more favourable interaction.[61] Further research to deepen our understanding of the interaction of CPNT with bacteria-like membrane models is necessary, accounting for the presence of lipopolysaccharides (LPS) and peptidoglycans. Characterisation on more advanced membrane models should be used to tailor these charged CPNT systems for antibacterial properties. Mammalian cell viability assays are ongoing to evaluate the effect of charged CPNT on cells.

4.3 Conclusions

A library of neutral and charged polymer and self-assembling CPNT was successfully generated in this work. The potential for membrane interactions of these systems was evaluated on model membranes, using complementary techniques. Investigation of changes in mass and viscoelasticity associated with the interaction by QCM-D demonstrated that the interaction of charged CPNT was dependent on the lipid composition, with an increase in interaction with respect to the amount of negatively charged lipids in the lipid bilayer. In terms of design, charge was shown to be essential to the interaction of CPNT, as the neutral CPNT did not show any noticeable interaction with a 80 DMPC: 20 DMPG lipid bilayer. Interestingly, a clear difference in membrane interaction could be observed between charged polymer **8** and CPNT **10**, suggesting a non-negligible contribution of CP self-assembly to membrane interaction. Evaluation of the fluorescence of the Trp present in the CP showed that CP moieties were not embedding in the hydrophobic region of the bilayer for charged CPNT **10** and **11**, unlike CP nano-assemblies lacking conjugated hydrophilic polymers. By combining data from ATR-FTIR and neutron reflectivity measurements, it was found that the interaction of CPNT **10** did not lead to any significant lipid removal, excluding surfactant-like disruption. Fitting of the neutron reflectivity data to a 9-layer model suggested that the CPNT was simultaneously forming pores within the bilayer and a diffuse hydrated layer above the outer leaflet. The current hypothesis to explain this phenomenon is a preferential anchoring of guanidinium segments to PG moieties *via* electrostatic interactions, leading to large-scale disruption of the lipid bilayer. The antibacterial properties of these CPNT was assessed and some activity could be observed at high concentration of CPNT **10** on *S. Epidermidis*. Further optimisation is necessary to create antibacterial CPNT with low off-target toxicity. In terms of CPNT design, the ideal balance between surface charge and self-assembly remains to be found. Studies on more advanced bilayer models should also be considered, in order to investigate the effect of other membrane components on the interaction such as liposaccharides or peptidoglycans which are non-negligible components of bacterial membranes.

4.4 Experimental

4.4.1 Materials

Protected amino acids (Fmoc-D-Leu-OH, Fmoc-L-Lys(Boc)-OH, Fmoc-L-Trp(Boc)-OH) and 2-(6-Chloro-1-H-benzotriazole-1-yl)-1,1,3,3-tetramethylaminium hexafluorophosphate (HCTU) were purchased from Iris Biotech GmbH (Germany). 4-(4,6-dimethoxy-1,3,5-triazin-2-yl)-4-methyl-morpholinium tetrafluoroborate (DMTMM.BF_4) was synthesised from DMTMM.Cl (Sigma Aldrich, UK) as previously described.[66] The Initiators Dimethyl 2,2'-azobis(2-methylpropionate) (V-601) and 2,2'-azobis[2-(2-imidazolin-2-yl) propane] dihydrochloride (VA-044) were obtained from Wako Chemicals (UK). 4-acryloylmorpholine (NAM), and butyl acrylate (BA), were purchased from Sigma Aldrich (UK) and were deinhibited with basic aluminium oxide prior to polymerisation reactions. diBocGEAM and the RAFT agent (propanoic acid)yl butyl trithiocarbonate (PABTC) were synthesised by Agnes Kuroki, following a procedure previously described in the literature.[36] All hydrogenated lipids, 1,2-dimyristoyl-sn-glycero-3-phosphocholine (DMPC), 1,2-Dimyristoyl-sn-glycero-3-phosphoglycerol, sodium salt (DMPG) and cardiolipin were purchased from Avanti Polar Lipids (USA). Tail deuterated d54 dDMPC was also purchased from Avanti Polar Lipids (USA). All other reagents, solvents and buffer components were purchased from Sigma Aldrich (UK).

4.4.2 Characterisation techniques

4.4.2.1 Nuclear magnetic resonance

^{1}H NMR spectrum were measured using a Bruker DPX-300 or DPX-400 NMR spectrometer that operated at 300.13 and 400.05 MHz respectively. The residual solvent peaks were used as internal references. Deuterated dimethylsufoxide (d-DMSO) (δ_H = 2.50 ppm) or deuterated chloroform ($CDCl_3$) (δ_H = 7.27 ppm) were used to record spectral data for the polymers and cyclic peptide-polymer conjugates tested.

4.4.2.2 Size exclusion chromatography

Agilent Infinity II MDS instrument equipped with differential refractive index (DRI), viscometry (VS), dual angle light scatter (LS) and variable wavelength UV detectors. The system was equipped with 2 x PLgel Mixed D columns (300 x 7.5 mm) and a PLgel 5 µm guard column. The eluent is DMF with 5 mmol NH_4BF_4 additive. Samples were run at 1 ml/min at 50'C. Poly(methyl methacrylate) standards (Agilent EasyVials) were used for calibration between 955,000 – 550 g/mol.

Analyte samples were filtered through a nylon membrane with 0.22 μm pore size before injection. Respectively, experimental molar mass (M_n, SEC) and dispersity ($Đ$) values of synthesized polymers were determined by conventional PMMA calibration using Agilent SEC/SEC software.

4.4.2.3 Zeta potential measurements

Zeta potential measurements were carried out on a Malvern Zetasizer in pure water in a DTS1070 folded capillary zeta cell at a concentration of 1 mg/mL (3 independent measurements, between 10 and 100 runs).

4.4.2.4 Small Angle X-ray Scattering (SAXS)

Small Angle X-ray scattering (SAXS) was performed by Dr Steven Huband at the University of Warwick X-ray Diffraction facility. The instrument was a 5 m Xenocs Xeuss 2.0 SAXS instrument, equipped with a micro-focus Cu Kα (λ = 1.54189 Å) source collimated with Scatterless slits with a beam diameter of 0.8 mm. The angular dependence of scattering intensity was measured using a Pilatus 300k detector with a pixel size of 0.172 mm x 0.172 mm. The distance between the detector and the sample was calibrated using silver behenate ($AgC_{22}H_{43}O_2$), giving a value of 2.481 m. The samples were dissolved in in D_2O HEPES buffer (20 mM, PD = 7.2) and transferred to a capillary. The q-range, where the scattering wave vector **q** is defined as ($\boldsymbol{q} = \frac{4\pi}{\lambda} sin\frac{\theta}{2}$, with θ being the scattered angle, λ the incident X-rays wavelength) for all measurements was 0.0054 - 0.16 $Å^{-1}$. A radial integration of the 2D scattering profile was performed using FOXTROT software and the resulting data corrected for the absorption, sample thickness and background.[67] Finally, the scattering intensity was then rescaled to absolute intensity using glassy carbon as a standard. SAXS patterns were collected at 25°C for 4 hours.[68] The reduced data was fitted to different form factors using the SASview software package.[39] Details about the fitting parameters and the form factors employed can be found in the Appendix to this chapter.

4.4.3 Synthesis

4.4.3.1 Cyclic peptide synthesis

The cyclic peptide synthesis and characterisation is identical to the one reported in Chapter 2 (see section 2.4.3.1).

Note: The conditions for the synthesis of polymers 2, 3, 4 and 5 are summarised in **Table 4-9**.

4.4.3.2 Synthesis of poly(NAM_{65}) **2**

The PABTC CTA (17.6 mg, 0.074 mmol, 1.0 eq.), NAM (0.700 g, 4.96 mmol, 67 eq.), V601 (0.343 mg, 1.49 µmol, 0.0168 eq.) and 1,4-dioxane (1.25 mL) an water (0.330 mL) were added to a 20 mL glass vial. The reaction mixture was sealed with a rubber septum and degassed for 10 min with a flow of nitrogen, before being heated at 70°C for 2.5 h in an oil bath, to reach quasi-quantitative monomer conversion. The polymer was then precipitated three times in cold diethyl ether and dried in a vacuum oven at 40°C for 16 h, affording poly(NAM_{65}) as a yellow-white powder (600 mg).

M_n (NMR) = 9,500 g/mol, M_n (SEC- DMF) = 9,200 g/mol, Đ = 1.09

^{1}H-NMR (300 MHz, DMSO-d_6, ppm, n = 65): 3.9 – 3.0 (8nH, (OC**H$_2$**C**H$_2$**N)$_2$), 2.7 -2.3 (1nH, CH_2C**H**C=O), 1.8 – 1.3 (2nH, C**H$_2$**CH backbone), 0.88 (3H, C**H$_3$**-CH_2-CH_2-CH_2-SCS_2).

4.4.3.3 Synthesis of poly(BA_{12}-b-NAM_{65}) **3**

This polymer was synthesised by block extension of polymer **3** in Chapter 3 (M_n(NMR) = 7,700 g/mol). The macroCTA (1,120 mg, 0.150 mmol, 1.0 eq.), NAM (556 mg, 3.94 mmol, 27 eq.), V601 (0.726 mg, 3.20 µmol, 0.021 eq.) and 1,4-dioxane (4.90 mL) were added to a 20 mL glass vial. The reaction mixture was sealed with a rubber septum and degassed for 10 min with a flow of nitrogen, before being heated at 65°C for 2 h 45 in an oil bath, to reach 86% monomer conversion. The polymer was then precipitated three times in cold diethyl ether and dried in a vacuum oven at 40°C for 16 h, affording poly(BA_{12}-*b*-NAM_{65}) as a yellow-white powder (1380 mg).

M_n (NMR) = 11,100 g/mol, M_n (SEC- DMF) = 12,200 g/mol, Đ = 1.07.

^{1}H-NMR (300 MHz, DMSO-d_6, ppm, n = 65, n'= 12): 4.1 – 3.9 (2n'H CH_3-CH_2-CH_2-C**H$_2$**-O from BA), 3.9 – 3.0 (8nH, (OC**H$_2$**C**H$_2$**N)$_2$), 2.7 – 2.3 (1nH and 1n'H, CH_2C**H**C=O), 1.8 – 1.5 (2nH and 2n'H, C**H$_2$**CH backbone + 2n'H CH_3-CH_2-C**H$_2$**-CH_2-O from BA) 1.4 –1.2 (2n'H CH_3-C**H$_2$**-CH_2-CH_2-O from BA), 1.0 – 0.83 (3n'H C**H$_3$**-CH_2-CH_2-CH_2-O from BA+ 3H C**H$_3$**-CH_2-CH_2-CH_2-SCS_2 from CTA).

4.4.3.4 Block extension with diBoc(GEAM) (typical procedure, example of polymer **5***)*

MacroCTA polymer **3** (290 mg, 0.0255 mmol, 1.0 eq.), diBocGEAM (36.3 mg, 0.102 mmol,4.0 eq.), VA-044 (0.560 mg, 1.73 µmol, 0.066 eq.) and 1,4-dioxane (0.964 mL) were added to a 8 mL glass vial. The reaction mixture was sealed with a rubber septum and degassed for 10 min with a flow of nitrogen, before being heated at 46°C for 16 h in an oil bath, to reach quasi quantitative monomer conversion. The polymer was then precipitated three times in cold diethyl ether and dried in a vacuum oven at 40°C for 16 h, affording poly(BA_{12}-*b*-NAM_{65}-b-diBocGEAM$_4$) as a yellow-white powder (182 mg).

M_n (NMR) = 12,800 g/mol, M_n (SEC- DMF) = 13,200 g/mol, Đ = 1.09.

^{1}H-NMR (300 MHz, DMSO-d_6, ppm, n = 65, n' = 12, n'' = 4): 4.1 – 3.9 (2n'H CH_3-CH_2-CH_2-C**H$_2$**-O from BA), 3.9 – 3.0 (8nH, (OC**H$_2$**C**H$_2$**N)$_2$), 2.7 – 2.3 (1nH, 1n'H and 1 n''H, CH_2C**H**C=O), 1.8 – 1.5 (2nH, 2n'H and 2n''H, C**H$_2$**CH backbone + 2n'H CH_3-CH_2-C**H$_2$**-CH_2-O from BA), 1.49-1.37 (18n''H, Boc tBu groups from diBocGEAM), 1.4 –1.2 (2n'H CH_3-C**H$_2$**-CH_2-CH_2-O from BA), 1.0 – 0.83 (3n'H C**H$_3$**-CH_2-CH_2-CH_2-O from BA+ 3H C**H$_3$**-CH_2-CH_2-CH_2-SCS_2 from CTA).

For polymer **4**, the peaks are the same as for polymer 2, with the addition of the Boc tBu peaks 1.49-1.37 (18n''H, Boc tBu groups from diBocGEAM).

Table 4-9: Summary of the conditions used for RAFT polymerisations, to synthesise polymers **2**, **3**, **4** and 5.

	Monomer concentration (M)	Temperature (°C)	CTA: initiator	Conversion (%) (NMR)	Estimated cumulative livingness (%)
poly(NAM_{65}) **2**	3	70	50	98	99.8
poly(BA_{12}-*b*-NAM_{65}) **3**	0.75	70	46	86	98.5
Protected polymer **4**	0.12	46	20	>99%	93.6
Protected polymer **5**	0.09	46	15	>99%	93.7

4.4.3.5 *Typical procedure for cyclic peptide conjugation, example of CP-poly(BA_{12}-b-NAM_{65})* **7**

Poly(BA_{12}-*b*-NAM_{65}) (224 mg, 20 µmol, 1.15 eq.) and HCTU (8.36 mg, 20 µmol, 1.15 eq.) were dissolved in 2 mL of DMF and left stirring for 10 min. A solution of cyclic peptide (20 mg, 17.3 µmol, 1.0 eq.) with NMM (4.00 mg, 40 µmol, 3.0 eq.) was prepared in DMF (1 mL). This solution was added to the activated polymer, and the mixture was stirred at room temperature for 16 h. The conjugate was then precipitated in diethyl ether once then redissolved in DCM before slow addition of diethyl ether, to reach a final ratio of 70 DCM: 30 ether allowing for selective precipitation of the conjugate (and removal of the free polymer). The precipitated solid was then dried in the vacuum oven at 40°C overnight, affording CP- poly(BA_{12}-*b*-NAM_{65})) (74%, 160 mg).

M_n(NMR) = 12,200 g/mol, M_n(SEC) = 13,700 g/mol, $Đ$ = 1.10.

^{1}H-NMR (400 MHz, DMSO-d6, ppm, n = 65 (NAM), n'=12 (BA)) (only indicating distinctive CP peaks):

8.3 – 7.6 (L-Trp protons), 7.33 – 7.25+ 7.15 – 6.9 (L-Trp aromatic protons), 4.1 – 3.9 (2n'H CH_3-CH_2-CH_2-C**H$_2$**-O from BA), 3.9 – 3.0 (8nH, (OC**H$_2$**C**H$_2$**N)$_2$), 2.7 – 2.3 (1nH and 1n'H, CH_2C**H**C=O), 1.8 – 1.5 (2nH and 2n'H, C**H$_2$**CH backbone + 2n'H CH_3-CH_2-C**H$_2$**-CH_2-O from BA) 1.4 –1.2 (2n'H CH_3-C**H$_2$**-CH_2-CH_2-O from BA), 1.0 – 0.83 (3n'H C**H$_3$**-CH_2-CH_2-CH_2-O from BA+ 3H C**H$_3$**-CH_2-CH_2-CH_2-SCS_2 from CTA), 0.80 – 0.60 (D-Leu isopropyl protons).

The same amounts in moles were used for the synthesis of neutral CPNT **6,** with a purification by dialysis in 30 kDa centrifuge tube and freeze-drying (similarly to the typical purification process mentioned in Chapter 2). For the assignment, please refer to similar CPNT in Chapter 3.

4.4.3.6 Synthesis of charged polymers by deprotection of protected polymers (typical procedure, example of polymer **9***)*

Protected polymer **5** (80 mg, 6.23 µmol, 1 eq.) was dissolved in a cleavage cocktail of TFA: TIPS: H_2O 9: 0.5: 0.5 (2.2 mL) and left to stir for 3 hours. The deprotected polymer was then precipitated in cold diethyl ether three times. The precipitated solid was then dried in the vacuum oven at 40°C overnight, affording deprotected polymer **9** and the deprotection reaction was deemed successful upon examination of the disappearance of the Boc peaks on the NMR spectrum (sharp peaks with maxima at 1.39 and 1.47 ppm). The polymer was then dialysed in a 1 M NaCl solution for 2 h to exchange TFA^- counterions with Cl^-, followed by dialysis in pure water overnight in a Float-A-Lyser (500-1000 Da cut-off). The polymer was then freeze-dried, affording a white powder. (71 mg, 95%)

M_n(NMR) = 12,000 g/mol, M_n(SEC) = 14,600 g/mol, Đ = 1.13.

^{1}H-NMR (400 MHz, DMSO-d_6, ppm, n = 65, n' = 12, n'' = 4): 4.1 – 3.9 (2n'H CH_3-CH_2-CH_2-C**H$_2$**-O from BA), 3.9 – 3.0 (8nH, (OC**H$_2$**C**H$_2$**N)$_2$), 2.7 – 2.3 (1nH, 1n'H and 1n''H, CH_2C**H**C=O), 1.8 – 1.5 (2nH, 2n'H and 2n''H, C**H$_2$**CH backbone + 2n'H CH_3-CH_2-C**H$_2$**-CH_2-O from BA), 1.4 –1.2 (2n'H, CH_3-C**H$_2$**-CH_2-CH_2-O from BA), 1.0 – 0.83 (3n'H C**H$_3$**-CH_2-CH_2-CH_2-O from BA+ 3H C**H$_3$**-CH_2-CH_2-CH_2-SCS_2 from CTA).

4.4.3.7 Typical procedure for synthesis of charged CPNT (example of charged CPNT **11***)*

Protected polymer **5** (102 mg, 8.03 µmol, 1.15 eq.) and HCTU (3.34 mg, 8.03 µmol, 1.15 eq.) were dissolved in 1.5 mL of DMF and left stirring for 10 min. A solution of cyclic peptide (8 mg, 6.98 µmol, 1.0 eq.) with NMM (2.12 mg, 20.9 µmol, 3.0 eq.) was prepared in DMF (1 mL) and added to the Polymer/HCTU mixture. The reaction was left to react for 16 hours. The protected CPNT intermediate was precipitated twice in diethyl ether, dried in a vacuum oven overnight at 40°C. The protected CPNT intermediate was then directly deprotected with a cleavage cocktail of TFA: TIPS: H_2O 9: 0.5: 0.5 (2.2 mL), which was left to stir for 3 hours. Deprotected CPNT **11** was then precipitated in cold diethyl ether three times. The deprotected CPNT was then dialysed in a 1 M NaCl solution for 2 h to exchange TFA^- counterions with Cl^-, followed by dialysis in pure water overnight in a 30 kDa dialysis centrifuge tube. (74 mg, 80%)

M_n(NMR) = 13,100 g/mol, M_n(SEC) = 14,000 g/mol, Đ = 1.48.

^{1}H-NMR (400 MHz, DMSO-d_6, ppm, n = 65, n' = 12, n'' = 4): 8.3 – 7.6 (L-Trp protons), 7.33 – 7.25+ 7.15 – 6.9 (L-Trp aromatic protons), 4.1 – 3.9 (2n'H CH_3-CH_2-CH_2-C**H$_2$**-O from BA), 3.9 – 3.0 (8nH, (OC**H$_2$**C**H$_2$**N)$_2$), 2.7 – 2.3 (1nH, 1n'H and 1n''H, CH_2C**H**C=O), 1.8 – 1.5 (2nH, 2n'H and 2n''H, C**H$_2$**CH backbone + 2n'H CH_3-CH_2-C**H$_2$**-CH_2-O from BA), 1.4 –1.2 (2n'H CH_3-C**H$_2$**-CH_2-CH_2-O from BA), 1.0 – 0.83 (3n'H C**H$_3$**-CH_2-CH_2-CH_2-O from BA+ 3H C**H$_3$**-CH_2-CH_2-CH_2-SCS_2 from CTA), 0.80 – 0.60 (D-Leu isopropyl protons).

For CPNT **10**, please refer to previous assignments in Chapter 3, including the backbone peaks of GEAM (for synthesis: final yield of 61% in the case of CPNT **10**).

All NMR spectra are available in Appendix C.

Table 4-10: Molecular weight (NMR, SEC) and dispersities of CPNT synthesised.

Sample	M_n (NMR) (g/mol)	M_n (SEC) (g/mol)	*Đ*
Neutral CPNT **6**	10,635	10,300	1.14
Neutral CPNT **7**	12,235	13,700	1.10
Charged polymer **8**	10,020	8,000	1.33
Charged polymer **9**	12,000	14,600	1.13
Charged CPNT **10**	11,155	10,300	1.36
Charged CPNT **11**	13,135	14,000	1.48

4.4.4 Lipid bilayer studies

4.4.4.1 *Lipid vesicle preparation (example for 80 DMPC: 20 DMPG)*

Chloroform solutions of 1,2-dimyristoyl-sn-glycero-3-phosphocholine (DMPC) and 1,2-Dimyristoyl-sn-glycero-3-phosphoglycerol, sodium salt (DMPG) lipids (10 or 25 mg/mL) were mixed at a molar ratio of DMPC:DMPG 80:20 in a 20 mL glass vial. The chloroform solution was then dried into a film under a stream of dry nitrogen before being further dried in a desiccator for 3 h. The dried lipid mix was hydrated on the day of measurement with a 20 mM hydrogenated (pH 7.2) or deuterated HEPES buffer (pD = 7.2), to make a 0.1 mg/mL lipid solution. The lipids were sonicated for 1 h at 35°C, until the suspension became optically transparent, indicative of small unlamellar vesicle formation. The vesicle solution was then centrifuged to remove residual large multilamellar aggregates. Calcium chloride ($CaCl_2$) was added to the lipid solution immediately before use, to obtain a final concentration of 5 mM only for supported bilayer formation. No calcium chloride was used for the Trp fluorescence study.

4.4.4.2 Quartz-Crystal Microbalance with Dissipation Monitoring (QCM-D)

4.4.4.2.1 Preparing the instrument

QCM-D bilayer deposition experiments and polymer/CPNT interaction studies were performed using the Q-Sense E4 (Biolin Scientific) at the University of Warwick and at ISIS Neutron Muon Source. All experiments were performed using silicon dioxide SiO_2 sensors (Biolin Scientific) that were treated in a UV/ozone cleaning chamber (Bioforce Scientific) for 15 min, immersed for 30 min in a 2% sodium dodecyl sulfate (SDS) aqueous solution, dried and treated once more in a UV/ozone chamber. The Q-Sense E4 instrument was cleaned prior to each measurement by successively flushing with 5 mL of: pure water, 1% Hellmanex solution, water, ethanol, water, running the sample chamber dry before and after each measurement.

4.4.4.2.2 Typical procedure

After placing the cleaned sensors and setting the instrument to 37°C, the system was flushed at a flow rate of 0.2 mL/min with water (1 mL) then with the buffer (1 mL) used for the experiment (PBS or HEPES buffer). The lipid vesicle suspension in buffer was then flushed in the system (1 mL), giving the expected response for lipid bilayer formation by vesicle fusion with: i) decrease in frequency (f) /increase in dissipation (D) due to vesicle adsorption; ii) increase in frequency/decrease in dissipation because of vesicle rupture and iii) fusion into a lipid bilayer as characterised by stabilisation of f and D).[42] Buffer (2 mL) was flushed to remove any excess vesicles remaining in solution.

For interaction studies, the compound of interest (1.5 mL, 50 μM) dissolved in buffer was injected into the flow cell and the resultant changes in f and D monitored above the fundamental harmonic. Buffer was finally flushed at a constant flow rate until stable to assess the interaction strength qualitatively.

4.4.4.1 Attenuated total reflection Fourier transform infrared (ATR-FTIR) spectroscopy

4.4.4.1.1 ATR-FTIR measurements

Attenuated total reflection Fourier transform infrared spectroscopy (ATR-FTIR) was used to perform a qualitative analysis of the chemical bonds at the lipid bilayer surface. An infrared (IR) beam is shined through the interface formed by a lipid bilayer in bulk solvent water, coating, etc.) with lower refractive index (n_2) under conditions allowing for total internal reflection. The beam penetrates into the medium with a depth d, given by the following equation:

$$d = \frac{\lambda}{2\pi\sqrt{sin^2(\theta) - (\frac{n_1}{n_2})^2}}$$

Where λ is the wavelength of the incident beam (IR), θ the angle of incidence and n_1 and n_2 correspond to the refractive index of the substrate and the bulk solvent.[69] The attenuation in the reflected radiation was linked to light absorption events as material adsorbed on the substrate surface. Infrared spectroscopy being a vibrational spectroscopy technique, the bond energy is dependent on the elements present, which allows for differentiation between deuterium and hydrogen-containing bond frequencies.

ATR-FTIR spectra were acquired at ISIS Neutron Muon source, using a ThermoNicolet Nexus instrument fitted with an ATR flow cell accessory (Specac) attached to a calibrated syringe pump, a cryo-cooled mercury cadmium telluride detector and a dry-air purge operating at a flow rate of 40 L/min in order to minimize absorbance from residual water vapour in the beam path. The resolution for spectra collection was of 4 cm^{-1} and 128 interferograms were collected for each spectrum. The temperature was maintained to 37°C during the entirety of the measurement.

Silicon substrates were cleaned by sonication in 2% (w/v) SDS for 30 minutes before being thoroughly rinsed with ultrapure water, dried with a stream of dry nitrogen and placed in a UV/ozone chamber for 10 min. The substrates were rinsed with ultrapure water, dried under a stream on N_2, and re-treated in a UV/ozone chamber for 10 min. The substrate was mounted in a dry flow cell and the volume was filled with deuterated Phosphate Buffer Saline (dPBS) buffer. A background spectrum was taken for the Si substrate in buffer; this spectrum was subtracted from all acquired data to remove water vapour absorbance.

The lipid vesicle solutions (dDMPC: hDMPG 80:20 mol%, 0.1 mg/mL) were prepared in dPBS buffer following the procedure detailed in 4.4.4.1. The lipid vesicle suspension (2 mL) of dDMPC: hDMPG 80:20 was injected manually to the cells and incubated for 20 min to allow for full bilayer deposition (the process was monitored by acquiring spectra continuously).

After stabilisation of the lipid bilayer, the flow cell was flushed with buffer (2 mL) at a flow rate of 1.0 mL/min to remove any excess vesicles and a spectrum of the supported bilayer was collected at the Si-water interface. Solutions of charged CPNT **10** at 50 µM were injected manually into the flow cell over the lipid bilayer. The lipid bilayer was incubated with the hydrogenated polymer materials for 60 min; spectra were continuously acquired with a time resolution of 80 s.

4.4.4.1.2 ATR-FTIR data analysis and kinetics

Fourier self-deconvolution was executed by the OMNIC data acquisition software, keeping the amplitude and bandwidth constant across all spectra; the spectra were corrected by subtraction of the background signal, in order to remove water vapour absorbance bands. ATR-FTIR peak integrations were done on lipid-specific C-D_n (2,230 – 2,050 cm^{-1}) stretching regions, to evaluate the propensity for lipid removal upon addition of polymer or CPNT. This spectral area includes contributions from the symmetric and asymmetric C-D_2 stretching vibrations and the C-D_3 stretching vibrations arising primarily from the aliphatic phospholipid tails. The peaks in the 1,700 – 1,580 cm^{-1} region corresponding to both the HNC=O amide stretch (1,690 - 1,630 cm^{-1}) and the C=N asymmetrical vibrations (1,586 and 1,608 cm^{-1} from the guanidine moieties)[70] were also integrated, to follow the kinetics of interaction (the polymers and cyclic peptide both having amide bonds).

4.4.4.2 Fluorescence spectroscopy

4.4.4.2.1 Interaction with LUV vesicles

The interaction of Trp-containing CPNT **10** and **11** and of control CP **1** with lipid bilayers was studied by monitoring the changes in the Trp emission spectra upon addition of lipid LUV, similarly to the study carried out by Christiaens *et al*.[50] Fluorescence measurements were run in a quartz cuvette (Hellma Analytics, 10 x 10 mm) on an Agilent Technologies Cary Eclipse Fluorescence Spectrophotometer, equipped with a thermostatic controlled cuvette holder set at 37°C. Intrinsic Trp fluorescence was first measured on the sample dissolved at a concentration of 50 µM in 20 mM HEPES buffer (1.8 mL, 50 µM except for CP **1** which was measured at 12.5 µM to avoid signal saturation).

An aliquot of lipid LUV solution of hDMPC:hDMPG 80:20 (1 mg/mL) was then added, to reach a final lipid concentration of 0.1 mg/mL, used to match the one used in supported lipid bilayers assay. Emission spectra were collected between 300 and 650 nm, with an excitation wavelength of 280 nm, at slit widths of 5 nm and a scan rate of 300 nm/min (0.2 s averaging time). Spectra were collected every0 min after addition of the lipid LUV for 20 min; the position of the emission maxima was determined, in order to determine the magnitude of the blue-shift for Trp-peptides embedded in the lipid bilayer.

4.4.4.2.2 Quenching experiment with acrylamide

The quenching of Trp fluorescence was performed on CP **1** (12.5 µM, 0.25% DMSO), in the absence or presence of hDMPC: hDMPG 80:20 lipid vesicles. For experiments with lipid vesicles, the system was left to equilibrate for 20 min after adding the vesicles. Aliquots of acrylamide dissolved in HEPES buffer (2 M) were added sequentially, leaving the system to equilibrate for 5 min after each addition. The concentrations of acrylamide quencher in the medium were: 0, 0.095, 0.18, 0.33, 0.46 and 0.57 M. Stern-Vollmer plots, representing the variations of ratio between initial fluorescence (F_0) and fluorescence at a concentration of quencher (F) F_0/F were generated.

4.4.4.3 Neutron reflectivity

All the neutron reflectivity (NR) experiments presented in this chapter were performed on the Fluid Interfaces Grazing Angles ReflectOmeter (FIGARO)[71] at the Institut Laue-Langevin (Grenoble, France).

Single side polished silicon blocks (1 1 1, dimensions: 80 x 50 x 15 mm, roughness rms < 3 Å SilTronix, Archamps, France) were cleaned by two cycles of washing with ultrapure water and 30 min incubation in a UV/ozone chamber. The block were mounted in sealed lamellar flow cells (volume: 1 mL) made of PolyEtherEtherKetone (PEEK), underwater to prevent the formation of bubbles during the cell assembly.

In all the rest of the NR procedure, D_2O and H_2O will refer to a 20 mM HEPES buffer with 5 mM $CaCl_2$ (pH 6.8, pD 7.2).

NR was measured at two angles on FIGARO: 0.80° and 3.2°, with an incident neutron wavelength range of 2-30 Å (corresponding to a q-range of 0.008–0.33 $Å^{-1}$). The Si blocks, mounted in flow cells, were placed on a sample stage equipped with x-y-z translation axis and a goniometer. The flow cells were connected to HPLC pumps in order to change the solution contrasts (D_2O, H_2O, Silicon-matched water, SiMW 38% v/v D_2O, 4MW 66% v/v D_2O contrasts) and maintained at 37°C by means of a circulating water bath. The reflected neutron intensity was normalised to the incident neutron flux measured in transmission for each substrate. Transmission was measured for one Si crystal block; the same normalisation was applied for all blocks used. FIGARO was used in time-of-flight mode (ToF) for full characterisation of the Si crystal cells, lipid bilayers and final interaction with the CPNT.

Si block characterisation: The four clean Si substrates used in this experiment were first characterised by NR in H_2O and D_2O buffers.

Lipid bilayer characterisation: The lipid vesicle suspension (dDMPC: hDMPG 80:20 mol%, 0.1 mg/mL) was prepared in D_2O buffer following the procedure detailed in 4.4.4.1 and was manually injected to the cells. The system was incubated for 60 min in order to maximise bilayer coverage and was flushed with H_2O buffer. The bilayers formed were characterised in H_2O, D_2O and SiMW.

Interaction: Neutral CPNT **6** and charged CPNT **10** were dissolved separately in D_2O buffer (50 μM). The compounds were injected *via* a HPLC pump at a rate of 1 mL/min and incubated for 90 min. After incubation, any excess of sample was flushed with D_2O and full characterisation was performed in FIGARO ToF mode in four contrasts: D_2O, H_2O, SiMW, 4MW.

4.4.4.4 Analysis of the bilayer structure at the Si-water interface (NR data)

Details about the fitting procedure and the model used can be found in Appendix D, section C.3.1.

4.4.5 Biology

4.4.5.1 Bacterial strains and growth conditions

The bacterial strains used were *Pseudomonas aeruginosa* (*P. aeruginosa)* PA14, *Staphylococcus aureus* (*S. aureus)* USA300, *Staphylococcus epidermidis* (*S. Epidermidis)* and *Escherichia coli* (*E. Coli*).

4.4.5.2 Antibacterial activity measurement

Minimum inhibitory concentrations (MICs) were determined according to the standard Clinical Laboratory Standards Institute (CLSI) broth microdilution method (M07-A9-2012). These experiments were performed by Dr. Agnes Kuroki and Ramon Garcia-Maset (University of Warwick). A single colony of bacteria in agar plates were picked and dissolved in fresh media (Mueller-Hinton broth only for *S. epidermidis* and *E. Coli*, synthetic wound media or artificial sputum media were used as well for the two other strains). The concentration of bacterial cells was adjusted by measuring the optical density at 600 nm (OD600) to obtain a Mackfarland of 0.5. in order to reach a bacterial concentration of ~ 108 colony forming unit per mL (CFU mL^{-1}). The solution was diluted further by a 100 fold to obtain a concentration of 106 CFU mL^{-1}. Polymers were dissolved in distilled water and 50 μL of each test polymer was added to micro-wells followed by the addition of the same volume of bacterial suspension (106 CFU mL^{-1}). The micro-well plates were incubated at 37°C for 18 hours, and growth was evaluated by eye to check turbidity and measuring the OD600 using a plate reader. Triplicates were performed for each concentration.

4.5 References

1. J. Lombard, *Biology Direct*, 2014, **9**, 32.
2. G. L. Nicolson, *Biochimica et Biophysica Acta (BBA) - Biomembranes*, 2014, **1838**, 1451.
3. S. J. Singer and G. L. Nicolson, *Science*, 1972, **175**, 720.
4. N. D. Donahue, H. Acar and S. Wilhelm, *Advanced drug delivery reviews*, 2019, **143**, 68.
5. S. Behzadi, V. Serpooshan, W. Tao, M. A. Hamaly, M. Y. Alkawareek, E. C. Dreaden, D. Brown, A. M. Alkilany, O. C. Farokhzad and M. Mahmoudi, *Chemical Society Reviews*, 2017, **46**, 4218.
6. E. Hinde, K. Thammasiraphop, H. T. T. Duong, J. Yeow, B. Karagoz, C. Boyer, J. J. Gooding and K. Gaus, *Nature Nanotechnology*, 2017, **12**, 81.
7. D. M. Copolovici, K. Langel, E. Eriste and Ü. Langel, *ACS Nano*, 2014, **8**, 1972.
8. J. M. Steinbach, Y.-E. Seo and W. M. Saltzman, *Acta Biomaterialia*, 2016, **30**, 49.
9. A. Rydström, S. Deshayes, K. Konate, L. Crombez, K. Padari, H. Boukhaddaoui, G. Aldrian, M. Pooga and G. Divita, *PLOS ONE*, 2011, **6**, e25924.
10. L. Crombez, G. Aldrian-Herrada, K. Konate, Q. N. Nguyen, G. K. McMaster, R. Brasseur, F. Heitz and G. Divita, *Molecular Therapy*, 2009, **17**, 95.
11. L. I. Selby, C. M. Cortez-Jugo, G. K. Such and A. P. R. Johnston, *WIREs Nanomedicine and Nanobiotechnology*, 2017, **9**, e1452.
12. OECD, *Stemming the Superbug Tide*, 2018.
13. U. Hofer, *Nature Reviews Microbiology*, 2019, **17**, 3.
14. U. Theuretzbacher, K. Outterson, A. Engel and A. Karlén, *Nature Reviews Microbiology*, 2019.
15. M. Mahlapuu, J. Håkansson, L. Ringstad and C. Björn, *Frontiers in Cellular and Infection Microbiology*, 2016, **6**.
16. N. Principi, E. Silvestri and S. Esposito, *Frontiers in Pharmacology*, 2019, **10**.
17. C. Ergene, K. Yasuhara and E. F. Palermo, *Polymer Chemistry*, 2018, **9**, 2407.
18. P. V. Baptista, M. P. McCusker, A. Carvalho, D. A. Ferreira, N. M. Mohan, M. Martins and A. R. Fernandes, *Frontiers in Microbiology*, 2018, **9**.
19. S. J. Lam, E. H. H. Wong, C. Boyer and G. G. Qiao, *Progress in Polymer Science*, 2018, **76**, 40.
20. D. Yao, Y. Guo, S. Chen, J. Tang and Y. Chen, *Polymer*, 2013, **54**, 3485.
21. M. Lundqvist, J. Stigler, G. Elia, I. Lynch, T. Cedervall and K. A. Dawson, *Proceedings of the National Academy of Sciences*, 2008, **105**, 14265.
22. U. Sakulkhu, M. Mahmoudi, L. Maurizi, G. Coullerez, M. Hofmann-Amtenbrink, M. Vries, M. Motazacker, F. Rezaee and H. Hofmann, *Biomaterials Science*, 2015, **3**, 265.
23. J. Sanchez-Quesada, M. R. Ghadiri, H. Bayley and O. Braha, *Journal of the American Chemical Society*, 2000, **122**, 11757.
24. S. Fernandez-Lopez, H.-S. Kim, E. C. Choi, M. Delgado, J. R. Granja, A. Khasanov, K. Kraehenbuehl, G. Long, D. A. Weinberger, K. M. Wilcoxen, *et al.*, *Nature*, 2001, **412**, 452.
25. W. S. Horne, C. M. Wiethoff, C. Cui, K. M. Wilcoxen, M. Amorin, M. R. Ghadiri and G. R. Nemerow, *Bioorganic & Medicinal Chemistry*, 2005, **13**, 5145.
26. M. R. Ghadiri, J. R. Granja and L. K. Buehler, *Nature*, 1994, **369**, 301.
27. H. S. Kim, J. D. Hartgerink and M. R. Ghadiri, *Journal of the American Chemical Society*, 1998, **120**, 4417.
28. Y. Fu, T. Yan and X. Xu, *The Journal of Physical Chemistry B*, 2017, **121**, 9006.
29. M. Danial, C. M. N. Tran, K. A. Jolliffe and S. Perrier, *Journal of the American Chemical Society*, 2014, **136**, 8018.
30. M. Danial, C. My-Nhi Tran, P. G. Young, S. Perrier and K. A. Jolliffe, *Nature Communications*, 2013, **4**, 2780.

31. M. Hartlieb, S. Catrouillet, A. Kuroki, C. Sanchez-Cano, R. Peltier and S. Perrier, *Chemical Science*, 2019, **10**, 5476.
32. J. C. Brendel, J. Sanchis, S. Catrouillet, E. Czuba, M. Z. Chen, B. M. Long, C. Nowell, A. Johnston, K. A. Jolliffe and S. Perrier, *Angewandte Chemie International Edition*, 2018, **57**, 16678.
33. E. Rascol, J.-M. Devoisselle and J. Chopineau, *Nanoscale*, 2016, **8**, 4780.
34. J. Y. Rho, H. Cox, E. D. H. Mansfield, S. H. Ellacott, R. Peltier, J. C. Brendel, M. Hartlieb, T. A. Waigh and S. Perrier, *Nature Communications*, 2019, **10**, 4708.
35. A. Kuroki, P. Sangwan, Y. Qu, R. Peltier, C. Sanchez-Cano, J. Moat, C. G. Dowson, E. G. L. Williams, K. E. S. Locock, M. Hartlieb, *et al.*, *ACS Applied Materials & Interfaces*, 2017, **9**, 40117.
36. L. Martin, R. Peltier, A. Kuroki, J. S. Town and S. Perrier, *Biomacromolecules*, 2018, **19**, 3190.
37. S. E. Exley, L. C. Paslay, G. S. Sahukhal, B. A. Abel, T. D. Brown, C. L. McCormick, S. Heinhorst, V. Koul, V. Choudhary, M. O. Elasri, *et al.*, *Biomacromolecules*, 2015, **16**, 3845.
38. A. M. Kuroki, PhD thesis, University of Warwick, 2019.
39. www.sasview.org).
40. T. R. Barlow, PhD thesis, University of Warwick, 2017.
41. L. A. Clifton, R. A. Campbell, F. Sebastiani, J. Campos-Terán, J. F. Gonzalez-Martinez, S. Björklund, J. Sotres and M. Cárdenas, *Advances in Colloid and Interface Science*, 2020, **277**, 102118.
42. N. Yousefi and N. Tufenkji, *Frontiers in Chemistry*, 2016, **4**, 1.
43. J. R. Silvius, in *Lipid-Protein Interactions*, John Wiley & Sons, Inc., New York, 1982.
44. R. M. Epand and R. F. Epand, *Biochimica et Biophysica Acta (BBA) - Biomembranes*, 2009, **1788**, 289.
45. A. Åkesson, T. K. Lind, R. Barker, A. Hughes and M. Cárdenas, *Langmuir*, 2012, **28**, 13025.
46. T. K. Lind, M. W. A. Skoda and M. Cárdenas, *ACS Omega*, 2019, **4**, 10687.
47. F. Nederberg, Y. Zhang, J. P. K. Tan, K. Xu, H. Wang, C. Yang, S. Gao, X. D. Guo, K. Fukushima, L. Li, *et al.*, *Nature Chemistry*, 2011, **3**, 409.
48. L. Liu, K. Xu, H. Wang, P. K. Jeremy Tan, W. Fan, S. S. Venkatraman, L. Li and Y.-Y. Yang, *Nature Nanotechnology*, 2009, **4**, 457.
49. A. I. P. M. De Kroon, M. W. Soekarjo, J. De Gier and B. De Kruijff, *Biochemistry*, 1990, **29**, 8229.
50. B. Christiaens, S. Symoens, S. Vanderheyden, Y. Engelborghs, A. Joliot, A. Prochiantz, J. Vandekerckhove, M. Rosseneu and B. Vanloo, *European Journal of Biochemistry*, 2002, **269**, 2918.
51. T. Keleti, *FEBS Letters*, 1970, **7**, 280.
52. L. Braun, M. Uhlig, R. von Klitzing and R. A. Campbell, *Advances in Colloid and Interface Science*, 2017, **247**, 130.
53. G. Fragneto, *The European Physical Journal Special Topics*, 2012, **213**, 327.
54. A. V. Hughes, S. J. Roser, M. Gerstenberg, A. Goldar, B. Stidder, R. Feidenhans'l and J. Bradshaw, *Langmuir*, 2002, **18**, 8161.
55. V. Rondelli, P. Brocca, N. Tranquilli, G. Fragneto, E. Del Favero and L. Cantù, *Biophysical Chemistry*, 2017, **229**, 135.
56. S. Stanglmaier, S. Hertrich, K. Fritz, J. F. Moulin, M. Haese-Seiller, J. O. Rädler and B. Nickel, *Langmuir*, 2012, **28**, 10818.
57. H. P. Wacklin, *Langmuir*, 2011, **27**, 7698.
58. S. Tatur, M. Maccarini, R. Barker, A. Nelson and G. Fragneto, *Langmuir*, 2013, **29**, 6606.
59. D. Di Silvio, M. Maccarini, R. Parker, A. Mackie, G. Fragneto and F. Baldelli Bombelli, *Journal of Colloid and Interface Science*, 2017, **504**, 741.

60. A. Luchini, Y. Gerelli, G. Fragneto, T. Nylander, G. K. Pálsson, M.-S. Appavou and L. Paduano, *Colloids and Surfaces B: Biointerfaces*, 2017, **151**, 76.
61. M. Hayami, A. Okabe, R. Kariyama, M. Abe and Y. Kanemasa, *Microbiology and Immunology*, 1979, **23**, 435.
62. P. Komaratat and M. Kates, *Biochimica et Biophysica Acta (BBA) - Lipids and Lipid Metabolism*, 1975, **398**, 464.
63. S. T. Albelo and C. E. Domenech, *FEMS Microbiology Letters*, 1997, **156**, 271.
64. L. A. Clifton, S. A. Holt, A. V. Hughes, E. L. Daulton, W. Arunmanee, F. Heinrich, S. Khalid, D. Jefferies, T. R. Charlton, J. R. P. Webster, *et al.*, *Angewandte Chemie International Edition*, 2015, **54**, 11952.
65. M. Otto, *Nature Reviews Microbiology*, 2009, **7**, 555.
66. S. A. Raw, *Tetrahedron Letters*, 2009, **50**, 946.
67. www.synchrotron-soleil.fr/en/beamlines/swing).
68. F. Zhang, J. Ilavsky, G. G. Long, J. P. G. Quintana, A. J. Allen and P. R. Jemian, *Metallurgical and Materials Transactions A*, 2010, **41**, 1151.
69. J. Oelichmann, *Fresenius' Zeitschrift für analytische Chemie*, 1989, **333**, 353.
70. A. Ghosh, M. J. Tucker and R. M. Hochstrasser, *The Journal of Physical Chemistry A*, 2011, **115**, 9731.
71. R. A. Campbell, H. P. Wacklin, I. Sutton, R. Cubitt and G. Fragneto, *The European Physical Journal Plus*, 2011, **126**, 107.

Chapter 5

Conclusion and Perspectives

5.1 Conclusions

Cyclic peptide-polymer nanotubes (CPNT) are a novel supramolecular system, with a clear potential for biological applications. In Chapter 1, CPNT were shown to be part of a wider ecosystem of self-assembled nanocylinders. Natural nanofibers, such as the ones formed by tubulin self-assembly or actin filaments, provided inspiration to nanoscientists. For instance, rod-like viruses (e.g. Tobacco Mosaic Virus) were tailored to form nanocylinders that have found diverse applications in drug delivery. Advances in synthetic polymer chemistry allowed for the conception of self-assembling polymer nanocylinders, using methods like block copolymer, crystallisation-driven and polymerisation-induced self-assembly. Numerous applications of self-assembling polymer nanocylinders were discussed: drug delivery, immunotherapy, cryo-preservation, *etc.*. Given their high aspect ratio, nanocylinders were shown to have a tremendous potential. The systems presented in Chapter 1 demonstrated clear biocompatibility, allowed for efficient cellular uptake and had promising *in vivo* properties. In parallel, peptide-based nanocylinders were also considered, with a focus on self-assembling cyclic octapeptides, comprising of alternating D- and L- amino acids. These cyclic octapeptides can form nanotubes, thanks to hydrogen bonding between the constituting amide groups. Cyclic peptide nanotubes were extensively studied, demonstrating their potential use for antibacterial and antiviral applications, as well as gene delivery. These interesting properties were however overshadowed by a general lack of control over their self-assembly, alongside with a poor solubility in aqueous media. By conjugating polymer chains to a cyclic peptide core, it was possible to form shorter and uniform nanocylinders: cyclic peptide-polymer nanotubes. CPNT with a range of useful features (stimuli-responsiveness, secondary self-assembly) have been conceived. CPNT have already been used for anticancer drug delivery purposes; additionally, initial studies were carried out to demonstrate membrane interaction properties. The behaviour of CPNT in biological systems, however, was not fully resolved. The aim of the experimental work in this thesis was to understand better the nature of the interactions at stake in multiple models, each having its own complexity: lipid bilayers, mammalian cells, small tumour models and animal models.

In Chapter 2, new insights on the relationship between chemical composition, self-assembling behaviour and cellular uptake were obtained. Fluorescently-labelled CPNT made from different polymers (poly(ethyleneglycol) or poly(2-ethyl-2-oxazoline) based) were shown to self-assemble to varying extents, depending on the polymer nature (linear vs brush) and the number of polymer arms present in a conjugate.

A library of CP-polymer self-assemblies was therefore generated and characterised by SANS, modelling the morphologies obtained as star-like for brush-polymer CP conjugates or cylinder-like (with floating polymer chains) structures, with varying lengths (4 to over 150 nm). Interestingly, the propensity for self-assembly was linked to variations in cellular uptake in several cell lines, overall showing a larger uptake for short nanotubes (10-20 nm long). Further investigations on the intratumoural behaviour of the conjugates using tumour spheroid models showed clear differences between the uptake of small and medium/large self-assemblies. Nanotubular structures were less likely to be found in lysosomes than star-like CP-polymer conjugates. Among all compounds, CP(PEG) was shown to have the highest levels of uptake and penetration overall, with a significant increase over time, characteristic of nanocylinders. These insights are essential to design efficient drug delivery systems.

In Chapter 3, two main structural changes were looked into: the influence of the stability of the self-assembly and the presence of targeting moieties at the surface of the CPNT; cellular and animal models were both investigated in this work.

First, stabilised and elongated CPNT (>100 nm) were synthesised and characterised by SANS. Their behaviour in cells and rat models was compared to short dynamic CPNT (10 nm), using a mix-and-match approach based on the dynamics of CPNT systems to introduce labelled conjugates (fluorescent or radioactive) in the supramolecular architecture. Trends from the cellular uptake study reveal that stabilised CPNT tended to have lower uptake levels than their dynamic counterparts, which corroborates results from Chapter 2 where very long CPNT were not taken up as efficiently as smaller CPNT. The comparison of pharmacokinetic profiles in rats for both types of CPNT showed that stabilised CPNT circulated for longer and therefore had lower blood clearance than dynamic CPNT. The organ distribution study and the evaluation of the urine content indicated lower levels of renal excretion after 24 h. The combination of high blood persistence and gradual elimination over time by slow disassembly make stabilised CPNT promising drug delivery systems.

Secondly, integrin-targeting moieties (cRGDfK peptide) were attached onto dynamic CPNT. Comparing targeting (30 mol. % of integrin-targeting material) to non-targeting CPNT, slight differences could be observed in endothelial HUVEC cells, which overexpress $\alpha_v\beta_3$ integrins. Integrin-targeting CPNT had significantly different pharmacokinetic profiles to non-targeting dynamic CPNT, exhibiting higher blood clearance.

This phenomenon was further understood when examining the biodistribution profiles, as integrin-targeting CPNT accumulated more readily in organs pertaining to the mononuclear phagocyte system (liver, spleen). These results suggest higher levels of recognition of integrin-targeting CPNT by the immune system. These results will help reconsidering our approach to active targeting for the future design of drug delivery vehicles.

In Chapter 4, the interaction of a library of cationic polymers and CPNT with model lipid bilayers was explored. A small range of short, neutral and charged CPNT (10-20 nm) with increasing complexity were conceived in this study, using guanidinium moieties to introduced positive charges. An initial screening study relying on the interaction of polymers and CPNT with supported lipid bilayers was performed monitoring changes in frequency and dissipation on a QCM-D instrument. The bilayers employed in this study were zwitterionic lipid DMPC and a more negatively charged lipid mixture DMPC:DMPG 80:20. Interestingly, for a given charged CPNT, the interaction was stronger in lipid mixtures with a high content of negatively charged lipids. Overall, charged CPNT outperformed charged polymers and neutral CPNT did not show any interaction on the PC:PG model. The interaction of charged CPNT was further investigated using different techniques. The lack of blue shift on Trp fluorescence spectroscopy showed that the Trp on the CPNT did not embed in the hydrophobic tail region of the bilayer, unlike free CP. ATR-FTIR measurements, using a mixture of dDMPG:hDMPC, demonstrated that no lipid removal was occurring in the course of the interaction; embedding in the bilayer seemed to occur as shown by the higher reflected signal visualised in the amide stretching region. Finally, neutron reflectivity measurements supported a model where charged CPNT were creating pores within the asymmetric bilayer whilst also forming a diffuse hydrated layer above the outer headgroup leaflet. Assessment of the antibacterial properties showed that some activity could be detected for charged hydrophilic CPNT at high concentrations, suggesting there is clear room for improvements to design more potent antibacterial CPNT.

5.2 Perspectives

5.2.1 General insights from this work

Several points of reflection can be contemplated from all the results summarised above. From the study carried out in Chapter 2 and 3, it is clear that moderate levels of self-assembly into CPNT are essential to efficient cellular uptake; however, the pharmacokinetic profile of longer stabilised CPNT could be more interesting in certain cases, given the long circulation time.

A right balance is to be found between uptake into cells of interest and satisfactory pharmacokinetic properties for a given CPNT. It is expected that such an equilibrium will strongly depend on the application being considered, for instance whether a rapid intracellular delivery is preferable (e.g. urgent antibiotic treatment) or if the goal is to have a slow and specific accumulation over time (e.g. in a tumour). The introduction of adequate stimuli-responsive moieties for drug release purposes could help facing such challenges; existing examples include pH, redox reactions, enzyme cleavage, light-responsiveness, etc. Caution needs to be taken when selecting an appropriate stimulus to induce a response, with regards to the level of specificity sought and the applicability *in fine*. In addition to this, the self-assembly of the CPNT must be characterised after any structural alteration as it was seen here that the insertion of certain moieties can affect the self-assembly (e.g.: c(RGDfK) labelling). In this regard, it would be interesting to adopt a *drug-first* approach for CPNT-based drug delivery vehicles, where each system is tailored to the specific drug it is aimed to deliver instead of attempting to develop a universal carrier.

For the specific example of anticancer drug delivery, additional animal studies with tumour-bearing animals are desirable. Future work should therefore simultaneously investigate the biodistribution of CPNT in tumour-bearing animal models and determine the drug release efficiency. The effect of protein corona formation on CPNT *in vitro* and *in vivo* behaviour should ideally also be studied more extensively, alongside with better characterisation of the self-assemblies in the presence of a corona. Unlike rigid nanoparticle systems (e.g. metal and polymer-based), it is very complex to isolate CPNT with the protein corona. A better understanding of the effect of protein corona on self-assembly could potentially be achieved by exploiting contrast matching in neutron scattering and should first focus on simple single protein mixes (e.g. albumin).

As for the study of membrane interactions, ongoing work is aiming to determine differences in lipid bilayer interaction between a free charged polymer and self-assembled CPNT by neutron reflectivity. More advanced lipid models, incorporating lipopolysaccharides (LPS) or peptidoglycan mimics would be interesting to consider, in order to obtain a fuller understanding of the membrane interaction. Similarly, it would be good to attempt making more accurate mammalian cell mimics, using cholesterol and other lipids and see how CPNT can interact with such models. It could also be of interest to attempt incorporating charged elements to promote cellular uptake of CPNT systems and to obtain more information on the nature of the resulting interaction (e.g. levels of direct translocation). In the quest for antibacterial CPNT, it will be essential to find the right balance between the number of charges in the system, its proclivity for self-assembly and the membrane disruption potential.

The question of the need for much longer charged CPNT self-assemblies remains open; cellular toxicity of such nanomaterials also requires further investigation. The addition of lipid-like moieties to the CPNT may also further enhance membrane interaction and should not be ruled out. Similarly to what has been mentioned above, the effect of protein corona formation on charged CPNT is worth investigating especially given that proteins tend to interact strongly with positively charged surfaces. Finally, a more comprehensive study of the interaction of some of the CPNT systems investigated in past work would be welcome, not least to compare the behaviour of CPNT "re-assembling" (e.g. the work from Hartlieb *et al.*)[1] to the charged systems presented here.

5.2.2 Additional considerations

A few challenges still need to be overcome to maximise the potential of CPNT for biological applications. The main shortcomings of CPNT-based systems lie in the relative lack of size control and the complex characterisation of the self-assemblies. Ongoing work is under consideration to evaluate the effect of each design parameter on self-assembly in a more systematic manner: polymer DP, monomer nature, presence of hydrophobic or aromatic units in the chain, etc. Besides these polymer-focused considerations, it is crucial to re-investigate the role of the amino acids side chain in the CPNT self-assembly process (in particular the use of Trp and compare it to other aromatic amino acids like Tyr or Phe) and to establish "structure-activity" relationships. As for characterisation techniques, more efforts should be put into observing these supramolecular self-assemblies using techniques *in solutio*, such as Liquid-Phase Electron Microscopy (LPEM). Insights on the size distribution of the CPNT, using a non-disrupting analytical method, would be welcome and are currently being investigated using techniques such as Asymmetrical flow field-flow fractionation (AF4). Finally, the dynamics of self-assembly for different CPNT (in particular, CPNT like CPNT **7** and **11** in Chapter 4 which contain a hydrophobic block but forms short nanotubes) could be explored in greater detail. In addition to studies relying on the Förster resonance energy transfer (FRET) fluorescence, neutron contrast matching studies, mixing deuterated and hydrogenated CPNT, could be considered. Overall, a better understanding of CPNT size control, size distribution and of the dynamics of self-assembly is essential to reach the full potential of these promising nanomaterials.

5.3 References

1. M. Hartlieb, S. Catrouillet, A. Kuroki, C. Sanchez-Cano, R. Peltier and S. Perrier, *Chemical Science*, 2019, **10**, 5476.

APPENDIX

Appendix A: Supplementary information to Chapter 2

A.1 NMR spectra

A.1.1 NMR spectrum linear peptide

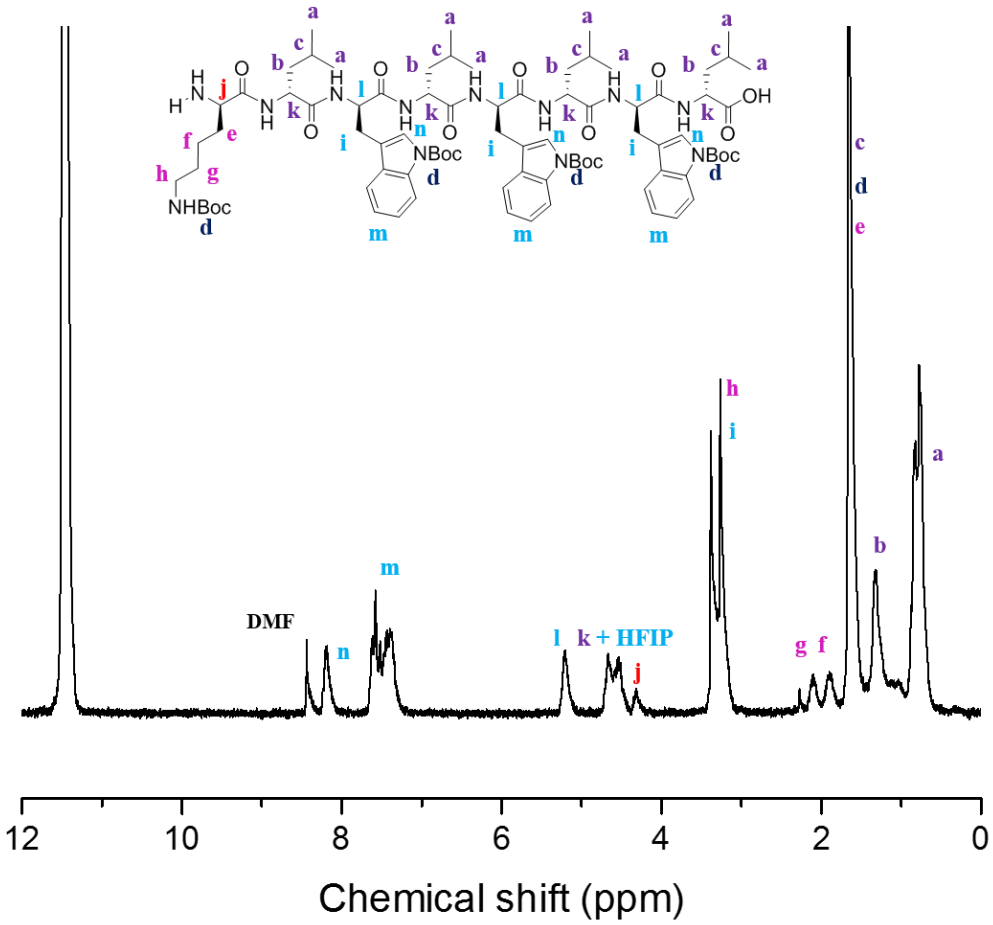

Figure A-1: NMR spectrum for the protected linear peptide used to synthesise CP **1**.

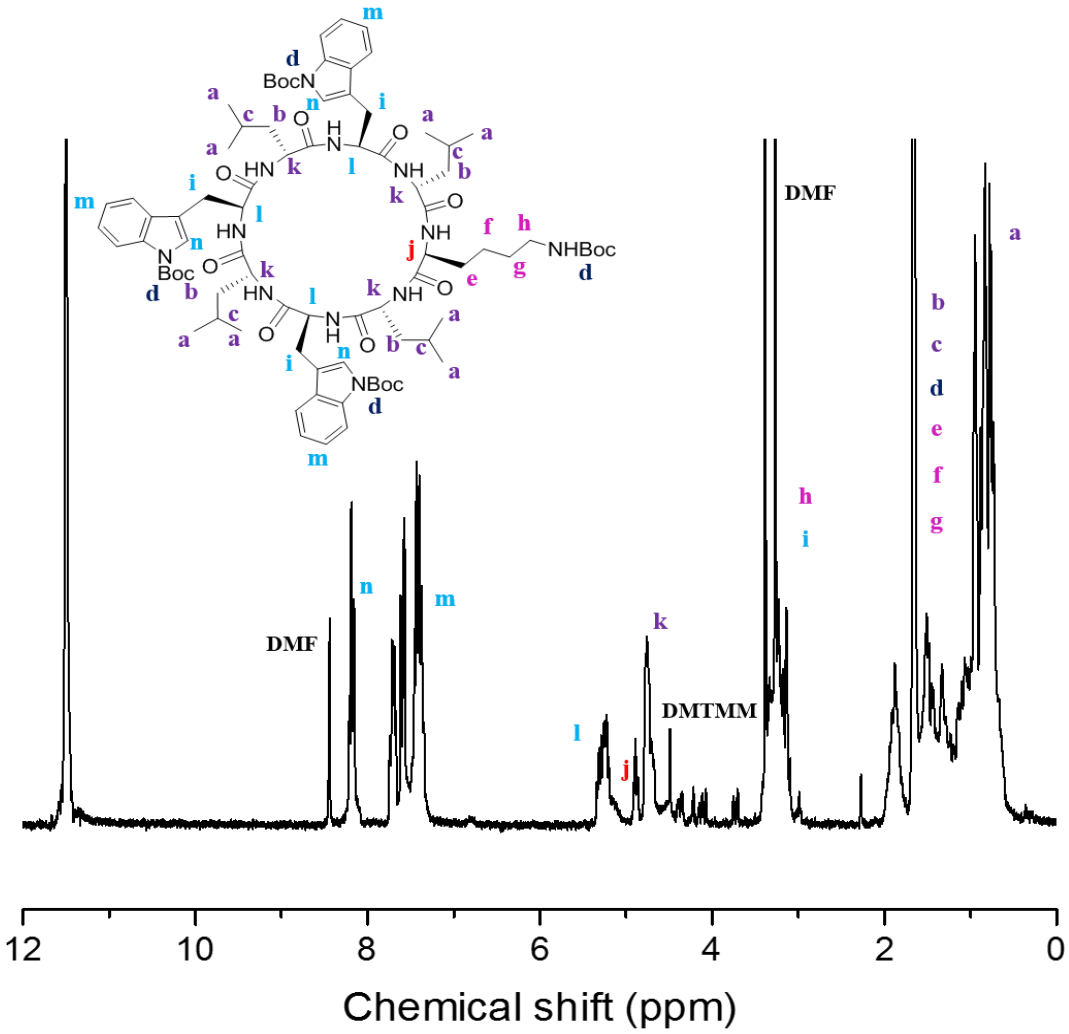

Figure A-2: NMR spectrum for the protected cyclic peptide used to synthesise CP **1.**

A.1.2 NMR spectrum cyclic peptide 1

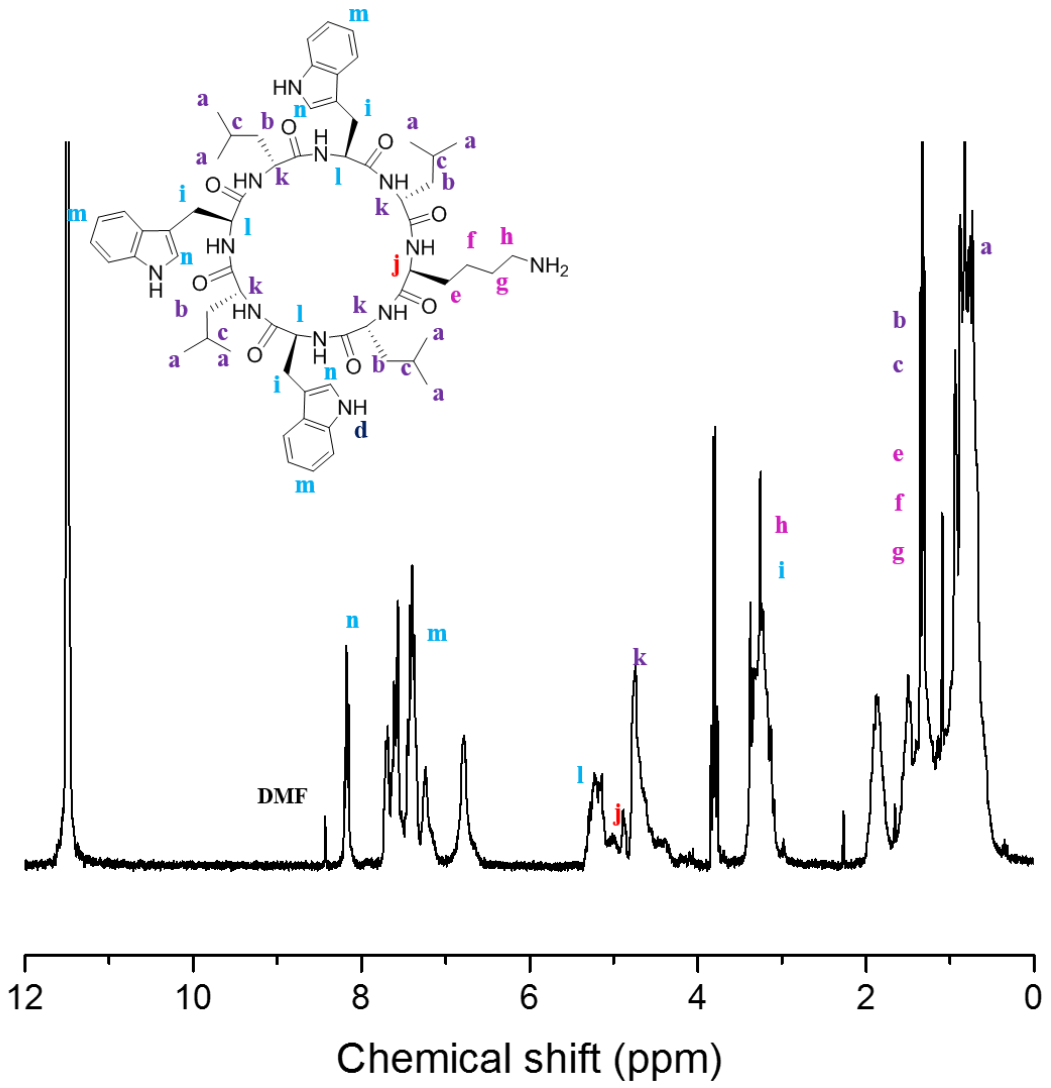

Figure A-3: NMR spectrum for cyclic peptide CP **1.**

A.1.3 NMR spectrum for PEtOx 13

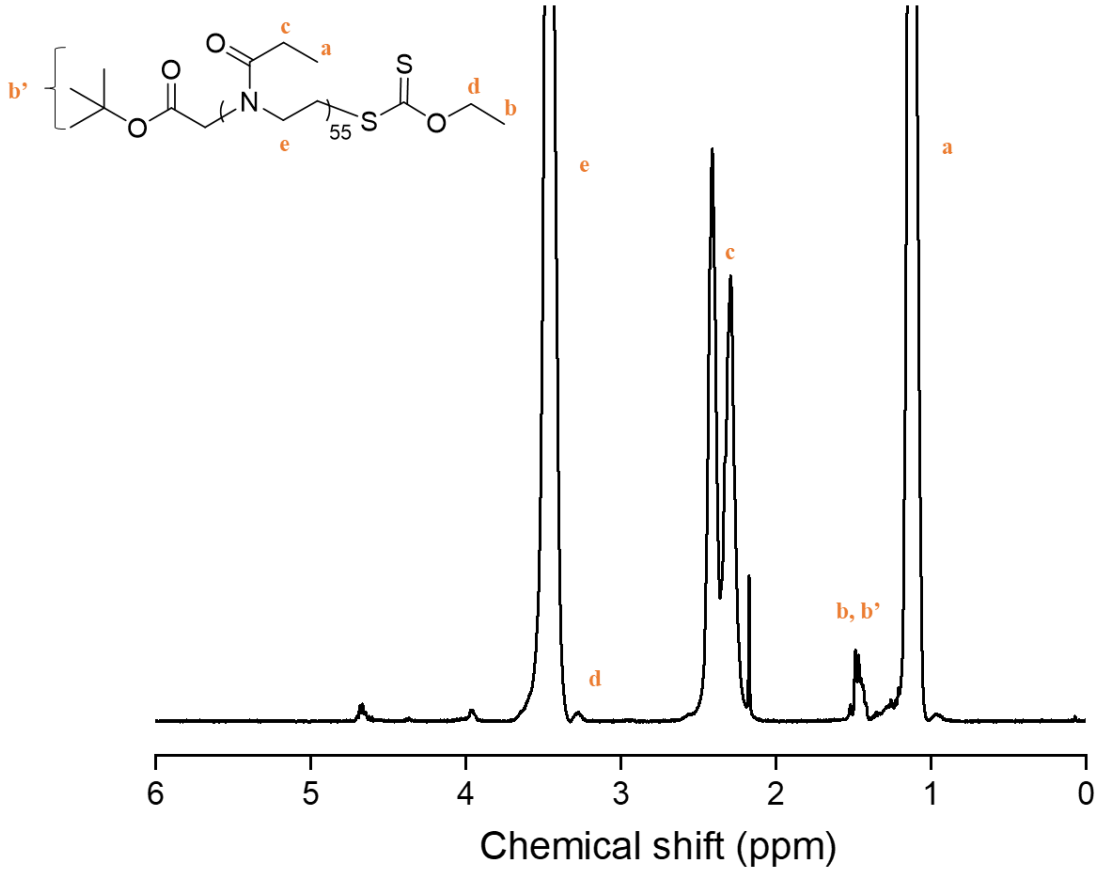

Figure A-4: NMR spectrum for PEtOx **13**.

A.1.4 NMR spectrum for PEtOx 14

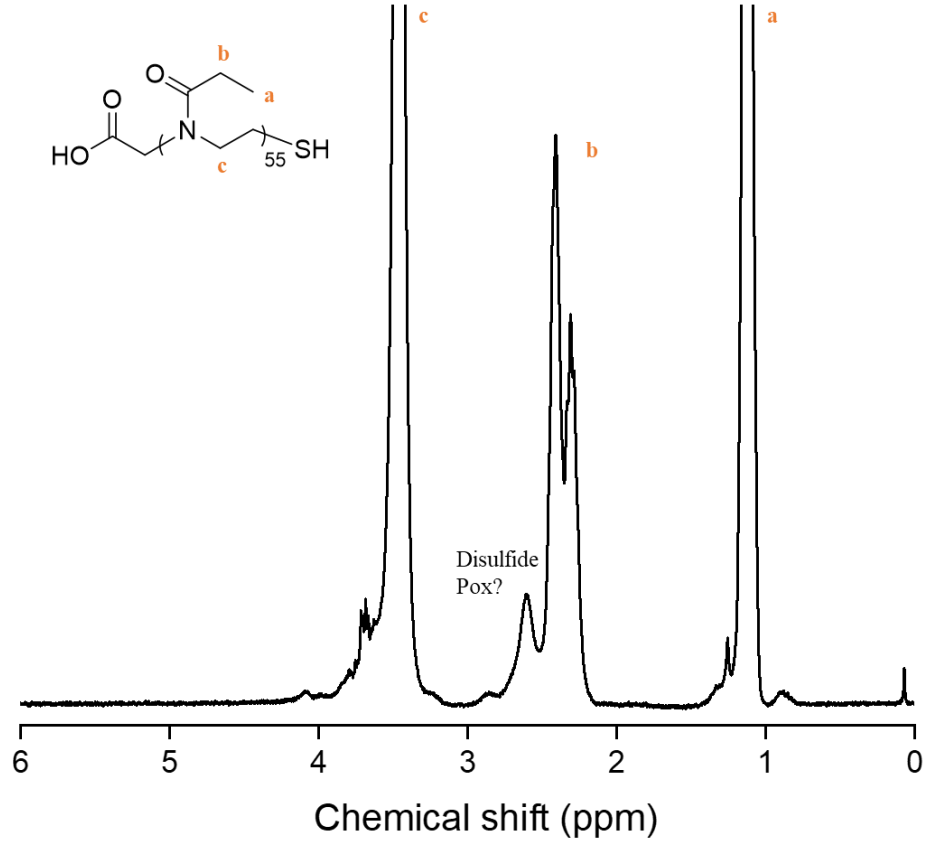

Figure A-5: NMR spectrum for PEtOx 14 (loss of the xanthate and tBu protecting groups can be noticed around 1.5 ppm).

A.1.5 NMR spectrum bifunctional PEG 4

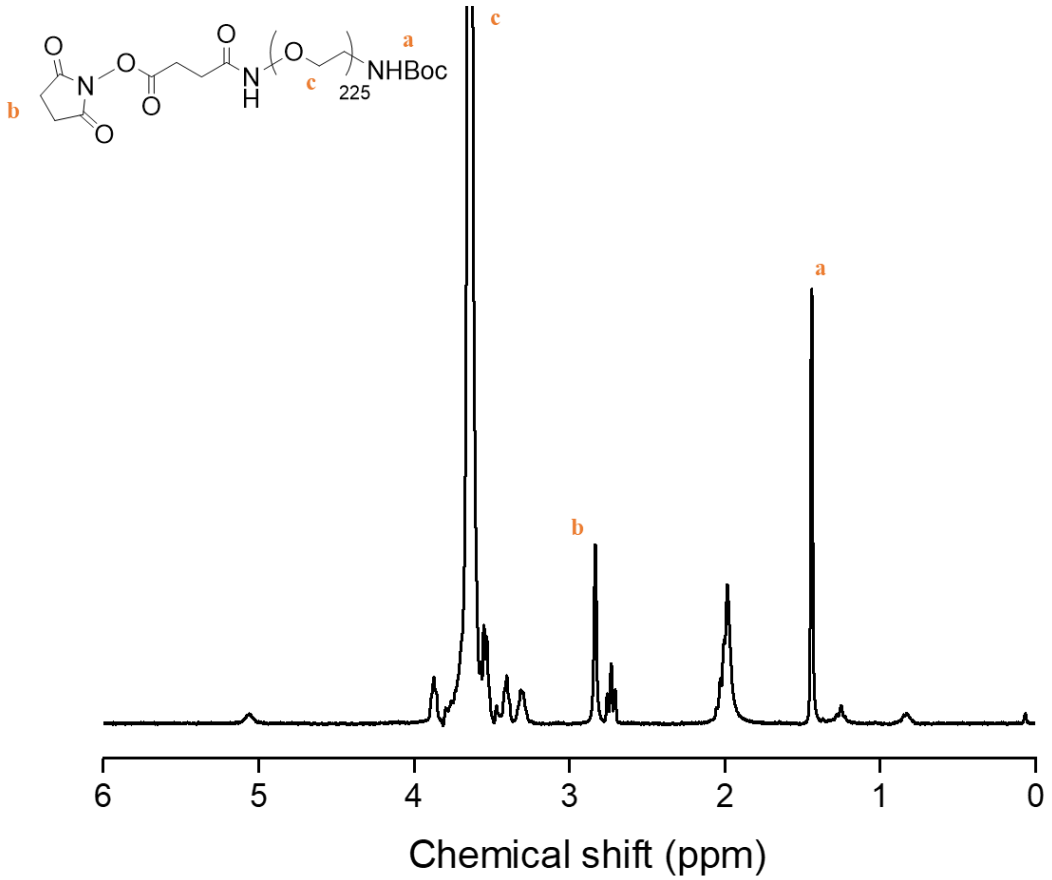

Figure A-6: NMR spectrum for commercial bifunctional PEG **4** used.

A.1.6 NMR spectrum poly(PEGA-*stat*-NAS) 19

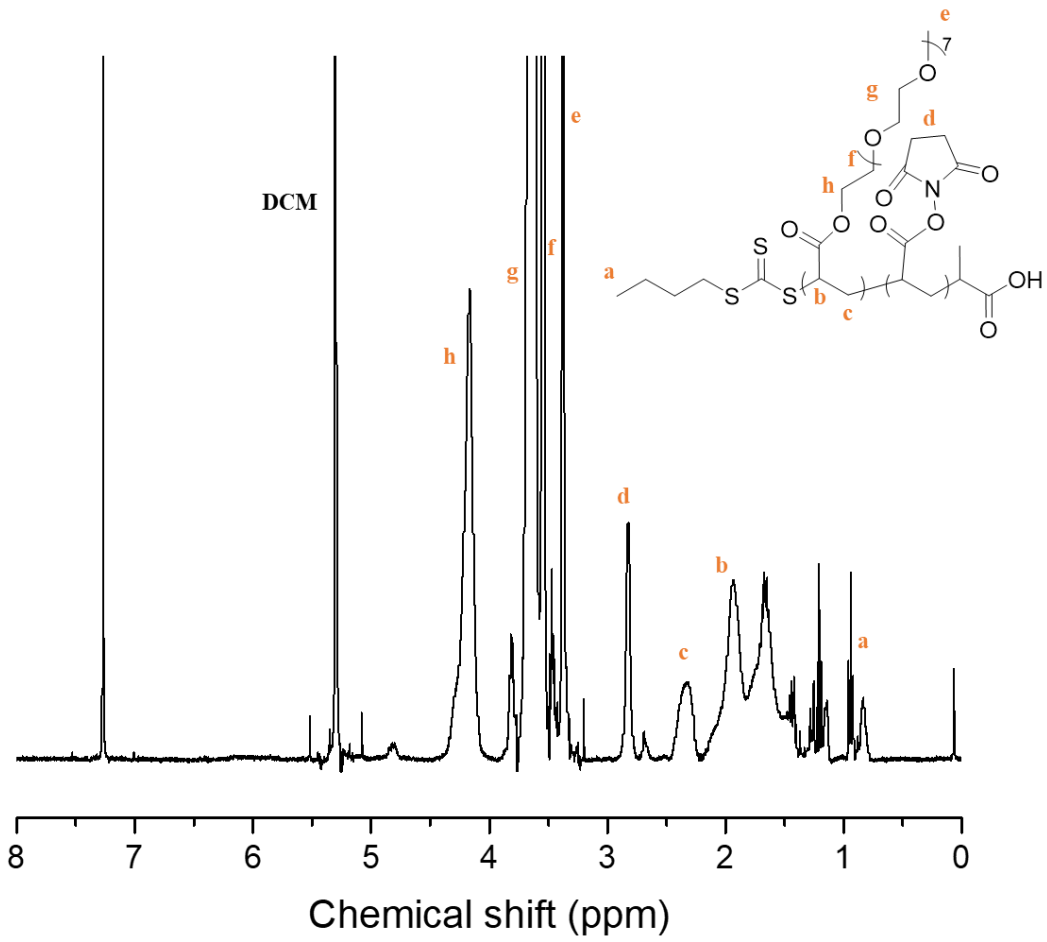

Figure A-7: NMR spectrum for poly(PEGA-*stat*-NAS) **19**

A.1.7 NMR spectrum poly(PEGA-*stat*-Cy3Am) 5

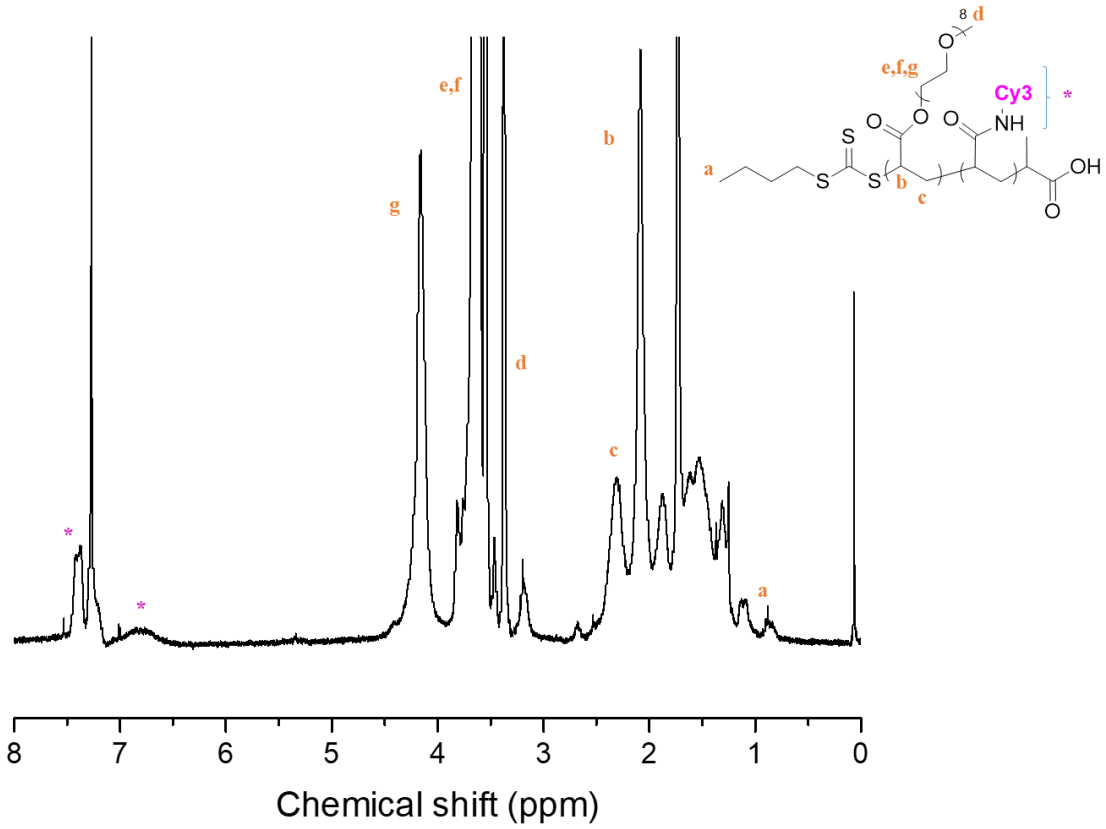

Figure A-8: NMR spectrum for poly(PEGA-*stat*-Cy3Am*)* **5.**

A.2 Mass spectrometry

A.2.1 Mass spectrometry of PEtOx 13

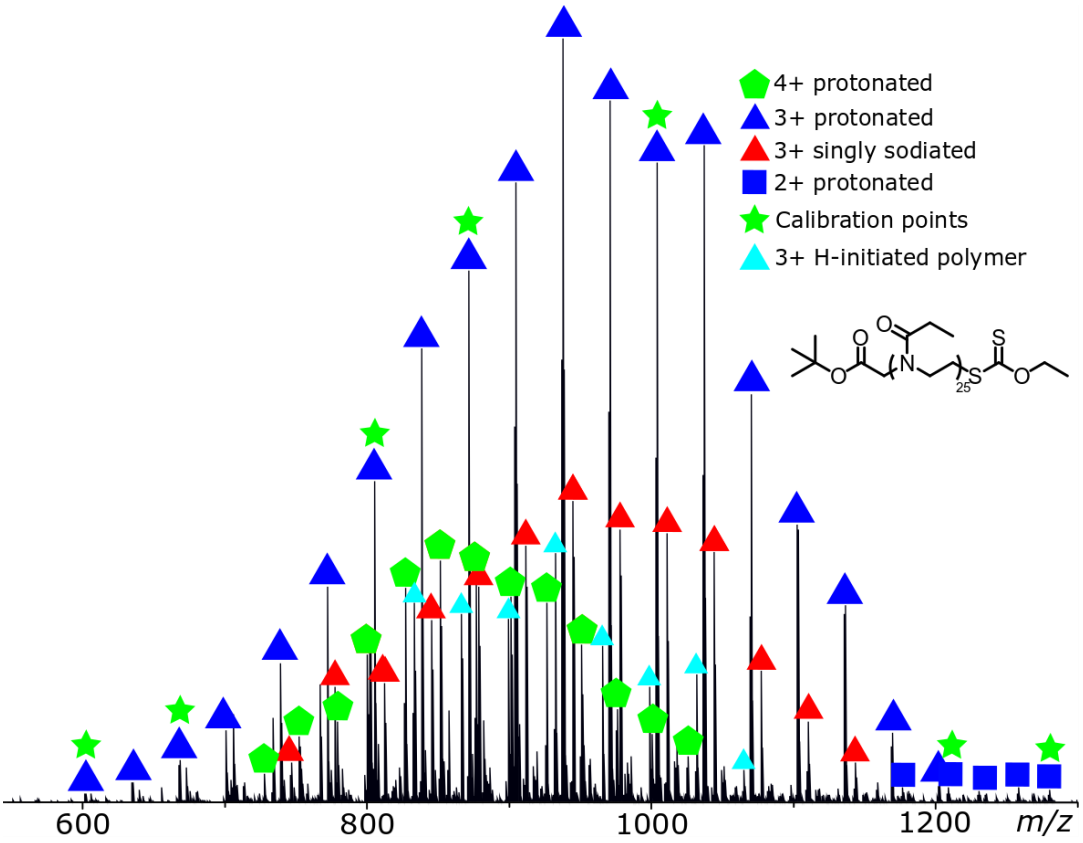

Figure A-9: ESI-microTOF measured for a smaller polymer equivalent of polymer **13.**

A.3 Characterisation of the self-assemblies

A.3.1 Fitting process

Fitting of the SANS data for this chapter was performed using both SasView and SasFit software packages.[1, 2] SasView was used for fitting data to the following models: Guinier-Porod, Core-shell cylinder, Star polymer, Gaussian coil. SasFit was employed for the CYL + CHAIN_RW and ELL + CHAIN_RW models, which represent either a cylinder or an ellipsoid core structure to which Gaussian coil-like polymer chains are attached. The fitting process was divided in multiple steps.

A.3.1.1 Guinier-Porod model

The data was first fitted to a shape-independent Guinier-Porod model.[3] The Guinier-Porod model is a unified model, taking into account a behaviour following a unified Guinier law for low q values (with the dimensionality parameter s, varying depending on the morphology) and a Porod law at high q (with the Porod exponent m).

The scale factors for each model can be related to each other as a result of the continuity of the scattering cross-section. This model returns the value of s with the following general indications: s = 0 for 3D globular objects (e.g. spheres), s = 1 for rod-like structures, s = 2 for structures with 1D symmetry (lamellae, platelets). The radius of gyration Rg can also be estimated. Depending on the s value returned from this initial fit, different models were tested.

For $0<s<0.5$, ellipsoid models were tested. If $0.5<s<1.5$, models using cylinders were tested. The core-shell cylinder from SasView and the SasFit cylindrical micelle model with Gaussian polymer chains were both tested. For very short cylindrical morphologies, a star polymer model was also used to describe the system. Gaussian coil fits were tested for most non-trivial fittings.

Note for all models requiring scattering length density (SLD) values: SLD were calculated using the sum of the coherent scattering lengths for all atoms (obtained from the literature) constituting the molecules of interest and dividing it by the calculated molecular volume.

A.3.1.2 Core-shell cylinder model

The core-shell cylinder employed from SasView considers the system to be composed of a cylindrical core with a certain scattering length density (SLD_{core}) and radius, surrounded by a shell enveloping it fully (SLD_{shell}), with a thickness t.[1, 4] The length of the total cylinder is the length of the core cylinder plus twice the thickness of the shell. A correction for polydispersity of thickness has been accounted for when necessary. The full equations ruling this model are detailed on the SasView website.[1] The scale and background factors are parameters associated to the X-ray or neutron source. For polymers, the density used for the molecular volume was approximated to the value for a monomer unit. The core was considered to be the CP (with a fixed core radius of 3.5 Å and neutron SLD of 1.61 or $1.42.10^{-6}Å^{-2}$, for CP **1** and CP **2** respectively). Data fitting returns the length and the thickness of the shell in this case.

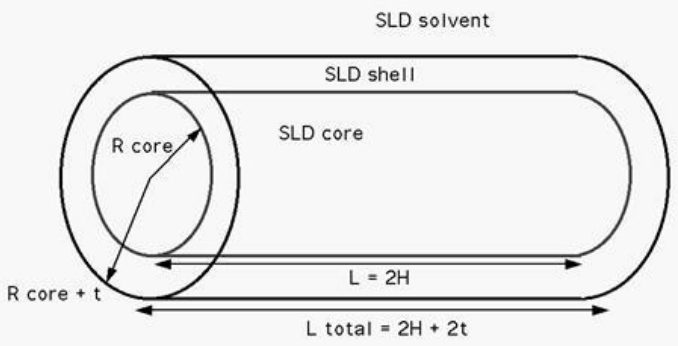

Figure A-10: Graphical description of the core-shell cylinder model.

A.3.1.3 Cylindrical micelle CYL+CHAINS_RW

The CYL+CHAINS_RW form factor model on SasFit describes the system as a core cylinder with Gaussian polymer chains.[5]

This system has similar input parameters than the core-shell cylinder model, with additional parameters such as the propensity for solvent penetration to the core x_{core} (which was set to 0 for cyclic peptide based materials), interpenetration of polymer chains d (set to 1 to mimic an absence of interpenetration into the core) and the molecular volume of the brush (V_{brush}). The polymer radius of gyration (R_g) is calculated here instead of a shell thickness. The model returns R_g and the height of the cylinder core (H).

Figure A-11: Graphical description of the cylindrical micelle model.

A.3.1.4 Ellipsoid

The ellipsoidal micelle ELL+CHAINS_RW model was chosen over the spherical model as a sphere fitting is just a particular case of an ellipsoid with an eccentricity ε=1. The input parameters are identical to CYL+CHAINS_RW, except that the core structure is an ellipsoid instead of a cylinder. The height present in the cylinder model is replaced with the ellipsoid eccentricity. This form factor was tested on non-trivial fits.

Figure A-12: Graphical description of the ellipsoidal micelle model.

A.3.1.5 Gaussian coil

The Gaussian coil model describes the scattering of polydisperse polymer chains in conditions under which the distances between segments follow a Gaussian distribution.[6] It returns the extrapolated intensity at q = 0 and the R_g value of the polymer chain, with no specific self-assembling feature. The mathematical expression is as follows:

$$(1)\ I(q) = \text{scale} \cdot I_0 \cdot P(q) + \text{background}$$

$$(2)\ I_0 = \phi_{poly} \cdot V \cdot (\rho_{poly} - \rho_{solv})^2 \ with\ V = \frac{M}{N_A \delta}$$

The I_0 value is calculated from the polymer molecular weight, which in these fits is the unimer molecular weight. The density δ and the polymers and solvent SLD are also used to calculate that value of I_0.

A.3.1.6 Star polymer

The star polymer model employed was based on the Benoit star and models the data to a star polymer with *f* Gaussian-coil like polymer arms. The model returns a fit with a certain number of polymer arms and the squared value of the radius of gyration. The molecular weight of the "self-assembly" can be estimated as the scale factor for low q value is equivalent to the Guinier term I_0 for a polymer coil, as described in A.3.1.5.

A.3.1.7 Model selection

In all fittings, the reduced chi^2 value is a statistical indicator of the goodness of the fit (a low value corresponding to a better fit). Model selection solely based on a comparison of the chi^2 values fail to account for chi^2 reduction in the presence of many parameters. In order to correct for the varying amount of fitting parameters in the fitting process, the Akaike information criterion (AIC) was used as a tool for unbiased model selection.[7] The AIC is calculated as described by (3):

$$(3)\ AIC = \chi^2 + 2p + \frac{2p(p+1)}{N-p-1}$$

In this equation, p represents the number of fitting parameters for a given model and N is the number of bins given by $N = 1.88.n^{2/5}$ where n is the number of points taken into account in the fitting. The best fit was the one with the lowest AIC value, excluding exploratory fits using the Guinier-Porod model. Results from AIC calculations are summarised in **Table A-1**.

Table A-1: AIC calculation for each compound analysed by SANS. Cyl/Ellipsepol: Cylindrical or Ellipsoidal micelle, CSC: core-shell cylinder. Best fits in bold green.

Model	n_{points}	Red chi2	Number of parameters	AIC
CP(PEG) **8**				
Guinier	56	84.4	5	112
CSC	56	304.9	8	675
Cylpol	**50**	**45.87**	**11**	**-20**
Ellipsepol	51	2230	11	2162
Gaussian	56	1606	5	1633
Star	56	82.82	4	100
$CP(PEG)_2$ **9**				
Guinier	68	4.798	5	29
CSC	68	113.9	8	253
Cylpol	**68**	**5.270**	**11**	**-117**
Ellipsepol	62	14.41	11	-83
Gaussian	68	34.87	5	59
Star	68	7.420	4	23
CP(PEtOx) **6**				
Guinier	56	1.430	5	29
CSC	68	6.390	8	146
Cylpol	**43**	**3.030**	**11**	**-50**
$CP(PEtOx)_2$ **7**				
Guinier	68	6.410	5	31
CSC	68	40.09	8	180
Cylpol	**65**	**10.93**	**11**	**-98**
CP-[poly(PEGA)] **10**				
Guinier	68	13.80	5	38
CSC	68	104.6	8	244
Cylpol	68	203.6	11	82
Gaussian	65	776.0	5	801
Star	**68**	**8.106**	**4**	**24**

A.3.2 Small angle neutron scattering (fitting)

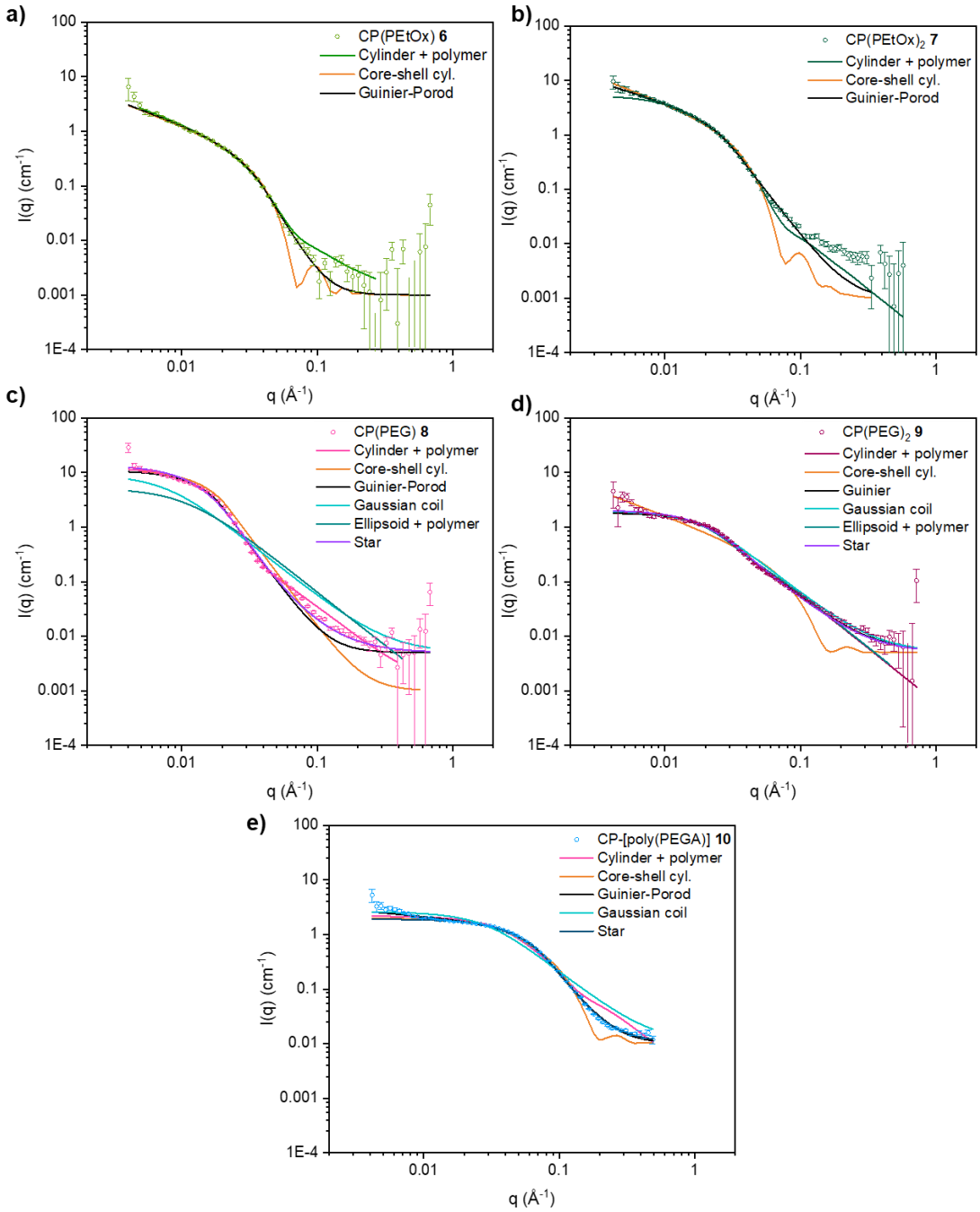

Figure A-13: SANS profiles for: a) CP(PEtOx) **6**, b) $CP(PEtOx)_2$ **7**, c) CP(PEG) **8**, d) $CP(PEG)_2$ **9** and e) CP-[poly(PEGA)] **10** with all fitting models attempted. The data is represented as hollow circles with the appropriate statistical error bars. The fits are represented by lines of different colours (hollow circle colour: best fit - Cylinder + Polymer OR star; core-shell cylinder: orange; Guinier-Porod model: black; Gaussian coil: blue; Ellipsoid + Polymer: teal; star polymer: purple).

The different fitting parameters for the cylindrical micelle-fitted conjugates presented here are detailed in the following tables. The compounds are referred to as cyclic peptide-polymer conjugates (CPPC), according to the previous numbering system.

Table A-2: Fitting parameters for CP(PEtOx) **6**, CP(PEtOx)$_2$ **7**, CP(PEG) **8**, CP(PEG)$_2$ **9** and CP-[poly(PEGA)] **10**, using the **cylindrical micelle model** CYL+CHAINS_RW.

	Nature of the parameter	CPPC **6**	CPPC **7**	CPPC **8**	CPPC **9**	CPPC **10**
SLD_{solv} (10^{-6} Å^{-2})	Calculated	6.39	6.39	6.39	6.39	6.39
SLD_{core} (10^{-6} Å^{-2})	Calculated	1.61	1.42	1.61	1.42	1.61
SLD_{chain} (10^{-6} Å^{-2})	Calculated	0.878	0.878	0.633	0.633	0.750
Radius core (Å)	Fixed	3.5	3.5	3.5	3.5	3.5
n_agg	Calculated	0.00967	0.01935	0.00967	0.01935	0.00967
Volume brush (Å^3)	Calculated	7,598	7,598	13,838	13,838	18,384
Rg (Å)	Fitted	25	25	44	35	10
d	Fixed	1	1	1	1	1
Height (Å)	Fitted	>1500	267	159	9	78
Xsolv	Fixed	0	0	0	0	0
N	Fitted	0.05778	0.2240	1.583	11.33	0.6612
Conc (mg mL^{-1})		1.5	1.5	5	5	5
Reduced Chi^2		45.8	5.27	3.03	10.9	203

Table A-3: Fitting parameters for CP(PEtOx) **6**, CP(PEtOx)$_2$ **7**, CP(PEG) **8**, CP(PEG)$_2$ **9** and CP-[poly(PEGA)] **10**, using the **core-shell cylinder** model from SasView.

	Nature of the parameter	CPPC **6**	CPPC **7**	CPPC **8**	CPPC **9**	CPPC **10**
Scale	Fitted	$1.62.10^{-4}$	$5.00.10^{-4}$	$4.54.10^{-4}$	$9.72.10^{-4}$	$5.22.10^{-3}$
Background	Fixed	0.001	0.001	0.005	0.005	0.01
SLD_{core} ($10^{-6}Å^{-2}$)	Calculated	1.61	1.42	1.61	1.42	1.61
SLD_{shell} ($10^{-6}Å^{-2}$)	Calculated	0.878	0.878	0.633	0.633	0.750
SLD_{solv} ($10^{-6}Å^{-2}$)	Calculated	6.39	6.39	6.39	6.39	6.39
Radius core (Å)	Fixed	3.5	3.5	3.5	3.5	3.5
Thickness (Å)	Fitted	50	47	85	19	16
Length (Å)	Fixed/Fitted	>1500	>1500	95	>1500	75
Polydispersity of thickness[1]	Fixed	-	0.10	-	-	-
Reduced Chi^2		6.39	40.1	305	114	104

Table A-4: Fitting parameters for CP(PEtOx) **6**, CP(PEtOx)$_2$ **7**, CP(PEG) **8**, CP(PEG)$_2$ **9** and CP-[poly(PEGA)] **10**, using the **Guinier-Porod** shape-independent model.

	Nature of the parameter	CPPC **6**	CPPC **7**	CPPC **8**	CPPC **9**	CPPC **10**
Scale	Fitted	$2.18.10^{-2}$	$1.54.10^{-1}$	10.9	1.82	$8.02.10^{-1}$
Background	Fixed	0.001	0.001	0.005	0.005	0.01
Rg (Å)	Fitted	44	52	108	65	24
s	Fitted	0.895	0.710	$1.66.10^{-9}$	$1.37.10^{-9}$	0.213
Porod exponent	Fitted	4.15	3.20	3.41	1.98	3.08
Reduced Chi^2		1.43	6.41	84.4	4.80	13.8

s: dimensionality parameter, with $0 \leq s \leq 3$.

[1] PD ratio: a normal logarithmic distribution was employed for all calculations involving polydispersity.

Table A-5: Fitting parameters for CP(PEG) **8**, CP(PEG)$_2$ **9** and CP-[poly(PEGA)] **10** using the **Gaussian coil** model.

	Nature of the parameter	CPPC **8**	CPPC **9**	CPPC **10**
Scale	Fitted	4.01	0.500	0.207
Background	Fixed	0.005	0.005	0.01
I0	Fitted	2.30	4.00	12.5
Rg (Å)	Fitted	200	81	50
Polydispersity	Fitted/Fixed*	1.15*	1.00	1.00
Reduced Chi^2		1606	34.8	776

Table A-6: Fitting parameters for CP(PEG) **8**, CP(PEG)$_2$ **9** and CP-[poly(PEGA)] **10** using the **star polymer** model on SasView.

	Nature of the parameter	CPPC **8**	CPPC **9**	CPPC **10**
Scale	Fitted	13.4	2.05	1.90
Background	Fixed	0.005	0.005	0.01
Rg^2 (Å^2)	Fitted	17,013	6,208	969
Number of arms	Fitted	39.5	3.47	26.8
Reduced Chi^2		82.8	7.42	8.10
Molecular weight	Calculated from scale	NC*	NC*	91,389 (N_{agg} = 8)

*: not calculated as the model was not further investigated upon examination of AIC values.

Table A-7: Fitting parameters for CP(PEG) **8**, $CP(PEG)_2$ **9,** using the **Ellipsoid + Polymer model** ELL+CHAINS_RW.

	Nature of the parameter	CPPC **8**	CPPC **9**
SLD_{solv} (10^{-6} Å^{-2})	Calculated	6.39	6.39
SLD_{core} (10^{-6} Å^{-2})	Calculated	1.61	1.42
SLD_{chain} (10^{-6} Å^{-2})	Calculated	0.633	0.633
Radius core (Å)	Fixed	3.5	3.5
n_agg	Calculated	0.00967	0.01935
Volume brush (Å^3)	Calculated	13,838	13,838
Rg (Å)	Fitted	98	43
d	Fixed	1	1
Eccentricity ε	Fitted	1.80	4.33
Xsolv	Fixed	0	0
N	Fitted	300	25.38
Conc (mg mL^{-1})		5	5
Reduced Chi^2		2230	14.4

In these tables:

- SLD_{solv}, SLD_{core} and SLD_{chain} respectively represent the scattering length densities of the solvent (water), the cyclic peptide core and the polymer chain(s).
- The radius of the cyclic peptide core has been fixed to 3.5 Å, according to results from previous crystallographic studies.
- n_agg is the specific aggregation number or number of chains per surface area.
- The volume of the brush is the molecular volume of a polymer chain unit.
- R_g is the gyration radius of the polymer chains in the corona.
- d is a parameter evaluating the interpenetration of the polymer chains into the core, d = 1 models the absence of this interpenetration phenomenon.
- The height described here is the cylinder core that we correlate to the length of the self-assemblies.
- x_solv_core is the amount of solvent in the core, that has been fixed to 0 here.]
- N or scale is the scaling factor from a Delta distribution.

A.3.3 Aspect ratio estimation for CPNT (adapted from ref.[8]):

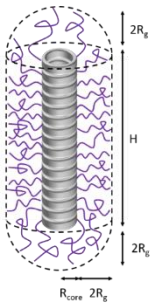

Total length: $L = H + 4R_g$

Total Diameter: $D = 2R_{core} + 4R_g$

Aspect ratio = L/D

A.3.4 Static light scatterings (Zimm plots)

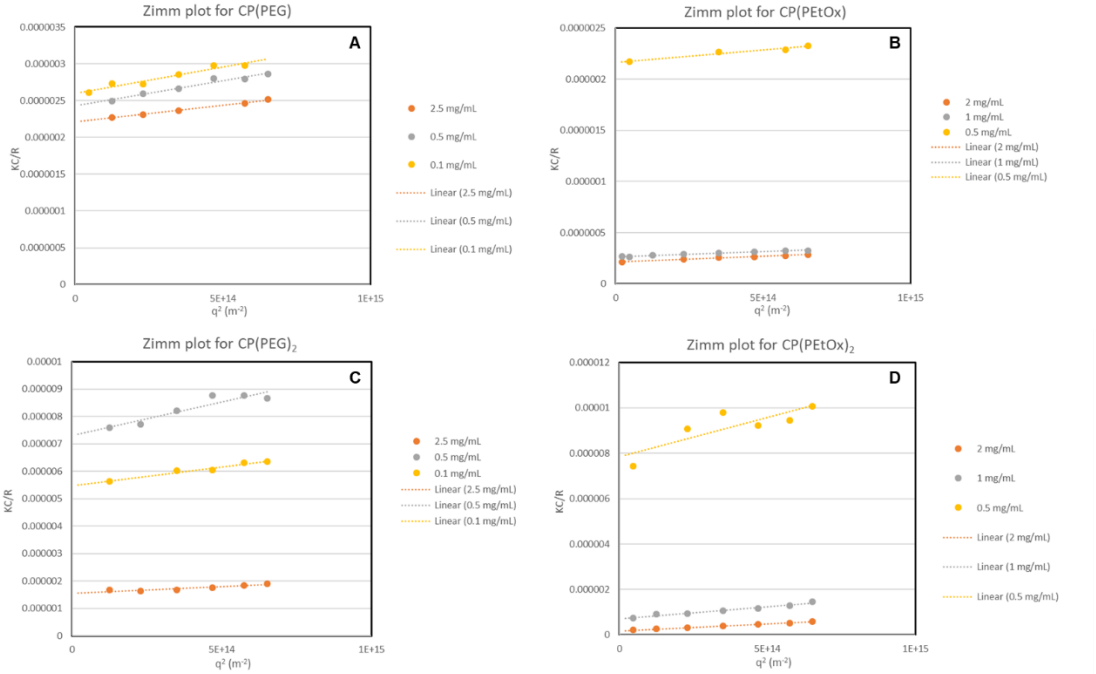

Figure A-14: Zimm plots showing the evolution of KC/R with q^2 measured by static light scattering in deionised water for different concentrations (0.1 or 0.5 – 2 or 2.5 mg/mL) mg/mL of (A): CP(PEG) **6**, (B): CP(PEtOx) **8**, (C): $CP(PEG)_2$ **7**, (D) $CP(PEtOx)_2$ **9**.

A.4 Biology

A.4.1 Plate-reading cellular uptake assay

Table A-8: Relative fluorescence of Cy3-labelled compounds in PBS and fluorescence correction factors for microplate reader fluorescence mean

Fluorescent compound	Slope	Relative correction factor*
Poly(PEGA) **5**	9561	5.10
CP-poly(PEGA) **10**	8472	5.76
CP-[poly(PEGA)]$_2$ 11	48798	1.00
CP(PEG) **8**	4422	11.04
CP(PEG)$_2$ **9**	19071	2.56
PEtOx **3**	13208	3.69
CP(PEtOx) **6**	12220	3.99
CP(PEtOx)$_2$ **7**	9565	5.10
PEG Cy3 20kDa	2108	23.15

*: Highest Slope/Slope, this factor is then multiplied with fluorescence means.

A.4.2 Processing of the pictures (on the plate reader)

All pictures acquired on the plate reader were processed on the Cytation 3 software (Gen5.2) in the following way, with slight differences depending on the cell line (mask definition):

- **Stitching** of the 3X3 pictures, using the Hoechst channel. The final montage is 1224 X 88890 format.
- **Background removal:** 20 µm, using the Rolling Ball algorithm on a dark background.
- **Cell analysis:** Hoechst mask extended by 20, 10 or 15 µm respectively for NIH 3T3, MDA-MB 231 or PC3 cells, to create a RFP/Cy3 channel mask. The varying value corresponds to the different cell morphologies.
- The mean fluorescence on the RFP/Cy3 channel on each picture was evaluated within the limits defined by the mask. An upper limit was set for each cell line, to remove any saturating signal from the calculations. The limit was set at 10,000 a.u. for NIH 3T3 and MDA-MB-231 and at 7,000 for PC3.

The mean fluorescence was evaluated in three technical replicates per repeat, with a total of two (NIH 3T3 and PC3) or three (MDA-MB-231) biological repeats.

A.4.3 Processing of the pictures (confocal microscopy on spheroids)

Fluorescence penetration

All pictures were processed using ImageJ. The brightness and contrast were not modified for calculations of the fluorescence from the Cy3 channel. The fluorescence was calculated after defining a region of interest (ROI) around the spheroid, for each stack using the MultiMeasure function and reporting the Integrated average fluorescence value. Those values were corrected using the correction factors known from **Table A-8**.

Colocalisation

Colocalisation was measured using the JaCoP plugin and the Pearson's coefficients were calculated as an average of the 50 stacks (they were not calculated for every single stack).

A.5 References

1. www.sasview.org.
2. I. Bressler, J. Kohlbrecher and A. F. Thunemann, *Journal of Applied Crystallography*, 2015, **48**, 1587.
3. B. Hammouda, *Journal of Applied Crystallography*, 2010, **43**, 716.
4. I. Livsey, *Journal of the Chemical Society, Faraday Transactions 2: Molecular and Chemical Physics*, 1987, **83**, 1445.
5. J. S. Pedersen and M. C. Gerstenberg, *Macromolecules*, 1996, **29**, 1363.
6. N. P. Balsara, *Journal of Polymer Science Part A: Polymer Chemistry*, 1996, **34**, 1827.
7. J. E. Cavanaugh and A. A. Neath, *WIREs Computational Statistics*, 2019, **11**, 1460.
8. S. C. Larnaudie, J. Sanchis, T.-H. Nguyen, R. Peltier, S. Catrouillet, J. C. Brendel, C. J. H. Porter, K. A. Jolliffe and S. Perrier, *Biomaterials*, 2018, **178**, 570.

Appendix B

B Appendix B: Supplementary information to Chapter 3

B.1 Synthesis and NMR spectra

B.1.1 NMR spectrum polymer 2

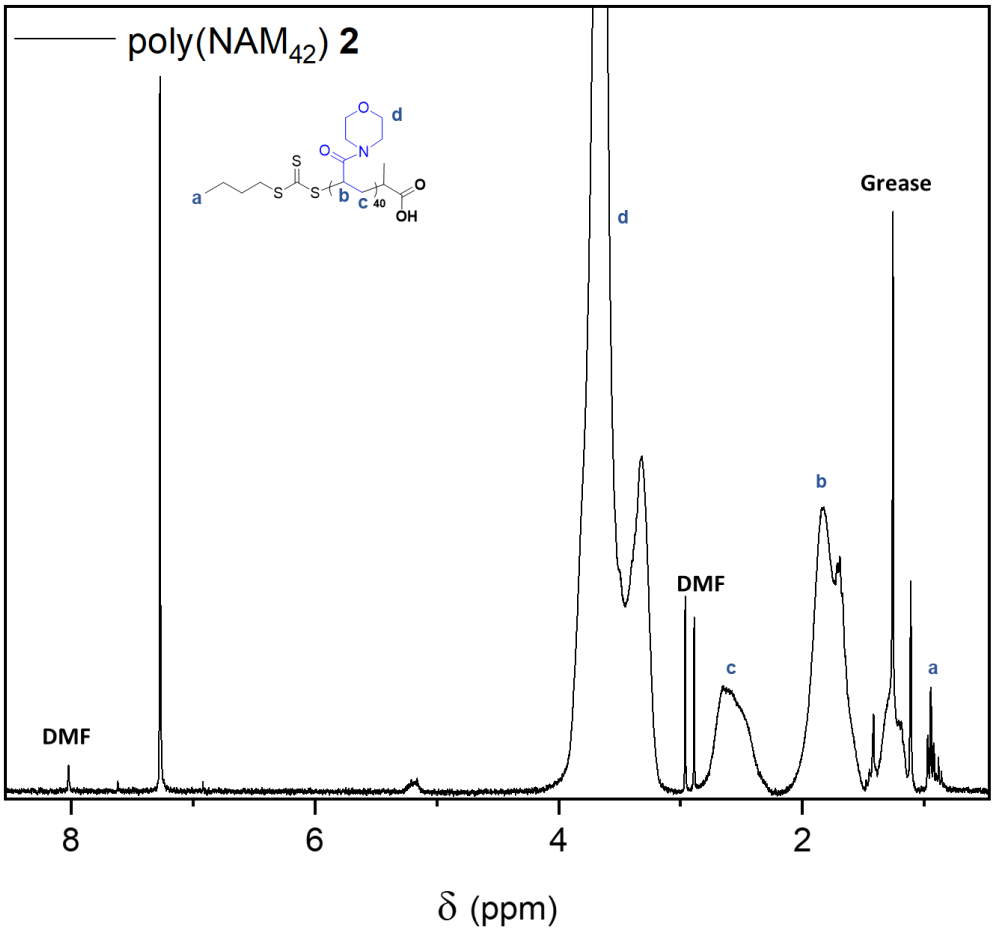

Figure B-1: Proton NMR spectrum with assignment for polymer **2**.

B.1.2 NMR spectrum polymer 3

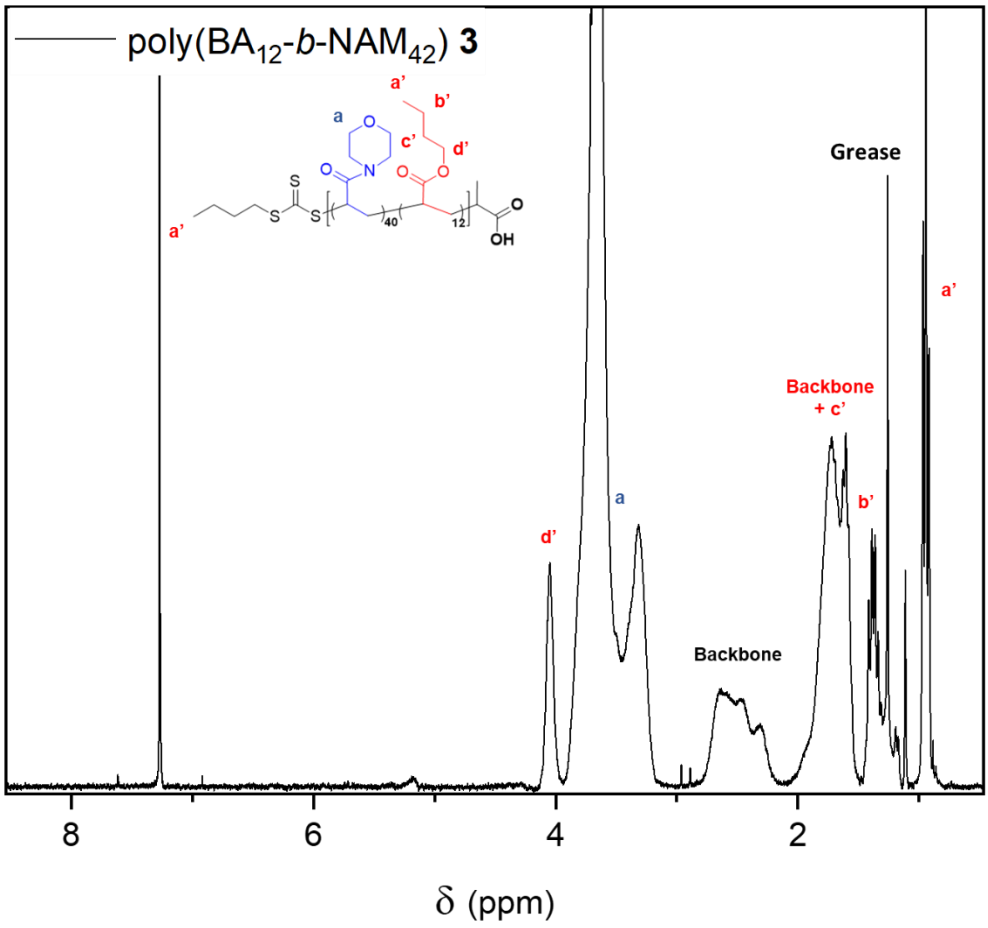

Figure B-2: Proton NMR spectrum with assignment for polymer **3**.

B.1.3 NMR spectrum CPNT 4

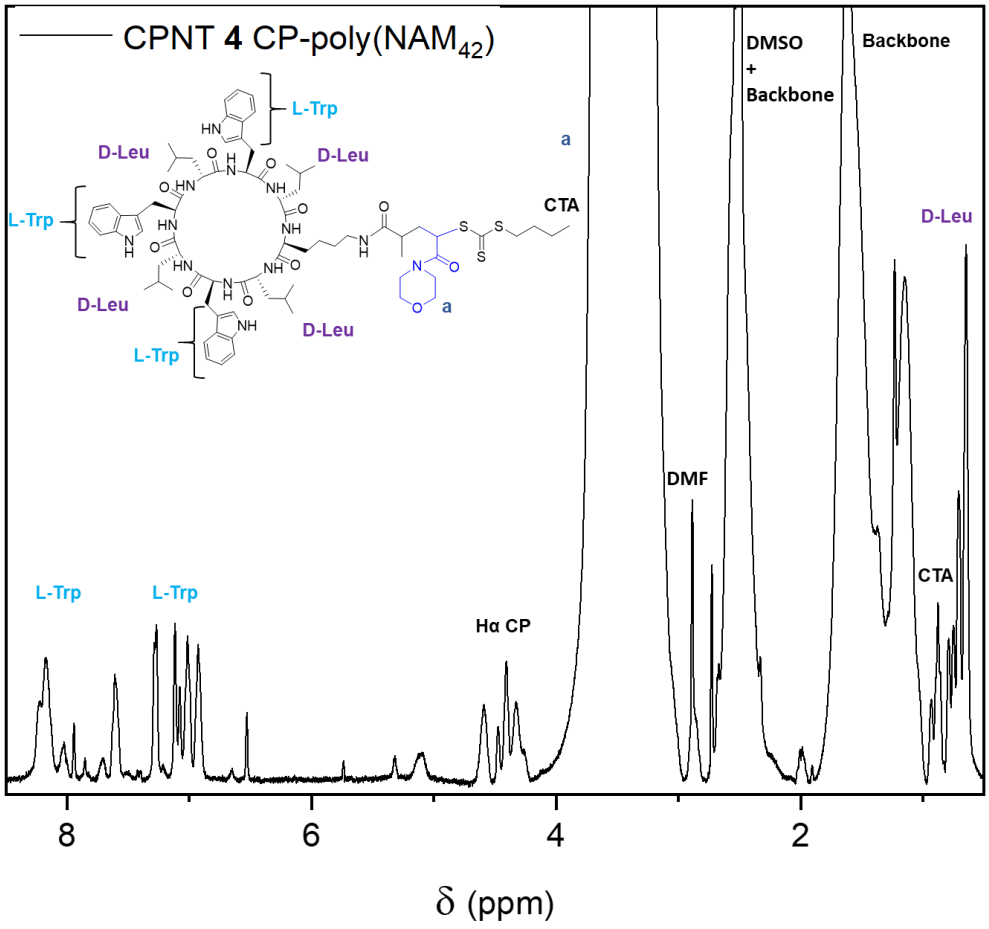

Figure B-3: Proton NMR spectrum with assignment for CPNT **4**.

B.1.4 NMR spectrum CPNT 5

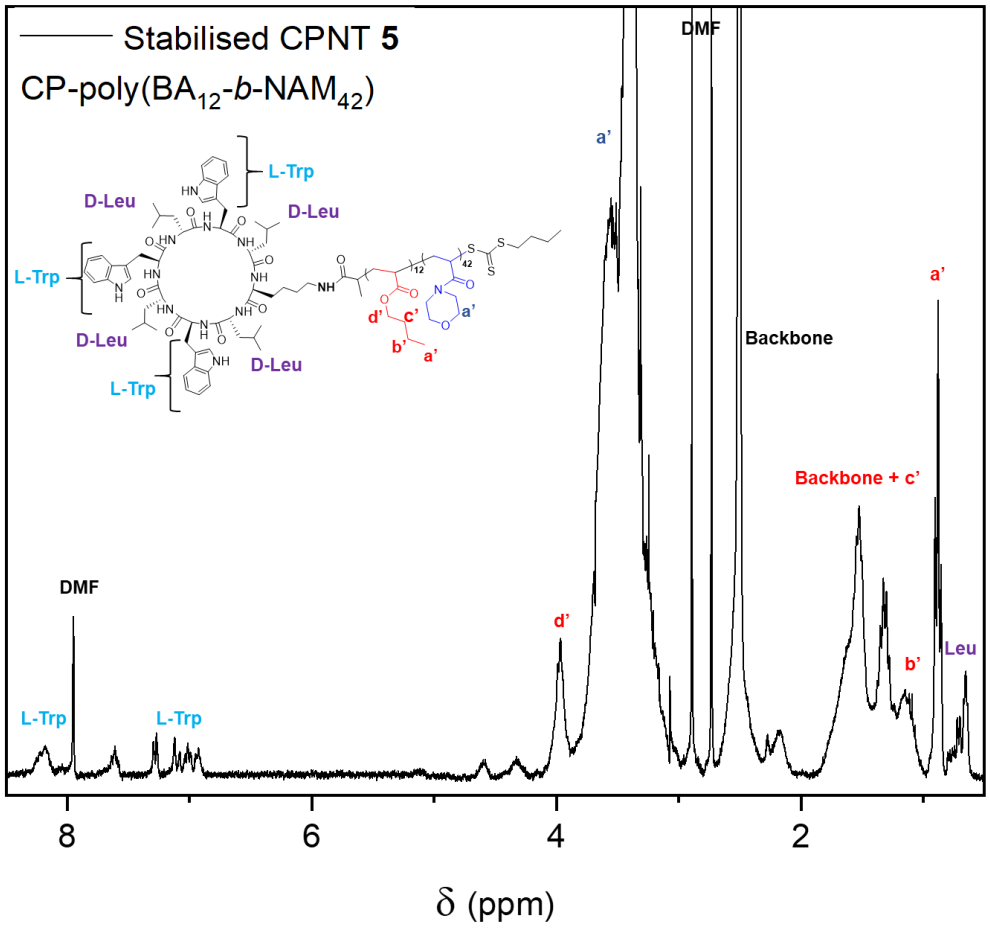

Figure B-4: Proton NMR spectrum with assignment for CPNT **5**.

B.1.5 NMR spectrum CPNT 8

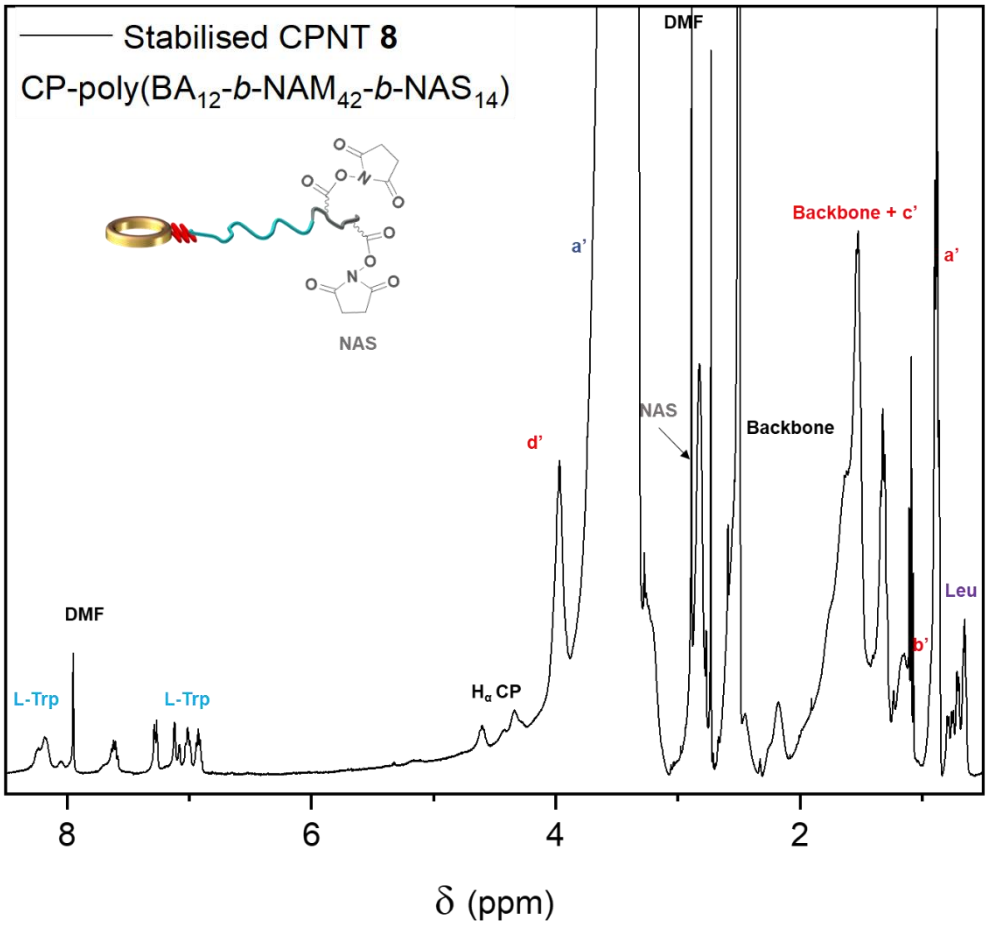

Figure B-5: Proton NMR spectrum with assignment for CPNT **8** (see assignments for all peaks on previous spectrum for CPNT **5**)

B.1.6 NMR spectrum CPNT 9

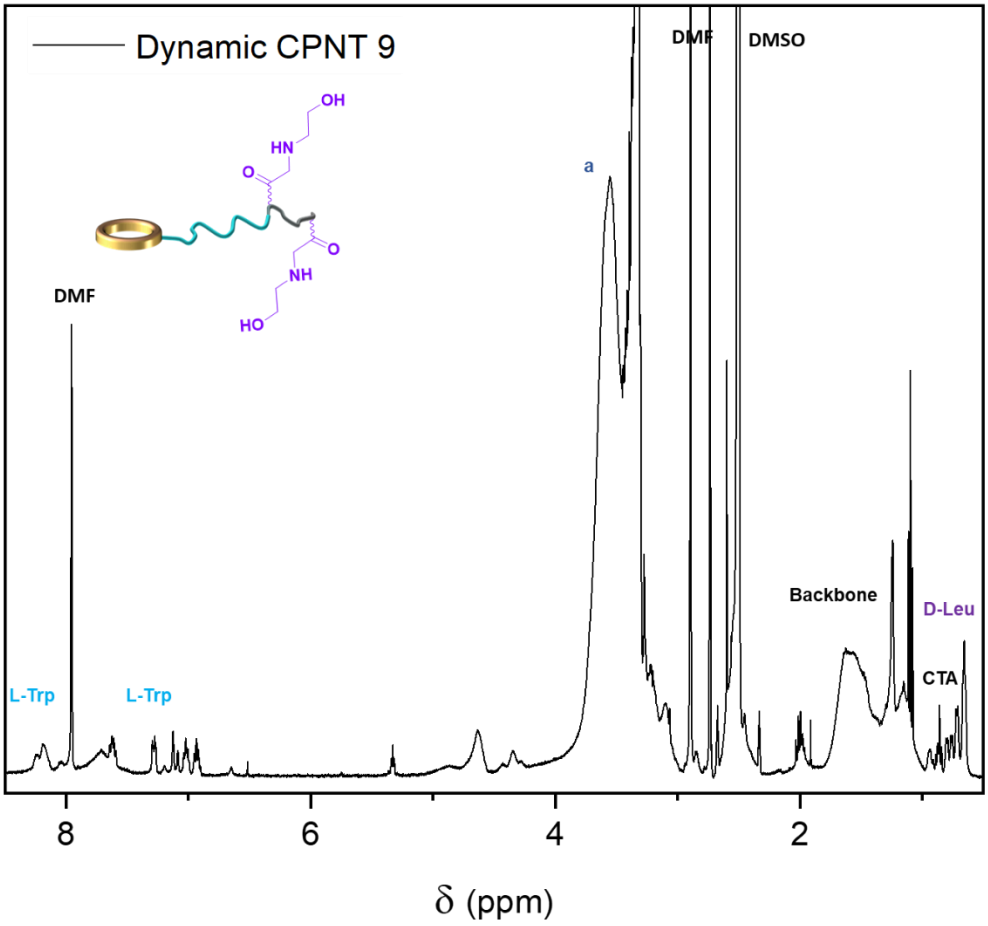

Figure B-6: Proton NMR spectrum with assignment for dynamic CPNT **9** (see assignments for all peaks on previous spectrum for CPNT **4**)

B.1.7 NMR spectrum CPNT 10

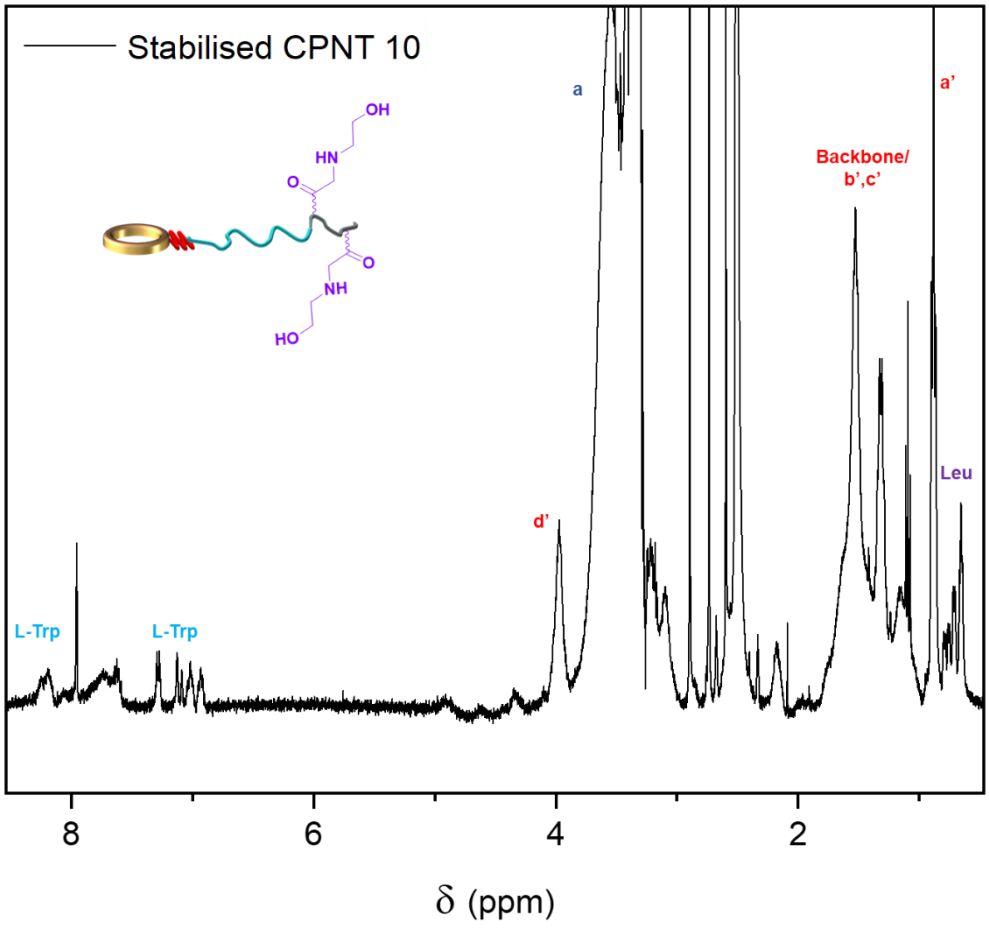

Figure B-7: Proton NMR spectrum with assignment for CPNT **10** (see assignments for all peaks on previous spectrum for CPNT **5**)

B.1.8 Synthesis of cRGDfK peptide

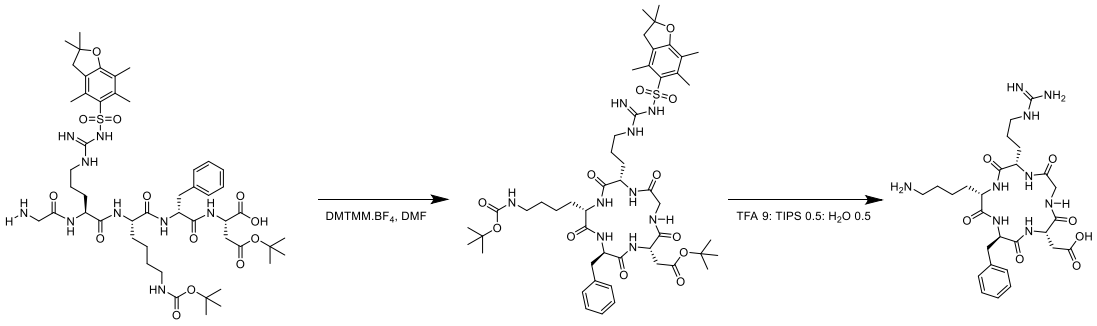

Scheme B-1: Synthetic route for the synthesis of cRGDfK

Protected linear peptide GRKfD synthesis: Solid phase peptide synthesis (SPPS) of H_2N-Gly-L-Arg(Pbf)-L-Lys(Boc)-D-Phe-L-Asp(tBu)-COOH was performed using a peptide synthesizer (Prelude – Protein Technologies), on a 2-chlorotrityl resin (6 x 40 mg, 1.6 mmol.g^{-1} resin loading), following a similar procedure than the one described in Chapter 2.

Cyclisation and deprotection: The protected linear peptide GRKfD (477 mg, 0.46 mmol, 1.0 eq.) was dissolved in 70 mL of DMF in a round bottom flask. After placing the reaction mixture under a N_2 atmosphere, a solution of DMTMM.BF_4 (198 mg, 0.60 mmol, 1.30 eq.) in 30 mL DMF was prepared then added dropwise to the reaction mixture. The mixture was left stirring for 93 h at room temperature and the conversion of the linear peptide into the corresponding cyclic peptide was assessed using ESI-MicroTOF. The solvent was evaporated *in vacuo* before redissolving the cyclic peptide in 7.7 mL of a cleavage cocktail (TFA 9.5: TIPS 0.5: H_2O 0.5) and leaving it to deprotect for 3 h. The deprotected cyclic peptide was then precipitated in cold diethyl ether three times and was then placed in 50 mL centrifuge tubes with 30 mL acetonitrile twice for 30 min to remove any residual DMTMM.BF_4. The vials were then dried overnight in the vacuum oven, affording the pure deprotected cRGDfK (130 mg, 46%).

NMR assignments: see on the spectrum (colour code: blue: L-Lys, red: L-Arg, purple: L-Trp, green: L-Asp, black: Gly).

ESI:

Protected Linear peptide: Expected: [M+H]=1030.52, measured [M+H] m/z = 1030.3, [M+Na] m/z = 1052.

Protected cyclic peptide: Expected [M+H] m/z = 1012.51, Measured [M+Na] = 1034.51

Deprotected cRGDfK: [M+H] 604.5, expected: m/z = 604.3

B.1.9 NMR spectrum cRGDfK (final)

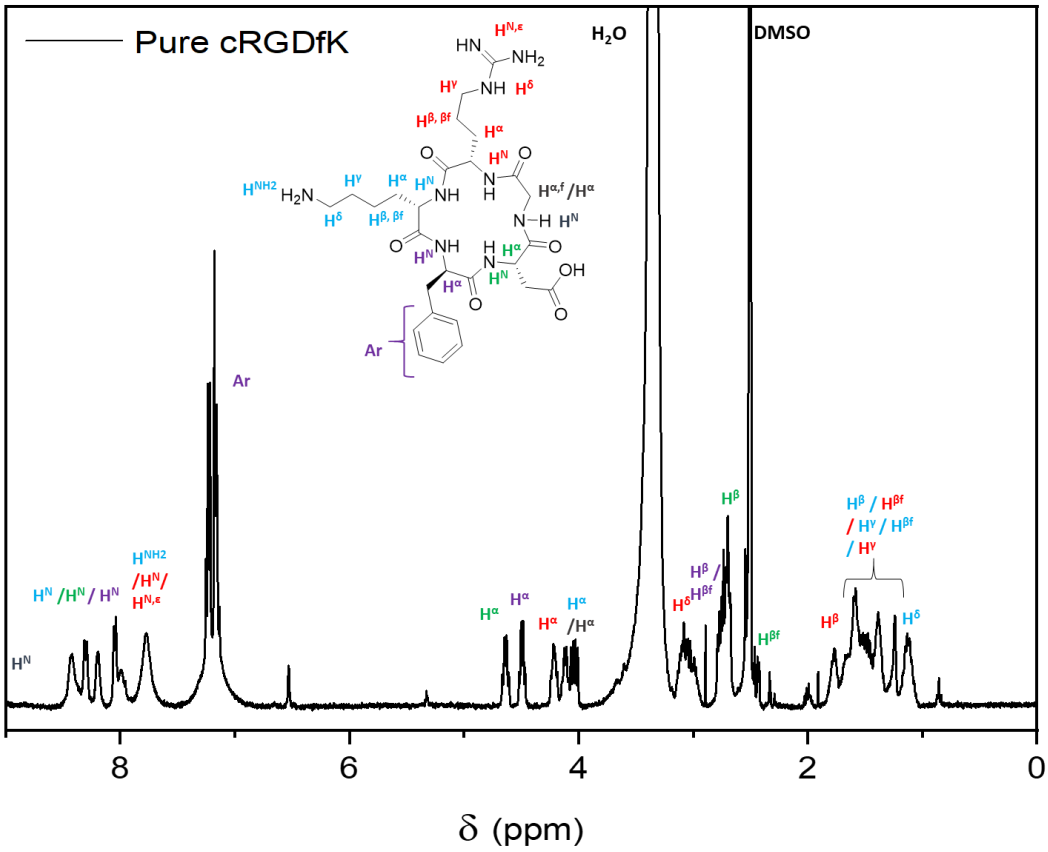

Figure B-8: Proton NMR spectrum with assignment for cRGDfK (aided by the assignment provided by Haubner *et al.*)[1]

B.1.10 NMR spectrum CPNT 11

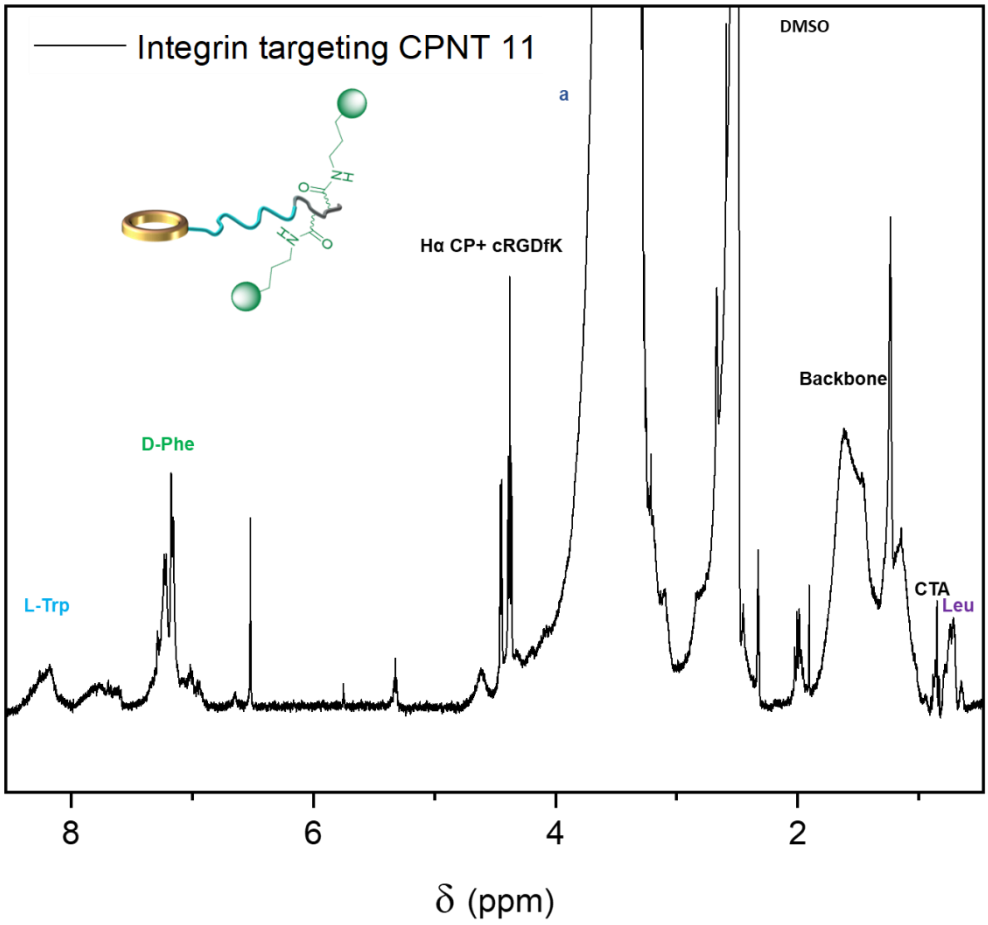

Figure B-9: Proton NMR spectrum with assignment for CPNT **11** (see assignments for all peaks on previous spectrum for CPNT **4**)

B.2 Characterisation (SAXS)

B.2.1 Fitting models employed

In this chapter the fitting process employed was similar to Chapter 2; given the excellent fit with models obtained, other models were not further considered for this dataset and therefore are not presented here.

B.2.1.1 Core-shell cylinder model (SasView)

The core-shell cylinder employed from SasView considers the system to be composed of a cylindrical core with a certain scattering length density (SLD_{core}) and radius, surrounded by a shell enveloping it fully (SLD_{shell}), with a thickness t.[1, 2] The length of the total cylinder is the length of the core cylinder plus twice the thickness of the shell. A correction for polydispersity of thickness (assuming a lognorm distribution) has been accounted for to correct the fringes in the curve. The full equations ruling this model are detailed on the SasView website.[2] The scale is related to the volume fraction of particles present in the system. The background was associated to the X-ray source. SLD were calculated using the sum of the coherent scattering lengths for all atoms (obtained from the atomic number) constituting the molecules of interest and dividing it by the calculated molecular volume. The molecular volume of a monomer unit was assumed to be an invariant upon polymerisation, therefore the molecular volume was calculated from the mass density of the monomer which was then used to calculate the scattering length density. The core was considered to be either the CP (with a fixed core radius of 3.5 Å and SLD of $11.54.10^{-6}Å^{-2}$) or to be CP-poly(BA) (SLD of $9.62.10^{-6}Å^{-2}$ calculated as the sum of the SLD of poly(BA) and the SLD of CP **1**, affected by the molar ratios of each component; the core was let to fit with a lower limit of 3.5 Å).

B.2.1.2 Combined model: Core-shell cylinder + Power Law

For charged systems with a sharp increase of intensity at low q, the contribution of a power law was added. The initial Power Law followed the equation:

$$\mathrm{I(q)} = \mathrm{scale} \cdot \mathrm{q}^{-power} + \mathrm{background}$$

The contribution was accounted for using SasView plugin for model mixtures, with scale contributions of A (core-shell cylinder) and B (power law). In all fittings, the reduced chi^2 value is a statistical indicator of the goodness of the fit (a low value corresponding to a better fit).

B.2.2 SAXS data fitting parameters for CPNT 9, 10 and 11 (PBS or 5% DMSO in PBS for CPNT 11)

Table B-1: SAXS data fitting parameters for CPNT **9**, **10** and **11**
(PBS or 5% DMSO in PBS for CPNT **11**, at 5 mg/mL),
using the core-shell cylinder model in SasView
(CP core: the cyclic peptide alone is considered to be the core and the radius of the core was fixed; BA core: the CP and the poly(BA) contribution are combined and considered as a core; in this case the radius of the core was fitted).

	Nature of the parameter	CPNT **9**	CPNT **10**	CPNT **10**	CPNT **11**	CPNT **11**
Model		CP core	CP core	BA core	CP core	CP core + Power law
Scale	Fitted	$4.99.10^{-3}$	$1.51.10^{-2}$	$6.55.10^{-3}$	$2.58.10^{-2}$	1.00
Background	Fixed	0.001	0.005	0.005	0.01	0.01
SLD_{core} ($10^{-6}Å^{-2}$)	Calculated	11.54	11.54	9.62	11.54	11.54
SLD_{shell} ($10^{-6}Å^{-2}$)	Calculated	10.34	10.01	10.34	10.01	10.01
SLD_{solv} ($10^{-6}Å^{-2}$)	Calculated	9.49	9.49	9.49	9.53	9.53
Radius core (Å)	Fixed/Fitted*	3.5	3.5	22*	3.5	3.5
Thickness (Å)	Fitted	50	73	57	38	38
Length (Å)	Fixed/Fitted	98	>1500	>1500	>1500	>1500
Polydispersity of thickness[2]	Fixed	0.05	0.10	0.10	-	-
A-scale	Fitted	-	-	-	-	$2.55.10^{-2}$
B-scale	Fitted	-	-	-	-	$1.08.10^{-9}$
Power	Fitted	-	-	-	-	4
Reduced Chi[2]		5.09	5.70	7.81	8.16	11.9

[2] PD ratio: a normal logarithmic distribution was employed for all calculations involving polydispersity.

B.2.3 SAXS data with 5% DMSO and fitting parameters for CPNT 9 and 10

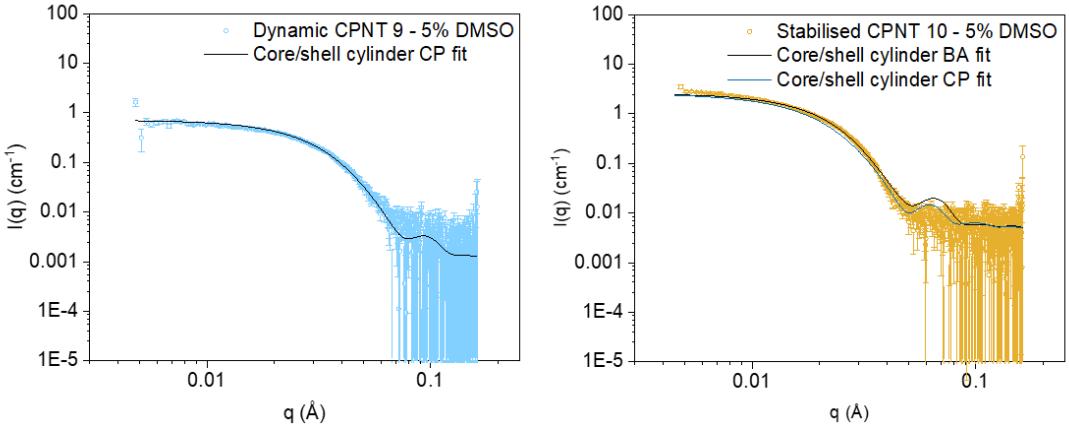

Figure B-10: SAXS data acquired for CPNT **9** (left, blue) and **10** (right, gold). Hollow circles are used for the data plots, fits are plotted as lines; error bars are statistical.

Table B-2: SAXS data fitting parameters for CPNT **9** and **10**
(5% DMSO in PBS ay 5 mg/mL), using the core-shell cylinder model in SasView
(CP core: the cyclic peptide alone is considered to be the core and the radius of the core was fixed; BA core: the CP and the poly(BA) contribution are combined and considered as a core; in this case the radius of the core was fitted).

	Nature of the parameter	CPNT **9**	CPNT **10**	CPNT **10**
Model		CP core	CP core	BA core
Scale	Fitted	$7.33.10^{-3}$	$2.25.10^{-2}$	$8.78.10^{-3}$
Background	Fixed	0.001	0.005	0.005
SLD_{core} ($10^{-6}Å^{-2}$)	Calculated	11.54	11.54	9.62
SLD_{shell} ($10^{-6}Å^{-2}$)	Calculated	10.34	10.01	10.34
SLD_{solv} ($10^{-6}Å^{-2}$)	Calculated	9.53	9.53	9.53
Radius core (Å)	Fixed/Fitted*	3.5	3.5	20*
Thickness (Å)	Fitted	48	77	59
Length (Å)	Fixed/Fitted	56	91	119
Polydispersity of thickness	Fixed	0.10	0.05	0.05
Reduced Chi^2		1.25	3.38	5.08

B.2.4 Comparison of the SAXS data between 9 and 9* in 5% DMSO solution

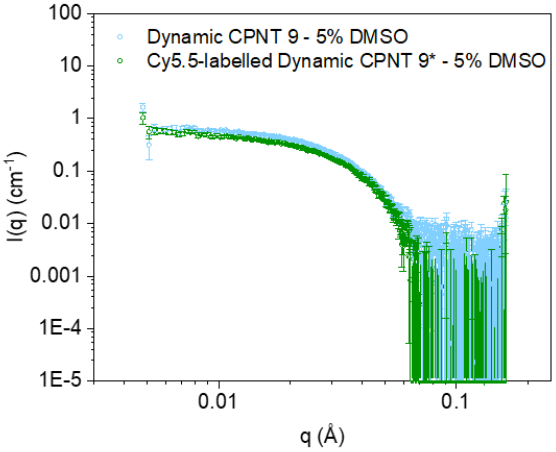

Figure B-11: SAXS profile comparison between Cy5.5 labelled dynamic CPNT **9*** (green) and the unlabelled material CPNT **9** (light blue), in 5% DMSO solution in PBS. Hollow circles are used for the data plots; error bars are statistical.

B.3 Cellular biology

B.3.1 Fluorescence calibration for Cy5.5 labelled compounds

The calibration was performed using the value of the fluorescence at the working concentration in media. Accounting for relative fluorescence, stabilised CPNT fluorescence uptake intensities were divided by 0.951 (dynamic CPNT were unchanged). For the targeting study, integrin-targeting CPNT **11** were corrected by a factor 0.64.

B.3.2 Flow cytometry profiles for MDA-MB 231 cells (stabilised vs dynamic)

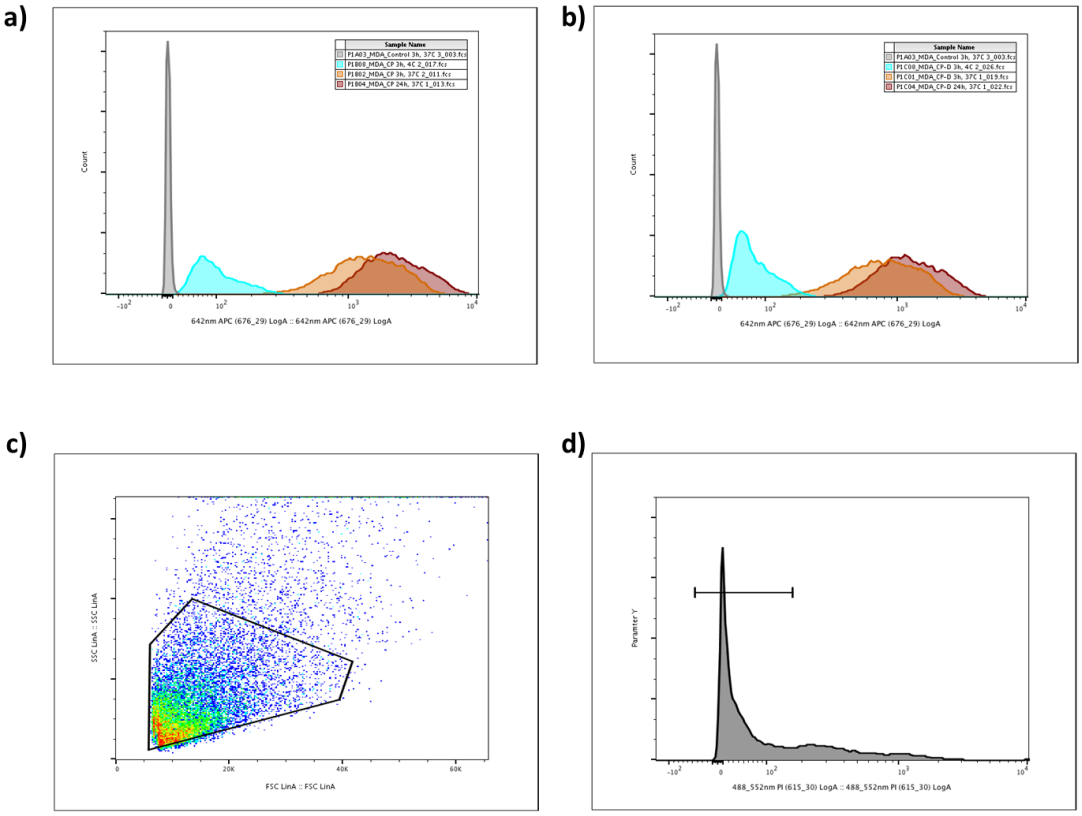

Figure B-12: Flow cytometry data for MDA: Histograms for the fluorescence intensity at the Cy5.5 channel (642 nm exc., 679-29 nm em.) in different conditions (3 h 4C in light blue, 3 h 37C in light brown, 24 h 37 C in dark brown) of a) dynamic CPNT **9**, b) stabilised CPNT **10**. c) FSC vs SSC plot for MDA cells, with the gate used to exclude dead cells with an emission in the propidium iodide (PI) channel above 102. Measurements were performed to reach 10,000 events within the gate. d) Representative histogram for the PI channel (488 nm exc., 615-30 em.), evaluating the number of dead cells (high PI emission).

B.3.3 Flow cytometry profiles for NIH 3T3 cells (stabilised vs dynamic)

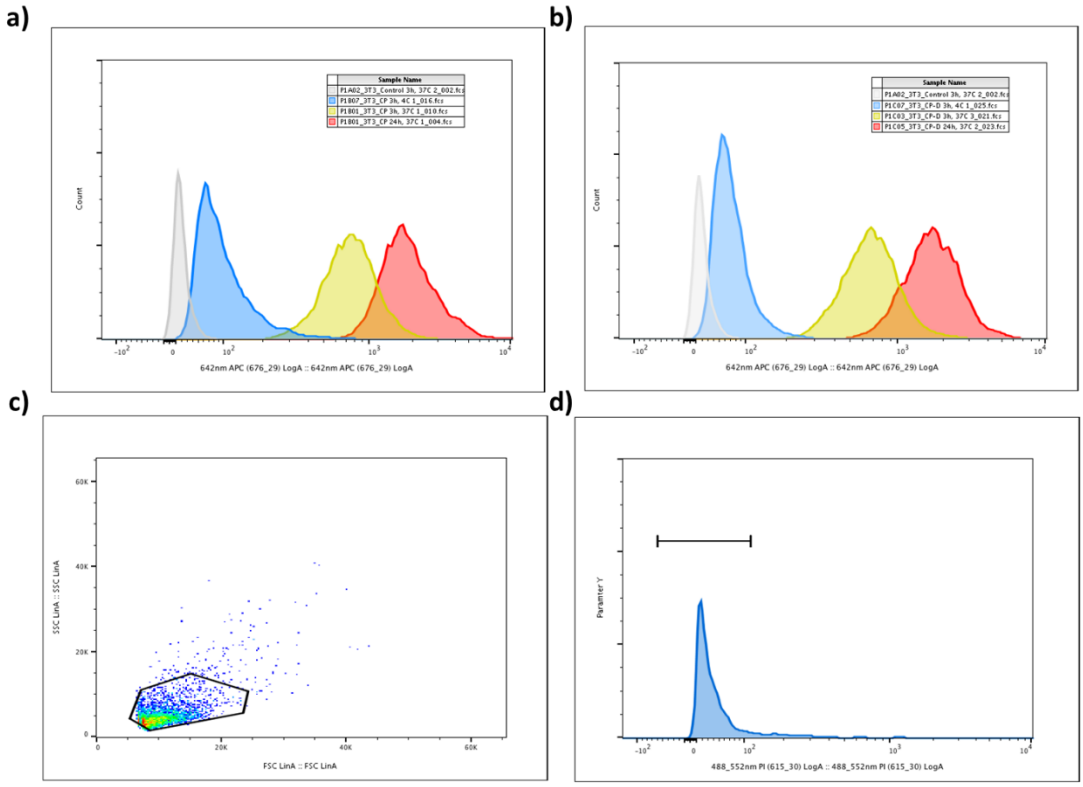

Figure B-13: Flow cytometry data for 3T3: Histograms for the fluorescence intensity at the Cy5.5 channel (642 nm exc., 679-29 nm em.) in different conditions (3 h 4C in blue, 3 h 37C in yellow, 24 h 37 C in red) of a) dynamic CPNT **9**, b) stabilised CPNT **1**0. c) FSC vs SSC plot for 3T3 cells, with the gate used to exclude dead cells with an emission in the propidium iodide (PI) channel above 102. Measurements were performed to reach 10,000 events within the gate.
d) Representative histogram for the PI channel (488 nm exc., 615-30 em.), evaluating the number of dead cells (high PI emission).

B.3.4 Flow cytometry profiles for 4T1 cells (targeting vs non-targeting)

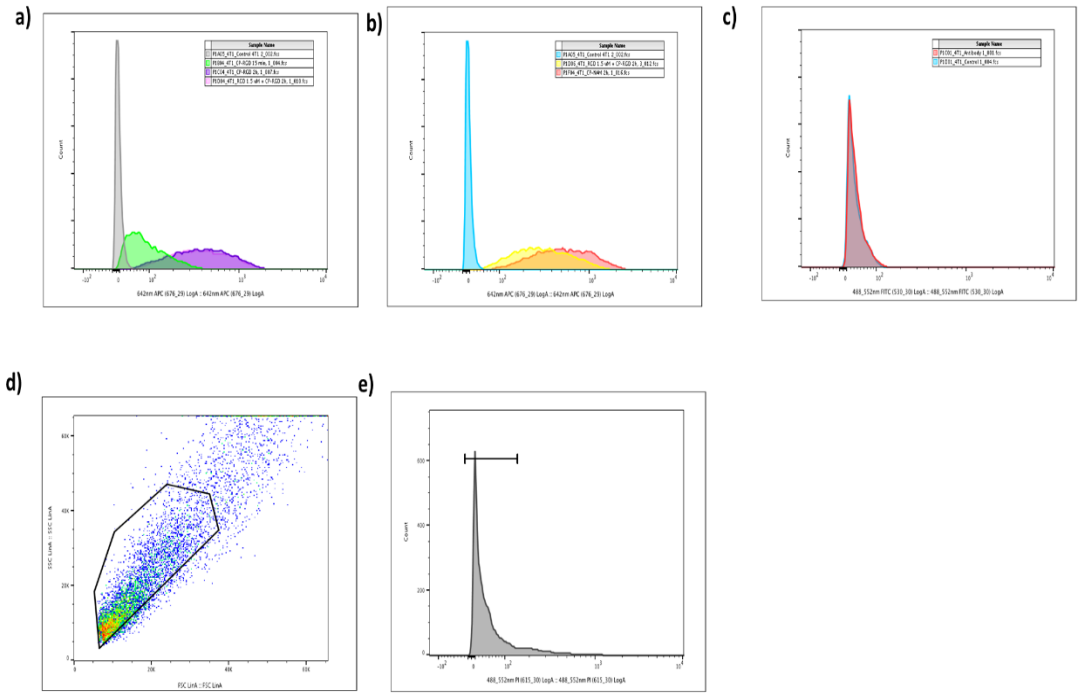

Figure B-14: Flow cytometry data for 4T1 - Histograms for the fluorescence intensity at the Cy5.5 channel (642 nm exc., 679-29 nm em.) at 15 min and 2 h incubation time of a) integrin-targeting CPNT **11**, b) dynamic CPNT **9**. (c) Histogram for the FITC channel (488 nm exc., 530-30 nm em.) after 1 h incubation with FITC-labelled MAB1976X anti-αvβ3 antibody.
(d) FSC vs SSC plot for 4T1 cells, with the gate used to exclude dead cells with an emission in the propidium iodide (PI) channel above 102.
Measurements were performed to reach 10,000 events within the gate.
(e) Representative histogram for the PI channel (488 nm exc., 615-30 em.), evaluating the number of dead cells (high PI emission)

B.3.5 Flow cytometry profiles for HUVEC cells (targeting vs non-targeting)

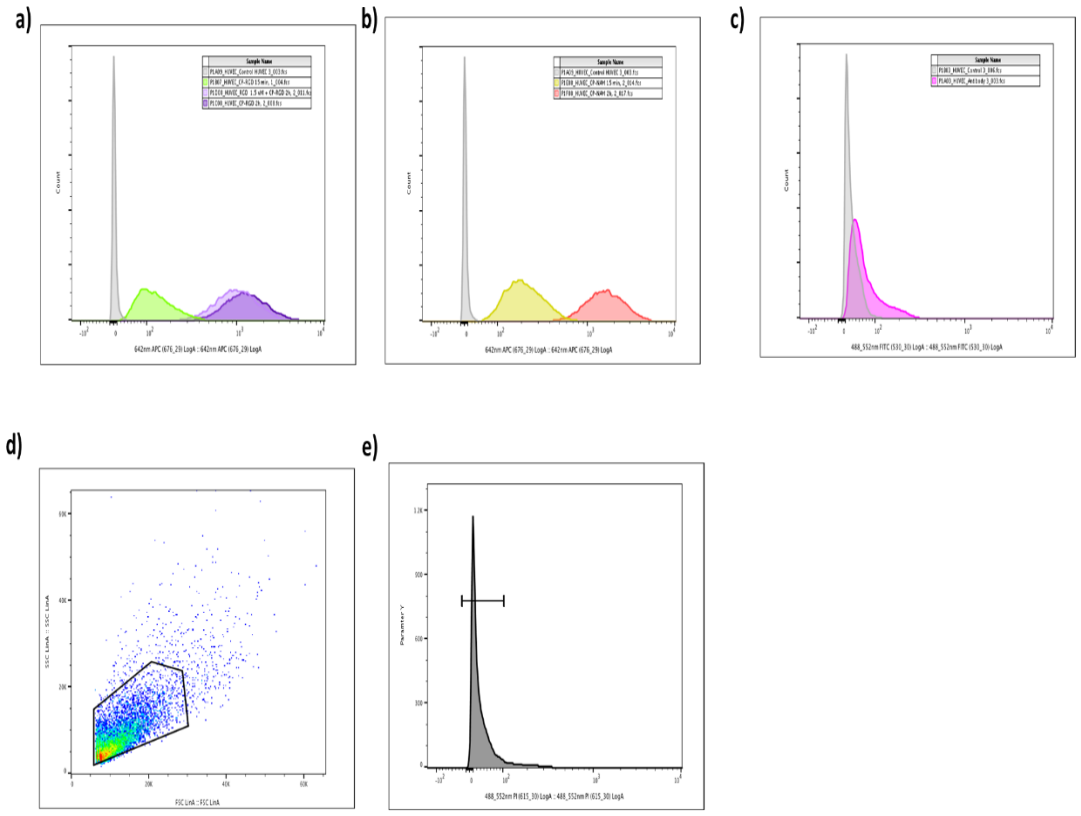

Figure B-15: Flow cytometry data for HUVEC - Histograms for the fluorescence intensity at the Cy5.5 channel (642 nm exc., 679-29 nm em.) at 15 min and 2 h incubation time of a) integrin-targeting CPNT **11**, b) dynamic CPNT **9**. (c) Histogram for the FITC channel (488 nm exc., 530-30 nm em.) after 1 h incubation with FITC-labelled MAB1976X anti-αvβ3 antibody.
d) FSC vs SSC plot for HUVEC cells, with the gate used to exclude dead cells with an emission in the propidium iodide (PI) channel above 102. Measurements were performed to reach 10,000 events within the gate.
e) Representative histogram for the PI channel (488 nm exc., 615-30 em.), evaluating the number of dead cells (high PI emission)

B.3.6 Confocal microscopy on MDA-MB-231

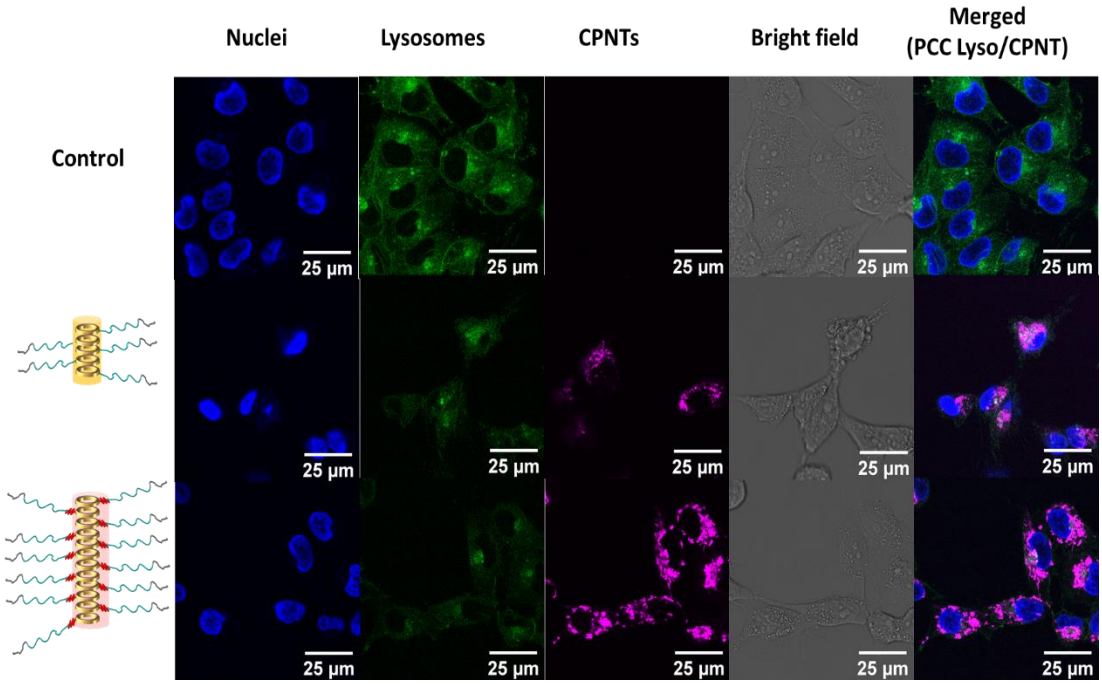

Figure B-16: Confocal images acquired on MDA-MB 231 cells on dynamic CPNT **9** (middle) and stabilised CPNT **10** (bottom). Channels: blue = Hoechst 33342, nucleus stain; magenta= 10% Cy5.5 CPNT 9 and 10; green = LysoSensor DND189 green; grey = bright field.

B.4 Pharmacokinetics

B.4.1 Comparison between dynamic CPNT 9 (1 polymer arm) and previous work on 2 arm CP-[poly(NAM)$_{37}$]$_2$

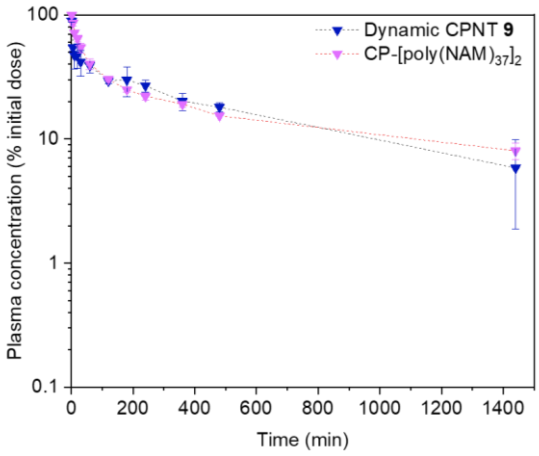

Figure B-17: Pharmacokinetic profiles acquired for dynamic CPNT with 1 (**9**, blue) or 2 (**CP-[poly(NAM$_{37}$)]$_2$,** pink) polymer arms, representing the plasma concentration (% initial radioactive dose) in function of time. Error bars represent the standard deviation; n=3 for CPNT **9** and **11**.

B.4.2 Tables with pharmacokinetic parameters for each repeat

Table B-3: PK parameters for all repeats for dynamic CPNT **9**

Dynamic CPNT **9**	Rat 1	Rat 2	Rat 3
Half-life $t_{1/2}$ (h)	4.42	11.02	13.26
Cl (mL/h)	6.65	3.33	3.47
AUC (μg/mL*h)	199.26	394.80	160.31
V_d (mL)	39.88	51.39	61.66
Urine (%dose)	43.4	49.3	19.5

Table B-4: PK parameters for all repeats for stabilised CPNT **10**

Stabilised CPNT **10**	Rat 1	Rat 2
Half-life $t_{1/2}$ (h)	19.20	37.27
Cl (mL/h)	1.27	0.77
AUC (μg/mL*h)	943.15	1503.71
V_d (mL)	33.72	40.25
Urine (%dose)	21.1	26.9

Table B-5: PK parameters for all repeats for integrin-targeting CPNT **11**

Integrin-targeting CPNT **11**	Rat 1	Rat 2	Rat 3
Half-life $t_{1/2}$ (h)	4.91	6.73	4.84
Cl (mL/h)	13.41	20.61	12.75
AUC (μg/mL*h)	104.36	67.33	117.45
V_d (mL)	60.81	94.68	82.65
Urine (%dose)	41.1	36.5	33.9

B.5 References

1. R. Haubner, R. Gratias, B. Diefenbach, S. L. Goodman, A. Jonczyk and H. Kessler, *Journal of the American Chemical Society*, 1996, **118**, 7461.
2. I. Livsey, *Journal of the Chemical Society, Faraday Transactions 2: Molecular and Chemical Physics*, 1987, **83**, 1445.
3. www.sasview.org.

Appendix C

Appendix C: Supplementary information to Chapter 4

C.1 Synthesis and NMR spectra

C.1.1 NMR spectrum polymer 2

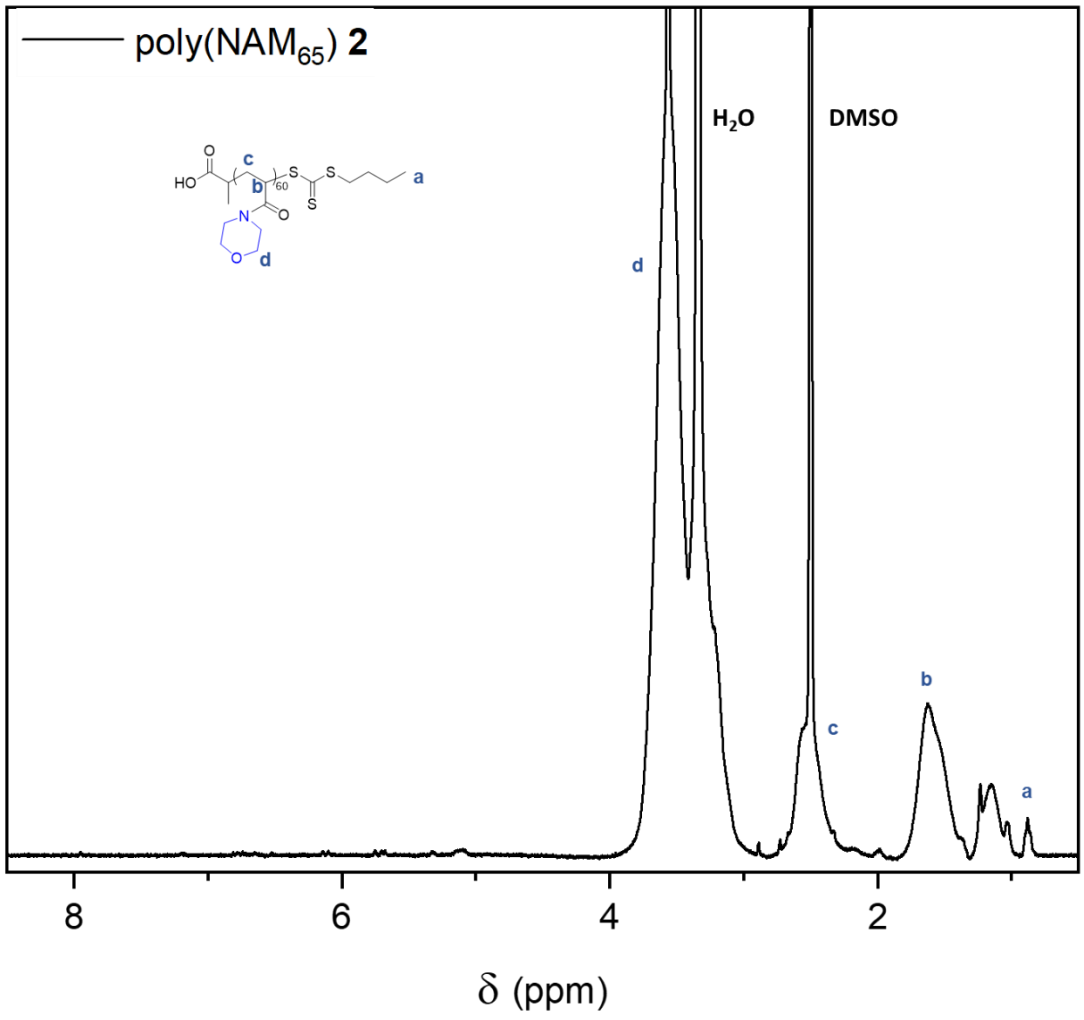

Figure C-1: Proton NMR spectrum with assignment for polymer **2**.

C.1.2 NMR spectrum polymer 3

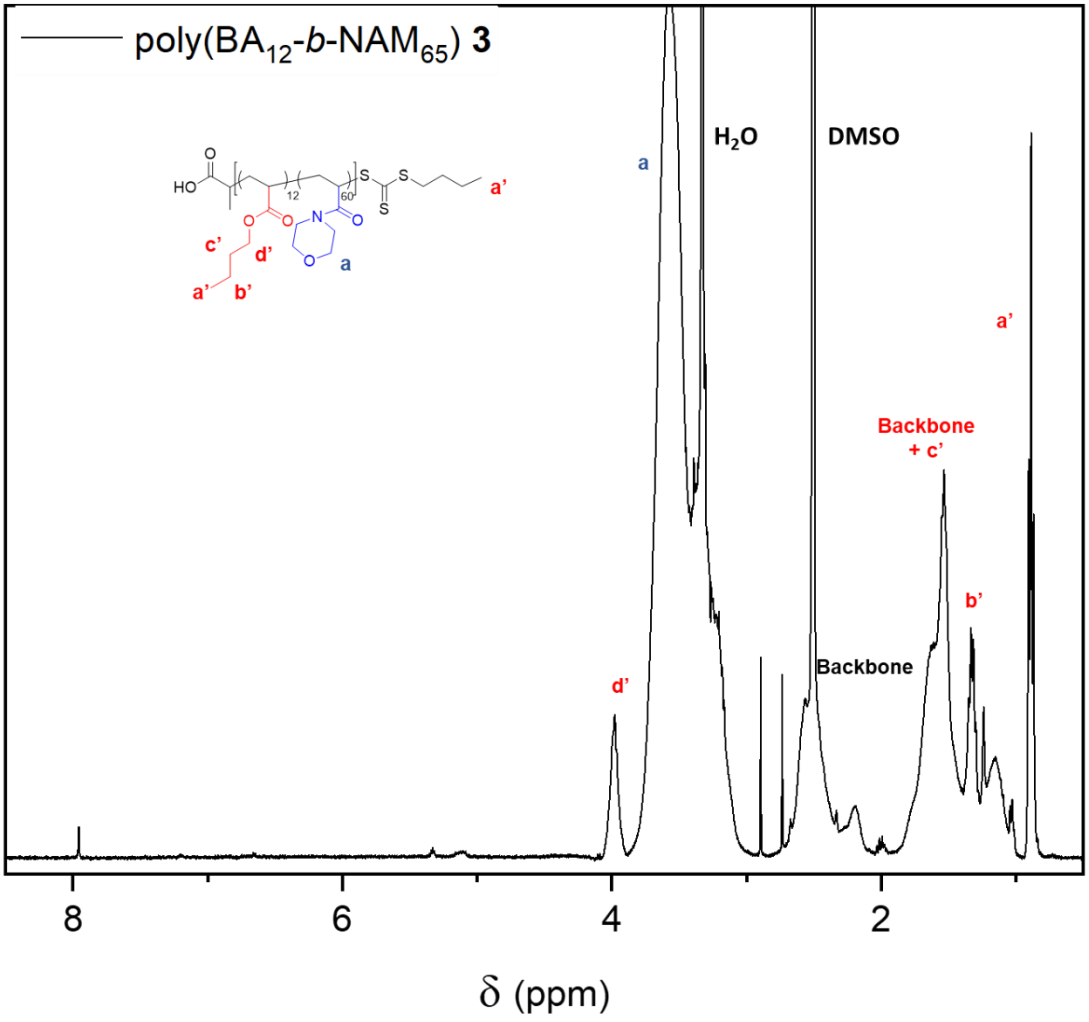

Figure C-2: Proton NMR spectrum with assignment for polymer **3**.

C.1.3 NMR spectrum polymer 4

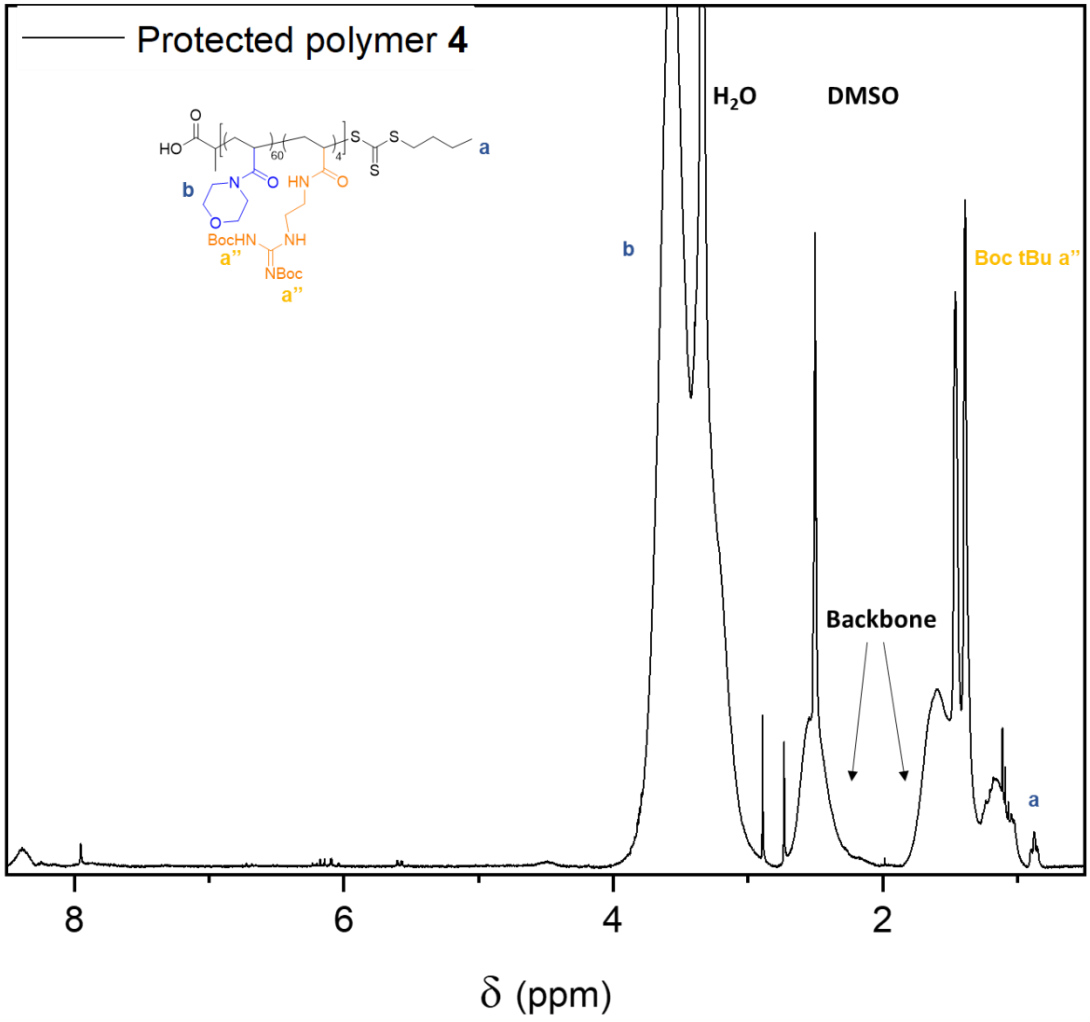

Figure C-3: Proton NMR spectrum with assignment for polymer **4**

C.1.4 NMR spectrum polymer 5

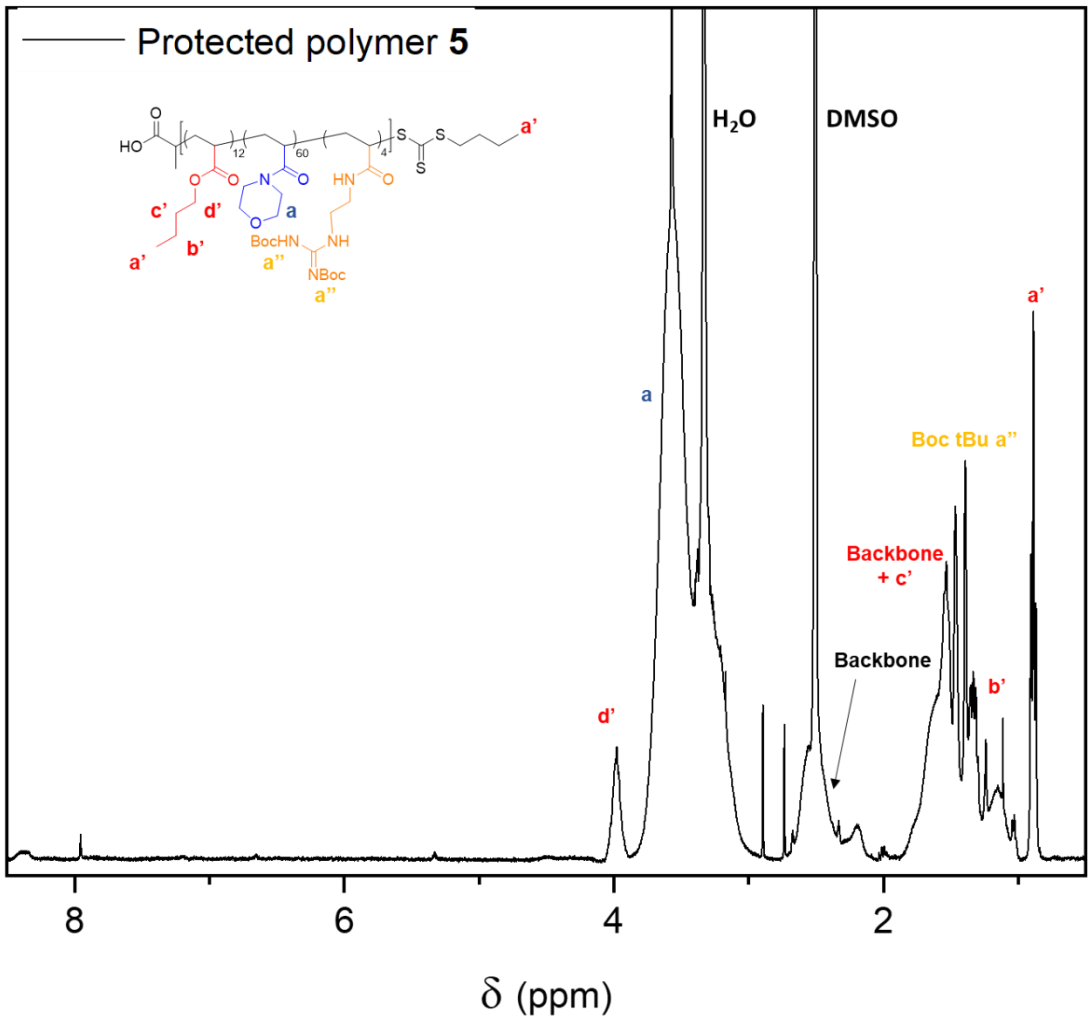

Figure C-4: Proton NMR spectrum with assignment for polymer **5**.

C.1.5 NMR spectrum CPNT 6

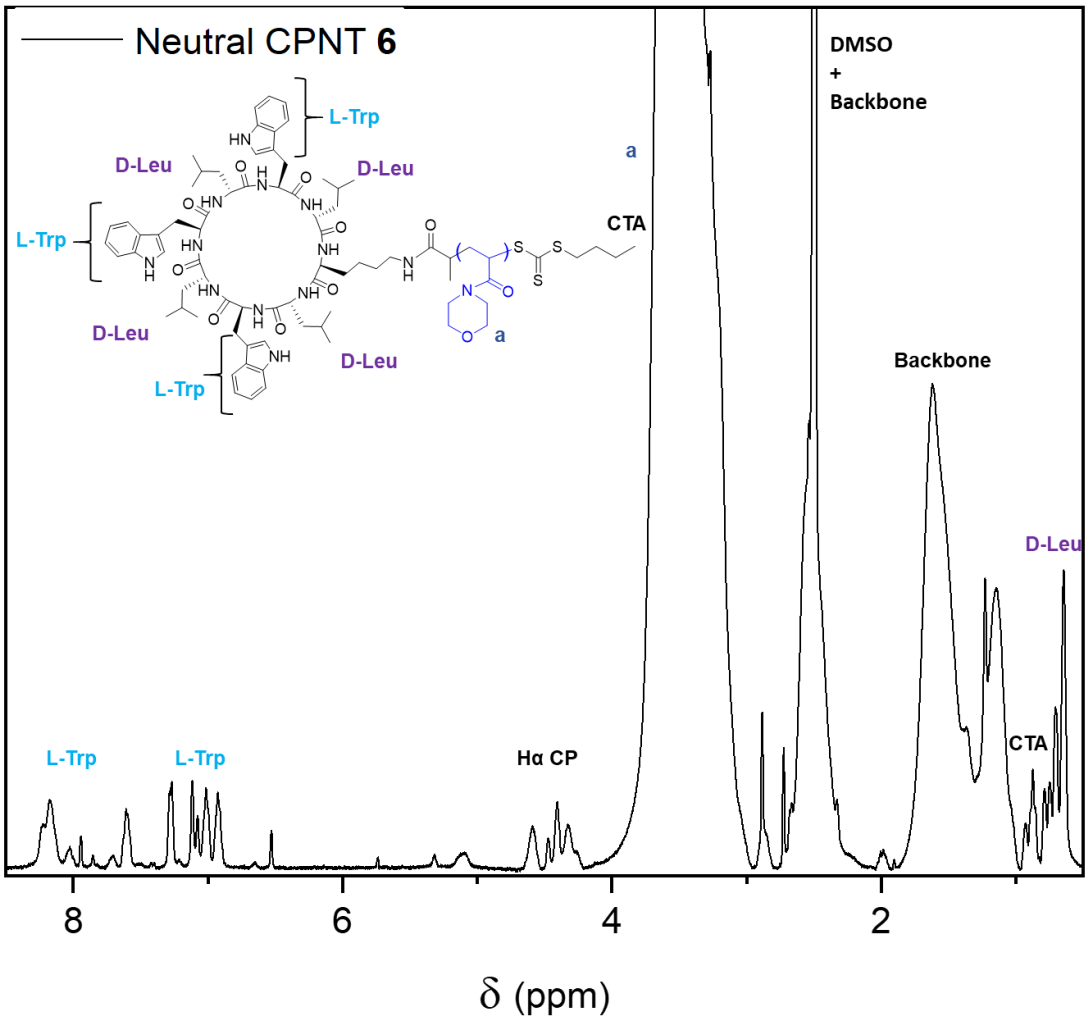

Figure C-5: Proton NMR spectrum with assignment for CPNT **6.**

C.1.6 NMR spectrum CPNT 7

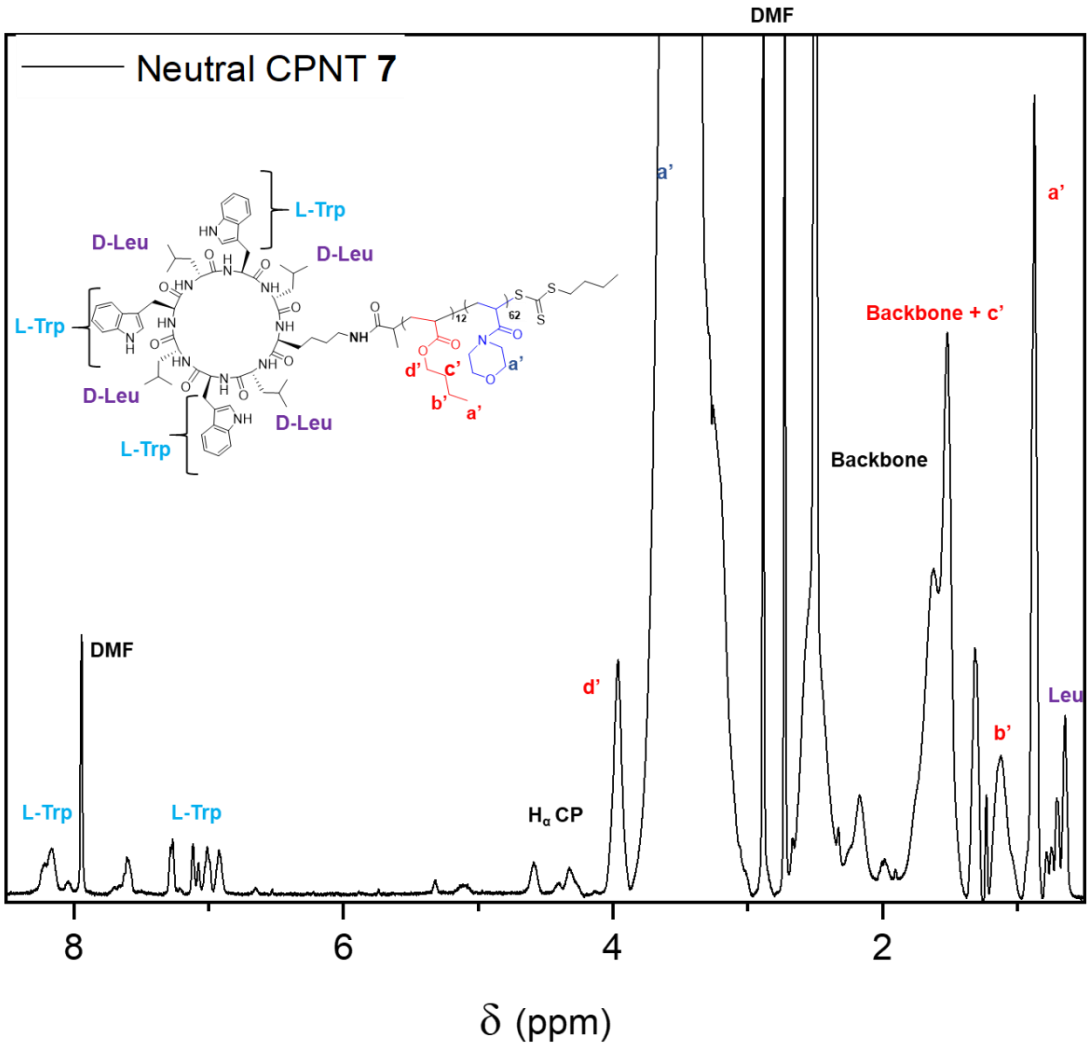

Figure C-6: Proton NMR spectrum with assignment for dynamic CPNT **7.**

C.1.7 NMR spectrum charged polymer 8

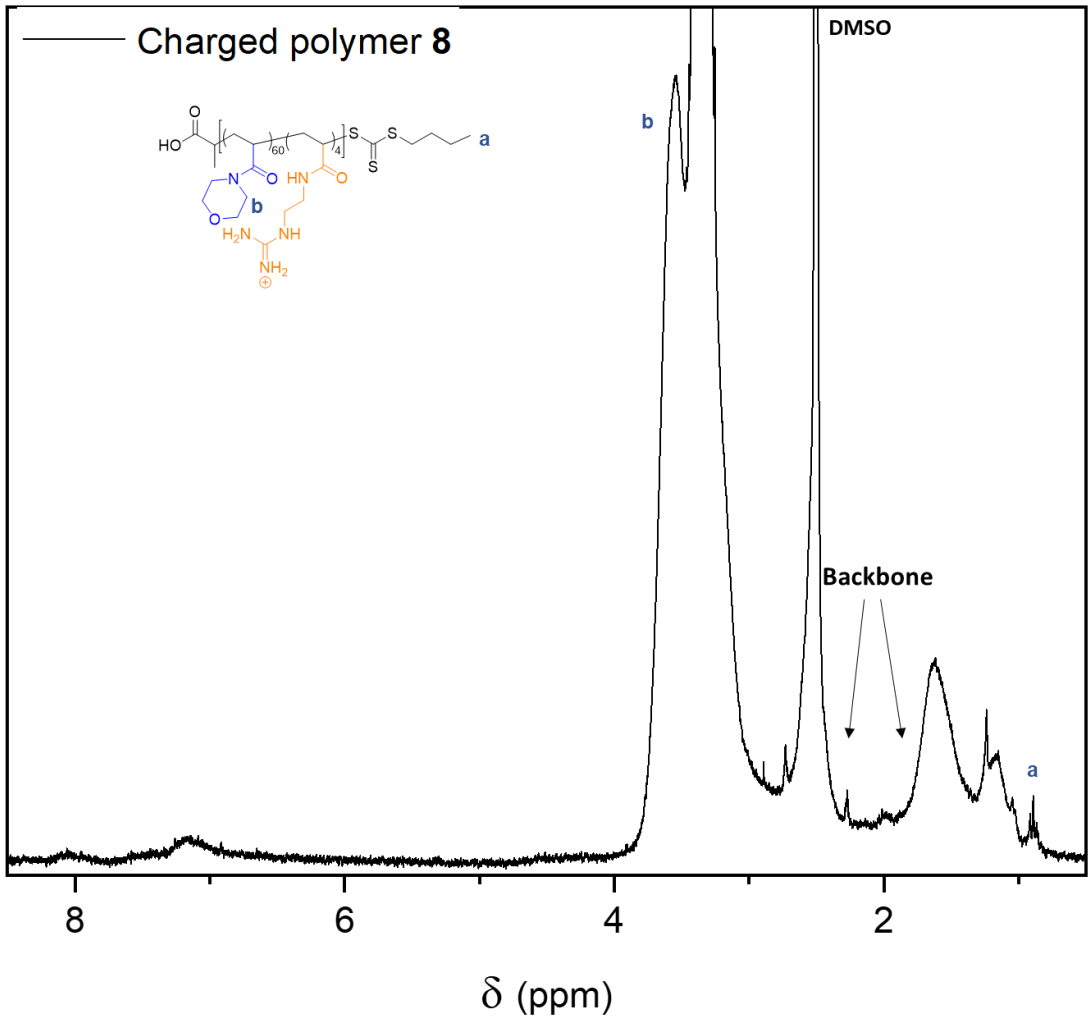

Figure C-7: Proton NMR spectrum with assignment for charged polymer **8.**

C.1.8 NMR spectrum charged polymer 9

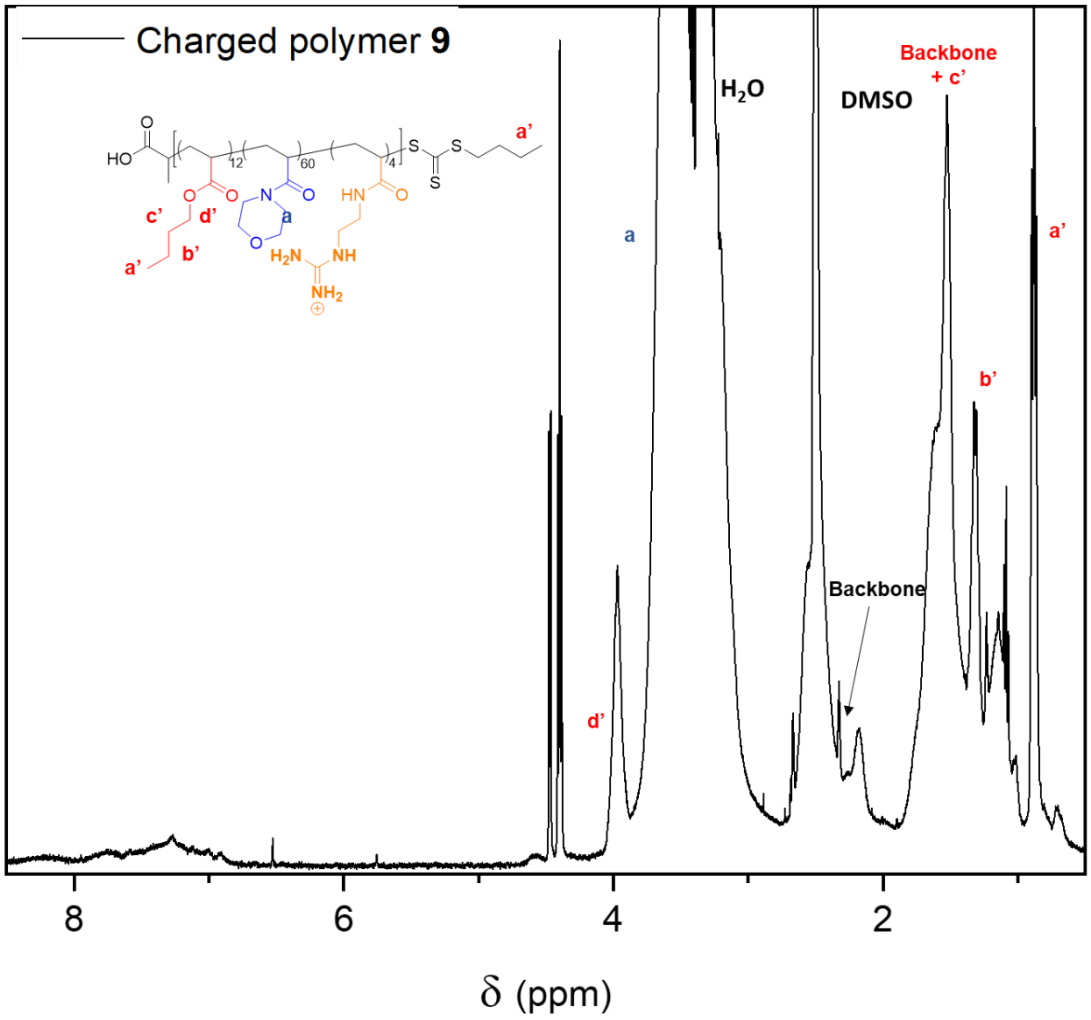

Figure C-8: Proton NMR spectrum with assignment for charged polymer **9**.

C.1.9 NMR spectrum of charged CPNT 10

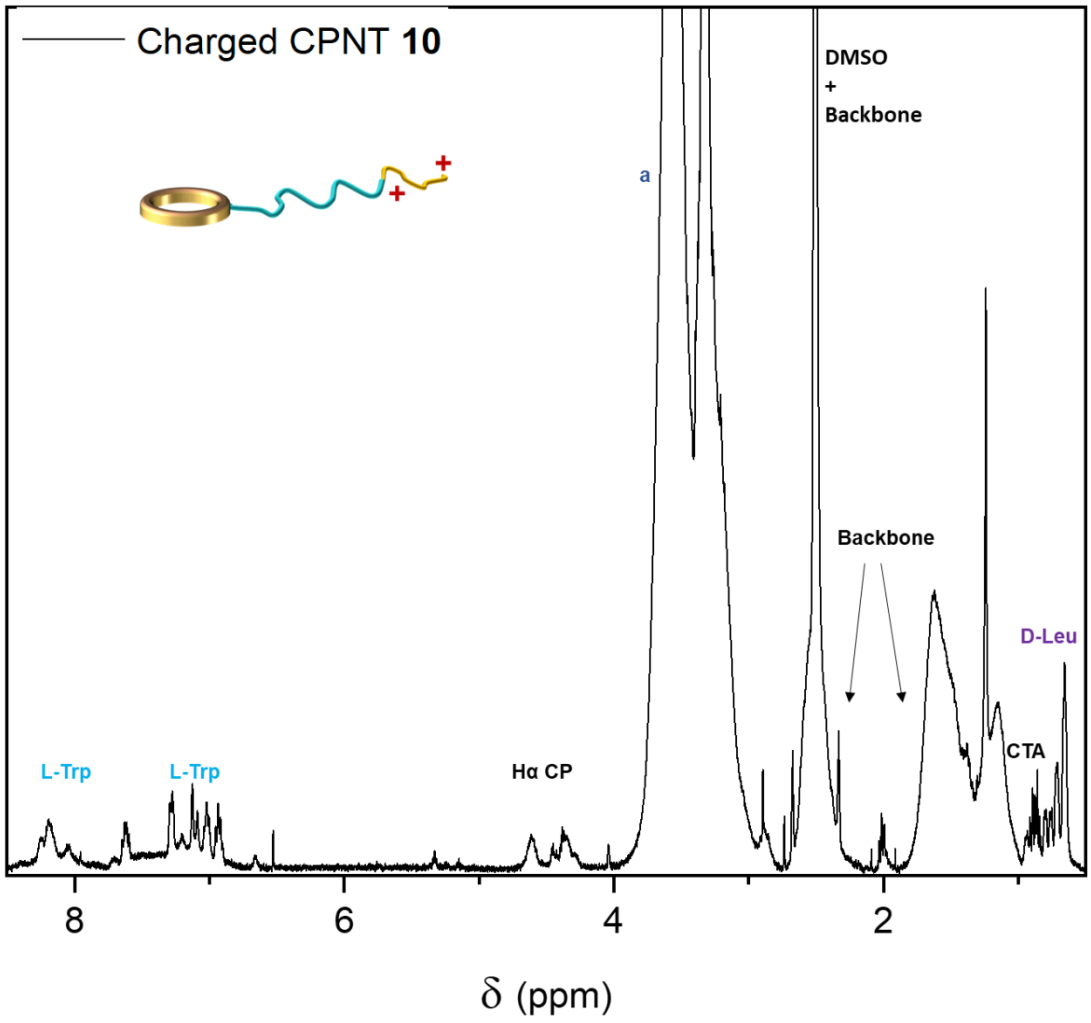

Figure C-9: Proton NMR spectrum with assignment for charged CPNT **10**.

C.1.10 NMR spectrum of charged CPNT 11

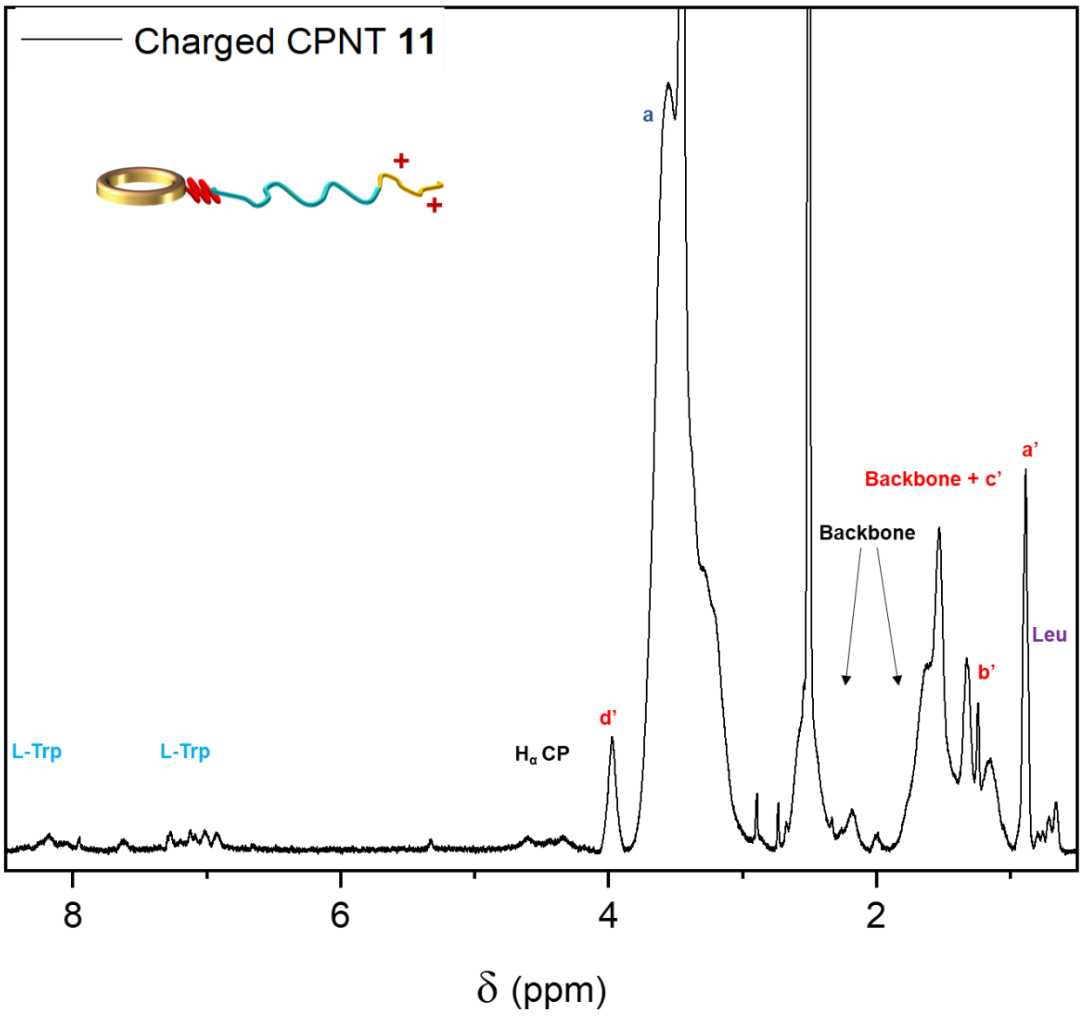

Figure C-10: Proton NMR spectrum with assignment for charged CPNT **11**.

C.2 Characterisation (SAXS)

C.2.1 Fitting models employed

In this chapter the fitting process employed was similar to Chapter 2; given the excellent fit with models obtained, other models were not further considered for this dataset and therefore are not presented here.

C.2.1.1 Core-shell cylinder model (SasView)

The core-shell cylinder employed from SasView considers the system to be composed of a cylindrical core with a certain scattering length density (SLD_{core}) and radius, surrounded by a shell enveloping it fully (SLD_{shell}), with a thickness t.[1, 2] The length of the total cylinder is the length of the core cylinder plus twice the thickness of the shell. A correction for polydispersity of thickness (assuming a lognorm distribution) has been accounted for to correct the fringes in the curve. The full equations ruling this model are detailed on the SasView website.[2] The scale is related to the volume fraction of particles present in the system. The background was associated to the X-ray source. SLD were calculated using the sum of the coherent scattering lengths for all atoms (obtained from the atomic number) constituting the molecules of interest and dividing it by the calculated molecular volume. The molecular volume of a monomer unit was assumed to be an invariant upon polymerisation, therefore the molecular volume was calculated from the mass density of the monomer which was then used to calculate the scattering length density. The core was considered to be either the CP (with a fixed core radius of 3.5 Å and SLD of $11.54.10^{-6}Å^{-2}$) or to be CP-poly(BA) (SLD of $9.62.10^{-6}Å^{-2}$ calculated as the sum of the SLD of poly(BA) and the SLD of CP **1**, affected by the molar ratios of each component; the core was let to fit with a lower limit of 3.5 Å).

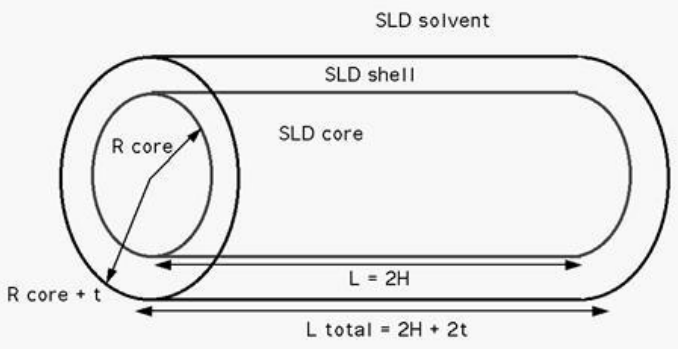

Throughout all model-dependant SAXS analysis in this chapter, the reduced chi^2 value was used as a statistical indicator of the goodness of the fit (a low value corresponding to a better fit).

C.2.2 SAXS data fitting parameters for CPNT 6, 7, 10 and 11 (D_2O HEPES buffer)

Table C-1: SAXS data fitting parameters for CPNT **6**, **7**, **10** and **11**
(D_2O HEPES buffer (20 mM, pD = 7.2) at 5 mg/mL),
using the core-shell cylinder model in SasView
(CP core: the cyclic peptide alone is considered to be the core and the radius of the core was fixed;
BA core: the CP and the poly(BA) contribution are combined and considered as a core; in this case the radius of the core was fitted).

	Nature of the parameter	CPNT **6**	CPNT **7**	CPNT **10**	CPNT **11**	CPNT **11**
Model		CP core	CP core	CP core	CP core	BA core
Scale	Fitted	$4.99.10^{-3}$	$4.25.10^{-3}$	$8.47.10^{-3}$	$2.14.10^{-2}$	$9.33.10^{-3}$
Background	Fixed	0.001	0.001	0.005	0.001	0.001
SLD_{core} ($10^{-6}Å^{-2}$)	Calculated	11.54	11.54	11.54	11.54	9.62
SLD_{shell} ($10^{-6}Å^{-2}$)	Calculated	10.34	10.09	10.34	10.01	10.34
SLD_{solv} ($10^{-6}Å^{-2}$)	Calculated	9.51	9.512	9.512	9.512	9.512
Radius core (Å)	Fixed/Fitted*	3.5	3.5	3.5	3.5	22*
Thickness (Å)	Fitted	50	69	46	74	54
Length (Å)	Fixed/Fitted	98	83	68	213	268
Polydispersity of thickness[3]	Fixed	0.05	-	-	0.05	-
Reduced Chi[2]		5.09	1.27	3.46	5.98	7.61

***:** value set to 22 according to previous fits in Chapter 3.

[3] PD ratio: a normal logarithmic distribution was employed for all calculations involving polydispersity.

C.3 Lipid bilayer studies

C.3.1 Fitting procedure for the reflectivity study

NR data corresponding to the lipid bilayers at the Si-water interface were analysed using RasCAL[3] by Dr. Stephen C. Hall. The analysis was based on a multilayer 'slab' model; SLD profiles were generated for each layer in the system, the reflectivity was then estimated and compared to the measured data. The following parameters could be obtained for each layer: thickness, hydration, roughness. The fitting of these parameters was constrained in order to respect physical and chemical limitations, similarly to previous work.[4, 5] Data for CPNT **10** consisted of 9 measurements.

The initial contrasts, acquired in H_2O and D_2O buffers, were for the Si block (and the SiO_2 layer on its surface) before incubation of the lipid bilayer. The SLD values were extracted from the literature and directly entered. Only the SLD of the bulk solvent solution was left to vary in order to account for the different isotopic contrasts measured and any potential exchange of the deuterated phase with water.

C.3.1.1 Bilayer formation

The next contrasts measured corresponded to the lipid bilayer incubation and were D_2O, H_2O and CMSi (38% v/v D_2O). Six layers were used to model this dataset: the Si substrate (with the silicon oxide layer), a small water gap as the bilayers were partially floating (good fits could not be obtained without this), the inner phospholipid head groups and lipid tails and the outer tails and head groups, accounting for the presence of two different lipids (dDMPC and hDMPG). Asymmetry between the inner and outer leaflet was accounted for in this model. Accordingly, constraints were applied in order to ensure that the mean molecular area was consistent between the head group and the tail layer within a leaflet (inner or outer) so that the model was physically realistic. A mean molecular area for each leaflet was calculated from the fitted thickness of the respective phospholipid tail layer, where:

$$A_{Inner\ Tails} = \frac{V_{m,DM}}{d_{Inner\ Tails}(1-\chi_{Solvent,in})}, A_{Outer\ Tails} = \frac{V_{m,DM}}{d_{Outer\ Tails}(1-\chi_{Solvent,out})}$$

Here, $A_{inner\ Tails}$ and $A_{Outer\ Tails}$ represent the mean molecular area determined from the thickness and hydration of the dimyristoyl tails (with the assumption that solvent penetration into such a hydrophobic layer is negligible, where solvent presence is due to incomplete bilayer coverage), $V_{m,DM}$ (782 $Å^3$) represents the partial specific molecular volume of the phospholipid tails[6] and $d_{Inner\ Tails}$ and $d_{Outer\ Tails}$ correspond to the fitted thickness of the inner or outer tail layer (before interaction, $d_{Inner\ Tails} = d_{Outer\ Tails}$).

To correct for any incomplete surface coverage of the bilayer, additional parameters, the solvent volume fraction within the inner or outer tail layer $\chi_{Solvent,in}$ and $\chi_{Solvent,out}$ were introduced (they were constrained to be the same before interaction).

The apparent hydrated area of the lipid headgroups (inner and outer), was also calculated, taking into account the presence of both phosphatidylcholine (PC) and phosphatidylglycerol (PG) head groups. For each leaflet, the apparent hydrated area was calculated following the equation:

$$A_{Inner\ HG,Hyd} = \chi_{PC,inner}\frac{V_{m,PC}}{d_{Inner\ HG}} + \left(1 - \chi_{PC,inner}\right)\frac{V_{m,PG}}{d_{inner\ HG}}$$

$$A_{Outer\ HG,Hyd} = \chi_{PC,outer}\frac{V_{m,PC}}{d_{Outer\ HG}} + \left(1 - \chi_{PC,outer}\right)\frac{V_{m,PG}}{d_{outer\ HG}}$$

Where $V_{m,PC}$ and $V_{m,PG}$ correspond to the partial specific molecular volume of PC and PG headgroups respectively and $d_{Inner\ HG}$ and $d_{Outer\ HG}$ represent the fitted thickness of the inner and outer headgroup layer.

To ensure that the model represents a chemically consistent structure, the mean molecular area of the headgroups must equal that of the phospholipid tails. Therefore, the volume fraction of 'dry' lipid headgroups, $\chi_{Inner\ HG}$ and $\chi_{Outer\ HG}$ within the inner and outer headgroup layers could be calculated as:

$$\chi_{Inner\ HG} = \frac{A_{Inner\ HG,Hyd}}{A_{Inner\ Tails}}, \chi_{Outer\ HG} = \frac{A_{Outer\ HG,Hyd}}{A_{Outer\ Tails}}$$

From this result, the volume fraction of solvent in the inner and outer headgroup layers, $\chi_{Solvent,in}$, and $\chi_{Solvent,out}$ could be determined as:

$$\chi_{Solvent,in} = 1 - \chi_{Inner\ HG}, \chi_{Solvent,out} = 1 - \chi_{Outer\ HG}$$

An additional constraint was applied, to make sure that the thickness of both head and tail layers could not exceed the maximum thickness for a fully extended (all-trans) tail conformation based on the Tanford equation.

SLD values for the inner and outer headgroup layers were calculated based on literature values for partial specific molecular volumes as described by Pan *et al.*[6] and were held as a constant throughout the fitting process. The contribution of each lipid head group was accounted for, affording the SLD for inner and outer headgroups:

$$SLD_{inner\ HG} = \chi_{PC,inner}.SLD_{dPC} + \left(1 - \chi_{PC,inner}\right).SLD_{hPG}$$

$$SLD_{outer\ HG} = \chi_{PC,outer}.SLD_{dPC} + \left(1 - \chi_{PC,outer}\right).SLD_{hPG}$$

Similarly, the SLD for tail layers were calculated:

$$SLD_{inner\ tail} = \chi_{PC,inner}.SLD_{dDM} + \left(1 - \chi_{PC,inner}\right).SLD_{hDM}$$

$$SLD_{outer\ HG} = \chi_{PC,outer}.SLD_{dDM} + \left(1 - \chi_{PC,outer}\right).SLD_{hDM}$$

In these equations, SLD_{dDM}, SLD_{dPC}, SLD_{hDM} and SLD_{hPG} corresponded to the calculated SLD of the deuterated DM tails, PC headgroups and hydrogenated DM tails and PG headgroups respectively (calculated as the ratio of the sum of atomic neutron scattering lengths and the molecular volume). Surface roughness was fitted to be equal for all layers within the lipid bilayer, since these layers are all physically coupled. Upon incubation of neutral CPNT **6**, this model was kept as very little changes could be observed on the acquired reflectivity profiles.

*C.3.1.2 After interaction with CPNT **10***

Adjustments were made to the aforementioned model lipid bilayer to account for interaction of CPNT **10** including embedding in the lipid bilayer and the formation of an additional diffuse layer. In addition to the three usual contrasts measured, a fourth contrast 4 MW (66% v/v D_2O) was acquired during the experiment to compensate for the added complexity induced by the addition of a compound capable of interaction. Similarly to the model lipid bilayer before adding CPNT **10**, physical constraints were implemented and a mean molecular area was calculated after interaction:

$$A_{Inner\ Tails,after} = \frac{V_{m,DM}}{d_{Inner\ Tails,after}.C_{inner,after}}$$

$$A_{Outer\ Tails,after} = \frac{V_{m,DM}}{d_{Outer\ Tails,after}.C_{outer,after}}$$

The notations are the same as above with the addition of after, referring to the values after incubation. The bilayer coverage fractions in each leaflet were annotated $C_{inner,after}$ and $C_{outer,after}$ (in here: $C_{inner,after} = C_{outer,after} = \chi_{Solvent}$, with being the volume fraction of solvent constrained to be equal to the one prior to injection). The calculation for the apparent inner and outer hydrated headgroups was carried out in the same way, simply using the fitted thickness values after incubation; the volume fraction of the dry lipid headgroups $\chi_{Inner\ HG,after}$ was also calculated in the same way than before. The embedding of CPNT **10** polymer chains into the bilayer was accounted for by combining solvent penetration and polymer embedding in the following set of equations; the volume fraction of solvent and "dry" CPNT **10** for each layer (example for inner head group and inner tail) were determined by:

For inner HG:

$$\chi_{Solvent,inner\ HG\ after} = \left(1 - \chi_{CPNT\ inner\ HG\ ,hyd}\right).\left(1 - \chi_{Inner\ HG,after}\right)$$

$$\chi_{CPNT\ inner\ HG} = \chi_{CPNT\ inner\ HG\ ,hyd}.\left(1 - \chi_{Inner\ HG,after}\right)$$

For inner tails:

$$\chi_{Solvent,inner\ tails\ after} = \left(1 - \chi_{CPNT\ inner\ tails\ ,hyd}\right).\left(1 - C_{inner,after}\right)$$

$$\chi_{CPNT\ inner\ HG} = \chi_{CPNT\ inner\ tail\ ,hyd}.\left(1 - C_{inner,after}\right)$$

$\chi_{CPNT\ inner\ HG\ ,hyd}$ was introduced as a fitting parameter representing the apparent volume fraction of embedded hydrated CPNT **10** in the inner headgroups. The same principles have been used to calculate the volume fractions of dry CPNT in the outer headgroup and tail layers. Subsequently, SLD values were calculated for each layer after interaction (example for inner headgroups and tails):

$$SLD_{inner\ HG,after} = \chi_{inner\ HG,after}.SLD_{inner\ HG} + \chi_{Solvent,inner\ HG\ after}.SLD_{solvent} + \chi_{CPNT\ inner\ HG}.SLD_{CPNT}$$

$$SLD_{inner\ \text{tails},after} = \chi_{inner\ tails,after}.SLD_{inner\ HG} + \chi_{Solvent,inner\ tails\ after}.SLD_{solvent} + \chi_{CPNT\ inner\ tails}.SLD_{CPNT}$$

These equations effectively correct the SLD of the bilayer alone by including contributions from CPNT **10** and any solvent that was incorporated to the bilayer with it. Again the same equations were used for outer tails and headgroups.

The fitting process was co-refined across all data sets. The resolution for each contrast was set to the real-space distance corresponding to the maximum value of q, $d_{max} = \frac{2\pi}{q_{max}}$. Any features below that cut-off could not be fully resolved but may still contribute to the features observed in the experimental dataset. Structural features and changes were extracted from the data using multiple experimental contrasts. The error associated with each parameter used in each model was estimated using a Bayesian Monte Carlo Markov Chain (MCMC) statistical analysis on RasCAL. The joint variability between each parameter (covariance) was accounted for in this analysis. The algorithm employed assumed a Gaussian distribution for each parameter (where 95% of the spread is covered by the mean ± standard deviation) as an initial condition. The number of iterations was set to 50,000, with 5,000 burn-in points (where the model is tested against data) to determine local minima. 95% Confidence intervals (CI) were then calculated for three independent repeats of this procedure. The assessment of statistical significance was done by looking at the absence of overlap between the confidence intervals for different data sets. Fits and associated errors are approximated to the nearest Angström to account for the limited number of contrasts and the finite q-range.

C.3.2 Fluorescence spectroscopy full spectra over time.

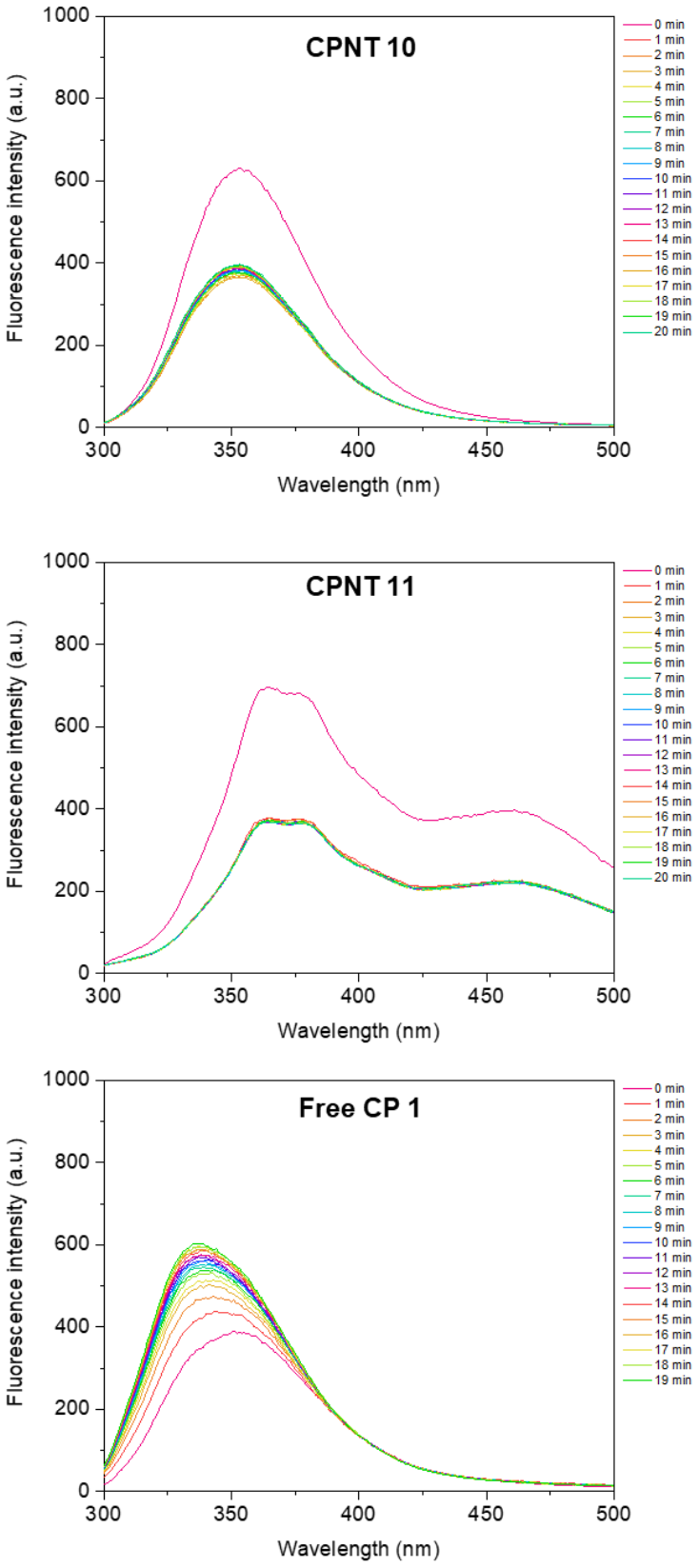

Figure C-11: Trp fluorescence profiles for CPNT **10**, **11** and free CP **1** in water in the presence of DMPC: DMPG 80:20 lipid vesicles (time-lapse: 0-20 min, 1 spectrum per minute).

C.4 References

1. I. Livsey, *Journal of the Chemical Society, Faraday Transactions 2: Molecular and Chemical Physics*, 1987, **83**, 1445.
2. www.sasview.org.
3. P. Klint, J. J. Vinju and T. v. d. Storm, Braga, Portugal, 2009.
4. M.-A. Sani, A. P. Le Brun and F. Separovic, *Biochimica et Biophysica Acta (BBA) - Biomembranes*, 2020, **1862**, 183204.
5. S. Tatur, M. Maccarini, R. Barker, A. Nelson and G. Fragneto, *Langmuir*, 2013, **29**, 6606.
6. J. Pan, F. A. Heberle, S. Tristram-Nagle, M. Szymanski, M. Koepfinger, J. Katsaras and N. Kučerka, *Biochimica et Biophysica Acta (BBA) - Biomembranes*, 2012, **1818**, 2135

Appendix D: List of Publications Associated with the Thesis

D.1 First author publications

Chapter 2:

1. Sean H. Ellacott; Carlos Sanchez-Cano; Edward D.H. Mansfield; Julia Y. Rho; Ji-Inn Song; Raoul Peltier; Sébastien Perrier. Comparative study of the cellular uptake and intracellular behaviour of a library of cyclic peptide-polymer nanotubes with different self-assembling properties, *Manuscript submitted*

In preparation (from Chapter 3):

2. Sean H. Ellacott; Erny Sagita; Estelle Suys; Joaquin Sanchis-Martinez; Christopher Porter; Sébastien Perrier. A pharmacokinetic and biodistribution study of dynamic and stabilised cyclic peptide-polymer nanotubes.

In preparation (from Chapter 4):

3. Sean H. Ellacott; Edward D.H. Mansfield; Ramon Garcia-Maset; Agnes Kuroki; Stephen C.L. Hall; Sébastien Perrier. Understanding the membrane interaction of cationic cyclic peptide-polymer nanotubes with model lipid bilayers.

D.2 Other contributions

4. Tomos E. Morgan; Sean H. Ellacott; Christopher A. Wootton; Mark P. Barrow; Anthony W. T. Bristow; Sébastien Perrier; Peter B. O'Connor. Coupling Electron Capture Dissociation and the modified Kendrick mass defect for sequencing of a poly(2-ethyl-2-oxazoline) polymer, *Anal. Chem.*, **2018**, 90, 11710

5. Julia Y. Rho; Henry Cox; Edward D.H. Mansfield; Sean H. Ellacott; Raoul Peltier; Johannes Brendel; Matthias Hartlieb; Thomas A. Waigh; Sébastien Perrier. Dual self-assembly of supramolecular peptide nanotubes to provide stabilisation in water, *Nat. Comm.*, **2019**, 10, 1

6. Edward D.H. Mansfield; Sean H. Ellacott; Pratik Gurnani; Julia Y. Rho; Sebastien Perrier. Mechanisms of self-assembly for cyclic peptide-polymer conjugates and subsequent interaction to form statistical supramolecular copolymers, *Manuscript submitted*.

7. Mitchell R. Silk; Biswaranjan Mohanty; Julia Y. Rho; Sean H. Ellacott; Sébastien Perrier; Martin J. Scanlon; Philip E. Thompson; David K. Chalmers. Developing the stability and function of modular nanorods built from cyclic D/L peptides, *Manuscript submitted*.

8. Pratik Gurnani; Carlos Sanchez-Cano; Helena Xandri-Monje; Junliang Zhang; Sean H. Ellacott; Edward D.H. Mansfield; Matthias Hartlieb; Kai Yu; Olivier Cayre; Robert Dallmann; Sébastien Perrier. Probing the effect of rigidity on the cellular uptake of core-shell nanoparticles: Stiffness effects are size dependent, *Manuscript in preparation.*